Doctoral Thesis

Mechanistic Insights into Inter-Organellar Membrane Contact Sites Based on Crystal Structures

Jumi Park

Department of Biological Sciences

Ulsan National Institute of Science and Technology

2021

Mechanistic Insights into Inter-Organellar Membrane Contact Sites Based on Crystal Structures

Jumi Park

Department of Biological Sciences

Ulsan National Institute of Science and Technology

Mechanistic Insights into Inter-Organellar Membrane Contact Sites Based on Crystal Structures

A thesis/dissertation submitted to
Ulsan National Institute of Science and Technology
in partial fulfillment of the
requirements for the degree of
Doctor of Philosophy

Jumi Park

09 / 24 / 2020 of submission

Approved by

Advisor
Changwook Lee

Mechanistic Insights into Inter-Organellar Membrane Contact Sites Based on Crystal Structures

Jumi Park

This certifies that the thesis/dissertation of Jumi Park is approved.

09 / 24 / 2020 of submission

Advisor: Changwook Lee

Byoung Heon Kang

Chunghun Lim

Jung-Min Kee

Young Chan Chae

Abstract

Eukaryotic cells contain various membrane-bound subcellular compartments called organelles. For cell survival, organelles perform specific functions respectively or cooperate through communication. Recently, as the development of electron microscopy, it has been discovered that organelles are located closely and make contact sites with about 10 nm distance between two membranes, which is called membrane contact sites (MCSs). MCSs are constructed and maintained stably or transiently by tethering structures mainly composed of proteins. It has been revealed that MCSs are important sites for various cellular functions such as intracellular signaling, lipid and ion exchange, organelle trafficking, and inheritance. Nucleus-vacuole junctions (NVJs) are one of the firstly identified MCSs in the budding yeast *Saccharomyces cerevisiae*. The formation of NVJs depends on the nuclear membrane protein Nvj1 and vacuolar protein Vac8. NVJs formed by the interaction between Vac8 and Nvj1 are critical for mediating piecemeal microautophagy of the nucleus (PMN), one of the selective microautophagy pathways in the yeast. Herein, we report the crystal structure of Vac8-Nvj1 complex. Vac8 comprises the H1 helix at the N terminus, followed by 12 armadillo repeats (ARMs). The 80 Å extended loop of Nvj1 binds to the conserved inner groove of Vac8 ARM domain in an antiparallel manner. Disruption of the Vac8-Nvj1 interaction results in the loss of NVJ formation and further PMN in *Saccharomyces cerevisiae*. Vac8 cationic triad (Arg276, Arg317, and Arg359) motifs interacting with Nvj1 are also critical to the recognition of Atg13, a key component of the cytoplasm-to-vacuole targeting (CVT) pathway, indicating competitive binding to Vac8. Indeed, the crystal structure of Vac8-Atg13 complex reveals that the 70 Å extended loop of Atg13 binds to the ARM domain of Vac8 in a similar manner with Nvj1. The interaction between Vac8 and Atg13 is also essential for mediating CVT pathway in *Saccharomyces cerevisiae*. Structural, biochemical, and in vivo experiments demonstrate that the H1 helix of Vac8 intramolecularly interacts with the first ARM and regulates its self-association, which is crucial for PMN and CVT pathway. Crystal structures also reveal that Vac8-Nvj1 and Vac8-Atg13 form heterotetramer with the different quaternary organization. The structural comparison provides a molecular understanding of how a single ARM domain protein adopts different quaternary structures depending on its binding proteins to differentially regulate two closely related but distinct cellular pathways.

Next, recent research suggested that 3′-5′ exonuclease domain-containing protein 2, EXD2 plays an essential role as a new component of DNA double-strand break repair machinery in the nucleus with a conserved DEDDy superfamily 3′-5′ exonuclease domain. However, the following researches raised the possibility that EXD2 might be localized to mitochondria with unclear mitochondrial sublocation. Herein, electron microscope imaging analysis and proximity labeling reveals that EXD2 is anchored to the mitochondrial outer membrane through a conserved N-terminal transmembrane domain, while

the C-terminal region is cytosolic. The crystal structure of the exonuclease domain reveals a domain-swapped dimer in which the central α5–α7 helices are mutually crossed over, resulting in chimeric active sites. Additionally, the C-terminal segments absent in other DnaQ family exonucleases enclose the central chimeric active sites. Structural analyses of crystal structures in complex with Mn^{2+}/Mg^{2+} and biochemical experiments demonstrate that unusual dimeric organization and additional C-segments stabilize the active site, facilitate discrimination between DNA and RNA substrates based on divalent cation coordination, and generate a positively charged groove that binds substrates. Based on structural studies and previously reported data, we suggest that EXD2 can play possible roles in the mitochondrial outer membrane or inter-mitochondrial membrane contact sites with its novel exonuclease activity.

Keywords

3′-5′ exonuclease, Autophagy, APEX2, Atg13, Crystal structure, Cytoplasm-to-vacuole targeting, DEDDy superfamily, DnaQ family exonuclease, EXD2, Membrane contact sites, Metal coordination, Nucleus-vacuole junction, Nvj1, Organelle membrane protein, Piecemeal microautophagy of the nucleus, Spot-BioID proximity labeling, Substrate discrimination, Vac8

Contents

List of Figures

Chapter 1. Mechanistic insight into the nucleus-vacuole junction based on the Vac8-Nvj1 Crystal structure

Chapter 2. Quaternary structures of Vac8 differentially regulate the CVT and PMN pathways

Chapter 3. The structure of human EXD2 reveals a chimeric 3′ to 5′ exonuclease domain that discriminates substrates via metal coordination

List of Tables

Chapter 1. Mechanistic insight into the nucleus-vacuole junction based on the Vac8-Nvj1 Crystal structure

Chapter 2. Quaternary structures of Vac8 differentially regulate the CVT and PMN pathways

Chapter 3. The structure of human EXD2 reveals a chimeric 3′ to 5′ exonuclease domain that discriminates substrates via metal coordination

Abbreviations

Ape1	Aminopeptidase I
ARM	Armadillo repeat
Atg	Autophagy-related
AUC	Analytical ultracentrifugation
CD	Circular dichroism
CVT	Cytoplasm-to-vacuole targeting
DAB	Diaminodenzidine
DIC	Differential interference contrast
EM	Electron microscopy
EXD2	3′-5′ exonuclease domain-containing protein 2
EXD2-exo	EXD2 construct comprising residues 76–295
GFP	Green fluorescent protein
GST	Glutathione-S-transferase
HORMA	Hop1, Rev7 and MAD2 domain
IMM	Inner mitochondrial membrane
IMS	Mitochondrial inter-membrane space
ITC	Isothermal titration calorimetry
KF	Klenow fragment
MCS	Membrane contact sites
MIM	Microtubule interacting and transport (MIT)-interacting motif
MS	Mass spectrometry
NVJ	Nucleus-vacuole junction
OMM	Outer mitochondrial membrane
PDB	Protein data bank
PMN	Piecemeal microautophagy of the nucleus

prApe1	Precursor Ape1
RMSD	Root-mean-square deviation
SAXS	Small-angle X-ray scattering
SD-N	Nitrogen starvation medium
SEC	Size-exclusion chromatography
Se-SAD	Single-wavelength dispersion using Se-Met derivatized crystals
tAtg13	Atg13 construct comprising residues 567–695
TEM	Transmission electron microscopy
tEXD2	EXD2 construct comprising residues 76–564
TM	Transmembrane domain
tNvj1	Nvj1 construct comprising residues 229–321
tVac8	Vac8 construct comprising residues 10–515
Vac8	Vacuole related 8
Vac8ΔH1	Vac8 construct lacking residues 19–33
WRN	Werner syndrome protein

Chapter 1. Mechanistic insight into the nucleus-vacuole junction based on the Vac8-Nvj1 crystal structure

(Original article : Jeong H, Park J, Kim H-I, Lee M, Ko Y-J, Lee S, Jun Y, Lee C. Mechanistic insight into the nucleus-vacuole junction based on the Vac8p-Nvj1p crystal structure. *Proceedings of the National Academy of Sciences*. 2017 June 6;*114*(23):E4539-48.)

1.1. Abstract

Formation of the nucleus-vacuole junction (NVJ) is mediated by direct interaction between the vacuolar protein Vac8 and the outer nuclear endoplasmic reticulum membrane protein Nvj1. Herein we report the crystal structure of Vac8 bound to Nvj1 at 2.4 Å resolution. Vac8 comprises a flexibly connected N-terminal H1 helix followed by 12 armadillo repeats (ARMs) that form a right-handed superhelical structure. The extended 80 Å long loop of Nvj1 specifically binds the highly conserved inner groove formed from ARM1−12 of Vac8. Disruption of the Nvj1-Vac8 interaction results in the loss of tight NVJs, which impairs piecemeal microautophagy of the nucleus in *Saccharomyces cerevisiae*. Vac8 cationic triad (Arg276, Arg317, and Arg359) motifs interacting with Nvj1 are also critical to the recognition of Atg13, a key component of the cytoplasm-to-vacuole targeting (CVT) pathway, indicating competitive binding to Vac8. Indeed, mutation of the cationic triad abolishes CVT of Ape1 in vivo. Combined with biochemical data, the crystal structure reveals a Vac8 homodimer formed from ARM1, and this self-association, likely regulated by the flexible H1 helix and the C terminus of Nvj1, is critical for Vac8 cellular functions.

1.2. Introduction

Membrane contact sites (MCSs) between subcellular compartments play pivotal roles in cellular processes such as cooperative lipid biosynthesis, ion homeostasis, and interorganellar trafficking of molecules in eukaryotic cells [1-3]. MCSs are physically formed through dynamic and direct interactions between proteins that are located in two distinct subcompartments. The nucleus-vacuole junction (NVJ), one of the best-characterized MCSs, is a physical contact site between perinuclear and vacuolar membranes and mediates essential cellular processes such as piecemeal microautophagy of the nucleus (PMN) and lipid biosynthesis in yeast [4, 5]. PMN is a selective autophagic recycling process stimulated by carbon or nitrogen starvation through the target of rapamycin signaling pathway in *Saccharomyces cerevisiae*. Upon nutrient starvation, the region of the nucleus in the vicinity of NVJs invaginates into the vacuolar lumen and forms a bleb-like structure, which is released as a vesicle and eventually degraded by vacuolar hydrolases [5, 6]. Because PMN occurs at the NVJ sites, their formation is essential for the initiation of the PMN process [7]. NVJs are also involved in lipid metabolism by recruiting the two lipid-modifying enzymes, oxystereol-binding proteins homology (Osh1) involved in nonvesicular lipid trafficking and the enoyl-CoA reductase Tsc13 that mediates the synthesis of very-long-chain fatty acids [8-11].

Previous studies revealed that NVJs are generated by forming tight interactions between Vac8, a vacuolar membrane protein, and Nvj1, a nuclear membrane protein [12]. Vac8 was initially found as a key player in vacuole inheritance by cooperating with Vac17, actin, profilin, and Myo2 [13]. In addition, Vac8 has a crucial role in mediating the processing of aminopeptidase I through interaction with Atg13 in the cytoplasm-to-vacuole targeting (CVT) pathway during this selective autophagy [13, 14]. Sequence analyses of Vac8 predicted several armadillo repeat (ARM) domains, each consisting of 40 residues that fold into three characteristic short helices tandemly organized into a superhelical structure that serves as a protein-binding platform for interaction with other physiologically relevant molecules [15]. Whereas Vac8 is involved in various processes by providing a protein-protein interaction module in the vacuole, Nvj1 is found exclusively in the circumscribed area of NVJs at the nuclear membrane [4, 10, 12, 16]. It has been suggested that Nvj1 acts as a scaffold to physically and functionally connect NVJs to lipid metabolism by interacting with both Vac8 and Tsc13 or Osh1.

Despite the biological importance of the Vac8-Nvj1 interaction for the formation of NVJs and the PMN process, the underlying mechanism by which Vac8 recognizes Nvj1 and exactly how the complex is organized to form NVJs and carry out PMN remain largely unknown. In this study, we determined the 2.4 Å resolution crystal structure of Vac8 bound to Nvj1. Together with biochemical

analyses and in vivo functional studies using the budding yeast *S. cerevisiae*, the structure provides fundamental insight into the structural and multifunctional roles of Vac8 in the formation of NVJs and physiological processes such as PMN and CVT pathways at the molecular level.

1.3. Results

1.3.1. Vac8 directly interacts with Nvj1

Vac8 is composed of 578 residues and is predicted to have several ARM repeats spread across the whole sequence (Figures 1.1A and 1.2). The N-terminal residues (1–10) are modified by lipidation in the form of myristoylation and palmitoylation and are anchored into vacuolar lipid bilayers [13], whereas the remaining regions are localized to the cytosol. Nvj1 comprises 321 amino acids and is a typical type I membrane protein consisting of a single transmembrane domain that passes through the nucleus and endoplasmic reticulum (ER) membranes in this case, whereas the C terminus is localized to the cytosol (Figure 1.1A). Previous studies using yeast two-hybrid analysis and coimmunoprecipitation revealed that the C-terminal domain (residues 281–321) of Nvj1 that is exposed to the cytosol binds to Vac8 [12]. To further examine whether this interaction is direct, we prepared full-length recombinant Vac8 and truncated Nvj1 comprising residues 229–321 (subsequently referred to as tNvj1) by overexpression and purification using *Escherichia coli* and analyzed their binding using size-exclusion chromatography (SEC). Figure 1.1B shows that purified Vac8 directly interacts with purified tNvj1, because the Vac8-tNvj1 complex was eluted from the gel-filtration column at a volume corresponding to the molecular size of the expected heterodimer. Furthermore, we used isothermal titration calorimetry (ITC) to measure the binding affinity between the two proteins, and the results showed that Vac8 bound to tNvj1 with a K_d value of 0.71 μM (Figure 1.1C). Both SEC and ITC indicated that Vac8 binds to Nvj1 in a 1:1 molar ratio.

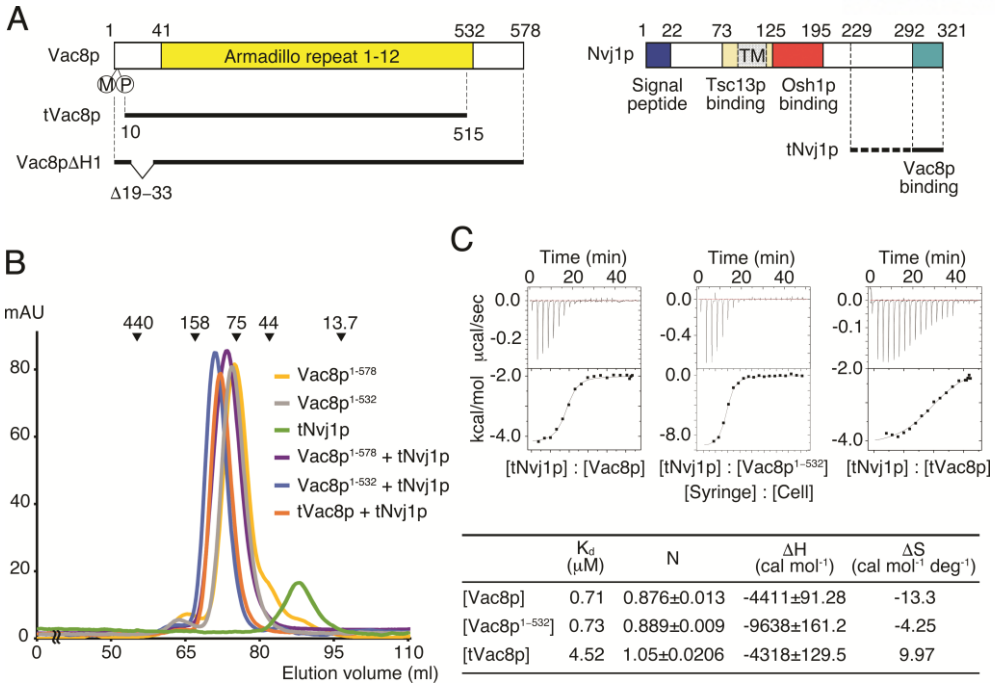

	K_d (μM)	N	ΔH (cal mol^{-1})	ΔS (cal mol^{-1} deg^{-1})
[Vac8p]	0.71	0.876±0.013	-4411±91.28	-13.3
[Vac8p$^{1–532}$]	0.73	0.889±0.009	-9638±161.2	-4.25
[tVac8p]	4.52	1.05±0.0206	-4318±129.5	9.97

Figure 1.1. Vac8 directly interacts with Nvj1

(A) Schematic diagram showing the domain structure of yeast Vac8 (Left) and Nvj1 (Right) truncation constructs used in this study. TM, transmembrane domain.

(B) Analysis of the direct interaction between Vac8 and Nvj1 by SEC. Full-length Vac8 (residues 1−578), Vac8$^{1–532}$ (residues 1−532), tNvj1 (residues 229−321), Vac8-tNvj1, Vac8$^{1–532}$-tNvj1, and the tVac8–tNvj1 complex were injected on a Superdex 200 column equilibrated with buffer containing 25 mM Tris · HCl, 150 mM NaCl, and 5 mM DTT (pH 7.5). The molecular masses of the standards are indicated above the chromatogram curves to indicate the relative molecular masses of the samples.

(C) ITC measurements for tNvj1 binding to full-length Vac8, Vac8$^{1–532}$, and truncated tVac8. Thermodynamic parameters measured by ITC experiments are tabulated below the thermograms.

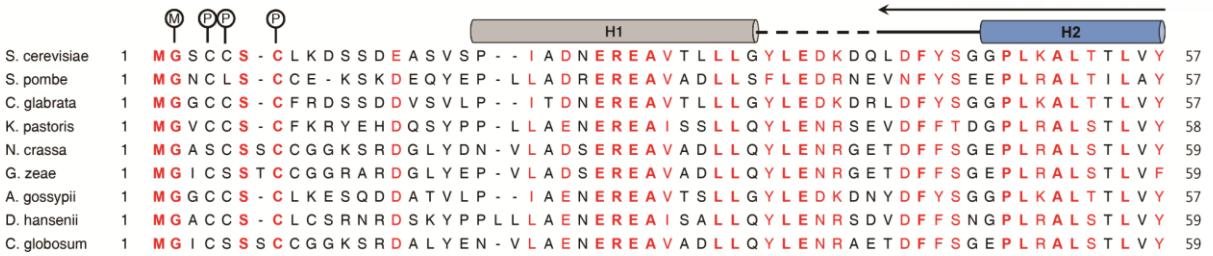

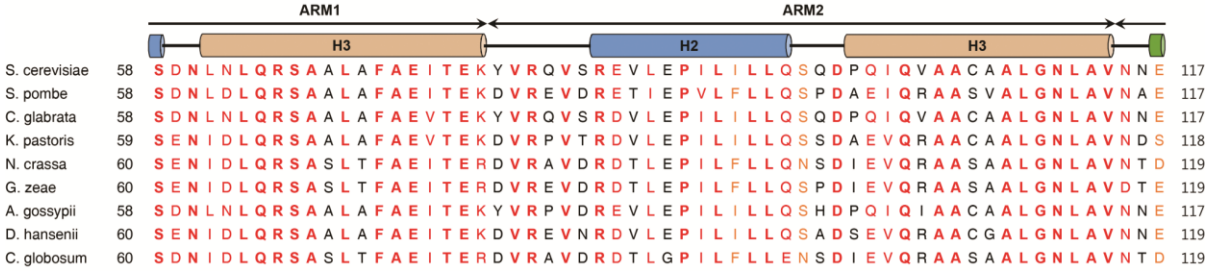

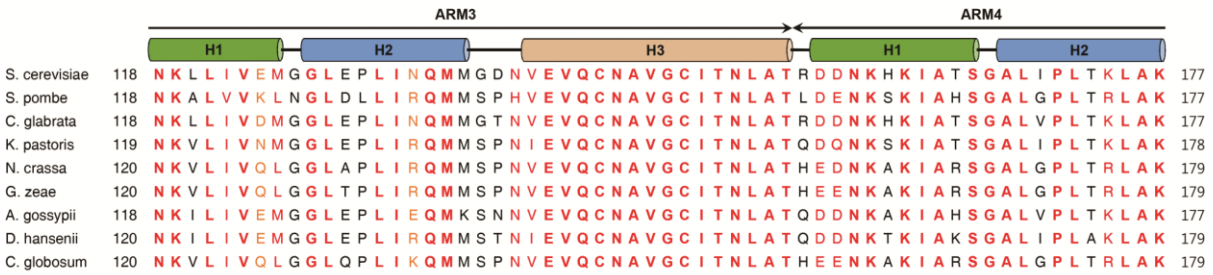

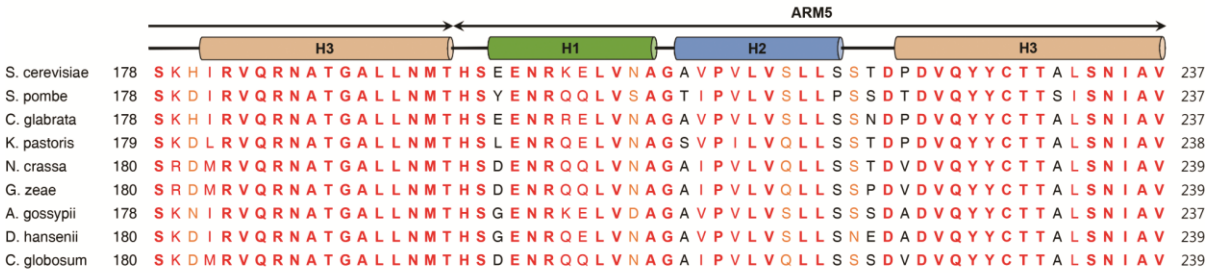

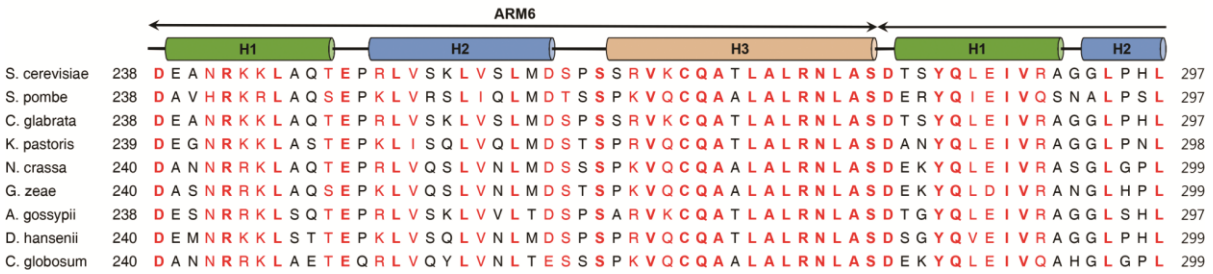

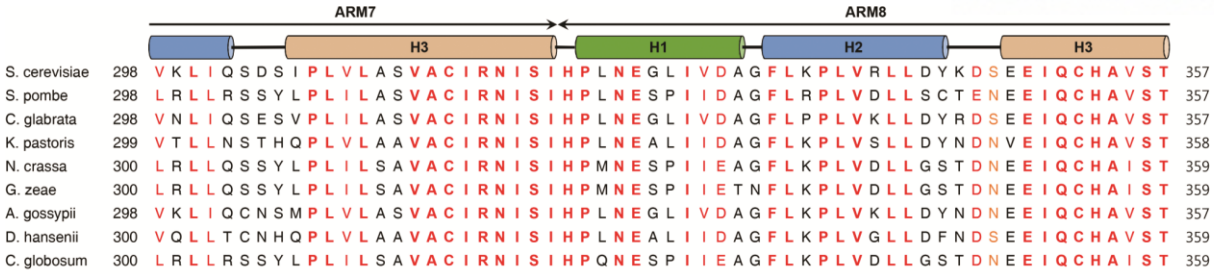


```
S. cerevisiae  298 VKLIQSDSIPLVLASVACIRNISIHPLNEGLIVDAGFLKPLVRLLDYKDSEEIQCHAVST 357
S. pombe       298 LRLLRSSYLPLILASVACIRNISIHPLNESPIIDAGFLRPLVDLLSCTENEEIQCHAVST 357
C. glabrata    298 VNLIQSESVPLILASVACIRNISIHPLNEGLIVDAGFLPPLVKLLDYRDSEEIQCHAVST 357
K. pastoris    299 VTLLNSTHQPLVLAAVACIRNISIHPLNEALIIDAGFLKPLVSLLDYNDNVEIQCHAVST 358
N. crassa      300 LRLLQSSYLPLILSAVACIRNISIHPMNESPIIEAGFLKPLVDLLGSTDNEEIQCHAIST 359
G. zeae        300 LRLLQSSYLPLILSAVACIRNISIHPMNESPIIETNFLKPLVDLLGSTDNEEIQCHAIST 359
A. gossypii    298 VKLIQCNSMPLVLASVACIRNISIHPLNEGLIVDAGFLKPLVKLLDYNDNEEIQCHAVST 357
D. hansenii    300 VQLLTCNHQPLVLAAVACIRNISIHPLNEALIIDAGFLKPLVGLLDFNDSEEIQCHAVST 359
C. globosum    300 LRLLRSSYLPLILSAVACIRNISIHPQNESPIIEAGFLKPLVDLLGSTDNEEIQCHAIST 359
```

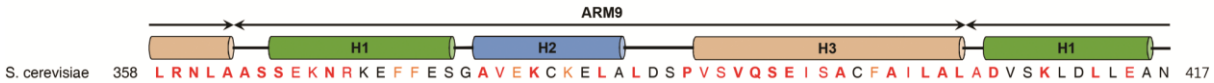


```
S. cerevisiae  358 LRNLAASSEKNRKEFFESGAVEKCKELALDSPVSVQSEISACFAILALADVSKLDLLEAN 417
S. pombe       358 LRNLAASSERNKRAIIEANAIQKLRCLILDAPVSVQSEMTACLAVLALSDEFKSYLLNFG 417
C. glabrata    358 LRNLAASSEKNRKEFFESGAVKKCKELALDSPVSVQSEISACFAILALADVSKQDLLDAD 417
K. pastoris    359 LRNLAASSERNRLALLESGAVEKCEKLVLNSPISVQSEISACFAILALADDLKMKLLDSN 418
N. crassa      360 LRNLAASSDRNKALVLEAGAVQKCKQLVLEVPVTVQSEMTAAIAVLALSDELKTNLLELG 419
G. zeae        360 LRNLAASSDRNKALVLDAGAVQKCKQLVLDVPITVQSEMTAAIAVLALSDDLKSHLLNLG 419
A. gossypii    358 LRNLAASSEKNRQEFFESGAVEKCKQLALVSPISVQSEISACFAILALADNSKLELLDAN 417
D. hansenii    360 LRNLAASSERNRLALLAAGAVDKCKELVLKVPLSVQSEISACFAILALADDLKPKLYESH 419
C. globosum    360 LRNLAASSDRNKSLVLEAGAVQKCKQLVLEVPVTVQSEMTAAIAVLALSDELKTHLLELG 419
```

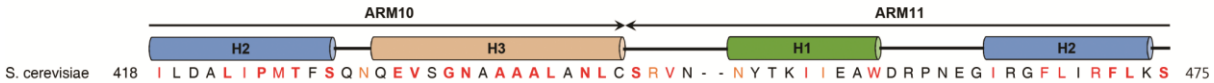


```
S. cerevisiae  418 ILDALIPMTFSQNQEVSGNAAAALANLCSRVN--NYTKIIEAWDRPNEGIRGFLIRFLKS 475
S. pombe       418 ICNVLIPLTDSMSIEVQGNSAAALGNLSSSNVD--DYSRFIECWDSPAGGIHGYLVRFLSS 475
C. glabrata    418 ILQALIPMTFSTNQEVSGNAAAALANLCSRID--NYSKIISSWDQPKEGIRGFLKRFLQS 475
K. pastoris    419 IIEVLLPLTSSENGEVCGNAAAALANLCSRIP--DYTIILKNY----EQISKFIAKFLNS 472
N. crassa      420 VFEVLIPLTKSPSIEVQGNSAAALGNLSSSKVG--DYSVFIHNWNEPSDGIHGYLSRFLAS 477
G. zeae        420 VCGVLIPLTHSPSIEVQGNSAAALGNLSSSKVG--DYSIFVQNWTEPQGGIHGYLCRFLQS 477
A. gossypii    418 ILEALIPMTFSTNQEVAGNAAAALANLCSRIN--NYEKIIESWTEPSKGVCGFLIRFLQS 475
D. hansenii    420 IIDVLIPLTFSENGEVCGNSAAALANLCSRVSSEHKQYIFKNWSEPNEGIYGFLLRFLQS 479
C. globosum    420 VFDVLIPLTMSPSVEVQGNSAAALGNLSSSKVG--DYSIFVQNWMEPRDGIHGYLNRFLAS 477
```

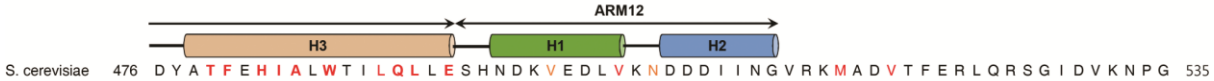


```
S. cerevisiae  476 DYATFEHIALWTILQLLESHNDKVEDLVKNDDDIINGVRKMADVTFERLQRSGIDVKNPG 535
S. pombe       476 EDSTFAHIAAWTIVQLLEAGVPRLTAFIQSSD---DIIELLNDIVARDAN---------- 522
C. glabrata    476 NYATFEHIALWAILQLSESHNDKVIYLIKNDKEIINSVRKMADVTYDRLQKSGVDVNKNG 535
K. pastoris    473 QNPTFEHIALWTTLQLLESEDETIKAKLKKQ--INSGEISLNNLTTSTLNN---------- 521
N. crassa      478 GDATFQHIAIWTLLQLLESEDKKLIGLIGKSN---DIVDMIRQIANRQIE---------- 524
G. zeae        478 GDATFQHIAVWTLLQLFESEDKTLIGLIGKAE---DIIEHIRSIANRQIE---------- 524
A. gossypii    476 EYPTFEHIALWTILQLLESHNETMLGLIKSNKEIVKSIKRLSDINYENAQK---------- 526
D. hansenii    480 GSATFEHIALWTILQLLESNNTEINSLIKE------NESILSGIKNLSASQ---------- 524
C. globosum    478 GDATFQHIAIWTLLQLLESEDKKLIGLIGKSD---GVVDMIKQIANRQMME---------- 525
```

```
S. cerevisiae  536 SNNNPSSNDNNSNNND----TGSEHQPVEDASLELYNITQQILQFLH 578
S. pombe       523 ---------NGEYEDG------EGDVILLSGRALHLIEQDTDS----- 550
C. glabrata    536 NSEERGDNEDHQSNNDRNLANSTSSDQYEDASMELYNITQQILQFLD 582
K. pastoris    522 --HS--DTSNIINNDG--------EEGEFND-GDDIINLTQQILEMIK 556
N. crassa      525 -------SDNELEDDD-----EGEVVSLAQRCLELLGQGNAKAHIEG 559
G. zeae        525 -------PDNEFEDED-----EGEVVNLAQRCLELLGQSMSKAHIEG 559
A. gossypii    527 -ASSLHSRLQQVNGGS----VASGSEQYEHASLELYNITQQIMQFLN 568
D. hansenii    525 --QQ--TQQSQVNNPD--------SSDQFDDPKVELFNLTQQILQILG 560
C. globosum    526 -------SDNEAEDDD-----EGEVVNLAQRCLELLGQGGSKSHIEG 560
```

Figure 1.2. Sequence alignment of yeast Vac8 orthologs

Sequence alignment of full-length Vac8 orthologs in fungi. The N terminus of Vac8 is known to be modified by lipidation. The circled M and P indicate N-myristoyl glycine and S-palmitoyl cysteine, respectively. Secondary structural elements are indicated above the sequences with helices, β-stands, loops, and disordered regions depicted as cylinders, arrows, solid lines, and dashed lines, respectively. The crystal structure revealed that Vac8 is composed of an N-terminal helix (gray) followed by 12 ARMs. The three helices forming each ARM repeat are colored differently. Absolutely conserved, highly similar, and similar sequences are highlighted in bold red, red, and orange, respectively. UniProt entries for the sequences are as follows: *S. cerevisiae* (P39968), *Schizosaccharomyces pombe* (O43028), *Candida glabrata* (Q6FJV1), *Komagataella pastoris* (Q5EFZ4), *Neurospora crassa* (Q7RXW1), *Gibberella zeae* (Q4I1B1), *Aphis gossypii* (Q757R0), *Debaryomyces hansenii* (Q6BTZ4), and *Chaetomium globosum* (Q2GW27).

1.3.2. Crystal structure of the Vac8-Nvj1 complex

To gain structural insight into the recognition of Nvj1 by Vac8 we crystallized the Vac8-Nvj1 complex. Attempts to obtain crystals from full-length Vac8 were unsuccessful, but we were instead able to crystallize a truncated version (residues 10–515, referred to as tVac8) in complex with the Vac8-binding domain of Nvj1 comprising residues 229–321 (referred to as tNvj1). The N- and C-terminal truncated variant of Vac8 showed reduced but still substantial binding affinity for tNvj1, suggesting that the truncation did not profoundly affect the overall structure and function of Vac8 (Figure 1.1C). Crystals of the tVac8-tNvj1 complex belong to the $P2_1$ space group and diffracted to a maximum of 2.4 Å resolution using synchrotron radiation. The structure was determined by single-wavelength dispersion (SAD) using Se-Met derivatized crystals, and the final model was refined with native data to 2.4 Å resolution (Figure 1.3A). X-ray crystallographic data and refinement statistics are listed in Table 1.1.

Figure 1.4 A and B show the overall structure of the tVac8-tNvj1 complex. Crystals contained two tVac8-tNvj1 complexes arranged by twofold internal symmetry in the asymmetric unit (Figure 1.4C). No structural differences were found between the two complexes, which had an RMSD of 0.8 Å for all Cα atoms. Each complex consists of one tVac8 and one tNvj1 (1:1 stoichiometry), consistent with the biochemical results (Figure 1.1 B and C). Overall, the tVac8-tNvj1 complex resembles a serpent column in which tNvj1 represents the axis and tVac8 represents the snake. tVac8 has an all α-helical topology with an elongated superhelical structure of 40 × 50 × 120 Å in size. The two structural elements consisting of (i) the N-terminal amphipathic helix spanning residues 19–33 (referred to as helix H1 throughout) and (ii) the central core domain of 12 ARM repeats (residues 41–512) are organized into a right-handed superhelical structure. This is a common structural feature in most ARM-containing proteins such as β-catenin and importin α (Figure 1.4A) [15]. Notably, the ARM repeats start from residue 41, and the two structural elements are connected with flexible loops comprising residues 34–40 that are disordered in the crystal structure. The truncated tVac8 construct used for crystallization ends at residue 515, which might remove part of H2 and all of H3 of the last of the ARM repeats (ARM12). Indeed, H2 and H3 of ARM12 were vulnerable to proteolytic degradation using limited proteolysis (Figure 1.3B). The C-terminal region (residues 533–578) of Vac8 was also sensitive to digestion by trypsin, suggesting that this region is structurally disordered. Interestingly, the N-terminal amphipathic helix H1 from a neighboring tVac8 molecule in the crystal lattice occupies the ARM12 H3 position and may play a similar role to the H3 helix in ARM repeats (Figure 1.3 C and D).

The 30-amino acid tNvj1 forms an extended straight structure. Even though the construct

used for crystallography starts at residue 229, only residues bound to Vac8 were clearly visible in the electron density, and residues 229–291 are disordered.

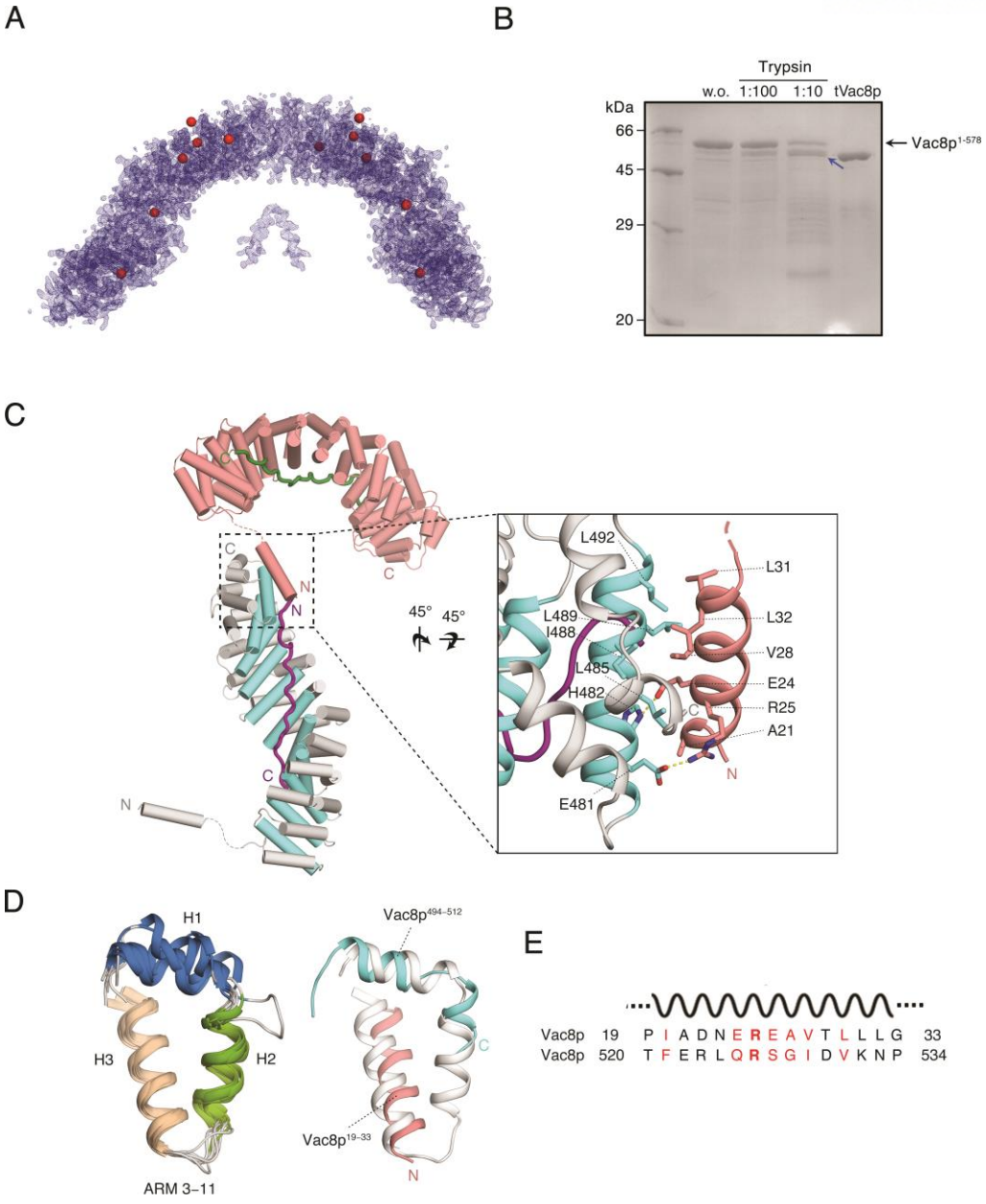

Figure 1.3. The H1 helix of tVac8 is critically involved in crystal packing

(A) Experimental electron density map (calculated using Se-SAD phasing at 2.4 Å resolution and contoured at 1.5σ) of the crystallographic asymmetric unit of the tVac8-tNvj1 complex. Selenium atoms found by the PHENIX program [17] are represented by red spheres.

(B) Trypsin digestion of full-length Vac8. Vac8 was mixed with trypsin at the indicated trypsin:Vac8 ratio for 1 h at 4°C. Reactions were stopped by adding 1 mM PMSF and SDS sample buffer, and the products were separated by SDS-PAGE. Sequencing analysis identified that the N terminus of the protease-resistant fragment, indicated by the blue arrow, is residue number 10 of Vac8. SDS-PAGE shows comparison of the relative molecular masses between protease-resistant product and tVac8 (residues 10−515).

(C) Cartoon representation of the tVac8 interface showing crystal contacts and highlighting the flexibly connected H1 helix from the neighboring molecule (pink) placed in the H3 position of the incomplete ARM12 lacking the H3 helix due to truncation. The 12 intact ARM repeats are also included. Residues involved in this interaction are shown in stick representation in the zoom view on the right.

(D) Structural alignment of tVac8 ARM repeats 3–11 (Left). To compare the structural role of the N-terminal H1 helix, the intact ARM11 (gray) and the composite ARM12 comprising H1 and H2 (blue) together with H1 (residues 19−33) from the neighboring molecule (pink) are superimposed (Right).

(E) Sequence alignment of Vac8 residues 19–33 corresponding to the H1 helix and residues 520–534 that might correspond to the H3 helix of ARM12. Conserved residues are colored red. The identical and similar residues between two sequences were highlighted in bold font and red text, respectively. w.o., without.

Table 1.1. X-ray diffraction data collection and refinement statistics

Dataset	**Native**	**Se-SAD**
X-ray source	Beamline 7A, PAL	Beamline 7A, PAL
Temperature (K)	100	100
Space group	$P2_1$	$P2_1$
Cell dimensions		
a, *b*, *c* (Å)	84.082, 115.630, 84.131	84.116, 115.500, 84.631
α, *β*, *γ* (°)	90.00, 114.677, 90.00	90.00, 114.896, 90.00
Data processing		
Wavelength (Å)	0.97933	0.97934
Resolution (Å)	50.0–2.40	50.0–2.40
R_{merge} (%)*	12.8 (61.9)	9.9 (60.0)
I/σ (I)	13.3 (1.90)	16.2 (2.21)
Completeness (%)	98.8 (97.4)	98.7 (99.7)
Redundancy	2.9 (2.6)	3.1 (3.2)
Measured reflections	166,859	176,447
Unique reflections	56,806	57,011
Refinement		
Resolution (Å)	31.9–2.40	
Number of reflections	57,022	
R_{work}†/R_{free}‡ (%)	19.30/21.72	
Number of atoms		
Protein	8,212	
Water	181	
RMSD§		
Bond lengths (Å)	0.004	
Bond angles (°)	1.118	
Ramachandran plot, residues in		
Most favored regions (%)	98.4	
Additional allowed regions (%)	1.6	
Generously allowed regions (%)	0.0	
Disallowed regions (%)	0	

Highest-resolution shell is shown in parentheses.

* $R_{merge} = 100 \times \sum_h \sum_i | I_i(h) - \langle I(h) \rangle | / \sum_h \langle I(h) \rangle$, where $I_i(h)$ is the *i*th measurement and $\langle I(h) \rangle$ is the weighted mean of all measurement of *I*(h) for Miller indices h.

† *R*-factor $= 100 \times \sum |F_P - F_{P(calc)}| / \sum F_P$.

‡ R_{free} was calculated with 5% of the data.

§ Root-mean-squared deviation (RMSD) from target geometries.

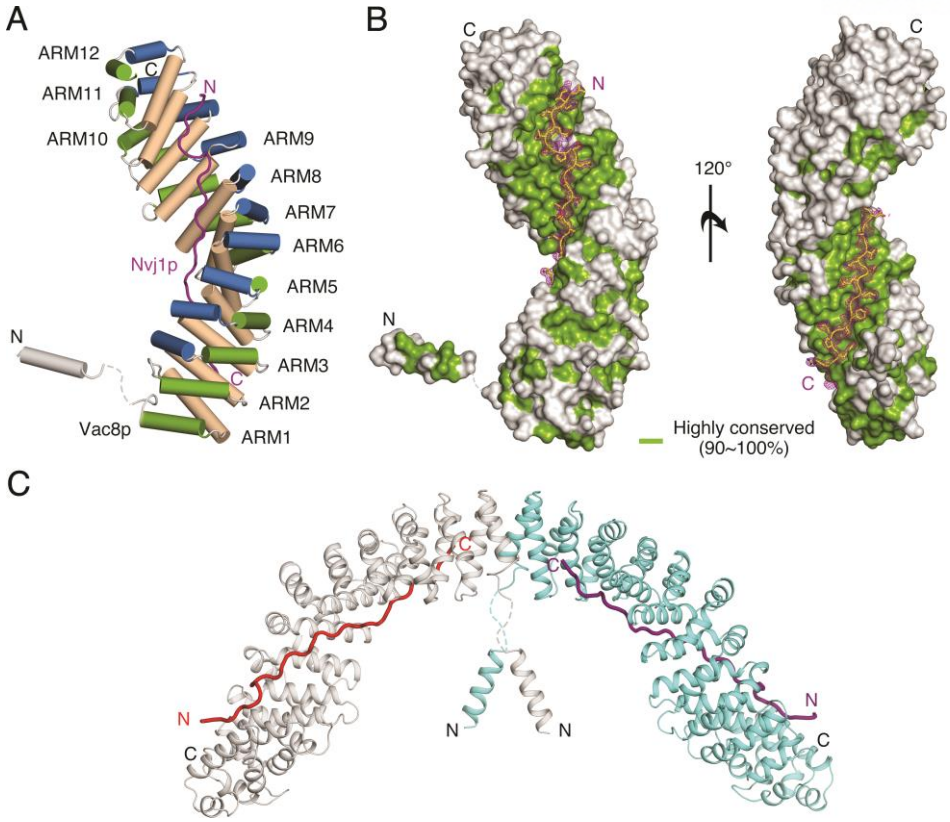

Figure 1.4. Overall structure of the tVac8-tNvj1 complex

(A) Cartoon representation showing the overall structure of tVac8 bound to tNvj1. tVac8 comprises two structural elements that contain an N-terminal H1 helix and 12 ARM domains. The extended loop of tNvj1 (magenta) binds in an antiparallel manner to the inner groove generated by the 12 ARMs of Vac8. The three helices characterizing each ARM are shown in a different color. The crystal structure was determined by Se-SAD phasing and refined with native data to 2.4 Å resolution.

(B) Surface representation of tVac8 based on the degree of sequence conservation from nine Vac8 orthologs generated using the Consurf website (consurf.tau.ac.il) [18]. tNvj1 bound to tVac8 is shown in stick representation. The Fo-Fc difference electron density map (magenta, contoured at 3σ) was calculated in the absence of tNvj1 at 2.4 Å resolution.

(C) Ribbon diagram showing two copies of the tVac8-tNvj1 complex in the asymmetric unit. The two tVac8 molecules are colored cyan and gray, and tNvj1 molecules are colored magenta and red.

1.3.3. Interfaces between tVac8 and tNvj1

The extended tNvj1 loop of 80 Å in length binds to tVac8 via the highly conserved inner groove formed by all H3 helices from the 12 ARM repeats (Figure 1.4 A and B). tNvj1 runs through tVac8 in an antiparallel fashion, and ~2,300 $Å^2$ of surface area is buried within the complex. The two tNvj1 fragments bound to tVac8 in the asymmetric unit could be superimposed precisely with an RMSD of 0.4 Å for all 30 Cα atoms, suggesting that the tVac8-tNvj1 complex is mediated by specific interactions rather than random recognition. We divided the contact sites into three main regions (interface I–III) ordered from the N to the C terminus of tNvj1 (Figures 1.5A and 1.6).

In interface I, residues 292–301 of tNvj1 adopt a thunderbolt-like structure containing two sharp bends. Residues 293–297 run antiparallel to the axis of the H3 helices of ARM10 and ARM11. Residues 297–300 form a loop that binds perpendicular to the H3 helices of ARM8–10, followed by residues 301 and 302 that run antiparallel to the axis of helix H3 of ARM8. The main chain atoms of Leu293, Ile295, and Gln296 are recognized by the side chains of Arg447 and Asn443 of tVac8 through intermolecular H-bonds, and two hydrophobic residues (Ile295 and Val297) of tNvj1 make nonpolar contacts with hydrophobic side chains Trp486, Ala442, His482, and Ile483 of tVac8 (Figures 1.5A and 1.6).

In interface II (residues 302–310) and interface III (residues 311–321), tNvj1 forms straighter β-strand-like structures. A slight bend formed from Thr311 and Glu312 of tNvj1 at the boundary between interfaces II and III facilitates the tight and extended interactions with the inner groove of tVac8. The nine-residue loop in interface II runs through ARM5–9 of tVac8 in a diagonal direction relative to the axes of the H3 helices and makes extensive contacts with H3 helices from the tVac8 repeats. In interface III (residues 311–321), the main chain atoms of tNvj1 residues 313–317 form hydrogen bonds with the side chains of Asn193, His196, and Asn152 from the H3 helices of ARM2 to ARM7 of tVac8. Additionally, tNvj1 Arg320 forms a salt bridge with tVac8 Glu141 (Figures 1.5A and 1.6). There are also hydrophobic contacts in interfaces II and III. Particularly, Ala307 and Val309 of tNvj1 make hydrophobic interactions with Val237 of tVac8 in interface II. Finally, the aromatic residues Phe319 and Tyr321 of tNvj1 make hydrophobic contacts with Cys149, Val114, Ala107, Ala72, and Leu69 of tVac8.

To verify whether the residues involved in the tVac8-tNvj1 interactions in the crystal are important in solution, we made a series of N-terminally hexa-histidine-tagged mutants of tNvj1 and tested their ability to interact with GST-tVac8 using histidine tag pull-down assays. Figure 1.5B shows that the binding affinity of I295R, K301E, and A307R of tNvj1 for tVac8 was reduced between

two- and threefold compared with the native protein. More surprisingly, the F319E single mutant lost almost all ability to interact with tVac8. Finally, the triple substitution mutant (I295R/A307R/F319E, referred to as tNvj1-triple) lost all ability to interact with tVac8.

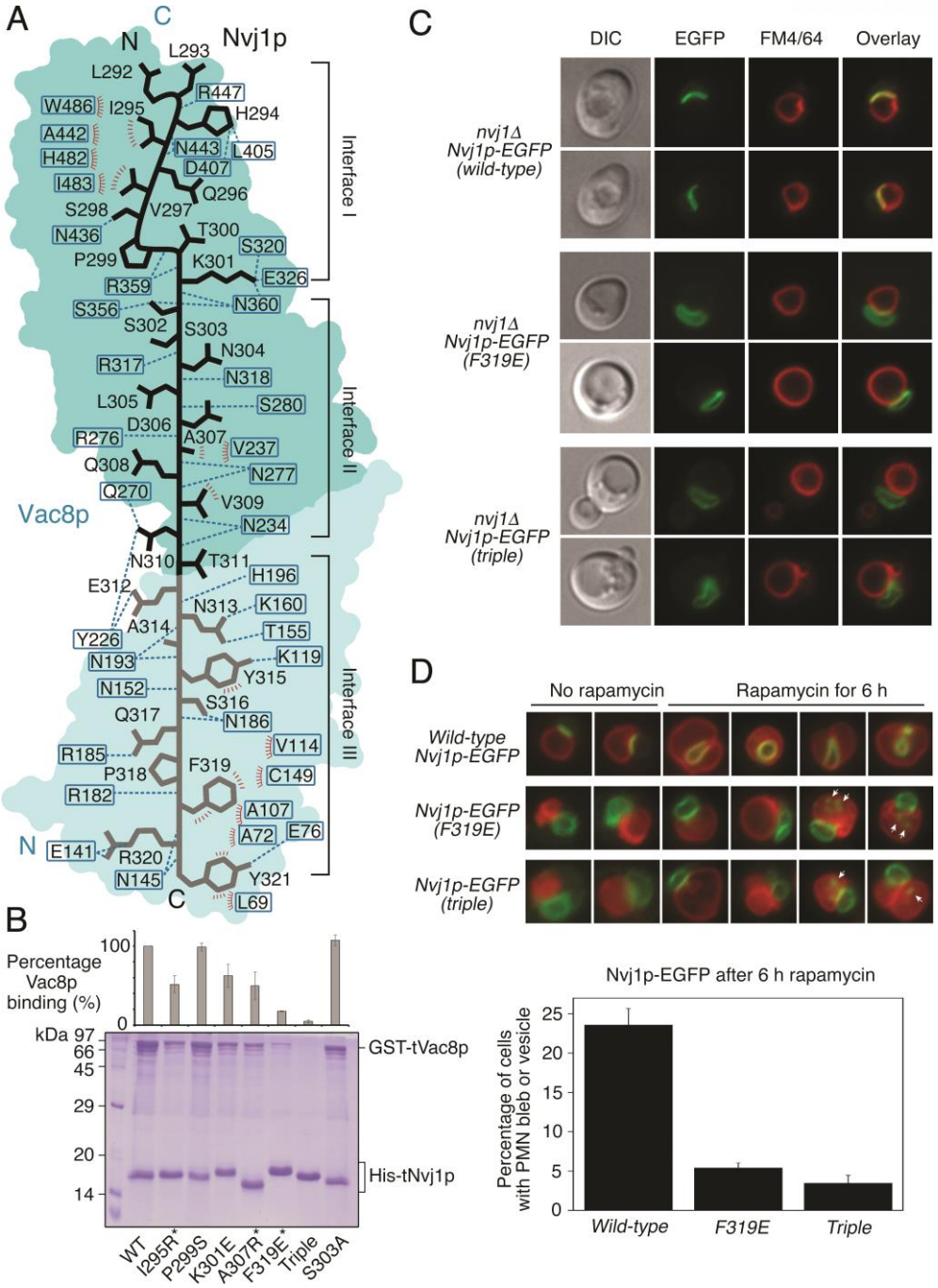

Figure 1.5. Binding interface between tVac8 and tNvj1

(A) Schematic diagram showing the tVac8 (blue)-tNvj1 (black line) binding interface (Figure 1.6 for more details). Red and blue dotted lines indicate hydrophobic contacts and intermolecular hydrogen bonds, respectively. tVac8 residue labels are boxed.

(B) Pull-down experiment demonstrating the direct tVac8-tNvj1 interaction in solution. The wild type and mutant of His-tagged tNvj1 were coexpressed with GST-tVac8 and immobilized on Ni-NTA resin. Proteins were analyzed by 15% SDS-PAGE and Coomassie blue staining. The asterisk indicates the residues included in the triple mutant.

(C) The Nvj1 mutants, Nvj1-F319E and Nvj1-triple, do not support the formation of a tight junction between the nucleus and the vacuole. Cells expressing wild-type Nvj1-EGFP, Nvj1-EGFP (F319E), or Nvj1-EGFP (triple) were labeled with FM4/64, a vacuole-specific lipophilic dye, in YPD media for 2 h at 30°C. After free dye was removed, cells were resuspended in fresh media and allowed to grow for 2 h at 30°C. GFP fluorescence for wild-type or mutant Nvj1 was then analyzed by fluorescence microscopy. Representative images from each cell type are shown. (Magnification: 100 ×.)

(D) PMN was largely impaired in cells expressing Nvj1-F319E or Nvj1-triple. Experiments were carried out as in (C) except for treatment with 0.2 μM rapamycin for 6 h to induce PMN. (Magnification: 100 ×.) GFP fluorescence for Nvj1 and red fluorescence for vacuoles were analyzed by fluorescence microscopy. Representative images (Top) of each cell type with or without rapamycin, and quantification (Bottom) of cells with PMN blebs or PMN vesicles is shown. The yeast strains lacked the major vacuolar protease Pep4 to block the degradation of PMN blebs or vesicles in the vacuolar lumen. White arrows indicate nuclear membrane-derived fragments in the vacuole. DIC, differential interference contrast.

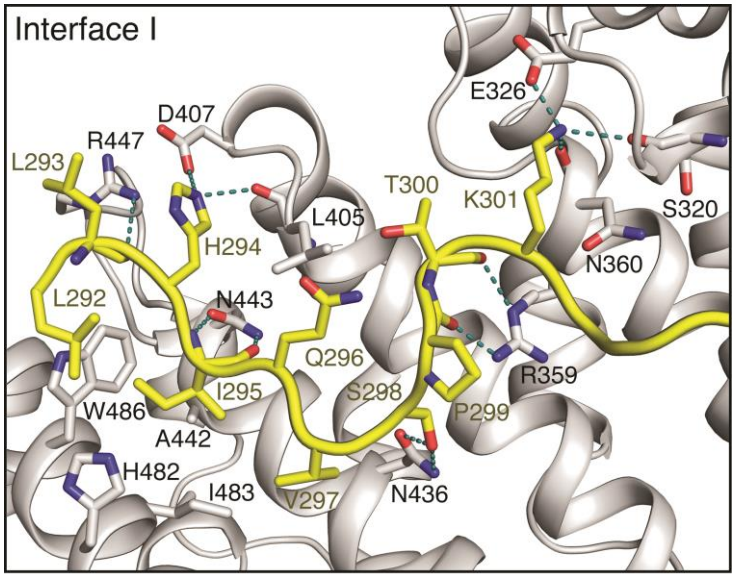

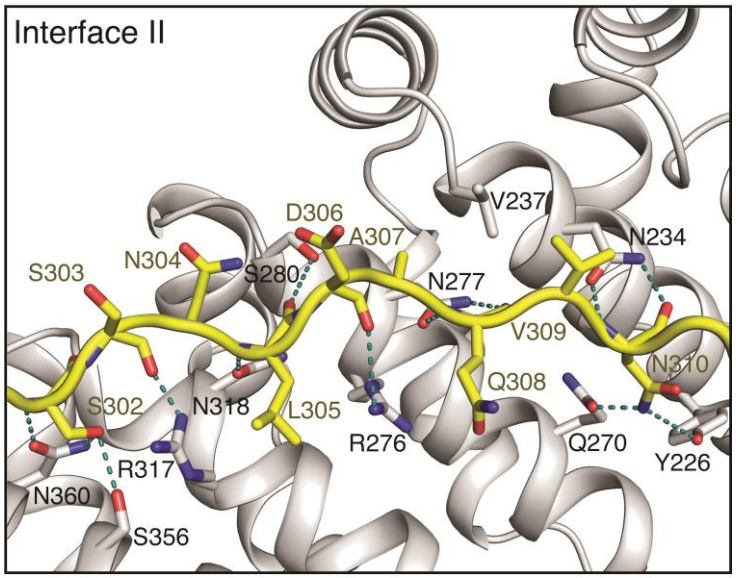

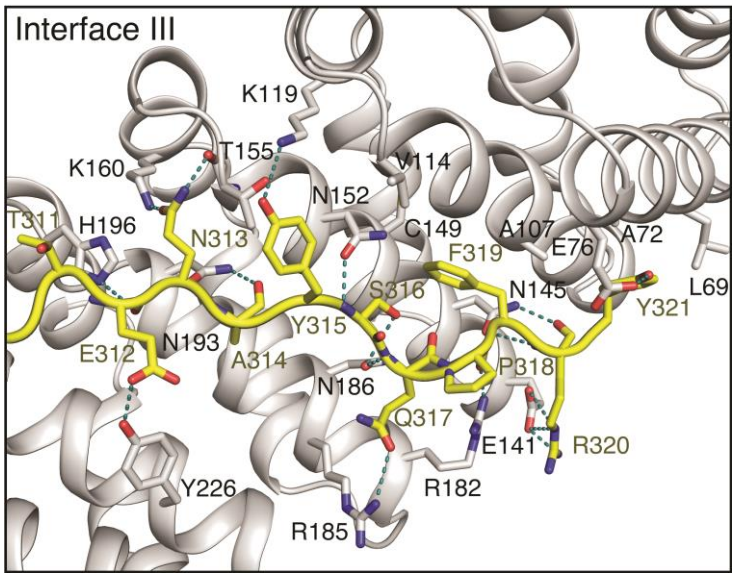

Figure 1.6. Interactions between Nvj1 and Vac8

Close-up view of the tNvj1 and tVac8 interface. The three interfaces of tVac8 (gray) and tNvj1 (yellow) described in Figure 1.5A are shown in cartoon representation. Oxygen and nitrogen atoms are colored red and blue, respectively. Blue dotted lines indicate H-bonds.

1.3.4. Disruption of the Vac8-Nvj1 interface damages NVJ formation and PMN in vivo

Next, we used *S. cerevisiae* to examine the functional relevance of the interaction interfaces between Vac8 and Nvj1 in vivo. Because Vac8-Nvj1 interactions are largely responsible for the formation of NVJs that rely on the tight apposition of a region of the nuclear envelope with the vacuolar membrane, Nvj1 is enriched in the contact region between the nucleus and the vacuole in wild-type yeast cells [12]. Consistent with this, when EGFP-conjugated wild-type Nvj1 was expressed in *nvj1Δ* yeast (Table 1.2), nearly all Nvj1-EGFP proteins were localized to normal NVJs (Figure 1.5C). By contrast, when Nvj1-EGFP (F319E), which has a reduced affinity for Vac8, was expressed, the mutant Nvj1 became dispersed almost evenly along the entire outer nuclear membrane region (Figures 1.5C and 1.7A). Similarly, Nvj1-EGFP (triple), which has no affinity for Vac8, was also distributed over the nuclear envelope, instead of being confined to NVJs (Figures 1.5C and 1.7A). Furthermore, substitution of wild-type Nvj1 with the triple mutant seemed to result in the loosening of the tight apposition between the nucleus and the vacuole.

NVJs are involved in various cellular functions including mediating PMN, a distinct form of nuclear microautophagy in budding yeast [5]. Upon nutrient depletion or rapamycin treatment NVJs proliferate and subsequently undergo engulfment into the lumen of the vacuole, leading to the eventual degradation of the engulfed nuclear membranes [6]. To test whether the interaction interfaces between Vac8 and Nvj1 revealed by our tVac8-tNvj1 crystal structure are also critical for mediating PMN, yeast cells expressing EGFP-conjugated wild-type Nvj1 or mutant Nvj1 were subjected to rapamycin treatment, and PMN-mediated engulfment of Nvj1-EGFP into the vacuole was analyzed by fluorescence microscopy. As shown in Figure 1.5D, PMN blebs or vesicles were readily observed in the vacuoles of *pep4Δ* yeast cells (in which vacuolar proteases are inactivated and thereby prevented from degrading PMN vesicles in the vacuole) expressing wild-type Nvj1. By contrast, only a few cells expressing Nvj1-EGFP (F319E) or Nvj1-EGFP (triple) exhibited PMN blebs or vesicles upon rapamycin treatment (Figure 1.5D). Instead, small nuclear fragments were often found in cells expressing mutant Nvj1 (white arrows), suggesting that another type of nucleophagy occurred independently of NVJ [19, 20]. Taken together, these in vivo results clearly demonstrate that the interaction interfaces between Vac8 and Nvj1 revealed by the crystal structure of the tVac8-tNvj1 complex (Figure 1.5A) play a critical role in NVJ formation and their cellular functions.

Table 1.2. Yeast strains used in this study

Strain	Genotype	Source
BY4742	MATα *his3Δ1 leu2Δ0 lys2Δ0 ura3Δ0*	[21]
BY4742 *nvj1*Δ	MATα *his3Δ1 leu2Δ0 lys2Δ0 ura3Δ0 nvj1Δ::KanMX4*	[21]
BY4742 *vac8*Δ	MATα *his3Δ1 leu2Δ0 lys2Δ0 ura3Δ0 vac8Δ::KanMX4*	[21]
BY4742 *pep4*Δ	MATα *his3Δ1 leu2Δ0 lys2Δ0 ura3Δ0 pep4Δ::KanMX4*	[21]
BY-Nvj1-EGFP	BY4742 *nvj1*Δ with *pYJ406-NVJ1-EGFP*	This study
BY-Nvj1(F319E)-EGFP	BY4742 *nvj1*Δ with *pYJ406-NVJ1*(*F319E*)*-EGFP*	This study
BY-Nvj1(triple)-EGFP	BY4742 *nvj1*Δ with *pYJ406-NVJ1*(*I295R/A307R/F319E*)*-EGFP*	This study
BY-Nvj1(Δ318–321)-EGFP	BY4742 *nvj1*Δ with *pYJ406-NVJ1*(*Δ318–321*)*-EGFP*	This study
BY-Vac8(triple)	BY4742 *vac8*Δ with *pRS316-VAC8*((*R276E/R317E/R359E*)	This study
BY-*VAC8*-N1-EGFP	BY4742 with *pYJ406-NVJ1-EGFP*	This study
BY-*vac8*Δ-N1-EGFP	BY4742 *vac8*Δ with *pYJ408-NVJ1-EGFP*	This study
BY-*vac8*(*t*)-N1-EGFP	BY-Vac8(triple) with *pYJ408-NVJ1-EGFP*	This study
BY-*vac8*(*A51R*)-N1-EGFP	BY4742 *vac8*Δ with *pRS316-VAC8*(*A51R*) and *pYJ408-NVJ1-EGFP*	This study
BY-*vac8*(*L55R*)-N1-EGFP	BY4742 *vac8*Δ with *pRS316-VAC8*(*L55R*) and *pYJ408-NVJ1-EGFP*	This study
BY-*pep4*Δ-N1-EGFP	BY4742 *pep4*Δ with *pYJ406-NVJ1-EGFP*	This study
BY-*pep4*Δ-N1a-EGFP	BY4742 *pep4*Δ with *pYJ406-NVJ1*(*F319E*)*-EGFP*	This study
BY-*pep4*Δ-N1b-EGFP	BY4742 *pep4*Δ with *pYJ406-NVJ1*(*I295R/A307R/F319E*)*-EGFP*	This study
BY-Ape1-EGFP	BY4742 with *pYJ408-APE1-EGFP*	This study
BY-*vac8*(*triple*)-Ape1-EGFP	BY-Vac8(triple) with *pYJ408-APE1-EGFP*	This study
BY-*vac8*Δ-Ape1-EGFP	BY4742 *vac8*Δ with *pYJ408-APE1-EGFP*	This study
BY-Vac8-EGFP/Vac8-myc	BY4742 *vac8*Δ with *pYJ406-VAC8-EGFP* and *pYJ408-VAC8-myc*	This study

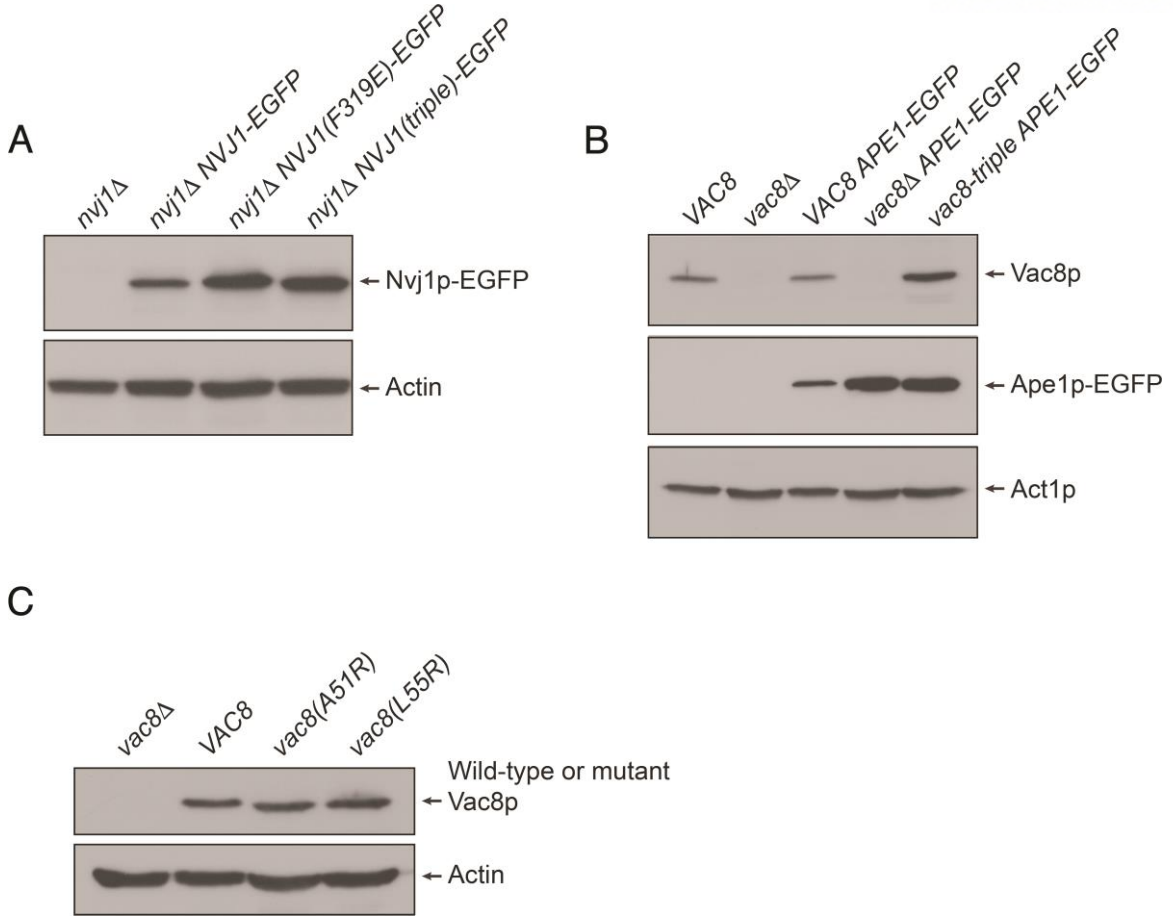

Figure 1.7. Expression of Vac8 and Nvj1 mutants

(A) Expression of EGFP-conjugated wild-type and mutant Nvj1. The expression of wild-type Nvj1-EGFP, Nvj1-EGFP (F319E), and Nvj1-EGFP (triple) was analyzed by immunoblotting. Actin was used as a loading control.

(B) The expression of Vac8-triple is comparable to that of wild-type Vac8. The expression of wild-type Vac8 and the Vac8-triple mutant in Ape1-EGFP-expressing cells was analyzed by immunoblotting. Actin (Act1) was used as a loading control.

(C) The expression of Vac8(A51R) and Vac8(L55R) is comparable to that of wild-type Vac8. The expression of wild-type Vac8, Vac8(A51R), and Vac8(L55R) was analyzed by immunoblotting. Actin was used as a loading control.

1.3.5. Competition between Nvj1 and Atg13 for Vac8 binding

It was previously shown that Vac8 interacts with Vac17 and Atg13, and these interactions play essential roles in vacuole inheritance and the CVT pathway, respectively [13, 14]. Additionally, β-catenin, a structural homolog of Vac8, shares the typical inner groove formed from the ARM repeats that serves as an interacting platform for their various binding partners [22]. We therefore wondered whether Vac8 would also share Nvj1-binding regions with Vac17 or Atg13 proteins. To test this, we prepared His-tagged tNvj1, Vac17 (residues 290–380), and Atg13 (residues 567–738) proteins and GST-fused tVac8 and the tVac8 triple mutant (R276E/R317E/R359E, referred to as tVac8-triple) by coexpression in bacterial cells. According to our structure, a triad of cationic residues (Arg276, Arg317, and Arg359) in the groove of tVac8 seems to be critically involved in the recognition of tNvj1 (Figure 1.8A). Figure 1.8B shows the results of pull-down experiments revealing interactions between wild-type tVac8 and tNvj1, Vac17, and Atg13, whereas the tVac8-triple mutant did not interact with tNvj1 or Atg13. Interestingly, however, the tVac8-triple retained its ability to interact with Vac17. Surprisingly, the pull-down data were consistent with the sequence conservation, because regions of Nvj1 involved in Vac8 binding were found to be quite well aligned with those of Atg13, but not strictly aligned with those of Vac17 (Figure 1.8C). Additionally, we found that Lam6 (residues 400–628) and Tco89 (residues 401–600) specifically interact with tVac8. These interactions were not significantly affected by the tVac8 triple mutation (Figure 1.9). Taken together, these results suggest that Atg13 likely binds Vac8 in a similar manner to that shown for the tVac8-tNvj1 interaction, although additional contacts might also occur between Vac8 and other binding partners including Vac17, Lam6, and Tco89.

Next, we tested whether Nvj1 could compete with Atg13 for interaction with Vac8 using ITC experiments. Atg13 was titrated into Vac8 alone and also into the Vac8-tNvj1 complex prepared by coexpression. As shown in Figure 1.8C, Vac8 alone bound Atg13 with an affinity (K_d) of 0.5 μM, whereas previously liganded Vac8 was unable to further associate with Atg13. Likewise, Vac8 already bound to Atg13 was not able to interact with tNvj1, suggesting that Vac8 exclusively and competitively interacts with its specific ligand. Competitive interaction of ligands to ARM-containing proteins has also been reported for β-catenin [23-25], which interacts exclusively with E-cadherin, Tcf-1, and APC in accordance with their molecular functions through a positively charged inner groove formed from H3 ARM helices. Similarly, we suggest that Vac8 interacts exclusively with Nvj1 or Atg13, in agreement with their known physiological relevance.

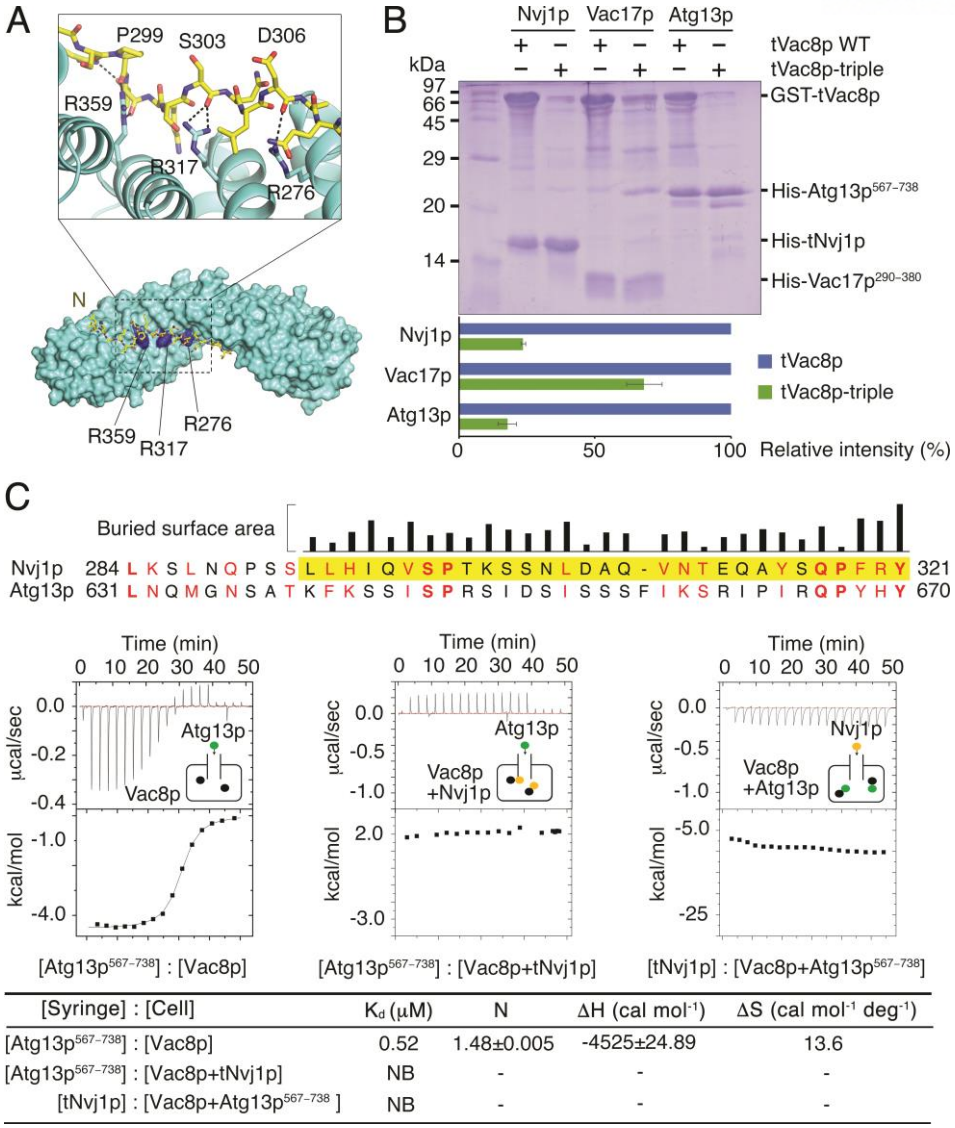

[Syringe] : [Cell]	K_d (µM)	N	ΔH (cal mol^{-1})	ΔS (cal mol^{-1} deg^{-1})
[Atg13p$^{567–738}$] : [Vac8p]	0.52	1.48±0.005	-4525±24.89	13.6
[Atg13p$^{567–738}$] : [Vac8p+tNvj1p]	NB	-	-	-
[tNvj1p] : [Vac8p+Atg13p$^{567–738}$]	NB	-	-	-

Figure 1.8. Nvj1 and Atg13 share a binding interface of Vac8

(A) Cartoon representation of the cationic triad of tVac8 comprising R276, R317, and R359 that are involved in the interaction with tNvj1. Critical hydrogen bonds are indicated by dotted lines between important residues shown in stick representation.

(B) His-tag pull-down experiments revealing tVac8 interactions with tNvj1, Vac17, and Atg13 via the conserved cationic triad. Wild-type and triple mutant (R276E/R317E/R359E) GST-tagged tVac8 were coexpressed with His-tagged tNvj1, Vac17 (residues 290–380), and Atg13 (residues 567–738) and immobilized on Ni-NTA resin. Copurified proteins were separated by 15% SDS-PAGE and stained with Coomassie blue. Quantitative data are shown below the gel.

(C) Sequence alignment of *S. cerevisiae* Nvj1 (residues 284−321) and Atg13 (residues 631−670). The visible residues of Nvj1 in the structure of tVac8-tNvj1 is highlighted in yellow. The identical and similar residues between Nvj1 and Atg13 sequences were indicated by bold font and red text, respectively. The alignment suggests that the interaction mode of Vac8 and Atg13 might resemble that

of Vac8 and Nvj1. Upper black bars indicate the relative surface area of Nvj1 buried by tVac8-tNvj1 complexation calculated using the PISA program [26]. The bottom figure shows ITC measurements of Vac8 and binding partners Atg13$^{567-738}$ and tNvj1. Atg13$^{567-738}$ or tNvj1 was titrated into Vac8 alone, the Vac8-tNvj1 complex, and the Vac8-Atg13$^{567-738}$ complex at 25°C as indicated. The results suggest that Vac8 exclusively and competitively binds to Nvj1 and Atg13.

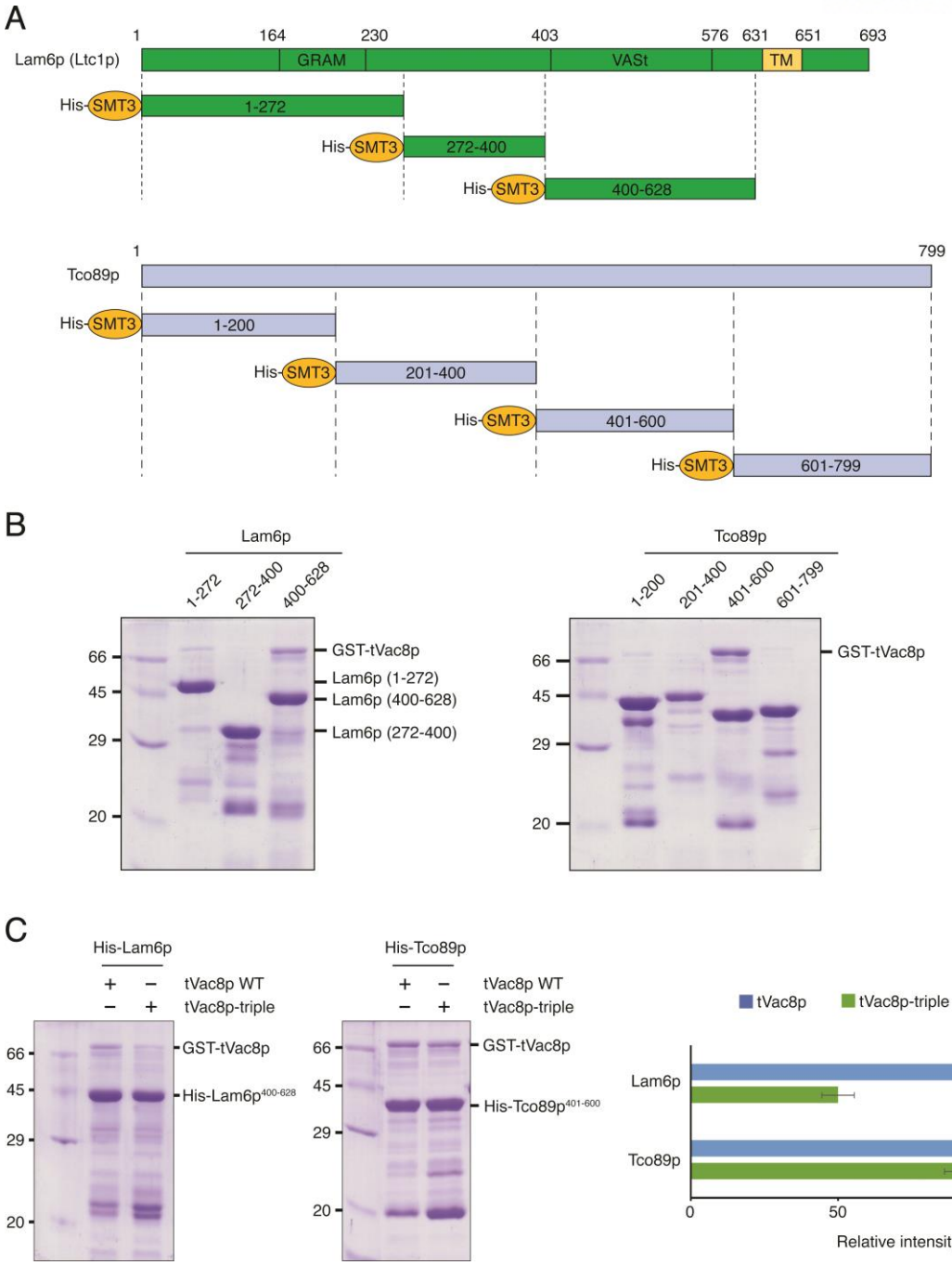

Figure 1.9. Particular regions of Lam6 and Tco89 directly interact with tVac8

(A) Schematic representations showing domain structures of Lam6 and Tco89. A series of truncated constructs used for pull-down experiments are indicated. All constructs were fused to the His_6-SMT3 tag at their N termini.

(B) His-tag pull-down experiments showing tVac8 interactions with Lam6 and Tco89. GST-tagged tVac8 was coexpressed with His_6-SMT3-tagged Lam6 or Tco89 and immobilized on Ni^{2+}-NTA resin. Experiments were carried out as described in Figure 1.8B.

(C) To test whether Vac8 shares the binding interface for Nvj1 with Lam6 or Tco89, wild-type and triple mutant (R276E/R317E/R359E) GST-tagged tVac8 were coexpressed with His-tagged Lam6 (residues 400–628) or Tco89 (residues 401–600) and immobilized on Ni^{2+}-NTA resin. Quantitative data are shown on the right. TM, transmembrane domain.

1.3.6. Mutation of Vac8 cationic residues disrupts the CVT pathway

To examine whether the differential affinity of the Vac8 triple mutant to Atg13 and Vac17 revealed by the in vitro binding experiments is relevant to their in vivo functions, we attempted to observe the CVT pathway of Ape1 and vacuole inheritance in budding yeast cells expressing wild-type or the mutant Vac8. Atg13 is known to mediate the transport of cytoplasmic Ape1 to the vacuole lumen through the CVT pathway upon starvation [14, 27]. In yeast cells expressing wild-type Vac8, Ape1-EGFP was dispersed in the lumen of vacuoles upon starvation (Figure 1.10A), suggesting that cytoplasmic Ape1-EGFP was transported to the vacuole via the CVT pathway. By contrast, Ape1-EGFP formed punctate structures in the cytoplasm of yeast cells lacking Vac8, indicating a defective CVT pathway (Figures 1.10 A and B, and 1.7B). A similar result was obtained with yeast cells expressing the Vac8-triple (Figures 1.10 A and B, and 1.7B), suggesting that the triad of cationic residues (Arg276, Arg317, and Arg359) in the groove of Vac8 are also critical for the in vivo interaction between Vac8 and Atg13, and thus for the CVT pathway.

Vac17 interacts simultaneously with Vac8 and Myo2, the yeast class V myosin motor, and this trimeric complex moves the vacuole to the bud, mediating vacuole inheritance during yeast cell budding [28]. To examine whether the Vac8-triple mutant could support vacuole inheritance, yeast cells expressing wild-type or mutant Vac8 were stained with the vacuole-specific dye FM4/64 and analyzed for vacuole inheritance in newly formed buds. As shown in Figure 1.11, no obvious defect in vacuole inheritance was observed in cells expressing the Vac8-triple mutant, consistent with the finding that Vac8-triple retained significant affinity for Vac17 (Figure 1.8B). However, Vac8-triple undoubtedly abolished the formation of NVJ as shown in the Nvj1-triple mutant (Figure 1.10C).

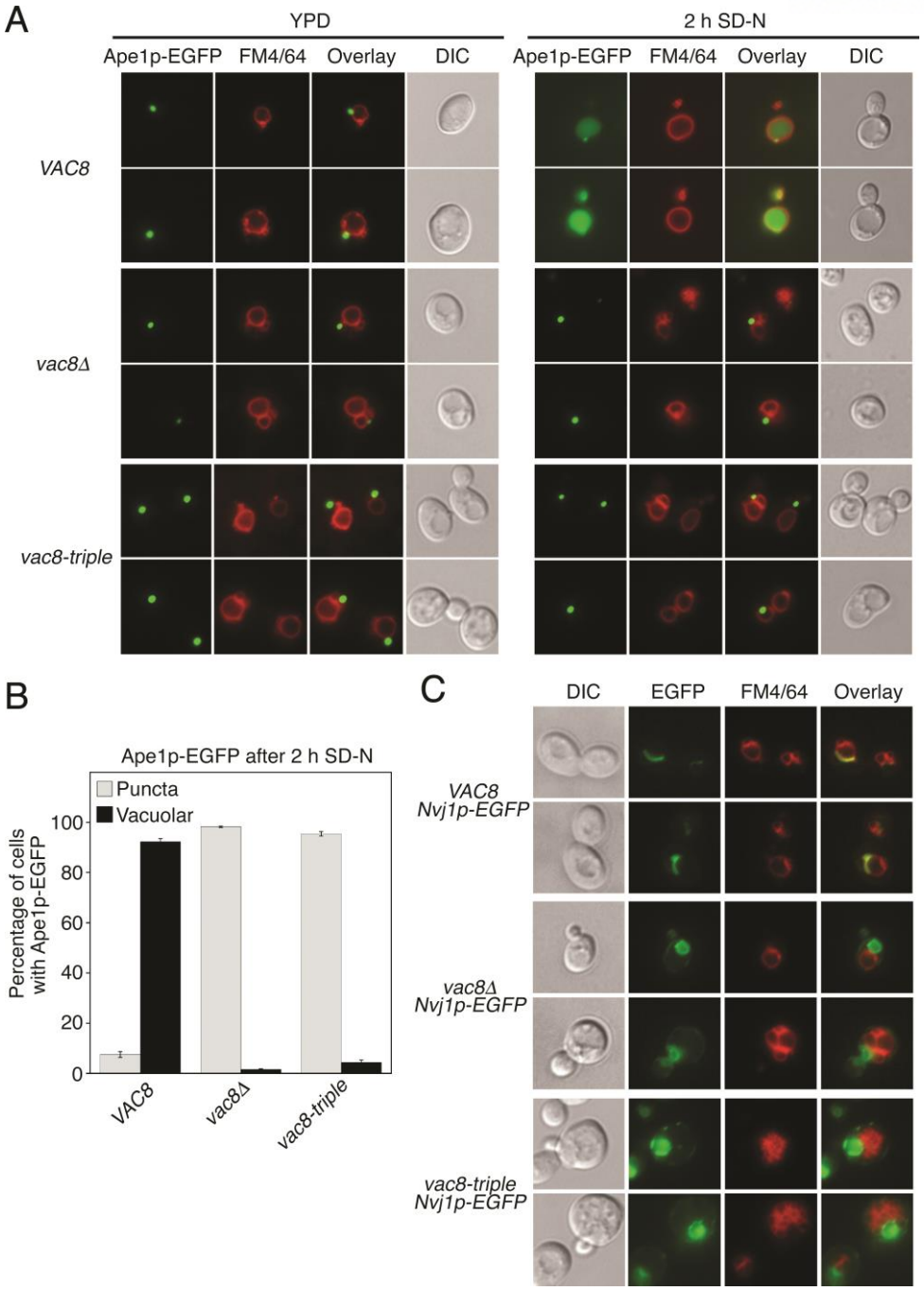

Figure 1.10. Mutation of the cationic triad in Vac8 causes disruption of the NVJ and CVT pathway

(A) The Vac8-triple mutant fails to support cytoplasm-to-vacuole transport of Ape1-EGFP upon starvation. The vacuoles of wild-type, *vac8Δ*, and *vac8-triple* mutant cells expressing Ape1-EGFP were labeled with FM4/64 in YPD media for 2 h at 30°C. After free dye was removed, cells were resuspended in nitrogen starvation medium (SD-N) and allowed to grow for 2 h at 30°C. GFP signals for Ape1 and FM4/64 signal in vacuoles were then analyzed by fluorescence microscopy. Representative images from each cell type are shown. (Magnification: 100 ×.)

(B) Graph showing quantitative data for cytoplasmic and vacuolar Ape1-EGFP obtained as described in (A).

(C) The Vac8-triple mutant does not support the formation of a tight junction between the nucleus and the vacuole. Experiments were performed as in (A) without starvation, and GFP fluorescence for Nvj1 was analyzed by fluorescence microscopy. (Magnification: 100 ×.) DIC, differential interference contrast.

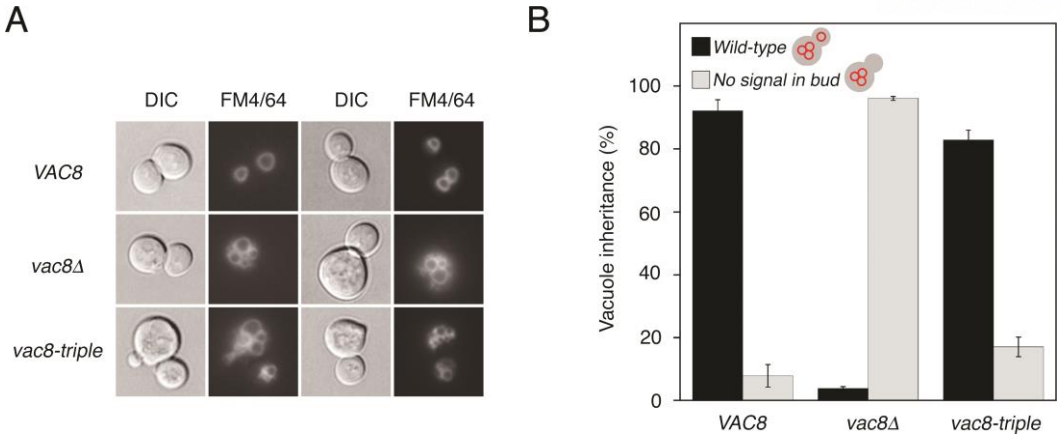

Figure 1.11. The Vac8-triple mutant supports vacuole inheritance

To analyze whether Vac8-triple affects the vacuole inheritance, the vacuoles of wild-type or Vac8-triple mutant cells were labeled with FM4/64 for 30 min at 30°C. After the free dye was removed, cells were resuspended in fresh media and allowed to grow for 3 h at 30°C. The vacuole morphology and inheritance were analyzed by fluorescence microscopy. Representative images from each cell type **(A)** and quantitation for vacuole inheritance **(B)** are shown. (Magnification: 100 ×.) DIC, differential interference contrast.

1.3.7. Vac8 self-associates through ARM1

The crystal structure revealed two tVac8-tNvj1 complexes arranged via twofold rotation symmetry into a four-helix bundle structure comprising H2 and H3 of ARM1 in the asymmetric unit (Figure 1.12A). The tVac8 homo-dimeric interface buries 622 $Å^2$ of surface area in the dimeric tVac8–tNvj1 complex and is mediated by van der Waals contacts between H2 and H3 of ARM1. In particular, the side chains of Ala51, Leu52, and Leu55 from H2 and Leu63, Ala70, and Ile74 from H3 make hydrophobic contacts with the same side chains of the opposing molecule in the homodimer. In addition to hydrophobic interactions, Ser66 and Glu73 make hydrogen bonds with Thr54 and Gly47 from the opposing molecule, respectively (Figure 1.12B).

At first, we assumed that the self-association of tVac8 might be an artifact of crystal contacts and not a biologically relevant interface because the Vac8-tNvj1 complex migrated as an apparent heterodimer rather than a heterotetramer in gel-filtration chromatography (Figure 1.1B). However, the following biochemical data strongly indicated the possibility that Vac8 self-associated in solution. First, the flexibly connected H1 helix was not vulnerable to proteases such as subtilisin or trypsin, and if Vac8 complexed Nvj1 as a monomer this would likely not be the case. However, a dimeric form of Vac8 would likely restrict access of proteases through steric hindrance, as shown in the crystal structure (Figure 1.4C). Second, truncated Vac8 (residues 40–515, referred to as $Vac8^{40–515}$) that included only the ARM repeats formed a tight heterotetramer based on both gel-filtration chromatography and analytical ultracentrifugation (Figure 1.12 C and D). Surprisingly, the single mutation A51R or L55R interfered with the dimer interface to the extent that the mutant forms of $Vac8^{40–515}$ were unable to self-associate, suggesting that residues at the dimer interface are important for self-association in solution (Figure 1.12 C and D). Collectively, the results strongly suggest that the Vac8-Nvj1 complex self-oligomerizes in solution into the assembly shown in the crystal structure (Figures 1.4C and 1.12A), and this may be related to the molecular function. This raises the question of why full-length Vac8 complexed with tNvj1 eluted as a monomer in gel-filtration chromatography. One explanation is that the flexibly linked H1 helix might interact with H2 and H3 of ARM1 from Vac8 to sterically mask the dimerization interface in solution. Indeed, a fold-back mechanism operating through the interaction between ARM repeats on the N- or C-terminal helices has been previously proposed for β-catenin [29-31]. To test this hypothesis, we generated a truncated mutant lacking helix H1 (residues 19−33, referred to as Vac8ΔH1) for the otherwise full-length Vac8. Because the H1 helix is flexibly connected to ARMs by disordered residues, we predicted that the removal of H1 would not affect the overall structure of Vac8. Surprisingly, we observed that Vac8ΔH1 complexed with tNvj1 to form a dimer in a concentration-dependent manner. However, Vac8ΔH1 mutants with the A51R or L55R mutation could not form a dimer at all, suggesting that self-

association of Vac8 might be regulated by the H1 helix in the presence of tNvj1 (Figure 1.12E).

Under appropriate cellular conditions, other (unknown) cellular factor(s) might induce a conformational change of helix H1 that causes it to dissociate from H2 and H3 of ARM1 to promote the self-association of Vac8 through the exposed H2 and H3. Structural analysis showed that the highly conserved final four residues (PFRY) of Nvj1 are directly oriented away from the H2 and H3 helices of tVac8 ARM1 (Figure 1.13D). In particular, Tyr321 of tNvj1 forms an H-bond with the conserved Glu76 of tVac8 and also forms hydrophobic contacts with conserved Leu69 and Ala72 of tVac8. Remarkably, we found that truncated Nvj1 lacking the last four residues (tNvj1$^{\Delta 318–321}$) could still bind to Vac8$^{40–515}$ but could not induce the dimerization of Vac8$^{40–515}$ (Figure 1.12 C and D). We tested whether Nvj1 could affect the self-oligomerization of Vac8 by comparing Vac8$^{40–515}$ alone and Vac8$^{40–515}$ complexed with tNvj1 using gel-filtration chromatography. We expected that Vac8$^{40–515}$ without tNvj1 may elute as a monomer if Nvj1 served as a regulatory factor. However, partially consistent with our expectations, Vac8$^{40–515}$ alone was not soluble and aggregated in solution and eventually eluted from the column in the void volume. From this observation, we speculate that H2 and H3 from ARM1 of Vac8$^{40–515}$ are highly disordered in the absence of Nvj1 and unable to form the four-helix bundle structure, which exposes the hydrophobic residues from H2 and H3, culminating in aggregation. Consistently, Vac8ΔH1 was unable to form a dimer at even a high concentration when not complexed with Nvj1 (Figure 1.12E). Taken together, our results led us to propose that binding of Nvj1 organizes the H2 and H3 helices of Vac8 and induces them to form a four-helix bundle structure when required, rather than directly initiating the self-oligomerization of Vac8 (Figure 1.13D).

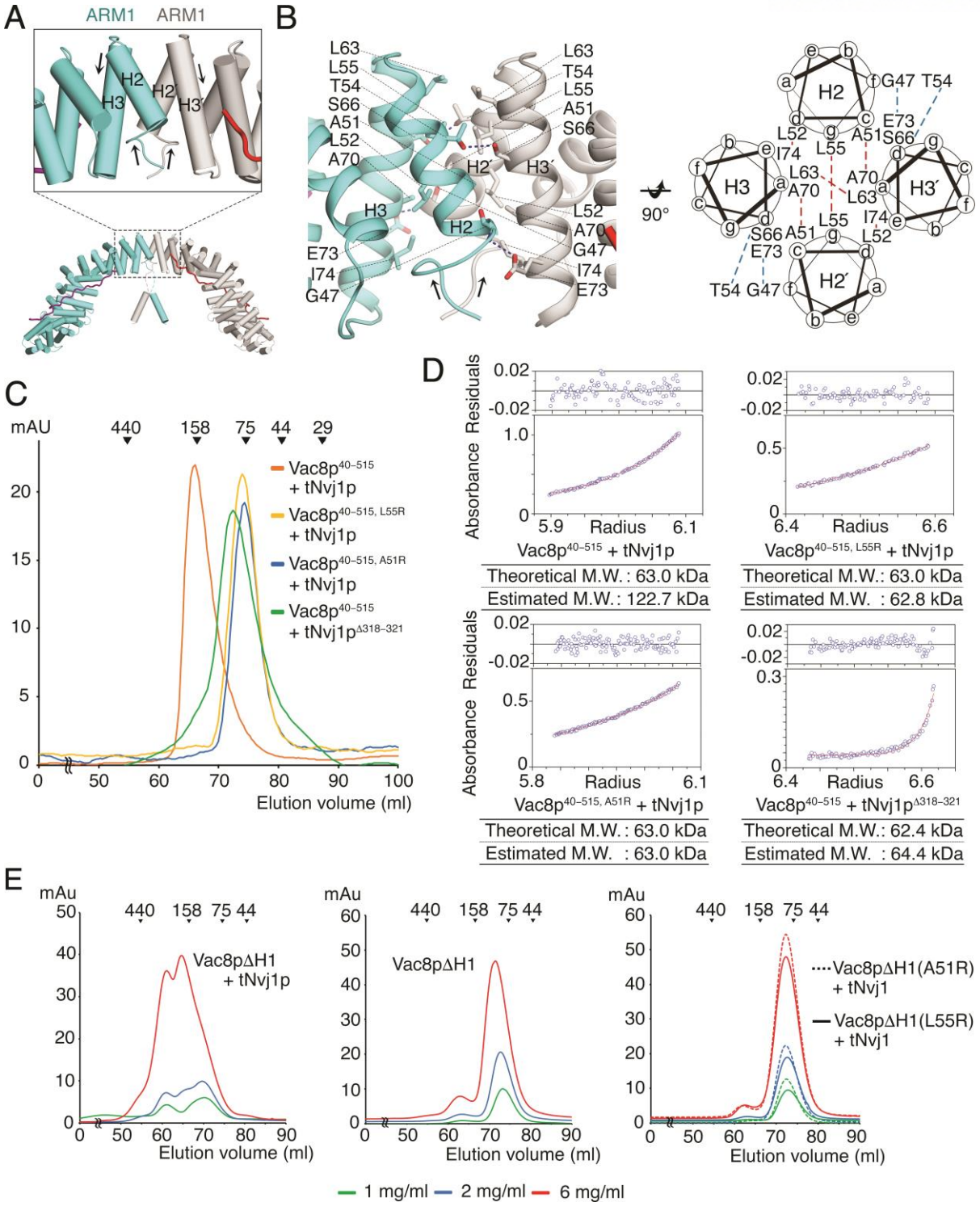

Figure 1.12. The first ARM of tVac8 mediates self-association of Vac8

(A) Cartoon representation of the tVac8-tNvj1 complex in the crystal asymmetric unit. Two copies of the tVac8-tNvj1 heterodimer are organized via twofold symmetry, forming a four-helix bundle from ARM1. The black box highlights the orientation of helices from ARM1 repeats in the tVac8 homo-dimeric interface, and black arrows indicate the direction of the helices.

(B) Close-up view of the four-helix bundle in the tVac8 homo-dimeric interface (Left). Blue dotted lines indicate intermolecular H-bonds. (Right) A schematic helical wheel showing the organization of the four helices that form the twofold interface. Blue and red dashed lines indicate hydrogen bonds and hydrophobic contacts, respectively.

(C) SEC profiles of $Vac8^{40-515}$-tNvj1, $Vac8^{40-515,\ A51R\ or\ L55R}$-tNvj1, and $Vac8^{40-515}$-$tNvj1^{\Delta 318-321}$ complexes. The results reveal the behavior of wild-type Vac8 and its variants in solution. Experiments were performed as shown in Figure 1.1B.

(D) Analytical ultracentrifugation measurement of the molecular mass of wild-type and mutant $Vac8^{40-515}$ in complex with tNvj1 using the sedimentation equilibrium method. The upper panel shows the residuals, and the results are summarized on the bottom.

(E) Chromatograms comparing the SEC behaviors of Vac8ΔH1-tNvj1, Vac8ΔH1 alone, and $Vac8\Delta H1^{A51R\ or\ L55R}$-tNvj1. Proteins at three different concentrations (1, 2, and 6 mg/mL) were injected into a Superdex 200 column and analyzed as shown in (B). M.W., molecular weight.

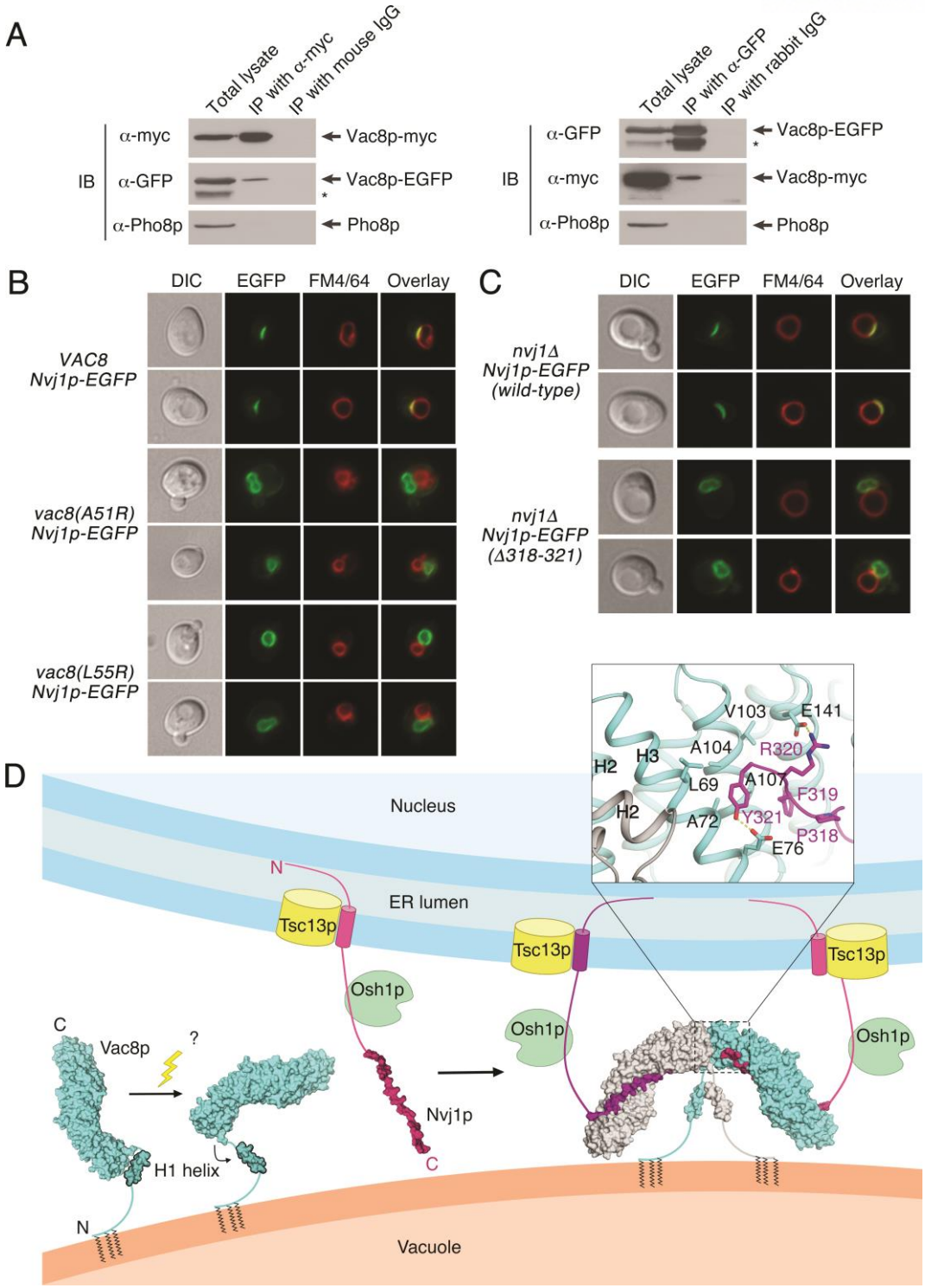

Figure 1.13. Vac8 forms a homo-dimer in vivo for NVJ formation

(A) Vac8-EGFP coprecipitates with Vac8-myc. Vacuoles isolated from BY4742 expressing both Vac8-EGFP and Vac8-myc were detergent-solubilized and incubated with either anti-myc antibodies or control mouse IgG, or with either anti-GFP antibodies or control rabbit IgG in the presence of protein A Sepharose. Protein A Sepharose-bound material was then analyzed by immunoblotting using the indicated antibodies. The asterisk indicates degradation products of Vac8-EGFP. All experiments were performed multiple times with similar results, and the data shown are representative of all results.

(B) Normal NVJs do not form in cells expressing the dimerization-defective mutant Vac8(A51R) or Vac8(L55R). The experiment was carried out as described in Figure 1.10C.

(C) The Nvj1 mutant Nvj1(Δ318−321) fails to support the formation of a tight junction between the nucleus and the vacuole. The experiment was performed as Figure 1.5C.

(D) Schematic representation showing the putative working model of the self-association of the Vac8-Nvj1 complex regulated by both the H1 helix and Nvj1. Unknown factors likely cause dissociation of the flexible H1 helix of Vac8 from the ARM repeats, and binding of Nvj1 might induce the reorganization of helices H2 and H3 of ARM1 to form the four-helix bundle structure at the complex interface. These conformational changes eventually establish a Vac8-Nvj1 hetero-tetramer that could be functionally critical for NVJ formation and/or PMN signaling. DIC, differential interference contrast; ER, endoplasmic reticulum; IB, immunoblotting; IP, immunoprecipitation.

1.3.8. Vac8 dimerization is required for normal NVJ formation

Our in vitro experiments (Figure 1.12) strongly suggest that Vac8 forms a dimer under the regulatory control of Nvj1. To confirm whether Vac8 dimerizes in vivo, EGFP-conjugated Vac8 and myc-tagged Vac8 were coexpressed in yeast cells, and their interactions were analyzed by coimmunoprecipitation. As shown in Figure 1.13A, Vac8-EGFP was coprecipitated with Vac8-myc, suggesting that Vac8 forms a homodimer in vivo. To examine whether Vac8 dimerization is critical for its functions, in particular to NVJ formation, Nvj1-EGFP was expressed in wild-type *VAC8* yeast cells or *vac8Δ* cells expressing Vac8(A51R) or Vac8(L55R). Whereas endogenous Vac8 supported the formation of normal NVJs in wild-type *VAC8* cells, Nvj1-EGFP fluorescence was dispersed over the entire nuclear membrane in Vac8(A51R)- and Vac8(L55R)-expressing cells (Figures 1.13B and 1.7C). Consistently, EGFP-conjugated Nvj1(Δ318−321), a mutant that cannot induce Vac8 dimerization, failed to form normal NVJs (Figure 1.13C). Thus, these data strongly suggest that Vac8 homodimerization is critical for its function in NVJ formation.

1.4. Discussion

In this study we determined the crystal structure of the tVac8-tNvj1 complex and established the protein organization mediating NVJs at the molecular level. To obtain diffraction-quality crystals of the Vac8-Nvj1 complex we truncated both the N and C termini of Vac8. It is noteworthy that truncation of the C terminus of Vac8 was critical to producing crystals because the flexibly connected H1 helix of Vac8 was plausibly located in the H3 helix position of ARM12 of neighboring molecules that stabilized lattice contacts and crystal packing (Figure 1.3 C and D). Indeed, the binding affinity of tVac8 for tNvj1 was reduced by around eightfold compared with the native protein. We assumed that the reduced affinity might be because the truncated regions are somewhat involved in the Nvj1 interaction, and/or because the truncations affected protein stability by generating incomplete ARM repeats for ARM12. Structural analysis revealed that ARM12 itself is not directly associated with the Nvj1 interaction. Interestingly, we found that the binding affinity (K_d of 0.7 μM) between tNvj1 and Vac8 (residues 1−532), in which all 12 ARMs are intact, was almost comparable to that of tNvj1 and full-length Vac8 based on ITC measurements (Figure 1.1C). This suggests that no additional binding energy would be gained from the presence of the C terminus of Vac8. Rather, the ARM12 H3 truncation likely affects the stability of tVac8. From this observation, we suggest that the structural integrity resulting from the correct formation of all 12 ARM repeats in Vac8 might be important for protein stability and interaction with Nvj1 [13].

As expected, the overall architecture of the tVac8-tNvj1 complex resembles the β-catenin/E-cadherin complex (RMSD = 4.3 Å) and the importin α/Heh2 complex (RMSD = 2.4 Å) and has similar structural features, despite the low sequence similarity between them (Figure 1.14) [15, 32-34]. First, the central domains of Vac8 and β-catenin are composed of 12 tandem ARM repeats that are organized into a right-handed superhelical structure. Second, Vac8 binds Nvj1 in an antiparallel fashion, and β-catenin interacts with E-cadherin, Tcf-1, and APC exclusively or partially in an antiparallel manner. Third, the interacting partners of ARM domain proteins adopt a mainly extended loop structure within the groove formed by the ARM repeats. Additionally, client ligands compete for the same ARM domain-mediated binding platform formed. Finally, the self-interaction referred to as the fold-back mechanism that involves the N- and C-terminal ARM repeats is present in both Vac8 and β-catenin. Because these structural features may be common among all ARM-containing proteins, we propose that the Vac8-Nvj1 complex might be evolutionarily conserved with β-catenin. Despite the structural similarity, some unique features were apparent. First, the binding affinity of the Vac8-Nvj1 complex is weaker than that between β-catenin and E-cadherin [25]. Second, whereas charged interactions are stronger in the β-catenin/E-cadherin interface, the Vac8-Nvj1 interface is formed from both H-bonds and nonpolar contacts, and the charged buttons shown in β-catenin are not conserved.

Finally, self-association of ARM domains is a unique feature of Vac8. In summary, although it has been reported that Vac8 and β-catenin do not share all functions, they clearly share some biologically important features in common, specifically the formation of a structural platform through ARM repeats that can interact with other functional molecules and that responds to cellular demands.

The self-association of Vac8 through a specific ARM repeat was unexpected, and the functional implications of this self-association in the working model of Vac8 require further investigation (Figure 1.13D). Our accumulated biochemical data suggest that the self-association of Vac8 is dependent on the interaction with Nvj1, indicating that the oligomerization of Vac8 is associated with a particular function such as forming NVJs or PMN pathway signaling (Figure 1.13 B–D). Future work should therefore focus on other potential binding partners such as Atg13 or Vac17 that could drive the self-association of Vac8.

Recently, several proteins have been suggested to mediate nuclear–vacuolar junctions [35-37]. Ltc1 (also known as Lam6), an ER integral membrane protein, is localized to NVJ via its binding to Vac8 [35, 37]. Another integral ER membrane protein, Mdm1, binds vacuolar phosphatidylinositol-3-phosphate through its PX domain, forming NVJs [36]. Although the molecular composition or architecture of NVJs formed by these proteins remains unknown, their contribution to the formation of a tight NVJ is likely to be limited because disruption of the Nvj1-Vac8 interaction largely impaired the tight apposition between the nucleus and the vacuole (Figure 1.5C, Nvj1-triple). Thus, it is very likely that the NVJ mediated by Nvj1-Vac8 constitutes the main contact site between the two organelles whereas other NVJs may play a complementary or even a redundant role.

In conclusion, this study provides insight into understanding how Vac8 recognizes Nvj1, and how the resulting protein complex physically mediates this organelle contact site and promotes the molecular events that occur at these specialized intracellular zones.

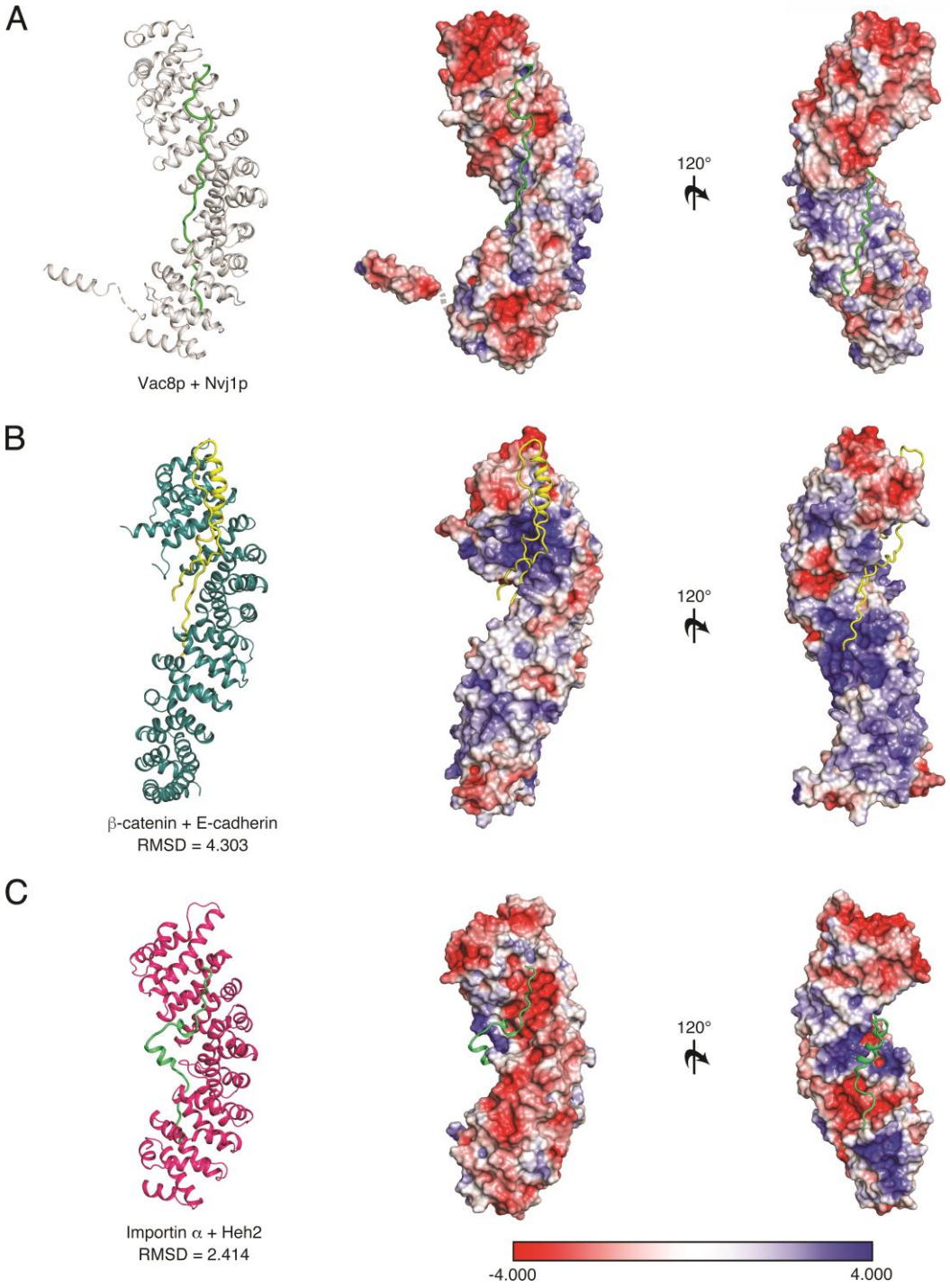

Figure 1.14. Comparison of the tVac8-tNvj1 complex with other ARM-containing proteins

Ribbon and surface charge representations of the tVac8 (gray)-tNvj1 (green) complex **(A)**, β-catenin (dark green)-E-cadherin (yellow) complex **(B)**, and Importin α (magenta)-Heh2 (light green) complex **(C)** shown in the same orientations. The electrostatic potential of the surface area was calculated using the APBS program [38] and contoured at ± 4 KT/e (blue, positive; red, negative).

1.5. Materials and Methods

1.5.1. Cloning

The full-length Vac8 gene was amplified by PCR using *S. cerevisiae* genomic DNA and fused into the pGEX-6P-1 vector. DNA fragments encoding *S. cerevisiae* Nvj1 and Atg13 were cloned into the pCDFDuet-1 vector that had been modified previously to include a tobacco etch virus (TEV) protease cleavage site before the first residues of Nvj1 and Atg13. Each plasmid was transformed into competent *E. coli* BL21 (DE3) cells, and protein expression was induced with 0.4 mM isopropyl β-D-1-thiogalactopyranoside when the cell density reached an A600 value of 0.6. After culturing for a further 18 h at 18°C, cells were harvested by centrifugation at 3,200 × g for 15 min at 4°C. Cells expressing Vac8 were resuspended in PBS, and cells expressing Nvj1, Atg13, or Vac8-Nvj1 were resuspended in buffer A (25 mM sodium phosphate, pH 7.8, 400 mM sodium chloride, and 10 mM imidazole).

1.5.2. Protein production

Nvj1 and Atg13 were purified by Ni^{2+}-immobilized metal affinity chromatography (Ni^{2+}-IMAC). His_6-tags were removed by TEV protease during dialysis against buffer B comprising 25 mM Tris-HCl, pH 7.5, 150 mM NaCl, and 5 mM β-mercaptoethanol (β-ME). After cleavage, reactions were subjected to subtractive Ni^{2+}-IMAC to remove tags and undigested protein, followed by SEC with a Superdex 200 (16/600) column (GE Healthcare) preequilibrated with buffer C comprising 25 mM Tris-HCl, pH 7.5, 150 mM NaCl, and 5 mM DTT. Vac8 proteins were purified by GST affinity chromatography, and the GST tag was removed using PreScission protease. Proteins were further purified using ion-exchange chromatography on a HiTrap Q HP column and gel-filtration chromatography on a Superdex 200 column.

For purification of the tVac8-tNvj1 complex, plasmids encoding GST-tagged tVac8 and His_6-tagged tNvj1 were cotransformed and overexpressed in *E. coli* BL21 (DE3) cells. Proteins were purified by Ni^{2+}-IMAC (GE Healthcare), and tags were cleaved by TEV and PreScission protease, followed by dialysis overnight against buffer B at 4°C. Proteins were subsequently subjected to subtractive Ni^{2+}-IMAC and GST affinity chromatography to remove cleaved tags and then further purified using SEC with a Superdex 200 column (GE Healthcare) in buffer C.

Selenomethionine-labeled tVac8-tNvj1 complex was expressed in *E. coli* B834 (DE3) cells using M9 minimal media and purified using the same procedure as described above for the native

protein. All mutants used in this study were generated by PCR-based site-directed mutagenesis. Mutations were confirmed by DNA sequencing, and proteins were purified as described previously.

1.5.3. Crystallization and structure determination

For crystallization of the tVac8-tNvj1 complex, proteins were concentrated to 10 mg/mL using an Amicon Ultra-15 centrifugal filter (molecular mass 50 kDa cutoff; Merck Millipore). Crystals for both native and Se-Met tVac8-tNvj1 proteins were grown in 22% PEG 400, 0.1 M bis-Tris propane (BTP), pH 6.5, and 1.5% t-butanol by the hanging-drop vapor diffusion method at 20°C. Crystals were transferred to a cryoprotectant solution comprising 30% PEG 400, 0.1 M BTP, pH 6.5, and 1.5% t-butanol and frozen in liquid nitrogen. Diffraction data for both native and Se-Met crystals were collected at the Pohang Accelerator Laboratory (7A beamline) and processed using the HKL2000 package [39]. Phases were calculated from a SAD dataset collected at a Se peak wavelength of 0.9793 Å using the PHENIX program [17]. Structures were built using Coot [40] and refined with PHENIX [17]. The final model was refined to R_{work}/R_{free} values of 0.193/0.217 using native data and included two complexes in the asymmetric unit. Residues 10–18, 35–39, and 513–515 of Vac8 and residues 229–291 of Nvj1 in the first copy, and residues 10–18, 35–39, and 513–515 of Vac8 and residues 229–291 of Nvj1 in the second copy are not visible in the electron density maps and were omitted from the final model. Crystallographic data and refinement results are summarized in Table 1.1.

1.5.4. Size-exclusion chromatography analysis

To assess the interaction between Vac8 and Nvj1 (as indicated in Figure 1.1B) and analyze the relative molecular mass of Vac8 and Vac8 mutants ($Vac8^{40–515}$ + tNvj1, $Vac8^{40–515,\ A51R\ or\ L55R}$ + tNvj1, and $Vac8^{40–515}$ + $tNvj1^{\Delta318–321}$ in Figure 1.12C; Vac8ΔH1 alone and complexed with tNvj1 in Figure 1.12E), purified proteins were injected onto a Superdex 200 (16/600) column (GE Healthcare) equilibrated with buffer C. Protein standards used in the experiment were ferritin, 440 kDa; aldolase, 158 kDa; conalbumin, 75 kDa; ovalbumin, 43 kDa; and ribonuclease A, 13.7 kDa.

1.5.5. Isothermal titration calorimetry

All protein samples (Vac8, $Vac8^{1–532}$, tVac8, tNvj1, $Atg13^{567–738}$, Vac8-tNvj1, and Vac8-$Atg13^{567–738}$) used in ITC measurements were prepared in buffer B using a HiTrap desalting column (GE Healthcare). ITC experiments were performed using a Microcal ITC200 instrument (GE Healthcare) at 25°C. The molar concentrations used in the sample cell and the syringe were 40 μM

and 0.6 mM, respectively (Figure 1.1C and Figure 1.8C). Measurements were carried out over 20 injections of 2 μL, with a reference power of 5 μcal/s, and a stirring speed of 1,000 rpm. Titration curves were fitted to the one set of sites model using Origin software provided by the manufacturer.

1.5.6. Analytical ultracentrifugation

The absolute molecular mass of Vac8$^{40-515}$-tNvj1, Vac8$^{40-515, A51R}$-tNvj1, Vac8$^{40-515, L55R}$-tNvj1, and Vac8$^{40-515}$-tNvj1$^{\Delta 318-321}$ was measured by sedimentation equilibrium analysis in an XL-A analytical ultracentrifuge (Beckman Coulter) as described previously [41]. Protein samples were prepared in a buffer consisting of 25 mM Tris-HCl, pH 7.5, 200 mM NaCl, and 5 mM β-mercaptoethanol.

1.5.7. Pull-down assay

For His-tag pull-down experiments (Figure 1.5B), 10 μL of Ni-NTA agarose (Qiagen) was incubated with supernatants from *E. coil* cells coexpressing GST-tVac8 and wild-type tNvj1 or GST-tVac8 and tNvj1 mutants for 1 h at 4°C. Beads were washed three times with 500 μL of buffer A supplemented with 50 mM imidazole plus 0.1% Triton X-100 and 0.1% Nonidet P-40. Proteins were eluted with 4 × SDS sample buffer, analyzed by 15% SDS-PAGE, and stained with Coomassie blue. To assess the binding of Nvj1, Atg13, Lam6, Tco89, and Vac17 to tVac8 and the tVac8-triple mutant, as shown in Figure 1.8B and Figure 1.9, GST-tVac8 or the GST-tVac8-triple mutant (R276E/R317E/R359E) was coexpressed with histidine-tagged tNvj1, Vac17, and Atg13 and His_6-SMT3-tagged Lam6 and Tco89 in *E. coli* BL21 (DE3) cells. His-tag pull-down experiments were performed as described above.

1.5.8. Yeast strains and vacuole staining with FM4/64

Yeast strains used in this study are listed in Table 1.2. Vacuoles of growing yeast cells were labeled with FM4/64 as previously described with minor modifications [42]. Briefly, cells were grown at 30°C to an OD600 of 0.8 in YPD (10 g/L yeast extract, 20 g/L peptone, and 20 g/L dextrose) medium. Then, the cells were incubated with aeration in YPD medium containing 20 μM FM4/64 (Molecular Probes) for 30 min at 30°C. The cells were then harvested by centrifugation (2,400 × g) at room temperature for 1 min, washed, and resuspended in fresh medium. The cells were then allowed to grow for 3 h at 30°C. After harvesting by centrifugation, the cells were analyzed by a fluorescence microscope (Nikon Eclipse Ti-U) with a Nikon Plan Apo × 100, 1.45/N.A. oil immersion objective.

1.5.9. PMN and CVT induction

Cells were grown overnight at 30°C with shaking in YPD. Cultures were adjusted to OD600 = 0.5 and 0.5 μM FM4/64 was added to visualize vacuoles. The cells were then allowed to grow for 2 h at 30°C. For PMN induction, 0.2 μM rapamycin (Sigma-Aldrich) was added and the cells were further incubated for 6 h at 30°C. For CVT induction, cells grown in YPD were washed with autoclaved water three times and resuspended in nitrogen starvation (SD-N) media. The cells were further allowed to grow for 2 h at 30°C.

1.5.10. Coimmunoprecipitation

Yeast vacuoles were isolated as described [43]. Vacuoles were resuspended in ice-cold solubilization buffer (PBS containing 0.5% Triton X-100, 1 mM EDTA, 1 mM PMSF, and 10 mM leupeptin) and incubated on ice for 20 min. Detergent-insoluble material was removed by centrifugation at 16,200 × g (10 min, 4°C). The resulting postcentrifugation supernatants were precleared by incubation with protein A Sepharose (GE Healthcare) at 4°C for 1 h. Anti-myc antibodies, control mouse IgG, anti-GFP antibodies, or control rabbit IgG were added to the precleared supernatants and incubated 4°C on a nutator mixer for 2 h. Protein A Sepharose was then added and further incubated for 1 h. Protein A Sepharose beads were collected by centrifugation at 3,000 × g (1 min, 25°C) and washed three times with ice-cold solubilization buffer. Bound proteins were eluted with SDS sample buffer for SDS/PAGE analysis followed by immunoblotting using anti-myc, anti-GFP, and anti-Pho8 antibodies.

1.6. References

[1] Y. Elbaz and M. Schuldiner, "Staying in touch: the molecular era of organelle contact sites," *Trends in biochemical sciences,* vol. 36, no. 11, pp. 616-623, 2011.

[2] M. J. Phillips and G. K. Voeltz, "Structure and function of ER membrane contact sites with other organelles," *Nature reviews Molecular cell biology,* vol. 17, no. 2, pp. 69-82, 2016.

[3] S. C. Helle, G. Kanfer, K. Kolar, A. Lang, A. H. Michel, and B. Kornmann, "Organization and function of membrane contact sites," *Biochimica et Biophysica Acta (BBA)-Molecular Cell Research,* vol. 1833, no. 11, pp. 2526-2541, 2013.

[4] P. Roberts, S. Moshitch-Moshkovitz, E. Kvam, E. O'Toole, M. Winey, and D. S. Goldfarb, "Piecemeal microautophagy of nucleus in Saccharomyces cerevisiae," *Molecular biology of the cell,* vol. 14, no. 1, pp. 129-141, 2003.

[5] E. Kvam and D. Goldfarb, "Nucleus-vacuole junctions and piecemeal microautophagy of the nucleus in S. cerevisiae," *Autophagy,* vol. 3, no. 2, pp. 85-92, 2007.

[6] R. Krick *et al.*, "Piecemeal microautophagy of the nucleus: genetic and morphological traits," *Autophagy,* vol. 5, no. 2, pp. 270-272, 2009.

[7] R. Dawaliby and A. Mayer, "Microautophagy of the nucleus coincides with a vacuolar diffusion barrier at nuclear–vacuolar junctions," *Molecular biology of the cell,* vol. 21, no. 23, pp. 4173-4183, 2010.

[8] T. P. Levine and S. Munro, "Dual targeting of Osh1p, a yeast homologue of oxysterol-binding protein, to both the Golgi and the nucleus-vacuole junction," *Molecular biology of the cell,* vol. 12, no. 6, pp. 1633-1644, 2001.

[9] S. D. Kohlwein *et al.*, "Tsc13p Is Required for Fatty Acid Elongation and Localizes to a Novel Structure at the Nuclear-Vacuolar Interface inSaccharomyces cerevisiae," *Molecular and Cellular Biology,* vol. 21, no. 1, pp. 109-125, 2001.

[10] E. Kvam and D. S. Goldfarb, "Nvj1p is the outer-nuclear-membrane receptor for oxysterol-binding protein homolog Osh1p in Saccharomyces cerevisiae," *Journal of cell science,* vol. 117, no. 21, pp. 4959-4968, 2004.

[11] E. Kvam, K. Gable, T. M. Dunn, and D. S. Goldfarb, "Targeting of Tsc13p to nucleus–vacuole junctions: a role for very-long-chain fatty acids in the biogenesis of microautophagic vesicles," *Molecular biology of the cell,* vol. 16, no. 9, pp. 3987-3998, 2005.

[12] X. Pan *et al.*, "Nucleus–vacuole junctions in Saccharomyces cerevisiae are formed through the direct interaction of Vac8p with Nvj1p," *Molecular biology of the cell,* vol. 11, no. 7, pp. 2445-2457, 2000.

[13] Y.-X. Wang, N. L. Catlett, and L. S. Weisman, "Vac8p, a vacuolar protein with armadillo repeats, functions in both vacuole inheritance and protein targeting from the cytoplasm to

vacuole," *The Journal of cell biology,* vol. 140, no. 5, pp. 1063-1074, 1998.

[14] S. V. Scott *et al.*, "Apg13p and Vac8p are part of a complex of phosphoproteins that are required for cytoplasm to vacuole targeting," *Journal of Biological Chemistry,* vol. 275, no. 33, pp. 25840-25849, 2000.

[15] R. Tewari, E. Bailes, K. A. Bunting, and J. C. Coates, "Armadillo-repeat protein functions: questions for little creatures," *Trends in cell biology,* vol. 20, no. 8, pp. 470-481, 2010.

[16] L. S. Weisman, "Organelles on the move: insights from yeast vacuole inheritance," *Nature reviews Molecular cell biology,* vol. 7, no. 4, pp. 243-252, 2006.

[17] P. D. Adams *et al.*, "PHENIX: a comprehensive Python-based system for macromolecular structure solution," *Acta Crystallographica Section D: Biological Crystallography,* vol. 66, no. 2, pp. 213-221, 2010.

[18] H. Ashkenazy, E. Erez, E. Martz, T. Pupko, and N. Ben-Tal, "ConSurf 2010: calculating evolutionary conservation in sequence and structure of proteins and nucleic acids," *Nucleic acids research,* vol. 38, no. suppl_2, pp. W529-W533, 2010.

[19] K. Mochida *et al.*, "Receptor-mediated selective autophagy degrades the endoplasmic reticulum and the nucleus," *Nature,* vol. 522, no. 7556, pp. 359-362, 2015.

[20] D. Mijaljica, M. Prescott, and R. J. Devenish, "A late form of nucleophagy in Saccharomyces cerevisiae," *PloS one,* vol. 7, no. 6, p. e40013, 2012.

[21] E. A. Winzeler *et al.*, "Functional characterization of the S. cerevisiae genome by gene deletion and parallel analysis," *science,* vol. 285, no. 5429, pp. 901-906, 1999.

[22] W. Xu and D. Kimelman, "Mechanistic insights from structural studies of β-catenin and its binding partners," *Journal of cell science,* vol. 120, no. 19, pp. 3337-3344, 2007.

[23] J. Hülsken, W. Birchmeier, and J. Behrens, "E-cadherin and APC compete for the interaction with beta-catenin and the cytoskeleton," *The Journal of cell biology,* vol. 127, no. 6, pp. 2061-2069, 1994.

[24] J. P. von Kries *et al.*, "Hot spots in β-catenin for interactions with LEF-1, conductin and APC," *Nature structural biology,* vol. 7, no. 9, pp. 800-807, 2000.

[25] H.-J. Choi, A. H. Huber, and W. I. Weis, "Thermodynamics of β-Catenin-Ligand Interactions: The roles of the N- and C-terminal tails in modulating binding affinity," *Journal of Biological Chemistry,* vol. 281, no. 2, pp. 1027-1038, 2006.

[26] E. Krissinel, "Stock-based detection of protein oligomeric states in jsPISA," *Nucleic acids research,* vol. 43, no. W1, pp. W314-W319, 2015.

[27] T. Funakoshi, A. Matsuura, T. Noda, and Y. Ohsumi, "Analyses of APG13 gene involved in autophagy in yeast, Saccharomyces cerevisiae," *Gene,* vol. 192, no. 2, pp. 207-213, 1997.

[28] F. Tang, E. J. Kauffman, J. L. Novak, J. J. Nau, N. L. Catlett, and L. S. Weisman, "Regulated degradation of a class V myosin receptor directs movement of the yeast vacuole," *Nature,* vol.

422, no. 6927, pp. 87-92, 2003.

[29] R. T. Cox, L.-M. Pai, C. Kirkpatrick, J. Stein, and M. Peifer, "Roles of the C terminus of Armadillo in Wingless signaling in Drosophila," *Genetics,* vol. 153, no. 1, pp. 319-332, 1999.

[30] J. Piedra, D. Martínez, J. Castaño, S. Miravet, M. Duñach, and A. G. a. de Herreros, "Regulation of β-catenin structure and activity by tyrosine phosphorylation," *Journal of Biological Chemistry,* vol. 276, no. 23, pp. 20436-20443, 2001.

[31] G. Solanas *et al.*, "β-Catenin and plakoglobin N-and C-tails determine ligand specificity," *Journal of Biological Chemistry,* vol. 279, no. 48, pp. 49849-49856, 2004.

[32] A. H. Huber, W. J. Nelson, and W. I. Weis, "Three-dimensional structure of the armadillo repeat region of β-catenin," *Cell,* vol. 90, no. 5, pp. 871-882, 1997.

[33] A. H. Huber and W. I. Weis, "The structure of the β-catenin/E-cadherin complex and the molecular basis of diverse ligand recognition by β-catenin," *Cell,* vol. 105, no. 3, pp. 391-402, 2001.

[34] G. Cingolani, C. Petosa, K. Weis, and C. W. Müller, "Structure of importin-β bound to the IBB domain of importin-α," *Nature,* vol. 399, no. 6733, pp. 221-229, 1999.

[35] Y. Elbaz-Alon *et al.*, "Lam6 regulates the extent of contacts between organelles," *Cell reports,* vol. 12, no. 1, pp. 7-14, 2015.

[36] W. M. Henne, L. Zhu, Z. Balogi, C. Stefan, J. A. Pleiss, and S. D. Emr, "Mdm1/Snx13 is a novel ER–endolysosomal interorganelle tethering protein," *Journal of Cell Biology,* vol. 210, no. 4, pp. 541-551, 2015.

[37] A. Murley, R. D. Sarsam, A. Toulmay, J. Yamada, W. A. Prinz, and J. Nunnari, "Ltc1 is an ER-localized sterol transporter and a component of ER–mitochondria and ER–vacuole contacts," *Journal of Cell Biology,* vol. 209, no. 4, pp. 539-548, 2015.

[38] N. A. Baker, D. Sept, S. Joseph, M. J. Holst, and J. A. McCammon, "Electrostatics of nanosystems: application to microtubules and the ribosome," *Proceedings of the National Academy of Sciences,* vol. 98, no. 18, pp. 10037-10041, 2001.

[39] Z. Otwinowski and W. Minor, "Processing of X-ray diffraction data collected in oscillation mode," *Methods in enzymology,* vol. 276, pp. 307-326, 1997.

[40] P. Emsley, B. Lohkamp, W. G. Scott, and K. Cowtan, "Features and development of Coot," *Acta Crystallographica Section D: Biological Crystallography,* vol. 66, no. 4, pp. 486-501, 2010.

[41] H. Jeong, J. Park, and C. Lee, "Crystal structure of Mdm12 reveals the architecture and dynamic organization of the ERMES complex," *EMBO reports,* vol. 17, no. 12, pp. 1857-1871, 2016.

[42] T. A. Vida and S. D. Emr, "A new vital stain for visualizing vacuolar membrane dynamics and

endocytosis in yeast," *Journal of cell biology,* vol. 128, no. 5, pp. 779-792, 1995.

[43] A. Haas, B. Conradt, and W. Wickner, "G-protein ligands inhibit in vitro reactions of vacuole inheritance," *The Journal of cell biology,* vol. 126, no. 1, pp. 87-97, 1994.

Chapter 2. Quaternary structures of Vac8 differentially regulate the CVT and PMN pathways

(Original article : Park J, Kim H-I, Jeong H, Lee M, Jang SH, Yoon SY, Kim H, Park Z-Y, Jun Y, Lee C. Quaternary structures of Vac8 differentially regulate the CVT and PMN pathways. *Autophagy*. 2020;*16*(6):991-1006.)

2.1. Abstract

Armadillo (ARM) repeat proteins constitute a large protein family with diverse and fundamental functions in all organisms, and armadillo repeat domains share high structural similarity. However, exactly how these structurally similar proteins can mediate diverse functions remains a long-standing question. Vac8 (vacuole related 8) is a multifunctional protein that plays pivotal roles in various autophagic pathways, including piecemeal microautophagy of the nucleus (PMN) and cytoplasm-to-vacuole targeting (CVT) pathways in the budding yeast Saccharomyces cerevisiae. Vac8 comprises an H1 helix at the N terminus, followed by 12 armadillo repeats. Herein, we report the crystal structure of Vac8 bound to Atg13, a key component of autophagic machinery. The 70 Å extended loop of Atg13 binds to the ARM domain of Vac8 in an antiparallel manner. Structural, biochemical, and in vivo experiments demonstrated that the H1 helix of Vac8 intramolecularly associates with the first ARM and regulates its self-association, which is crucial for CVT and PMN pathways. The structure of H1 helix-deleted Vac8 complexed with Atg13 reveals that Vac8ΔH1-Atg13 forms a heterotetramer and adopts an extended superhelical structure exclusively employed in the CVT pathway. Most importantly, comparison of Vac8-Nvj1 and Vac8-Atg13 provides a molecular understanding of how a single ARM domain protein adopts different quaternary structures depending on its associated proteins to differentially regulate two closely related but distinct cellular pathways.

2.2. Introduction

Yeast vacuoles, the equivalent of mammalian lysosomes, are membrane-bound organelles that serve a variety of pivotal functions including storage and digestion of waste products, regulation of cellular pH, and autophagy [1-7]. Vacuoles undergo constant fusion and fission that determines their inheritance during mitosis [8-10], and genetic screens of defects in vacuole inheritance have identified several genes specifically involved in the process [9, 11-13], including Vac8 (vacuole related 8), a protein with armadillo repeats (ARMs) [14, 15]. Vac8 binds to Myo2 (myosin 2) via the scaffold protein Vac17, and this ternary protein complex mediates vacuole migration toward the growing bud during cell division [16]. Vac8 is composed of ARMs, and myristoylation and palmitoylation lipid modification sites at the N-terminal region that anchor it into vacuolar membranes [14, 15, 17]. Consequently, the ARM domain is exclusively localized in the cytoplasm, where it is involved in the formation of membrane contact sites by acting as a scaffold to interact with various proteins from other organelles [14, 15].

Vac8 also plays an important role in piecemeal microautophagy of the nucleus (PMN) [18-20], during which a portion of the nucleus is transported to and degraded in the vacuole during nutrition starvation. PMN occurs at the nucleus-vacuole junction (NVJ), a well-characterized membrane contact site [18-20]. Vac8 anchored in vacuolar membranes directly associates with the outer nuclear membrane protein Nvj1, and physical interaction between Vac8 and Nvj1 mediates the formation of nucleus-vacuole membrane contact sites [21], thereby promoting PMN [18-20]. In addition, a recent study revealed that Vac8 forms a complex with Lam6/Ltc1 (lipid transfer protein anchored at membrane contact site 6) at ER-vacuole contact sites and mediates sterol transport to generate sterol-enriched vacuolar membrane domains [22].

Furthermore, Vac8 is involved in the cytoplasm-to-vacuole targeting (CVT) pathway, which transports cytoplasmic proteins to the vacuolar lumen in a manner similar to selective autophagy [15]. Upon nutrient starvation, Vac8 interacts with the key autophagy protein Atg13 (autophagy-related 13), and the resulting complex delivers cytoplasmic hydrolases such as Ape1 (aminopeptidase I) to the vacuole, where they become activated and functional [23]. Ape1 is synthesized as a precursor (prApe1) in the cytosol and transferred into the vacuole lumen through CVT vesicles [15, 23]. While much has been learned about the Vac8-Atg13 complex and its involvement in the CVT pathway, the molecular mechanism by which Atg13 is specifically recognized by Vac8 remains elusive. In addition, our previous study suggested that Nvj1 shares a binding interface for Vac8 with Atg13; therefore, Nvj1 or Atg13 competes for binding to Vac8 [24]. However, it is still unknown how Vac8 can discriminate between Nvj1 or Atg13, and thereby differentially regulate PMN or CVT pathways that occur

simultaneously in yeast.

In the present study, we present two crystal structures of Atg13 bound to Vac8. These structures, along with biochemical and in vivo experiments, reveal that Atg13 binding may induce the self-association of Vac8 by regulating the H1 helix, and the resulting Vac8-Atg13 heterotetramer adopts a superhelical structure. Furthermore, we demonstrate that the quaternary structural organization of Vac8 caused by binding of Atg13 or Nvj1 selectively supports CVT or PMN pathways, respectively.

2.3. Results

2.3.1. Structure of tVac8 in complex with tAtg13

The *Saccharomyces cerevisiae* Atg13 protein is composed of 738 residues (Figure 2.1A). The sequences from the N terminus to residue 521 are well conserved among mammalian ATG13 orthologs, and required for interaction with essential components of the autophagy machinery, including Atg1, Atg17, and Atg9 [25-27]. By contrast, the remaining residues from 522 to the end of the C terminus are present only in the yeast Atg13 protein. A previous yeast two-hybrid analysis and coimmunoprecipitation experiments revealed that the C-terminal region of Atg13 comprising residues 567–692 is required for association with Vac8 [23]. Based on these data, we made a truncated Atg13 construct (residues 567–695; designated as tAtg13) for structural analysis of the tVac8-tAtg13 complex. tVac8 (residues 10–515) was used in our previous study (Figure 2.1A) [24]. Analytical ultracentrifugation (AUC) experiment revealed that the tVac8-tAtg13 complex formed a heterodimer in solution (Figure 2.1B). Crystals of tVac8-tAtg13 were grown in a reservoir buffer containing polyethylene glycol (PEG) 400 as the main precipitant, and the structure was solved by the molecular replacement method using the Vac8 coordinates (PDB code: 5XJG) as a search model and refined to 2.9 Å resolution (Table 2.1).

Figure 2.1C shows the overall structure of tVac8 complexed with tAtg13 in ribbon representation. In our previous study, we revealed that tVac8 is composed of an H1 helix (residues 19–33) at the N terminus, followed by 12 central armadillo repeats (ARMs; Figure 2.1D) [24]. The loop (residues 35–40) bridging the H1 helix and the first ARM (ARM1) is disordered in the structure (Figure 2.1D). The overall conformation of the 12 concerted ARMs of tVac8 observed in the crystal structure of the tVac8-tAtg13 complex was essentially identical to that observed in the tVac8-tNvj1 complex [24], with a root-mean-square deviation (RMSD) value of 0.88 Å for all Cα atoms. The 70 Å extended loop of Atg13 binds across the inner groove formed by the central ARMs of Vac8 (Figure 2.1C). Similar to the tVac8-tNvj1 complex, Atg13 binds to Vac8 in an antiparallel fashion (Figure 2.1 C and D). Electron density for Atg13 was clearly visible only in the Vac8 contact region (residues 660–685), and all other residues were disordered in the structure, consistent with the structure of tNvj1 bound to tVac8 (Figure 2.2A) [24]. It is noteworthy that, while the tVac8-tNvj1 complex forms a heterotetramer comprising two tVac8-tNvj1 molecules that are organized via contacts with ARM1 of Vac8 (Figure 2.1D, right), such self-association of tVac8 was not observed in the structure of the tVac8-tAtg13 complex. Instead, as we proposed in a putative working model in our previous study [24], the H1 helix directly binds to ARM1 and eventually masks the dimeric interface (Figure 2.1E, left). The residues comprising the H1 helix in the tVac8-tAtg13 complex are different from those in

the tVac8-tNvj1 complex. In particular, this helix is extended by six residues that are disordered in the structure of the tVac8-tNvj1 complex (Figure 2.1E). The side chain of Glu24 and the main chain carbonyl oxygen of Lys38 from the H1 helix engage in direct H-bonds with Ser58 and Lys77 of ARM1, respectively. In addition, the side chain of Lys38 of the H1 helix forms a salt bridge with the side chain of Glu73 of ARM1. Furthermore, Val28, Leu31, and Leu35 of H1 helix form a hydrophobic core with Ala51, Leu52, and Leu55 of ARM1 that are known to be key residues for self-association of Vac8 (Figure 2.1F).

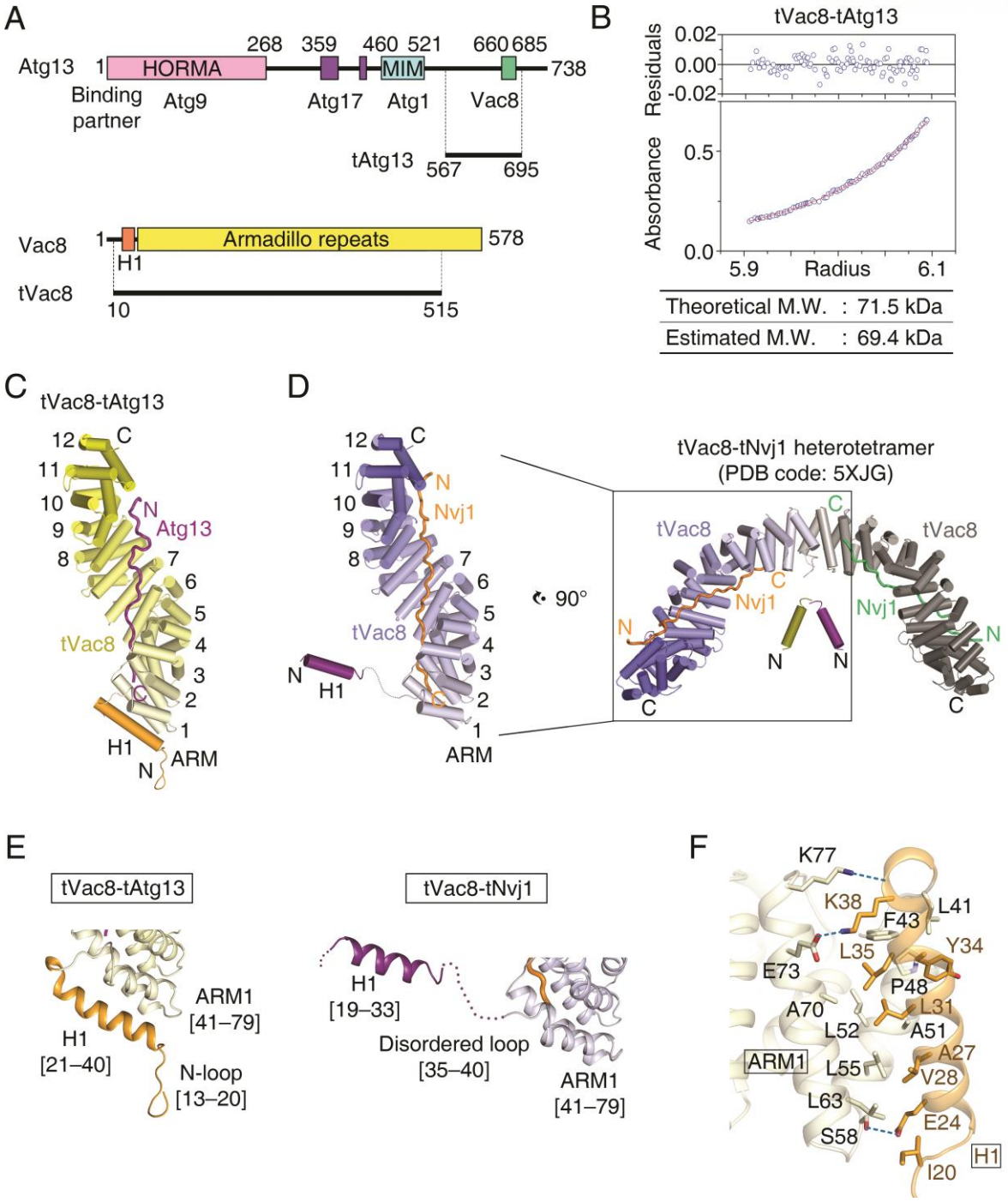

Figure 2.1. Structure of the tVac8-tAtg13 complex

(A) Domain structures of *Saccharomyces cerevisiae* Atg13 and Vac8. Previously identified conserved domains are marked by colored boxes, and the binding regions of associated proteins are indicated below. Residues 567–695 of Atg13 (designated as tAtg13) and residues 10–515 of Vac8 (designated as tVac8) were used for crystallization and biochemical experiments in this work. HORMA, Hop1, Rev7 and MAD2 domain; MIM, microtubule interacting and transport (MIT)-interacting motif.

(B) Analytical ultracentrifugation (AUC) analysis of the molecular weight (M.W.) of the tVac8-tAtg13 complex in solution. The bottom panel indicates a representative plot of absorbance profiles of 2.5 μM tVac8-tAtg13 following a centrifugation run at 13,604 × g for 16 h at 20°C, and the top panel presents the residuals between the experimental data and the fitted line.

(C) Overall structure of tAtg13 (purple) bound to the armadillo (ARM) repeat core of Vac8 (yellow). The structure was determined by molecular replacement using tVac8 as a search model (PDB code: 5XJG) and refined to 2.9 Å resolution (Table 2.1). The H1 regulatory helix of Vac8 is highlighted in orange (see the main text for an explanation of the role of the H1 helix).

(D) Comparison of the overall structures of tVac8-tAtg13 in (C) and tVac8-tNvj1, and the structure of the tVac8 (blue)-tNvj1 (orange) complex displayed in the same orientation as in (C). A previous study revealed that the tVac8-tNvj1 complex forms a heterotetramer as shown on the right [24], while the tVac8-tAtg13 complex in (C) forms a heterodimer. The arrangement of the H1 helix in the tVac8-tNvj1 complex is emphasized as a purple cylinder.

(E) Cartoon representation comparing the conformation of the H1 helices of tVac8-tAtg13 and tVac8-tNvj1 complexes. In the tVac8-tAtg13 structure (left), the H1 helix (orange) is composed of residues 21–40, and is directly associated with two helices of the first ARM (ARM1). By contrast, the H1 helix in the tVac8-tNvj1 complex (right, purple) consists of residues 19–33, which point away from ARM1 via a disordered loop comprising residues 35–40 (dotted line).

(F) Cartoon representation showing the interactions between the H1 helix (orange) and ARM1 (pale yellow) of tVac8 in the structure of the tVac8-tAtg13 complex. Residues involved in the interaction are shown in ball-and-stick representation. Oxygen and nitrogen atoms are colored red and blue, respectively, and blue dotted lines indicate hydrogen bonds.

Table 2.1. X-ray diffraction data collection and refinement statistics

Dataset	**tVac8-tAtg13**	**Vac8ΔH1-tAtg13**
X-ray source	Beamline 5C, PAL	Beamline 5C, PAL
Temperature (K)	100	100
Space group	$P2_12_12_1$	$P2_12_12_1$
Cell dimensions		
a, *b*, *c* (Å)	62.727, 92.391, 139.879	69.475, 85.268, 272.820
α, *β*, *γ* (°)	90, 90, 90	90, 90, 90
Data processing		
Wavelength (Å)	0.97949	0.97949
Resolution (Å)	50.0–2.90 (2.95–2.90)	50.0–3.20 (3.26–3.20)
R_{merge} (%)	12.0 (43.5)	10.3 (53.7)
I/σ (I)	11.27 (1.86)	17.88 (2.18)
High resolution shell CC1/2	0.496	0.270
Redundancy	3.3 (2.8)	3.8 (3.1)
Completeness (%)	95.2 (86.9)	98.7 (97.0)
Total number of reflections	59,423	105,995
Number of unique reflections	17,745	27,903
Refinement		
Resolution (Å)	32.84–2.9	35.11–3.16
Number of reflections	17,726	27,864
R_{work}/R_{free} (%)	20.6/24.6	21.6/25.5
Number of atoms		
Protein	4055	8069
Water	44	0
RMSD		
Bond lengths (Å)	0.004	0.008
Bond angles (°)	0.824	1.667
B-factors (Å^2)		
Protein	49.67	79.98
Water	36.09	0

*Values in parentheses are for the highest resolution shell.

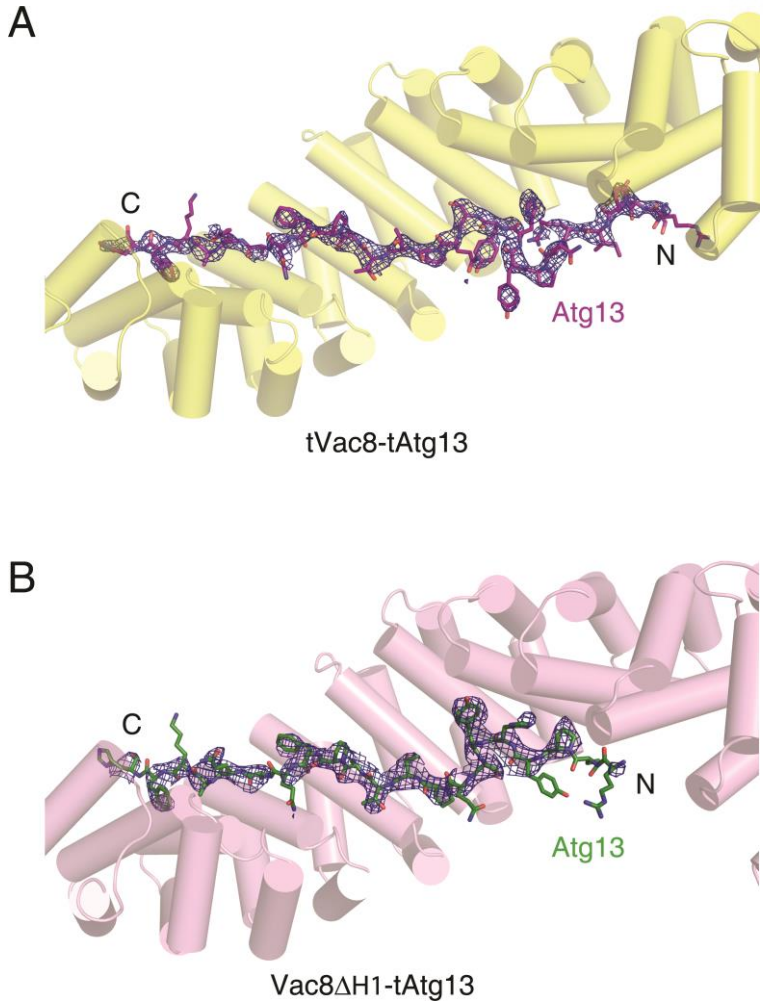

Figure 2.2. The difference electron density maps for tAtg13

The difference electron density maps (Fo-Fc) for tAtg13 bound to tVac8 **(A)** and Vac8ΔH1 **(B)** at 2.9 and 3.2 Å resolution, respectively. The maps were calculated in the absence of tAtg13 (contoured at 2.5σ).

2.3.2. Binding interface of tVac8 and tAtg13

Next, we further explored the interaction between tVac8 and tAtg13. Based on the structural conservation between tAtg13 and tNvj1, we divided the tVac8-binding region of tAtg13 into two parts (interface I and II) (Figure 2.3A). The N-terminal residues 660–671 (interface I) appear to interact loosely with ARMs 7–10 of tVac8, whereas the C-terminal residues 672–685 (interface II) are specifically recognized and tightly bound by ARMs 2–6 via both H-bonds and van der Waals interactions, resulting in a buried surface area of 956.28 $Å^2$, which is nearly twice that of interface I (Figure 2.3B). In interface II, the structure of tAtg13 strongly resembles that of tNvj1 despite their negligible sequence homology (6% sequence identity between Atg13 and Nvj1; Figure 2.3 A and B). In particular, Ile662 and Pro663 of tAtg13 in interface I form hydrophobic contacts with the side chains of Ala398, Ala401, Ile402, and Leu405 of tVac8, and His669 of tAtg13 forms intermolecular H-bonds with Arg317 and Glu395 of tVac8 (Figure 2.3C). In interface II, Phe678 of tAtg13 engages in extensive hydrophobic interactions with the side chains of Tyr226, Tyr227, and Leu192 of tVac8. Ala680, Phe684, and His685 at the C terminus of tAtg13 also form a tight hydrophobic network with Leu192, Ala107, and Val103 of tVac8 (Figure 2.3C). In addition to these extensive hydrophobic contacts, the side chains of Gln679 and Gln681 from tAtg13 form intermolecular H-bonds with the side chains of Lys160 and Asn152 from tVac8, respectively. The main chain atoms of Gln679, Phe684, and His685 of tAtg13 are recognized by the side chains of Asn193, Asn186, and Asn145 of tVac8 through intermolecular H-bonds (Figure 2.3C).

To characterize the interaction of Vac8 and Atg13 in solution, we generated a series of tAtg13 mutants conjugated with a hexa histidine (His_6)-tag at the N terminus, and coexpressed each mutant with glutathione-S-transferase (GST)-tagged tVac8. As shown in Figure 2.3D, pull-down experiments revealed that mutations in interface I did not affect the interaction, whereas single mutation of residues Phe678, Ala680, or Phe684 in interface II reduced association with tVac8. Consistently, triple mutation (F678R/A680E/F684E) of interface II completely abolished association with tVac8. We also measured binding constants (K_d) between Vac8 and tAtg13 mutants using isothermal titration calorimetry (ITC), and confirmed the results of pull-down experiments (Figure 2.4). To investigate the importance of interface II in vivo, we examined the CVT pathway of Ape1, which requires the Vac8-Atg13 interaction [23], by expressing one of the Atg13 mutants harboring a mutation in interface II in *atg13Δ* yeast cells (Figure 2.3E and Table 2.2). While green fluorescent protein (GFP)-conjugated Ape1 was transported to the vacuolar lumen via the CVT pathway in nearly 90% of wild-type yeast cells upon nitrogen starvation, only 10% of *atg13Δ* cells contained GFP-Ape1 in the vacuolar lumen. Cytoplasmic GFP puncta, indicative of defects in the CVT pathway, were observed in most *atg13Δ* cells, confirming that Atg13 is essential for the CVT pathway of Ape1 (Figure 2.3E). Furthermore,

although each of the single mutations in interface II resulted in a minor defect in the CVT pathway of Ape1, the defect was multiplied in cells expressing the Atg13 mutant with all three mutations (F678R/A680E/F684E), demonstrating that interface II is critical for the interaction between Atg13 and Vac8, and thereby their function in the CVT pathway (Figure 2.3E). Consistently, vacuolar processing of prApe1, which requires the CVT pathway, was impaired by these mutations in interface II (Figure 2.5 A–C). By contrast, the mutant bearing all 3 mutations (I662E/P667E/H669A; referred to as N-triple) in interface I supported the CVT pathway comparably to wild-type, consistent with the results of the in vitro pull-down assay of the N-triple mutant (Figures 2.3D and 2.5D).

In addition, a recent study elucidated two sets of motifs comprising positively charged residues ($_{640}$KFK$_{642}$ and $_{683}$KFHK$_{686}$) in the Atg13 intrinsic disordered region (IDR, residues 571–700), which are responsible for interactions with phospholipids that are essential for efficient autophagy [28]. Among these positively charged residues, Lys683 and His685 are observable in the tVac8-tAtg13 structure, and their side chains are exposed to bulk solvent at the surface of the molecule (Figure 2.3C), further supporting their interactions with phospholipids. The presence of this second motif ($_{683}$KFHK$_{686}$) in interface II is also consistent with our observation that interface II is critical for the CVT pathway (Figure 2.3E).

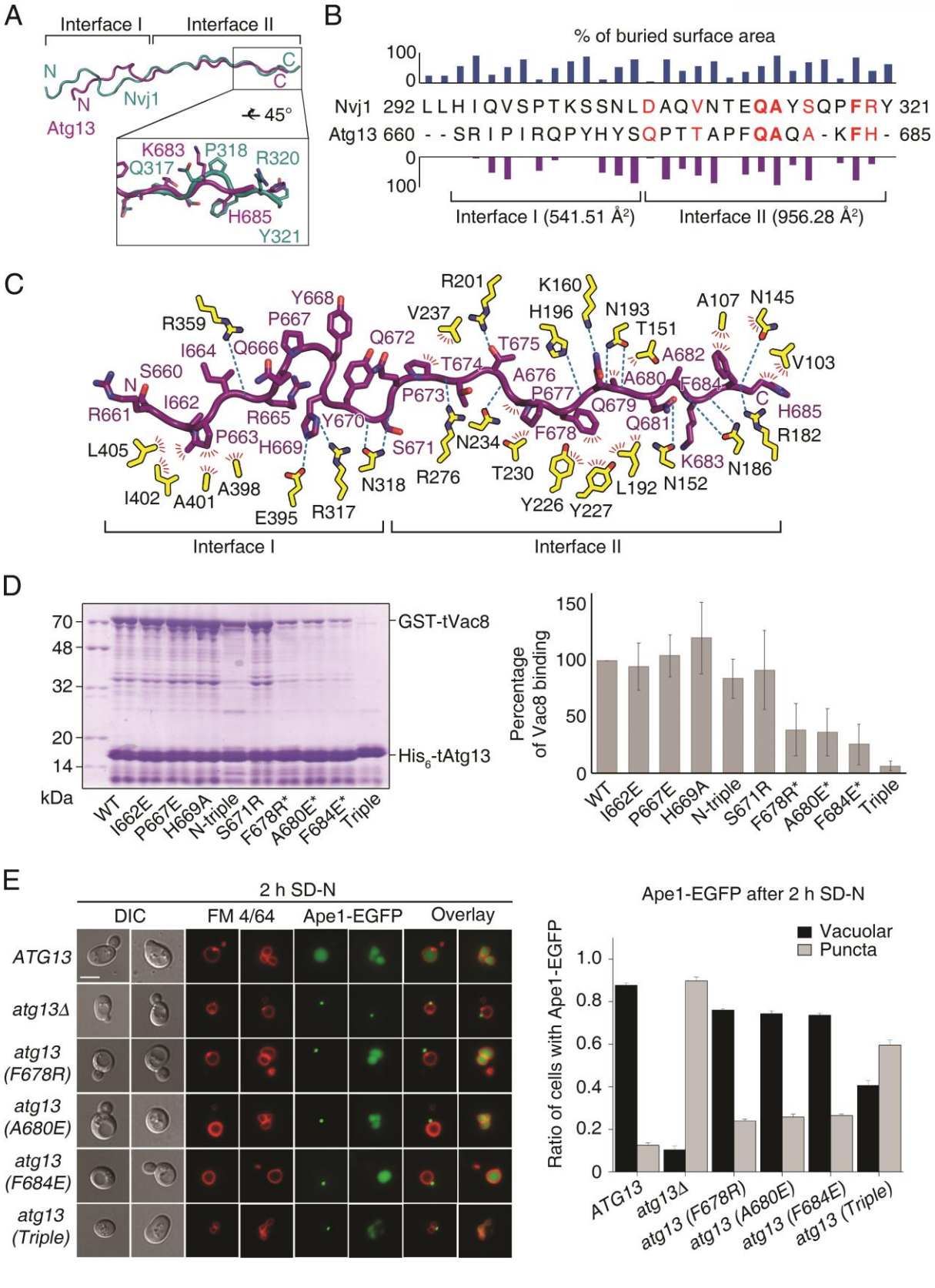

Figure 2.3. Binding interface between tAtg13 and tVac8

(A) Ribbon representation showing the superposition of tNvj1 (blue green) and tAtg13 (purple), which are bound to tVac8. Based on structural conservation, the structures of tAtg13 and tNvj1 can be divided into two subregions (designated as interface I and II). The bottom box shows a close-up view of the C terminus, highlighting the structural comparison.

(B) Sequence alignment of tNvj1 and tAtg13 based on their structures shown in (A). Bar graphs indicate the percentage of buried surface area of each residue of tNvj1 (top) and tAtg13 (bottom), which were generated by the interaction with tVac8. Each buried surface area of interface I and II of tAtg13 to tVac8 is shown in parentheses. Identical and similar sequences are highlighted in bold red and normal red, respectively.

(C) Ribbon representation showing protein-protein contacts identified in the crystal structure. Contacts between tVac8 (yellow) and tAtg13 (purple) are indicated by dotted lines (H-bonds) and red lines (hydrophobic interactions). Oxygen atoms are colored red, and nitrogen atoms are blue.

(D) His_6-tag pull-down analysis of the interaction of tVac8 and tAtg13. N-terminal glutathione-S-transferase (GST)-fused tVac8 was coexpressed with wild-type (WT) and mutants of hexa histidine (His_6)-tagged tAtg13, and immobilized on Ni^{2+}-NTA resin. Proteins were separated by 12% SDS-PAGE and visualized by Coomassie Brilliant Blue staining. The N-triple mutant was generated by mutation of three residues in interface I (I662E/P667E/H669A). For the triple mutant, residues indicated by asterisks were simultaneously mutated. Quantification data are shown on the right (n = 3).

(E) Interface II is important for the Atg13-Vac8-mediated CVT pathway of Ape1. Vacuoles of yeast strains expressing wild-type or mutant Atg13 were labeled with FM 4/64 in YPD media at 30°C for 2 h. After free dye was removed, cells were resuspended in a nitrogen starvation medium (SD-N) and further cultured at 30°C for 2 h. GFP fluorescence from Ape1 and FM 4/64 fluorescence in vacuoles were then analyzed by fluorescence microscopy. Representative images from each cell type are shown (left). The graph shows quantification of cytoplasmic or vacuolar Ape1-EGFP (right). More than 100 cells with Ape1-EGFP were analyzed per strain. Scale bar = 5 μm.

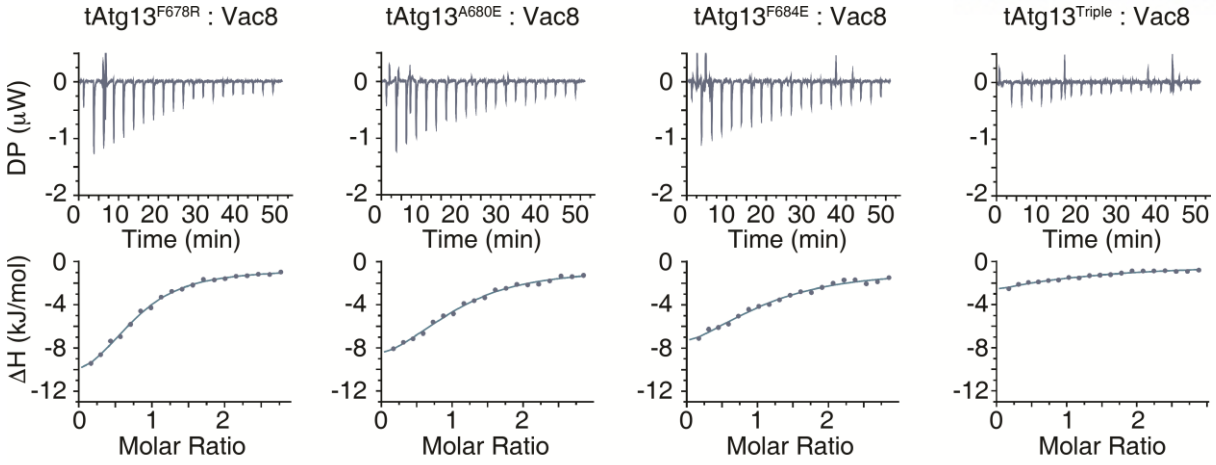

	K_d (μM)	N	-TΔS (kJ/mol)	ΔH (kJ/mol)
F678R	12.2	0.75 ± 0.025	-15.8	-12.2 ± 0.937
A680E	19.5	1.04 ± 0.047	-16.1	-10.8 ± 1.39
F684E	28.4	1.06 ± 0.089	-22.2	-10.0 ± 2.77
Triple	No binding			

Figure 2.4. Isothermal titration calorimetry (ITC) analysis of tAtg13 mutants in interface II binding to Vac8

Single (F678R, A680E, or F684E) and triple (F678R/A680E/F684E) mutants of tAtg13 were titrated with full-length Vac8 at 25°C. Upper and lower panels represent raw data and fitted data of binding isotherms for affinity determination. Thermodynamic parameters are measured and tabulated below.

Table 2.2. Yeast strains used in this study

Strain	Genotype	Source
BY4742	MAT*Δ his3Δ1 leu2Δ0 lys2Δ0 ura3Δ0*	[29]
BY4742 *vac8Δ*	BY4742 *vac8Δ::KanMX4*	[29]
BY4742 *pep4Δ*	BY4742 *pep4Δ::KanMX4*	[29]
BY-*vac8(A51R)*-Ape1-EGFP	BY4742 *vac8Δ* with *pRS316-VAC8(A51R) & pYJ408-APE1-EGFP*	This study
BY-*vac8(L55R)*-Ape1-EGFP	BY4742 *vac8Δ* with *pRS316-VAC8(L55R) & pYJ408-APE1-EGFP*	This study
BY-*vac8(N60R/N62R)*-Ape1-EGFP	BY4742 *vac8Δ* with *pRS316-VAC8(N60R/N62R) & pYJ408-APE1-EGFP*	This study
BY-*pep4Δ-vac8(N60R/N62R)*-Nvj1-EGFP	BY4742 *pep4Δ vac8Δ* with *pRS316-VAC8(N60R/N62R) & pYJ408-NVJ1-EGFP*	This study
BY-*pep4Δ-vac8(S16A)*-Nvj1-EGFP	BY4742 *pep4Δ vac8Δ* with *pRS316-VAC8(S16A) & pYJ408-NVJ1-EGFP*	This study
BY-*pep4Δ-vac8(S16E)*-Nvj1-EGFP	BY4742 *pep4Δ vac8Δ* with *pRS316-VAC8(S16E) & pYJ408-NVJ1-EGFP*	This study
BY-*vac8(S16A)*-Ape1-EGFP	BY4742 *vac8Δ* with *pRS316-VAC8(S16A) & pYJ408-APE1-EGFP*	This study
BY-*vac8(S16E)*-Ape1-EGFP	BY4742 *vac8Δ* with *pRS316-VAC8(S16E) & pYJ408-APE1-EGFP*	This study
BY-*vac8(S16A)*-EGFP	BY4742 *vac8Δ* with *pRS406-VAC8(S16A)-EGFP*	This study
BY-*vac8(S16E)*-EGFP	BY4742 *vac8Δ* with *pRS406-VAC8(S16E)-EGFP*	This study
BY-*pep4Δ*-Nvj1-EGFP	BY4742 *pep4Δ* with *pYJ406-NVJ1-EGFP*	[24]
BY-*vac8Δ-pep4Δ*-Nvj1-EGFP	BY4742 *vac8Δ pep4Δ* with *pYJ406-NVJ1-EGFP*	This study
BY-Ape1-EGFP	BY4742 with *pYJ408-APE1-EGFP*	[24]
BY-*atg13Δ*-Ape1-EGFP	BY4742 *atg13Δ* with *pYJ408-APE1-EGFP*	This study
BY-*atg13(F678R)*-Ape1-EGFP	BY4742 *atg13Δ* with *pRS316-ATG13(F678R) & pYJ408-APE1-EGFP*	This study
BY-*atg13(A680E)*-Ape1-EGFP	BY4742 *atg13Δ* with *pRS316-ATG13(A680E) & pYJ408-APE1-EGFP*	This study
BY-*atg13(F684E)*-Ape1-EGFP	BY4742 *atg13Δ* with *pRS316-ATG13(F684E) & pYJ408-APE1-EGFP*	This study
BY-*atg13(Triple)*-Ape1-EGFP	BY4742 *atg13Δ* with *pRS316-ATG13(Triple) & pYJ408-APE1-EGFP*	This study
BY-*vac8Δ*-Ape1-EGFP	BY4742 *vac8Δ* with *pYJ408-APE1-EGFP*	[24]
BY-*vac8Δ*-Vac8-EGFP	BY4742 *vac8Δ* with *pYJ406-VAC8-EGFP*	[24]
BY-*vac8Δ*-Vac8(A51R)-EGFP	BY4742 *vac8Δ* with *pRS406-VAC8(A51R)-EGFP*	This study
BY-*vac8Δ*-Vac8(L55R)-EGFP	BY4742 *vac8Δ* with *pRS406-VAC8(L55R)-EGFP*	This study
BY-EGFP-Atg8	BY4742 *atg13Δ* with *pRS316-ATG13 & pYJ408-EGFP-ATG8*	This study
BY-*atg13Δ*-EGFP-Atg8	BY4742 *atg13Δ* with *pYJ408-EGFP-ATG8*	This study
BY-*atg13(F678R)*-EGFP-Atg8	BY4742 *atg13Δ* with *pRS316-ATG13(F678R) & pYJ408-EGFP-ATG8*	This study
BY-*atg13(A680E)*-EGFP-Atg8	BY4742 *atg13Δ* with *pRS316-ATG13(A680E) & pYJ408-EGFP-ATG8*	This study
BY-*atg13(F684E)*-EGFP-Atg8	BY4742 *atg13Δ* with *pRS316-ATG13(F684E) & pYJ408-EGFP-ATG8*	This study
BY-*atg13(Triple)*-EGFP-Atg8	BY4742 *atg13Δ* with *pRS316-ATG13(Triple) & pYJ408-EGFP-ATG8*	This study
BY-*atg13(N-triple)*-Ape1-EGFP	BY4742 *atg13Δ* with *pRS316-ATG13(N-triple) & pYJ408-APE1-EGFP*	This study
BY-*vac8Δ*-Vac8(A51R)	BY4742 *vac8Δ* with *pRS406-VAC8(A51R)*	This study
BY-*vac8Δ*-Vac8(L55R)	BY4742 *vac8Δ* with *pRS406-VAC8(L55R)*	This study
BY-*pep4Δ*-Vac8ΔH1-Nvj1-EGFP	BY4742 *pep4Δ vac8Δ* with *pRS316-VAC8ΔH1 & pYJ408-NVJ1-EGFP*	This study
BY-*Vac8ΔH1*-Ape1-EGFP	BY4742 *vac8Δ* with *pRS316-VAC8ΔH1 & pYJ408-APE1-EGFP*	This study

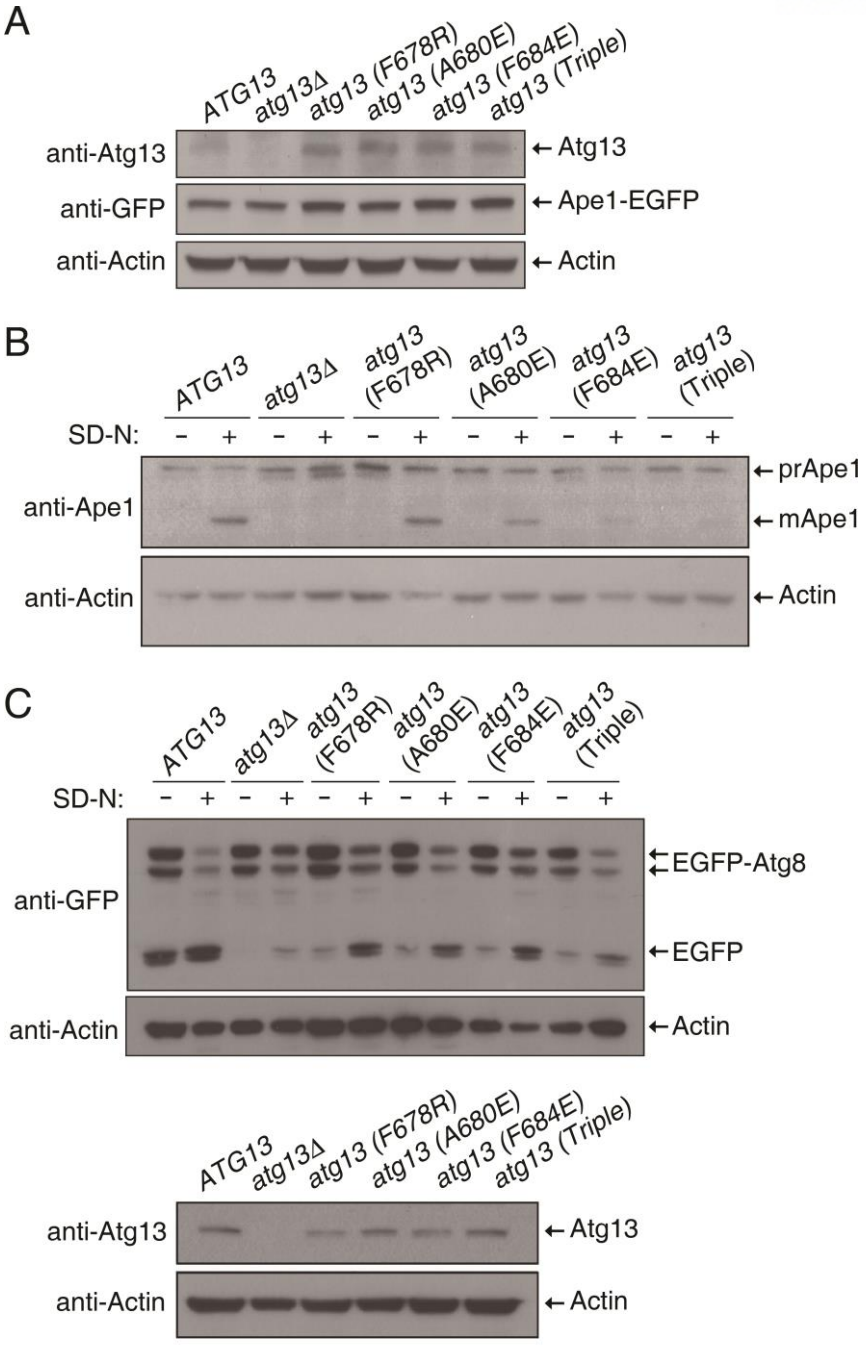

Figure 2.5. Interface II in Atg13 is important for vacuolar processing of prApe1

(A) Expression of wild-type Atg13 and Atg13 mutants is comparable between cells expressing wild-type Atg13 or mutant Atg13 used in Figure 2.3E.

(B) Interface II in Atg13 is important for vacuolar processing of prApe1. Expression of precursor Ape1 (prApe1) and mature Ape1 (mApe1) was analyzed by immunoblotting with anti-Ape1 antibody. Actin was used as a loading control.

(C) Mutations in interface II in Atg13 differentially affect bulk autophagy. Cells expressing EGFP-Atg8 were transferred to SD-N medium for 2 h to induce autophagy. Levels of EGFP-Atg8 and free EGFP were analyzed by immunoblotting with anti-GFP antibody (top). Actin was used as a loading control. Expression of wild-type Atg13 and Atg13 mutants was compared by immunoblotting with anti-Atg13 antibody (bottom).

(D) Mutations in interface I in Atg13 marginally affect the CVT pathway of Ape1. *ATG13*, *atg13Δ*, and *atg13 (N-triple)* cells were separately cultured in SD-N medium for 2 h, and GFP fluorescence from Ape1-EGFP was analyzed. The graph shows quantification of cytoplasmic and vacuolar Ape1-EGFP.

2.3.3. Structure of Vac8ΔH1 in complex with tAtg13

Based on combined structural and biochemical results, we proposed that a flexibly linked H1 helix is involved in regulating self-association of Vac8 through a folding-back mechanism in which the H1 helix binds ARM1 and masks the dimeric interface [24]. To advance our understanding of how the H1 helix regulates the self-association of Vac8, we generated an internal deletion construct lacking the H1 helix (residues 19–33; hereafter referred to as Vac8ΔH1; Figure 2.6A). We measured the binding affinity using ITC and found that Vac8ΔH1 bound to tAtg13 with a K_d of 1.46 μM, indicating that deletion of the H1 helix only had a slight influence on the binding affinity (Figure 2.6B). Notably, AUC analysis confirmed that Vac8ΔH1-tAtg13 indeed formed a heterotetramer in solution (Figure 2.6C). The Vac8ΔH1-tAtg13 complex was crystallized in space group $P2_12_12_1$ with two copies of the complex in the asymmetric unit, and the structure was solved by molecular replacement, and eventually refined at 3.2 Å resolution with R_{work}/R_{free} values of 0.22/0.25 (Figure 2.2B and Table 2.1 for data collection and refinement statistics).

A molecular model of Vac8ΔH1 bound to tAtg13 is presented in Figure 2.6D. As demonstrated by AUC experiment (Figure 2.6C), the Vac8ΔH1-tAtg13 complex forms a heterotetramer, with two complexes self-associated through ARM1 of Vac8, adopting a superhelical shape with overall dimensions of 51 × 57 × 213 Å, that turns twice along the superhelical axis. Unlike tVac8-tAtg13 or tVac8-tNvj1 complexes that include a truncated Vac8 terminating at C-terminal residue 515, full-length Vac8 was used in the Vac8ΔH1-tAtg13 complex, although the H1 helix was deleted. In the Vac8ΔH1-tAtg13 structure, Vac8 N-terminal residues 1–18 remain disordered, indicating that this region is intrinsically flexible, even though corresponding sequences are highly conserved in other species. More importantly, the structure revealed that the C-terminal end is absolutely required to form an intact final armadillo repeat (ARM12). In our previous tVac8-tNvj1 study, we showed that C-terminal truncation of Vac8 results in an incomplete α2 helix of Vac8 ARM12 [24]. According to the structure revealed in the present study, the α2 helix is extended up to residue 527, and the α3 helix starts at residue 560 and finishes at residue 578, which is the C-terminal end (Figure 2.6E). The 27 residues from 533 to 559 that connect α2 and α3 helices of ARM12 are disordered in the structure. Based on this observation, we conclude that full-length sequences are absolutely required to form all 12 ARMs in Vac8. Given that proper organization of all ARMs might be critical for structural integrity, the whole sequence of Vac8 is likely important for performing biological functions. Indeed, the binding affinity of tVac8 for tNvj1 is reduced by 7-fold compared with the full-length Vac8 despite the fact that ARM12 does not directly contribute to the interaction [24].

The structure of tAtg13 bound to Vac8ΔH1 at interface I revealed a different conformation compared with the tVac8-tAtg13 complex (Figures 2.6F and 2.7). In particular, the N-terminal 5 residues of tAtg13 are disordered in the structure of tAtg13 bound to Vac8ΔH1, and the interactions of Vac8ΔH1 and Atg13 in interface I differ from those in the tVac8-tAtg13 complex (Figures 2.3C, 2.6F, and 2.7 A and B). Consistent with the tVac8-tAtg13 complex, contacts contributed by interface I do not appear to be strong, and only 525 $Å^2$ of solvent-accessible surface area is buried. Detailed analysis in Figure 2.7 C and D indicated that the conformation of tAtg13 bound to Vac8ΔH1 is more likely in solution because the N-terminal structure of tAtg13 bound to tVac8 appears to be affected by neighboring molecules due to crystal packing. The structure of tAtg13 at interface II in the two crystal structures superimposed precisely, suggesting that these interactions are orderly and functionally important (Figure 2.7B).

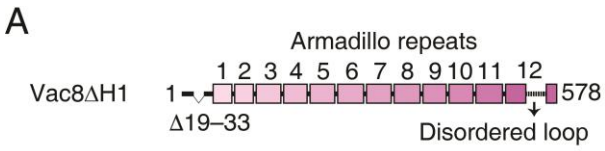

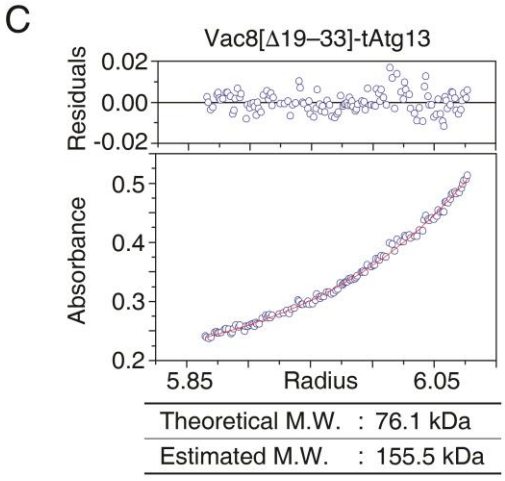

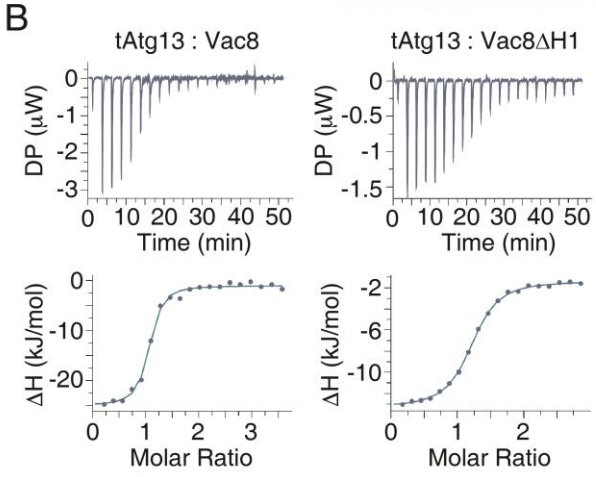

	K_d (μM)	N	-TΔS (kJ/mol)	ΔH (kJ/mol)
Vac8	0.60	0.99 ± 0.013	-11.5	-24.1 ± 0.53
Vac8ΔH1	1.46	1.01 ± 0.006	-19.3	-14 ± 0.144

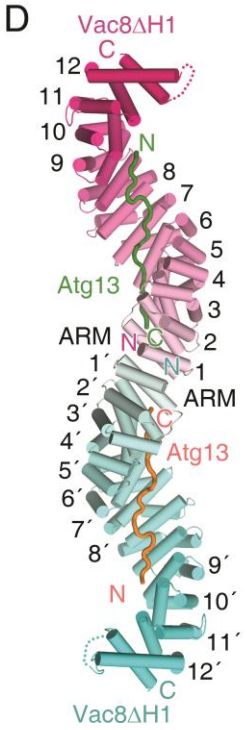

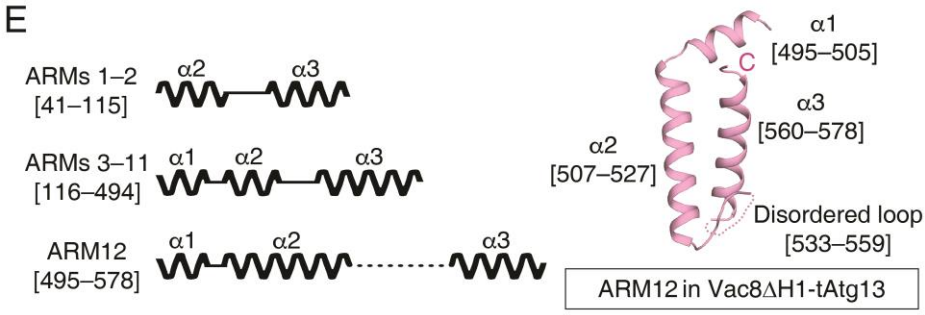

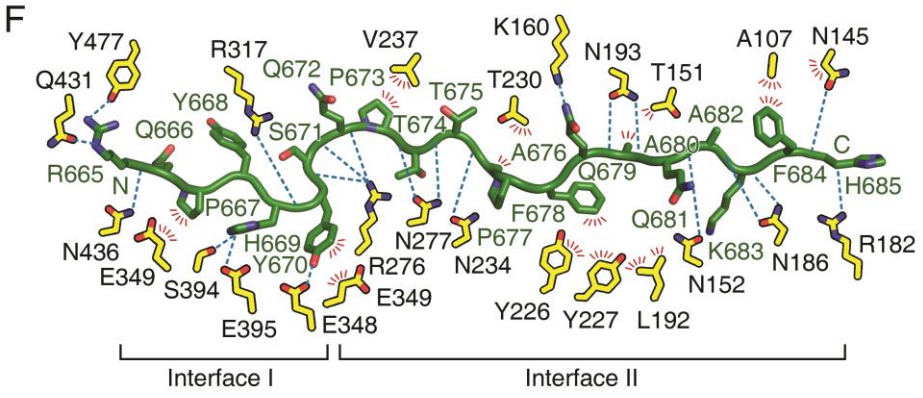

Figure 2.6. Structure of Vac8ΔH1 in complex with tAtg13

(A) Schematic diagram showing the organization of the ARMs of Vac8 revealed in this study. To investigate the role of the H1 helix in the self-association of Vac8, a truncated construct lacking the H1 helix (Vac8ΔH1) was generated.

(B) Isothermal titration calorimetry (ITC) analysis of tAtg13 binding to Vac8. The tAtg13 protein was titrated into full-length Vac8 (left) or Vac8ΔH1 (right) at 25°C. The upper panel shows raw data, and the lower panel shows data fitted to binding isotherms to calculate affinities. The table below thermograms summarizes the measured thermodynamic parameters.

(C) AUC analysis of the molecular weight (M.W.) of the Vac8ΔH1-tAtg13 complex performed as described in Figure 2.1B.

(D) Overall structure of the Vac8ΔH1-tAtg13 complex. Two copies of Vac8ΔH1 (cyan and pink) bound to tAtg13 (orange and green) are associated in the crystal asymmetric unit. Unlike tVac8-tAtg13 (Figure 2.1C), Vac8ΔH1-tAtg13 forms a heterotetramer organized by self-association of ARM1 of Vac8ΔH1. In the structure, Vac8ΔH1 has 12 intact ARMs, and tAtg13 binds to the inner groove generated by the ARMs of Vac8ΔH1 in an antiparallel manner.

(E) Schematic diagram (left) illustrating the three types of ARMs present in the structure of Vac8ΔH1. ARMs 1–2 consist of only two helices (α2 and α3; labeled to show the organization of helices in ARMs) that play important roles in Vac8 self-association. ARMs 3–11 have a typical ARM repeat comprising two short helices (α1 and α2) and a long helix (α3). ARM12 consists of a short helix (α1) and a relatively long helix (α2) followed by a long disordered region (residues 533–559) and helix α3. The right panel shows the structure of ARM12 in the Vac8ΔH1-tAtg13 complex.

(F) Close-up view of Atg13 (green) bound to Vac8ΔH1 (yellow) oriented as in Figure 2.3C.

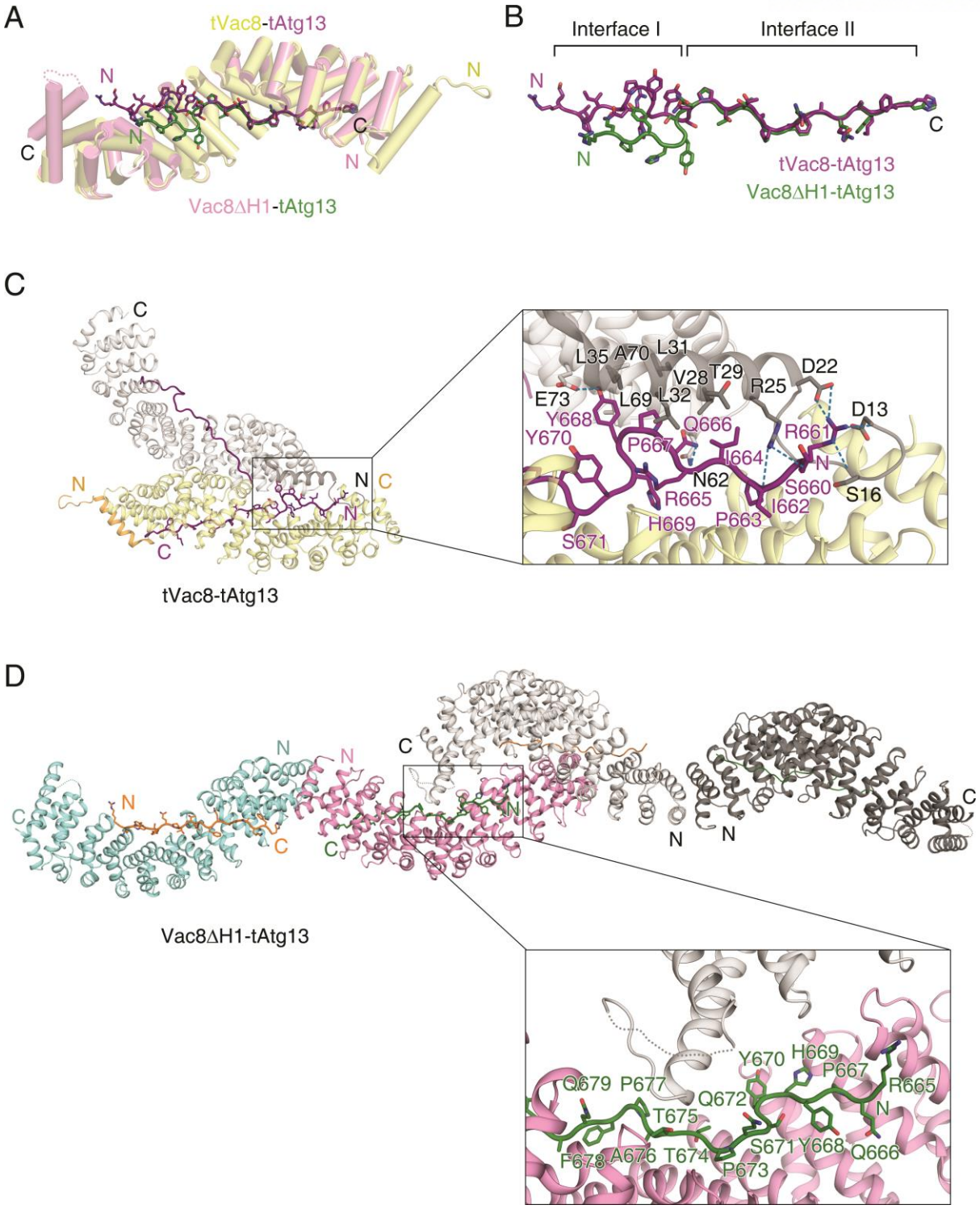

Figure 2.7. Different conformations of Atg13 at interface I

(A) Ribbon diagram showing the structural alignment of tVac8 (yellow)-tAtg13 (purple) and Vac8ΔH1 (pink)-tAtg13 (green).

(B) Close-up view of the structures of tAtg13 in (A). Although the structures of tAtg13 bound to Vac8 at interface I have different conformations, the two structures superimpose well at interface II.

(C) Cartoon representation (left) showing the overall structure of the tVac8-tAtg13 complex and its symmetry-related molecules (gray). The close-up view on the right clearly shows that the structure of tAtg13 at interface I is affected by neighboring molecules due to crystal packing. Residues involved in the interaction are highlighted in ball and stick representation and H-bonds are indicated with blue dotted lines.

(D) Unlike tVac8-tAtg13 shown in (C), tAtg13 in the Vac8ΔH1 (cyan and pink)-tAtg13 (orange and green) complex has no direct interactions with symmetry-related molecules (gray). Oxygen atoms are colored red and nitrogen atoms are blue.

2.3.4. Dimerization of Vac8 in the Vac8-Atg13 complex

Self-association of Vac8 is required for formation of the nucleus-vacuole junction (NVJ) [24]. Herein, we also showed that Vac8 bound to Atg13 oligomerized through ARM1 of Vac8 (Figure 2.6D). Figure 2.8A highlights the 2-fold interface generated by pairwise arrangement of helices α2 and α3 from ARM1 of each subunit. Ser66 lies at the center of the 2-fold symmetry axis, and Glu73 engages in an H-bond with Asn62 of the other subunit. In addition, Ala51 and Leu52 form van der Waals contacts with Leu55, Leu63, and Ala70 of the other subunit (Figure 2.8A). To confirm that ARM1 is important for Vac8 dimerization in solution, we performed site-directed mutagenesis to generate the A51R and L55R mutants with altered contact sites, and conducted size-exclusion chromatography (SEC) with $Vac8^{40–515}$ lacking residues 1–39, also used in our previous study [24]. The $Vac8^{40–515}$-tAtg13 complex migrated with a retention time consistent with the heterotetramer, while mutants eluted from the column as apparent heterodimers (Figure 2.8B).

To further assess if Vac8 self-association is critical for the CVT pathway, we replaced wild-type Vac8 with a mutant harboring A51R or L55R mutation, and examined whether the mutants support the CVT pathway of Ape1 (Figure 2.8C). The results revealed that the CVT pathway of Ape1 was impaired in yeast cells expressing the Vac8 mutants defective for self-association, clearly indicating that Vac8 dimerization in the Vac8-Atg13 complex is critical for the CVT pathway. Consistently, conversion of the precursor form of Ape1 (prApe1) to the mature form of Ape1 in the vacuole was markedly impaired by A51R or L55R mutation (Figure 2.9). Triton X-114 phase partitioning confirmed that the Vac8 mutants did not affect myristoylation or palmitoylation, and thus the vacuolar targeting of Vac8 (Figure 2.10).

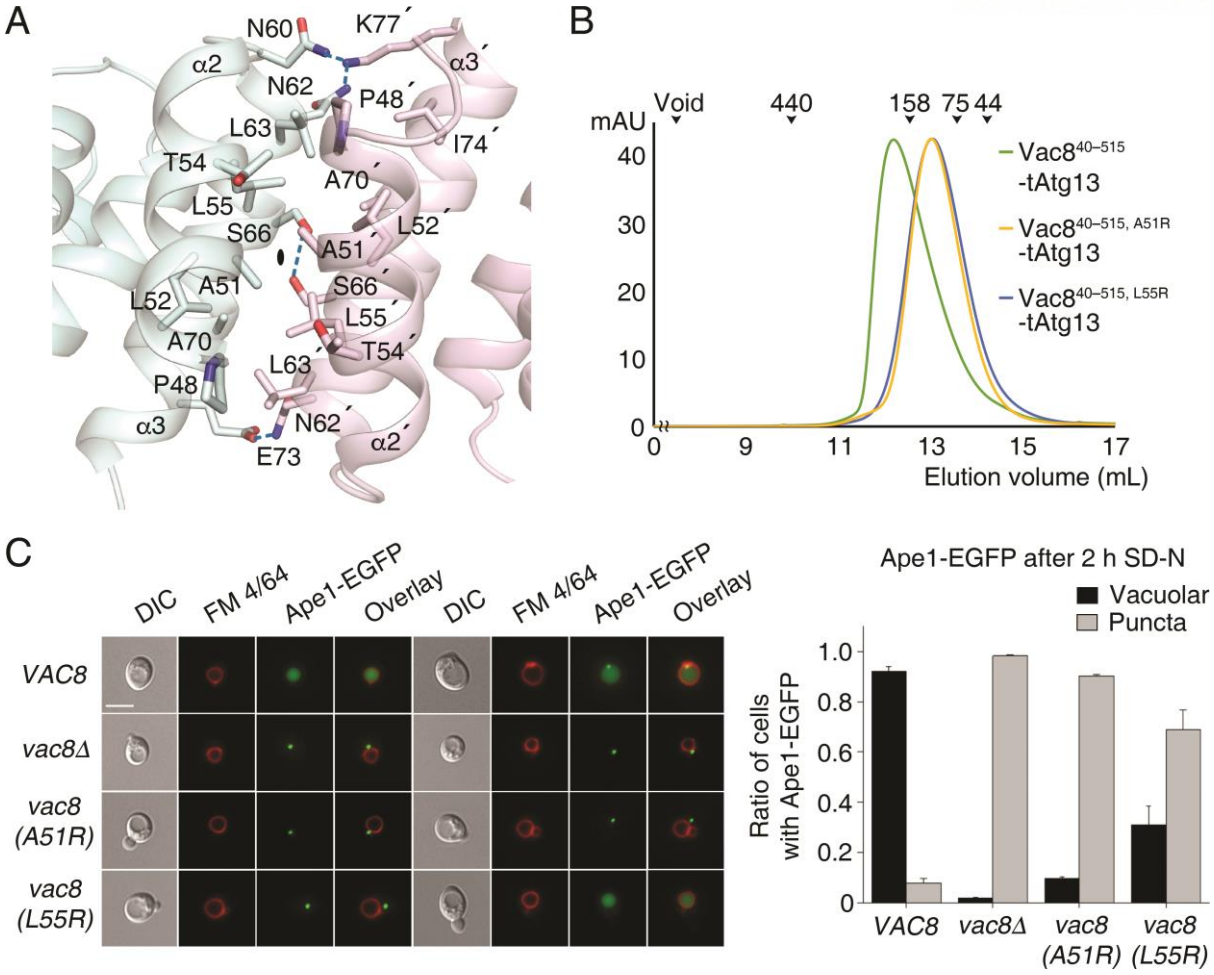

Figure 2.8. ARM1 of Vac8 mediates self-association of Vac8 in the Vac8-Atg13 complex

(A) Close-up view of the 2-fold dimeric interface of Vac8ΔH1. Residues involved in the self-association of ARM1 are displayed in ball-and-stick representation. Intermolecular hydrogen bonds are indicated with blue dotted lines, and oxygen and nitrogen atoms are colored red and blue, respectively.

(B) Size-exclusion chromatography (SEC) of wild-type and mutant (A51R or L55R) of $Vac8^{40–515}$ in complex with tAtg13. The indicated protein mixtures were applied to a Superdex 200 10/300 GL column equilibrated with buffer containing 25 mM Tris-HCl, pH 7.5, 150 mM NaCl, 5 mM DTT. The molecular weights of standard proteins are presented above the curves to compare the relative molecular mass (blue dextran 2000, void; ferritin, 440 kDa; aldolase, 158 kDa; conalbumin, 75 kDa; ovalbumin, 44 kDa).

(C) Vac8 self-association in the Vac8-Atg13 complex is critical for the CVT pathway of Ape1. Vacuoles of yeast strains expressing wild-type or mutant Vac8 were labeled with FM 4/64 in YPD media at 30°C for 2 h. Experiment was performed as described in Figure 2.3E. Representative images (left) are shown for each strain. The graph shows quantification of cytoplasmic or vacuolar Ape1-EGFP (right). Scale bar = 5 μm.

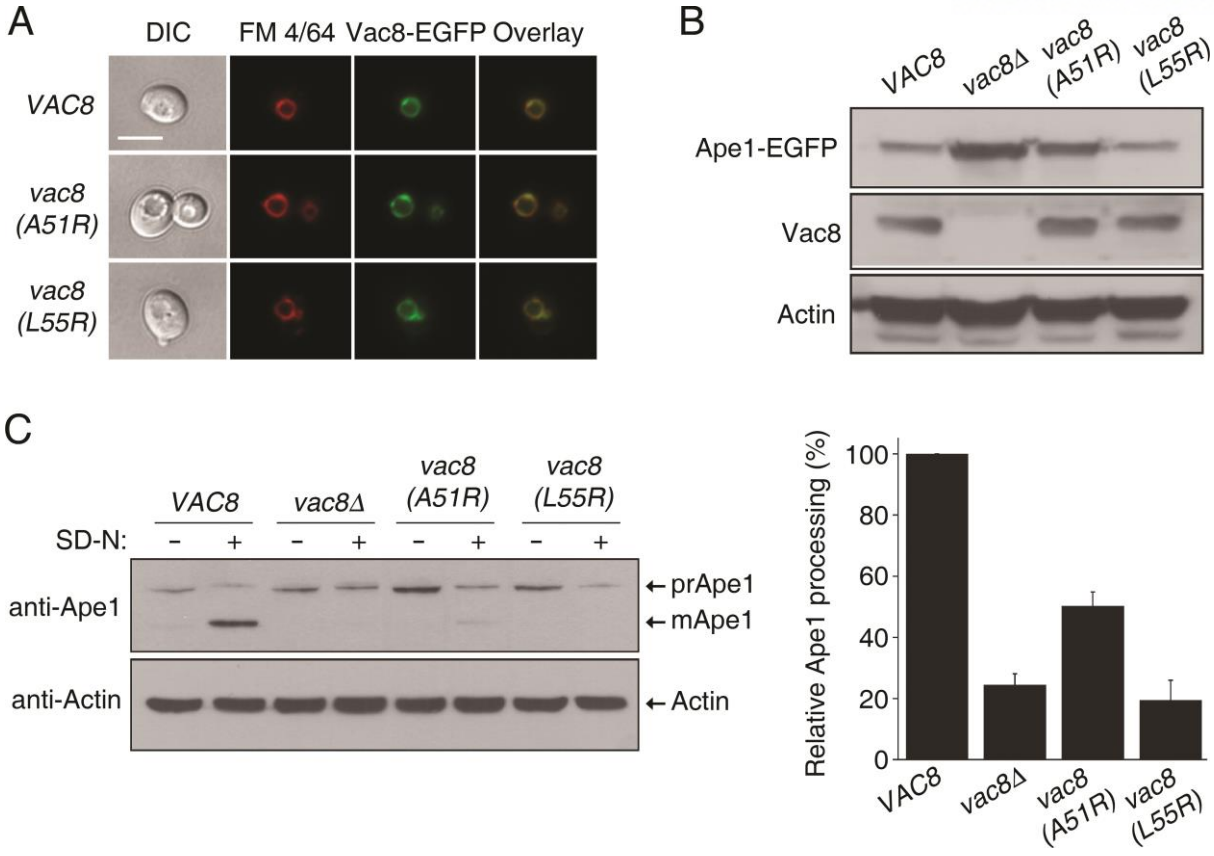

Figure 2.9. Vac8 self-association is important for vacuolar processing of prApe1

(A) Vac8-EGFP, Vac8-EGFP (A51R), and Vac8-EGFP (L55R) localization determined by fluorescence microscopy. Vacuoles of cells were labeled with FM 4/64 and Vac8 was tagged with EGFP. Overlay images show combined fluorescence from Vac8 and vacuole. Vac8-EGFP (A51R) and Vac8-EGFP (L55R) are clearly localized in vacuoles, along with Vac8-EGFP. Scale bar = 5 μm.

(B) Expression levels of Vac8 are comparable between wild-type and mutant Vac8 cells used in (A) and Figure 2.8C.

(C) *VAC8*, *vac8Δ*, *vac8(A51R)*, and *vac8(L55R)* cells were cultured in SD-N medium for 2 h, and maturation of endogenous Ape1 in vacuoles was analyzed by immunoblotting with anti-Ape1 antibody. Experiments were performed 3 times, and a representative blot is shown (left). The graph shows the relative ratios of mApe1 (100% for cells expressing wild-type Vac8; right).

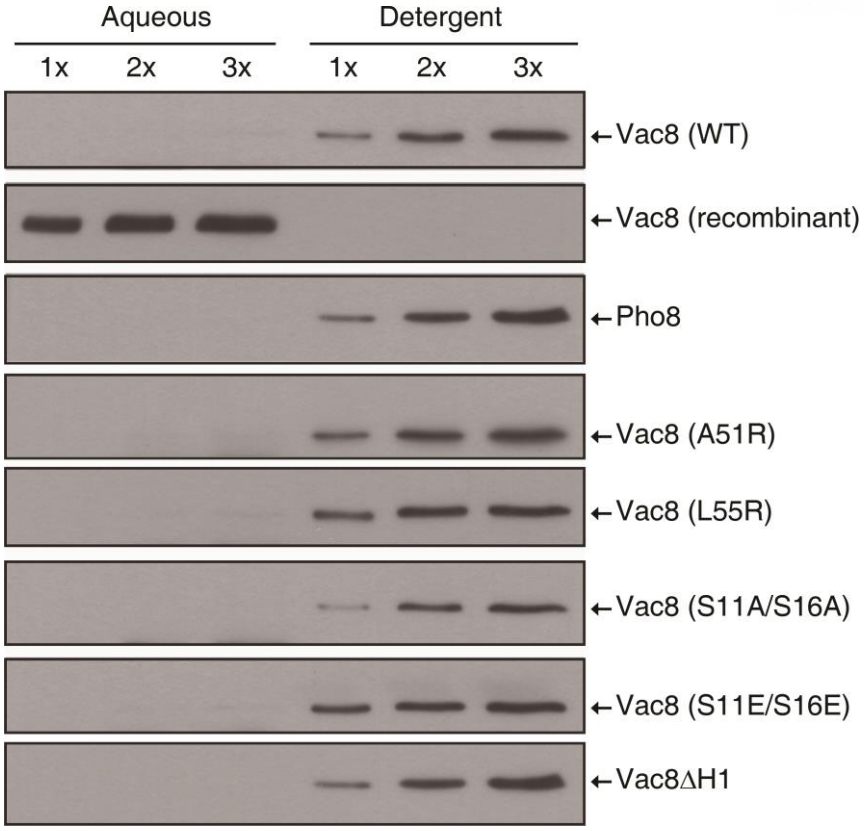

Figure 2.10. Mutations of Vac8 do not impair its lipidation and vacuolar targeting

Triton X-114 phase partitioning analysis shows that mutations of Vac8 have no effect on its myristoylation or palmitoylation, and therefore vacuolar targeting.

2.3.5. Structural comparison of Vac8-Atg13 and Vac8-Nvj1 complexes

As highlighted in Figure 2.11A, self-associated Vac8 exhibits striking differences in quaternary organization when binding to Atg13 or Nvj1. When bound to Nvj1, two Vac8 molecules are arranged via 2-fold symmetry around the axes of the ARM1 helices, resulting in an arch-shaped structure (Figure 2.11 A and B, left). By contrast, when bound to Atg13, two Vac8 molecules adopt a superhelical structure in which the first ARMs are organized via 2-fold rotation symmetry around the axis perpendicular to the plane (Figure 2.11 A and B, right).

To confirm the distinct organization of Vac8 dimers in solution, we performed synchrotron small-angle X-ray scattering (SAXS) experiments using Vac8$^{40–578}$-tNvj1 and Vac8$^{40–578}$-tAtg13 complexes (Figure 2.11 C and D, and Table 2.3), in which Vac8 construct comprising residues 40–578 was used for minimalizing flexible regions and obtaining information from the complete ARM domain. The radius of gyration (R_g) calculated from one-dimensional experimental scattering plot of the Vac8$^{40–578}$-tNvj1 complex (57.82 Å) was different from that of Vac8$^{40–578}$-tAtg13 (60.40 Å; Figure 2.11 C and D, left). However, experimental SAXS scattering data of Vac8$^{40–578}$-tNvj1 or Vac8$^{40–578}$-tAtg13 complexes fitted well to theoretical scattering curves calculated from the structure of Vac8ΔH1-tNvj1, in which tVac8 coordinates of the tVac8-tNvj1 were replaced by that of Vac8ΔH1, or Vac8ΔH1-tAtg13 crystal structures, respectively, in good agreement with theoretical R_g values (58.35 Å for Vac8ΔH1-tNvj1 and 62.01 Å for Vac8ΔH1-tAtg13; Figure 2.11 C and D, left). The maximum dimension (D_{max}) value for Vac8$^{40–578}$-tNvj1 (217.6 Å) calculated from the P(r) distance distribution function was different from that of Vac8$^{40–578}$-tAtg13 (229.3 Å; Figure 2.11 C and D, middle). Most strikingly, the envelopes derived from Vac8$^{40–578}$-tNvj1 and Vac8$^{40–578}$-tAtg13 revealed distinctive quaternary structures in solution (Figure 2.11 C and D, right). In particular, the SAXS envelope obtained from Vac8$^{40–578}$-tNvj1 displayed an arched shape that superimposed well with the structure of the Vac8ΔH1-tNvj1 heterotetramer (Figure 2.11C, right), whereas the envelope obtained from Vac8$^{40–578}$-tAtg13 clearly adopted an extended rod shape that aligned well with the superhelical structure of the Vac8ΔH1-tAtg13 complex (Figure 2.11D, right). In addition, the molecular weights of the Vac8$^{40–578}$-tNvj1 and Vac8$^{40–578}$-tAtg13 complexes measured by SAXS using Q_p [30] were 132.16 kDa and 139.13 kDa, respectively, and these were also consistent with the heterotetramer complexes (2 × Vac8$^{40–578}$-tNvj1 and 2 × Vac8$^{40–578}$-tAtg13; Table 2.3). Taken together, the SAXS data strongly support the crystal structures, revealing that Vac8 adopts different quaternary structures in solution depending on its binding partners.

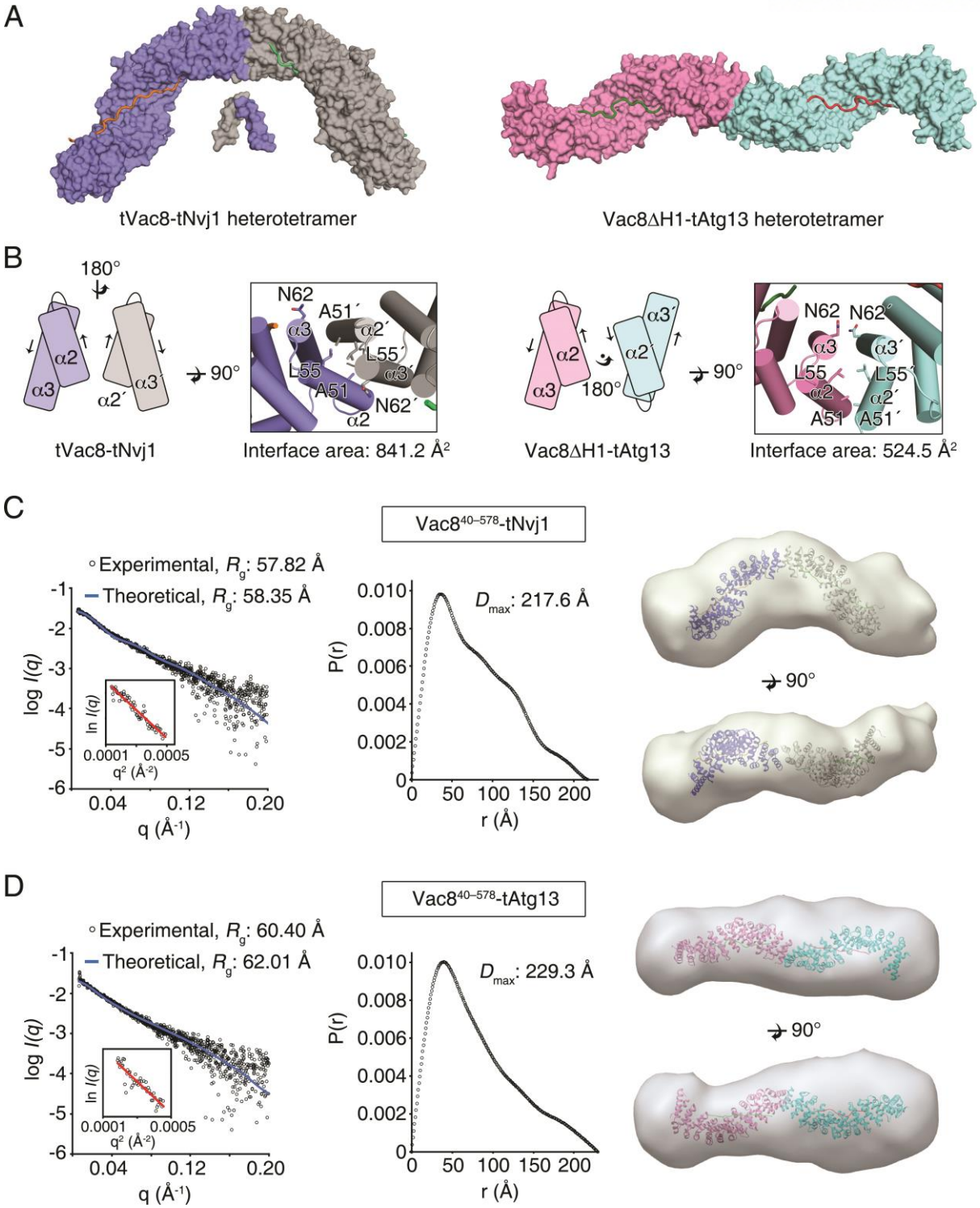

Figure 2.11. Binding of Atg13 or Nvj1 affects the quaternary structure of Vac8

(A) Surface representation of the tVac8-tNvj1 (left) and Vac8ΔH1-Atg13 (right) heterotetrameric structures. In the crystal structures, two complexes of tVac8-tNvj1 adopt an arched shape. By contrast, two copies of Vac8ΔH1-tAtg13 are arranged via 2-fold symmetry along the axis perpendicular to the plane, resulting in a superhelical shape.

(B) The organization of ARM1 at the 2-fold interface in tVac8-tNvj1 (left) and Vac8ΔH1-tAtg13 (right) heterotetramers. Arrows indicate the direction of the helical axis.

(C and D) Small-angle X-ray scattering (SAXS) experimental data showing different quaternary structures of Vac8-Nvj1 **(C)** and Vac8-Atg13 **(D)**. Experimental scattering data (hollow circles) of $Vac8^{40–578}$-tNvj1 (C, left) or $Vac8^{40–578}$-tAtg13 (D, left) agree well with theoretical scattering curves (blue line) calculated from structures of Vac8ΔH1-tNvj1 or Vac8ΔH1-tAtg13. A Guinier plot of $Vac8^{40–578}$-tNvj1 (C) and $Vac8^{40–578}$-tAtg13 (D) is shown on the left. The middle panels show the distance distributions and maximum dimensions (D max) of $Vac8^{40–578}$-tNvj1 (C) and $Vac8^{40–578}$-tAtg13 (D). Envelopes calculated from $Vac8^{40–578}$-tNvj1 (C, right) and $Vac8^{40–578}$-tAtg13 (D, right) SAXS data align well with structures of Vac8ΔH1-tNvj1 and Vac8ΔH1-tAtg13, respectively. The alignment was carried out using SUPCOMB [31], and model and envelope representations were generated by Chimera [32].

Table 2.3. Small-angle X-ray scattering statistics

	$Vac8^{40–578}$-tNvj1	**$Vac8^{40–578}$-tAtg13**
Data collection parameters		
Beamline	Beamline 6D, PAL	Beamline 6D, PAL
Temperature (K)	293	293
Beam geometry (mm)	1.5 × 1.5	1.5 × 1.5
Wavelength (Å)	1.072	1.072
q range ($Å^{-1}$)	0.00676–0.19925	0.00676–0.19925
Detector	MX225-HS	MX225-HS
Detector distance (mm)	2707.95	2707.95
Exposure time (s)	30	30
Structural parameters		
R_g (Å) [from Guinier]	57.82	60.40
R_g (Å) [from P(r)]	63.63	65.17
D_{max} (Å)	217.6	229.3
Molecular weight determination		
Molecular weight (M.W.) (kDa) [from Q_p]	132.16	139.15
Calculated M.W. from sequence	69.32	73.27
Software employed		
Primary data reduction	SAXSLee	
Data processing	PRIMUS	
Ab initio analysis	DAMMIF	
Validation and averaging	DAMAVER	

2.3.6. Quaternary structures of Vac8 differentially affect CVT and PMN pathways

To confirm whether the characteristic organization of Vac8 is altered by binding of Atg13 or Nvj1 in solution, $Vac8^{40–515}$ mutations were generated. Ala51, involved in the association in both the arched and superhelical Vac8 structures, was mutated first, followed by Asn60 and Asn62 that contribute to the superhelical organization of Vac8 but project outward in the arched structure, and thus are not involved in the interaction (Figure 2.11B). Chemical cross-linking experiments followed by immunoblotting analysis with Nvj1 or Atg13 antibodies revealed that the A51R mutant failed to undergo self-association in the presence of tNvj1 or tAtg13, consistent with the SEC experiments (Figures 2.8B and 2.12 A and B) [24]. Interestingly, the N62R single mutation or N60R/N62R double mutation did not affect self-association of $Vac8^{40–515}$ bound to tNvj1, whereas the self-association of $Vac8^{40–515}$ was significantly reduced in the $Vac8^{40–515, N60R/N62R}$-tAtg13 complex (Figures 2.12 A and B, and 2.13). Consistent with these results, the N62R single mutant of $Vac8^{40–515}$ complexed with tAtg13 eluted later from the SEC column, and the N60R/N62R double mutation resulted in a more severe defect than the N62R single mutation while these mutants bound to tNvj1 eluted at heterotetrameric size (Figure 2.12 C and D). Taken together, the results showed that mutation of residues Asn60 and Asn62 only affected the superhelical conformation generated by formation of the Vac8-Atg13 complexes, corroborating the idea that the quaternary organization of Vac8-Atg13 is clearly different from that of the Vac8-Nvj1 complex.

To investigate the biological relevance of Atg13-specific Vac8 organization, we examined whether the Vac8(N60R/N62R) mutant supported the CVT or PMN pathways (Figure 2.12 E and F). As shown in Figure 2.12F, the Vac8(N60R/N62R) mutant failed to support the CVT pathway, but interestingly, the PMN pathway was not affected (Figure 2.12E). These results strongly suggest that Vac8 adopts different quaternary structures depending on its binding partners, and in doing so mediates different cellular processes.

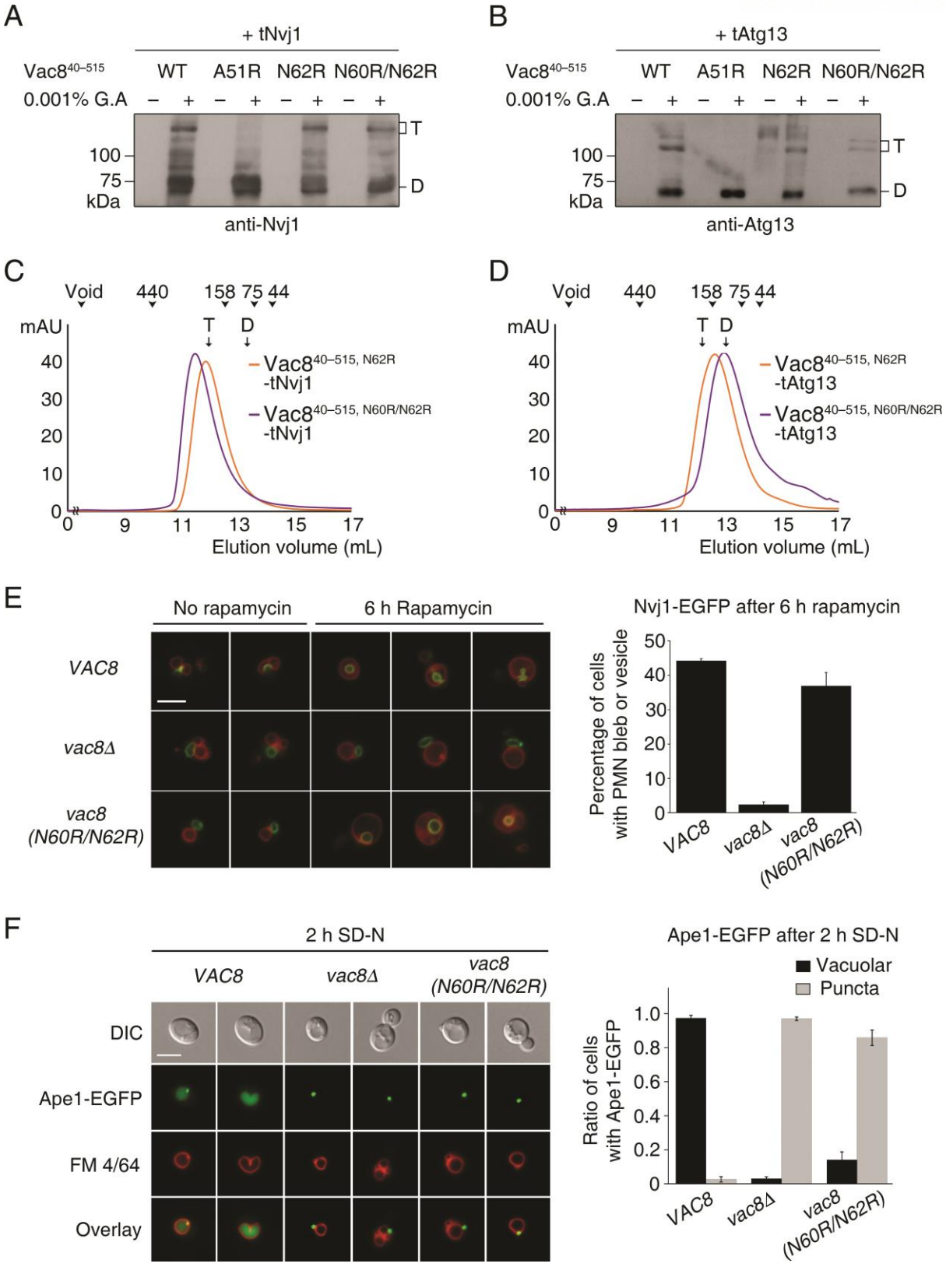

Figure 2.12. Different quaternary structures affect CVT and PMN pathways

(A and B) Glutaraldehyde-mediated cross-linking of WT and mutant $Vac8^{40–515}$ complexed with tNvj1 **(A)** or tAtg13 **(B)**. Proteins (0.5 mg/mL) were mixed with 0.001% glutaraldehyde (G.A) and incubated at 20°C for 30 min. Reaction products were separated by 8% SDS-PAGE, transferred to a PVDF membrane, and immunoblotted with anti-Nvj1 or anti-Atg13 antibody. T and D indicate $Vac8^{40–515}$-tNvj1 (A) or $Vac8^{40–515}$-tAtg13 (B) heterotetramer and heterodimer complexes, respectively.

(C and D) SEC analysis of the N62R single mutant and N60R/N62R double mutant of $Vac8^{40–515}$ complexed with tNvj1 **(C)** or tAtg13 **(D)**. The experiment was performed as described in Figure 2.8B. T and D indicate the elution volumes of $Vac8^{40–515}$-tNvj1 (C) or $Vac8^{40–515}$-tAtg13 (D) heterotetramer and heterodimer complexes obtained from our previous study [24] and Figure 2.8B, respectively.

(E) Piecemeal microautophagy of the nucleus (PMN) is largely intact in cells expressing the N60R/N62R Vac8 double-mutant. Cells expressing Nvj1-EGFP were treated with 0.2 μM rapamycin for 6 h to induce PMN. GFP fluorescence from Nvj1 and red fluorescence (FM 4/64) from vacuoles were analyzed by fluorescence microscopy. Representative images (left) from each cell type with or without rapamycin (scale bar = 5 μm) and quantification (right) of cells with PMN bleb or PMN vesicles are shown. Yeast strains lacking the major vacuolar protease Pep4 were used to block the degradation of PMN blebs or vesicles in the vacuolar lumen.

(F) The Vac8(N60R/N62R) mutant does not support the CVT pathway. Vacuoles of wild-type yeast cells, *vac8Δ* cells, and *vac8(N60R,N62R*) cells were labeled with FM 4/64 in YPD media at 30°C for 2 h. Experiment was performed as described in Figure 2.3E. Representative images (left) are shown for each strain. The graph shows quantification of cytoplasmic or vacuolar Ape1-EGFP (right). Scale bar = 5 μm.

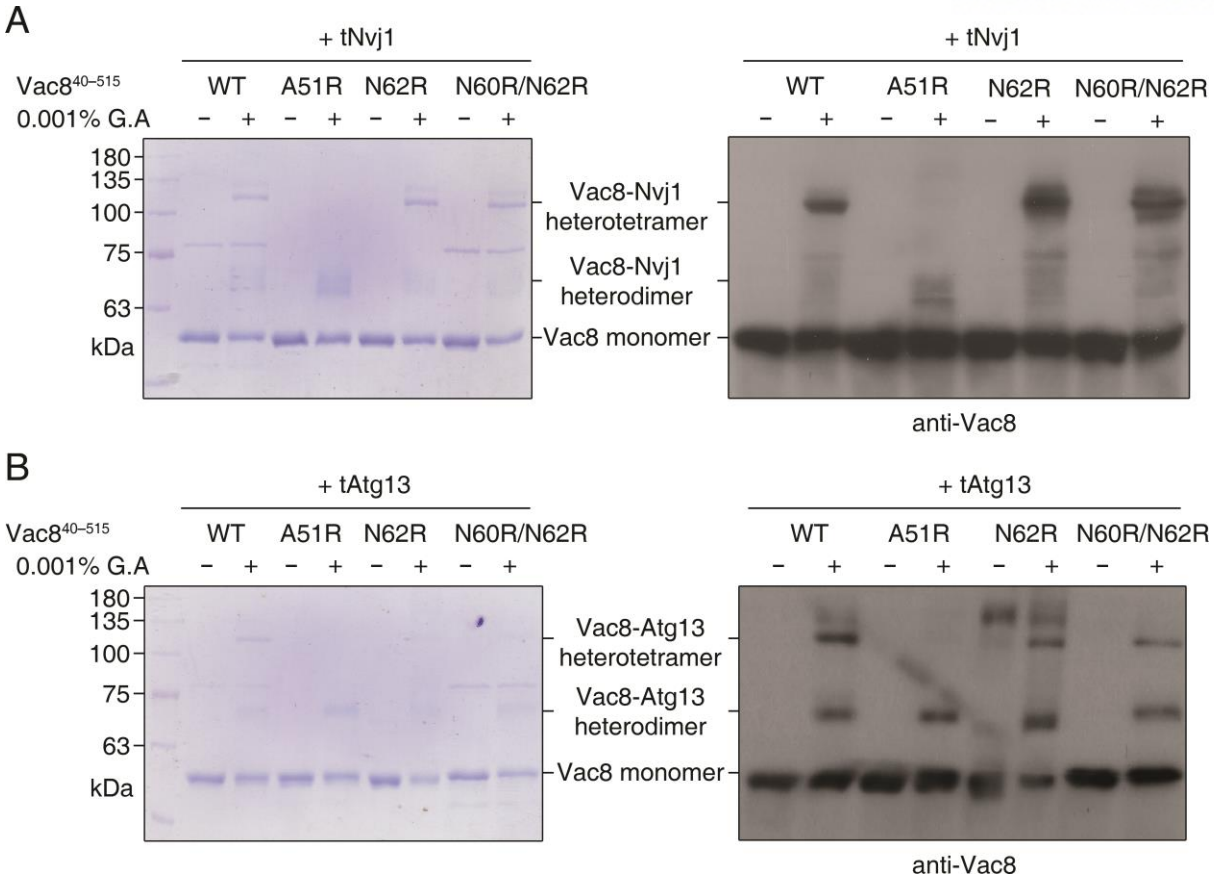

Figure 2.13. Cross-linking using N60R/N62R mutant reveals different quaternary structures of Vac8-Nvj1 and Vac8-Atg13 complexes

SDS-PAGE and immunoblotting analysis of chemical cross-linking of Vac8$^{40–515}$-tNvj1 **(A)** and Vac8$^{40–515}$-tAtg13 **(B)** in Figure 2.12 A and B. The 8% SDS-PAGE gel was stained with Coomassie Brilliant Blue (left) or transferred to a PVDF membrane and immunoblotted with anti-Vac8 antibody (1:2000, diluted in 5% skim milk; right).

2.4. Discussion

Vac8 is composed of 12 ARMs across the whole sequence, and has a myristoylation and three palmitoylation sites in the N-terminal region for anchoring into vacuolar membranes, followed by an H1 helix, and ARM1 starts at residue 41 (Figure 2.1E) [14, 15, 17, 24]. In a previous study, we suggested that the H1 helix plays a pivotal role in regulating the dynamic organization of Vac8 [24]. The present study confirmed this putative regulation mechanism by showing that the H1 helix directly interacts with ARM1 and hinders the dimeric interface (Figure 2.1 C and E). In more detail, the N-terminal H1 helix is placed next to ARM1 that also serves as a binding interface for the formation of the 2-fold dimer of Vac8 (Figure 2.1E). Intramolecular association of the H1 helix and ARM1 regions blocks exposure of the 2-fold interface, thereby hindering self-association of Vac8, which is crucial for the PMN and CVT pathways. We previously reported that disruption of Vac8 dimerization markedly affects both PMN and CVT pathways [24] (also see Figure 2.8C). Structural comparison of tVac8-tNvj1, in which the H1 helix is dissociated from ARM1 (referred to as “active”; Figure 2.1D), and tVac8-tAtg13 in which the H1 helix is bound to ARM1 (referred to as “inactive”; Figure 2.1C), revealed that the residues comprising the H1 helix are altered between active and inactive conformations. In the “inactive” conformation, the C terminus is extended by 6 residues that are disordered in the “active” conformation (Figure 2.1E). The dynamic organization of the sequence and structure of the H1 helix could in principle regulate the conversion from the “inactive” to the “active” states. The regulatory importance of the H1 helix is further supported by high sequence conservation across Vac8 homologs; even the residues in the disordered region (residues 35–40) of the “active” state are highly conserved among other species [24].

Given that the self-association of Vac8 is important for both PMN and CVT pathways, it is noteworthy that one role of the H1 helix might be to initiate these pathways. We therefore attempted to identify factors triggering conformational changes in the H1 helix by focusing on a possible covalent modification in the vicinity of this secondary structural element. Interestingly, global analysis of phosphorylation sites in the cyclin-dependent kinase Cdk1 in *S. cerevisiae* identifies residues Ser11 and Ser16 of Vac8 as strong candidate sites for Cdk1-mediated phosphorylation [33]. Ser11 is disordered in the structure of both tVac8-tAtg13 and Vac8ΔH1-tAtg13 complexes, suggesting that this region is structurally flexible. Meanwhile, Ser16 is visible in the tVac8-tAtg13 complex, and the side chain is exposed to the surface and hence solvent-accessible (Figure 2.14). Moreover, because its side-chain hydroxyl group does not participate in any intermolecular interactions with other residues, this residue could potentially be phosphorylated by kinases. More importantly, Ser16 is located just beneath the N terminus of the H1 helix, indicating that modification of this residue could affect the conformation of the H1 helix (Figure 2.14).

To explore whether Ser11 and/or Ser16 are phosphorylated in vivo, we attempted to identify phosphorylation sites of Vac8 by LC-MS/MS analysis (Figure 2.15A). The results revealed that Ser16 was indeed phosphorylated, but we failed to detect phosphorylation of Ser11. Although these results do not necessarily rule out the possibility that Ser11 is a phosphorylation site, we focused on investigating the importance of Ser16 in the regulation of CVT and PMN pathways by mutating this residue to alanine or glutamate. As shown in Figure 2.15 C and D, both PMN and CVT pathways were severely impaired when Ser16 was replaced with alanine. Intriguingly, these pathways were similarly impaired when Ser16 was replaced with glutamate, a phosphomimetic amino acid (Figure 2.15 E and F). Given that the alanine or glutamate mutation did not impair the vacuolar localization of Vac8 (Figure 2.15B), these results strongly suggest that Ser16 is essential for the PMN and CVT pathways, and its phosphorylation must be elaborately controlled in a spatiotemporal manner for these pathways [34]. Our results imply that the fundamental functions of Vac8 may potentially be regulated by signal-mediated processes through phosphorylation, although it remains elusive whether phosphorylation of Ser16 per se might directly cause structural changes in the H1 helix, resulting in switching between its active and inactive conformations (Figure 2.15G). In the same vein, our findings also imply that the formation of membrane contact sites, such as NVJs, may be regulated by external signaling pathways. Activation or inhibition of these pathways may trigger formation or disruption of NVJs, and thereby regulate PMN by modulating the structures and functions of Vac8.

An intramolecular folding-back mechanism acting on ARM-containing proteins has been suggested for the CTNNB1/β-catenin-CDH1/E-cadherin complex that plays essential roles in cell-cell adhesion [35]. The structure of CDH1/E-cadherin bound to CTNNB1/β-catenin, which possesses 12 ARMs [36], strongly resembles those of the Vac8-Atg13 and Vac8-Nvj1 complexes determined in the present study (Figure 2.1C) [24]. The additional secondary structural elements at the N- and C-termini of CTNNB1/β-catenin, rather than within the central ARM domain, are involved in interactions with other binding partners or self-association with the ARM domain itself, and thereby differentially regulate molecular functions in cell adhesion and WNT signaling [35, 37]. Although it has never been reported that the H1 helix of Vac8 mediates interactions with other proteins, we herein propose a similar versatile role for the H1 helix in regulating the function of Vac8 by modulating inter- and/or intramolecular binding in a comparable manner. Interestingly, however, expression of Vac8 mutant lacking the H1 helix, Vac8ΔH1, in *vac8Δ* yeast cells fully restored the PMN pathway, but not the CVT pathway, suggesting that the H1 helix plays a complex functional role, possibly acting as a switch elaborately regulated by phosphorylation (Figure 2.16).

Vac8 also plays an important role in forming NVJs, and therefore represents novel membrane

contact sites. NVJs are formed by direct interaction between Vac8 and Nvj1, and we demonstrated that disruption of this interaction prevents the formation of NVJs, and consequently blocks the PMN pathway [24]. Structural comparison of tVac8-tAtg13 and tVac8-tNvj1 complexes revealed several common features; both tNvj1 and tAtg13 form extended loops in the Vac8-binding region that competitively bind in an antiparallel manner to the inner groove generated by the Vac8 ARM domain (Figure 2.1 C and D) [24]. While obvious structural variations between the two extended loops were apparent at interface I of the N-terminal region, interface II in the C-terminal region of the two structures superimposed well, despite the low sequence identity shared between Nvj1 and Atg13 (Figure 2.3 A and B). Interestingly, the contact region at interface II is very close to ARM1 that is critical for self-association of Vac8. The most remarkable structural variation between Vac8ΔH1-tAtg13 and tVac8-tNvj1 was the clear difference in conformation of the quaternary structures of Vac8 bound to Nvj1 or Atg13. When bound to Nvj1, the Vac8 heterotetramer forms an arch-shaped structure, whereas it adopts a superhelical conformation in the Vac8-Atg13 complex (Figure 2.11). We experimentally confirmed that the organization of the quaternary structures of Vac8 selectively affected CVT or PMN pathways in yeast (Figure 2.12 E and F). We therefore investigated how the quaternary conformation of Vac8 is altered, and structure alignment of Nvj1 and Atg13 revealed an additional visible residue (Tyr321) in tNvj1, in interface II at the C terminus, that is clearly involved in dimerization of Vac8 (Figures 2.3 A and B, and 2.17). Consistently, we previously proposed a significant role for Tyr321 in self-association of Vac8 and formation of NVJs [24]. The absence of this residue in Atg13 could prevent Vac8 from adopting an arch-shaped structure, favoring a different Vac8 conformation. It is still unknown whether there are other proteins that specifically recognize the different quaternary structures of Vac8, and future work should address how the quaternary structures may contribute to the cellular functions of Vac8 at the molecular level. Nevertheless, our work provides a seminal framework for understanding the molecular mechanism by which the armadillo repeat protein Vac8 can differentially regulate the two distinct CVT and PMN pathways at the molecular level.

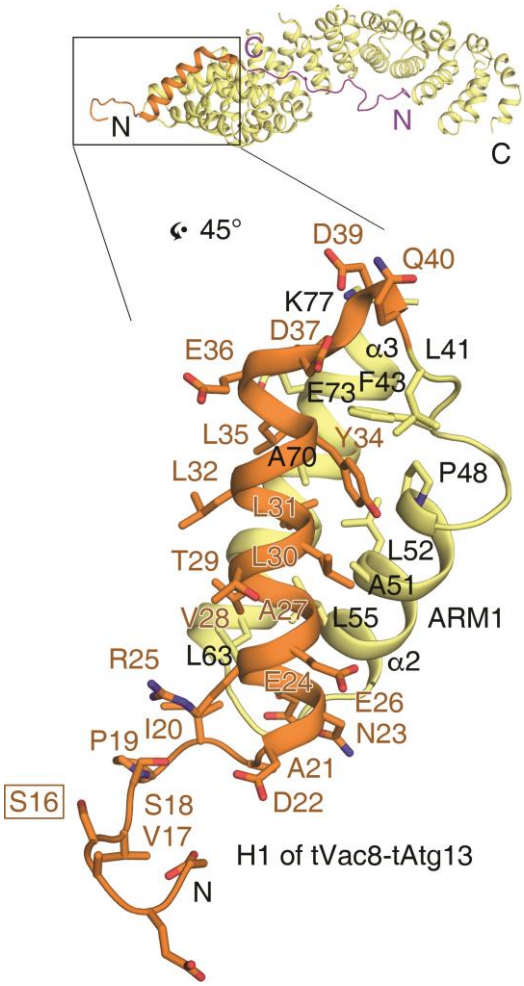

Figure 2.14. A phosphoserine residue is located close to the H1 helix

The ribbon diagram shows the H1 helix contacting the first ARM (ARM1) and the N-terminal loop of Vac8 in the tVac8 (yellow)-tAtg13 (purple) complex. The H1 helix is colored orange for clarity. Ser16 of Vac8, indicated by a box, is a phosphorylation site phosphorylated by Cdk1. Based on the structure, this residue is solvent-accessible and not involved in any interactions within the molecule.

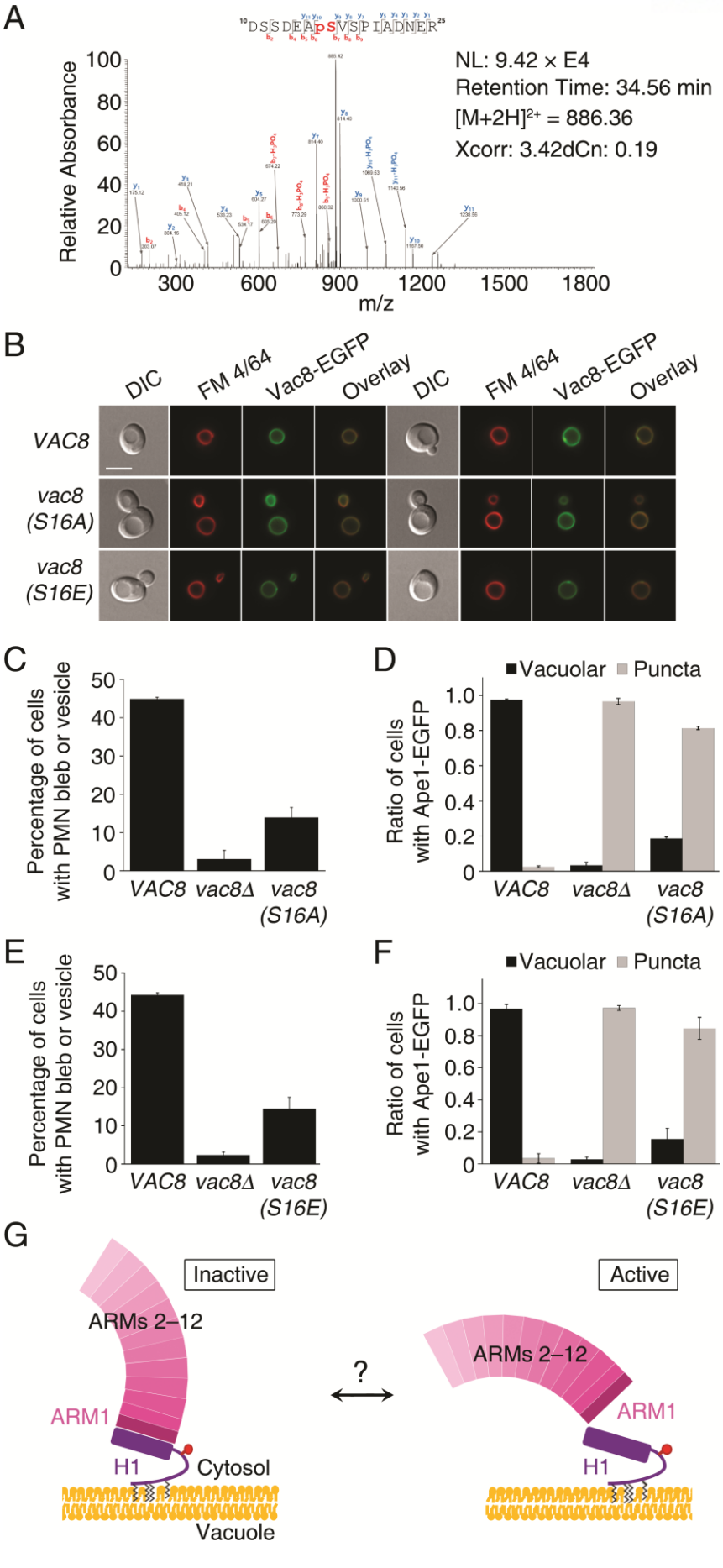

Figure 2.15. Phosphorylation of Ser16 in Vac8 may regulate the PMN and CVT pathways

(A) Mass spectrometric analysis of phosphorylated peptides from trypsin digestion of Vac8 reveals phosphorylation of residue Ser16 of Vac8.

(B) Replacement of Ser16 with alanine or glutamate does not influence the vacuolar localization of Vac8. GFP fluorescence from Vac8 and FM 4/64 fluorescence from vacuoles were analyzed by fluorescence microscopy.

(C and D) Vac8(S16A) mutant does not support the PMN **(C)** or CVT **(D)** pathways.

(E and F) Replacement of Ser16 with glutamate, a phosphomimetic amino acid, largely abolishes the function of Vac8 in both the PMN **(E)** and CVT **(F)** pathways.

(G) Putative model of H1 helix-mediated regulation of Vac8. Vac8 is anchored in the vacuolar membrane via lipidation at the N terminus. The H1 helix (purple) directly binds to ARM1 and hinders the self-association of Vac8 by masking the dimeric interface (left; “inactive” conformation). The H1 helix can be released from ARM1, resulting in exposure of the dimeric interface, allowing its self-association (right; “active” conformation). The cartoon representation proposes a putative model in which conformational changes of the H1 helix might be induced by phosphorylation (red circle) of Ser16 or unknown factors (question mark).

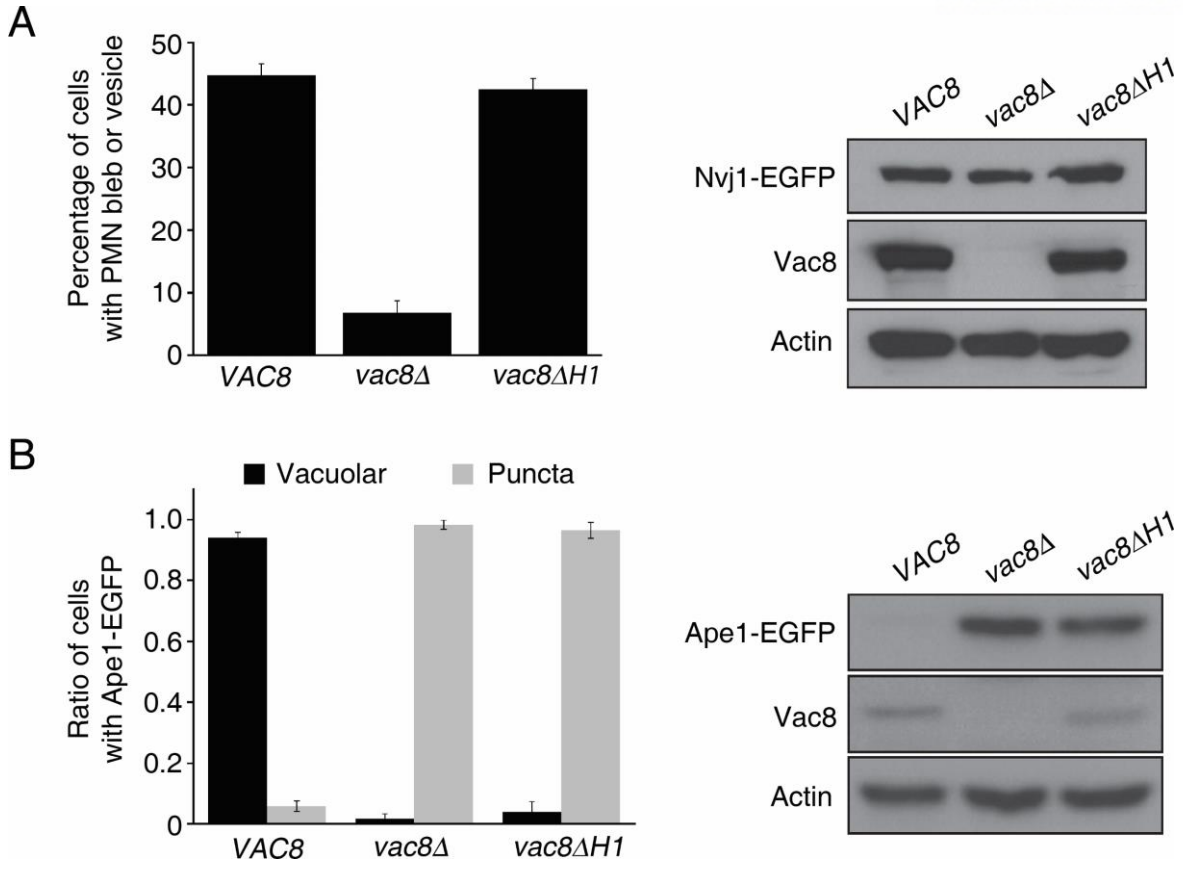

Figure 2.16. Deletion of the H1 helix abolishes the function of Vac8 in the CVT pathway of Ape1, but does not affect the Vac8-mediated PMN pathway

(A) The PMN pathway is largely intact in cells expressing mutant Vac8 lacking the H1 helix. Experiment was performed as described in Figure 2.12E. The graph shows quantification of cells with PMN blebs or PMN vesicles (left). The blot shows that expression of wild-type and mutant Vac8 is comparable, based on immunoblotting with anti-Vac8 antibody (right). Actin was used as a loading control.

(B) The CVT pathway is severely impaired in cells expressing mutant Vac8 lacking the H1 helix. Experiment was performed as described in Figure 2.3E. The graph shows quantification of cells with vacuolar and cytoplasmic Ape1-EGFP (left). The blot shows that expression of wild-type and mutant Vac8 is comparable, based on immunoblotting with anti-Vac8 antibody (right). Actin was used as a loading control.

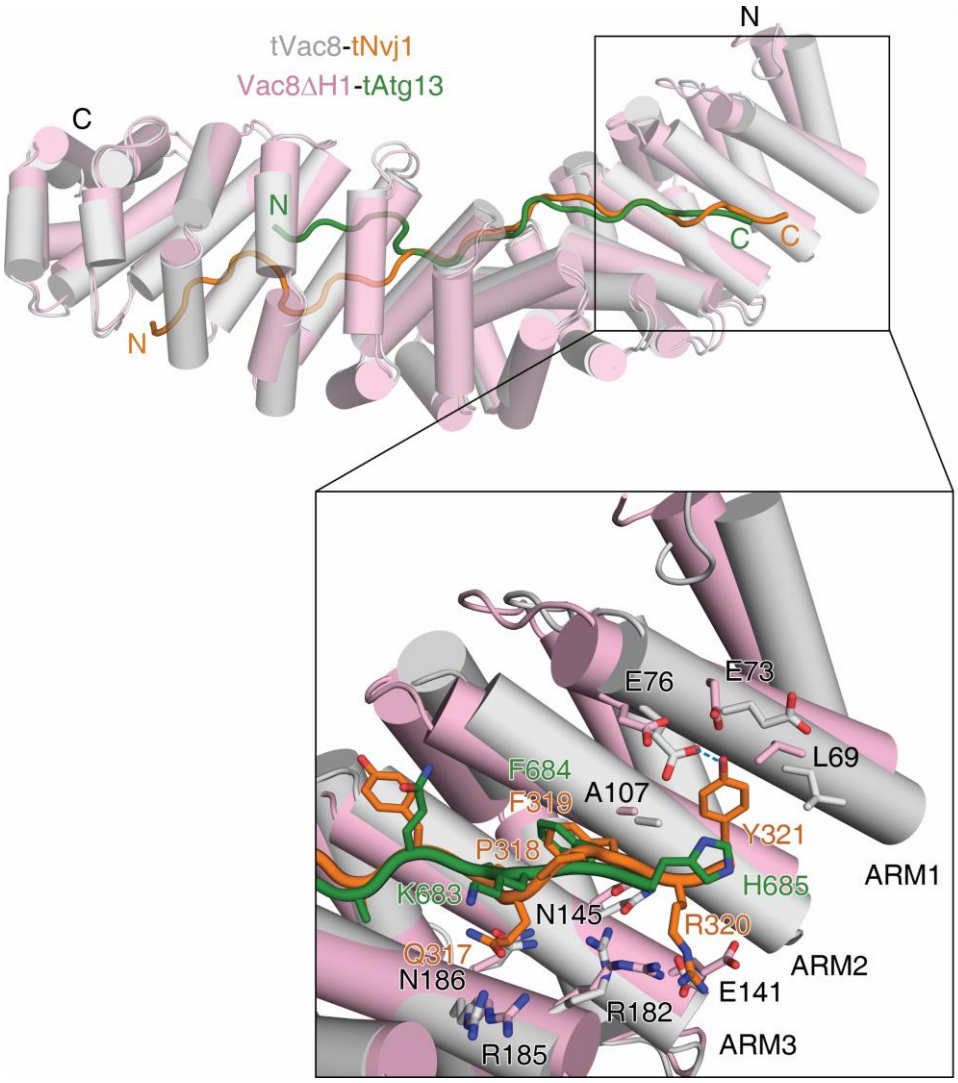

Figure 2.17. Structural comparison of Vac8ΔH1-tAtg13 and tVac8-tNvj1 complexes

The ribbon diagram shows the structural comparison of Vac8ΔH1-tAtg13 and tVac8-tNvj1 (PDB code: 5XJG). The structure of Vac8ΔH1-tAtg13 is superimposed with that of tVac8-tNvj1 (RMSD = 1.288 Å). Vac8 molecules bound to tAtg13 (green) and tNvj1 (orange) are colored pink and gray, respectively. The box below shows a close-up view of the N terminus of Vac8 (the C terminus of tNvj1 and tAtg13). Compared with the structure of tAtg13, tNvj1 bound to Vac8 includes an additional visible residue (Tyr321) that directly contacts ARM1 of Vac8. Oxygen and nitrogen atoms are colored red and blue, respectively. Blue dotted line indicates the intermolecular H-bond.

2.5. Materials and Methods

2.5.1. Cloning, expression, and protein purification

Overexpression constructs for glutathione-S-transferase (GST)-fused tVac8 and His_6-tagged tAtg13 proteins have been described previously [38]. For the Vac8ΔH1-tAtg13 complex, DNA encoding Vac8ΔH1 was generated by PCR and cloned into the vector pGEX-6P-1 (GE Healthcare Life Sciences). For coexpression and purification of tVac8-tAtg13 and Vac8ΔH1-tAtg13, plasmids were transformed into *Escherichia coli* BL21 (DE3) competent cells, and cells were grown in Luria-Bertani medium (MP Biomedicals, 113002032) to an absorbance at 600 nm (A600) of 0.6. Protein expression was then induced by the addition of 0.3 mM isopropyl-β-D-1-thiogalactopyranoside (IPTG; GoldBio, I2481), and culturing was continued at 18°C overnight. Cultured cells were harvested by centrifugation at 3,200 × g for 18 min and resuspended in buffer A containing 25 mM sodium phosphate, pH 7.8, 400 mM sodium chloride (NaCl), 10 mM imidazole. Proteins were first purified on a HiTrap chelating HP column (GE Healthcare Life Sciences, 17040901) charged with Ni^{2+} in buffer A. The GST-tag and His_6-tag were removed using PreScission (GE Healthcare Life Sciences, 27084301) and tobacco etch virus (New England BioLabs, P8112S) proteases, respectively, during dialysis overnight against buffer containing 25 mM Tris-HCl, pH 7.8, 150 mM NaCl, 4 mM β-mercaptoethanol (β-ME) at 4°C. Non-cleaved proteins and cleaved tags were removed by a second round of Ni^{2+}-immobilized metal affinity chromatography (IMAC) and GST affinity chromatography. Proteins were further purified by size-exclusion chromatography (SEC) using a HiLoad 16/600 Superdex 200 pg column (GE Healthcare Life Sciences, 28989335) in buffer B consisting of 25 mM Tris-HCl, pH 7.5, 150 mM NaCl, 5 mM dithiothreitol (DTT). Proteins were concentrated to 10 mg/mL for later use. Mutant variants of Vac8 and tAtg13 used in this study were obtained by site-directed mutagenesis and confirmed by DNA sequencing.

2.5.2. Crystallization and structure determination

The tVac8-tAtg13 complex was crystallized as described previously [38] from a reservoir solution comprising 25% polyethylene glycol (PEG) 400 (Sigma-Aldrich, 91893), 100 mM Tris-HCl, pH 8.5, 2% ethylene glycol (Sigma-Aldrich, 324558), 2% PEG 3350 (Sigma-Aldrich, 88276), 5 mM DTT. Crystals were transferred into reservoir buffer supplemented with 30% PEG 400 for cryoprotection, and flash-frozen in liquid nitrogen. X-ray diffraction data were collected at a wavelength of 0.979 Å on beamline 5C of the Pohang Accelerator Laboratory [39]. Data were processed with the program HKL2000 [40]. The structure was solved by molecular replacement using Phaser in the PHENIX suite [41] with published coordinates of Vac8 (PDB code: 5XJG) as a search

model. Following rigid-body and positional refinement of the model using PHENIX [42] and Coot [43], the sequence of tAtg13 (residues 660–685) could be positioned into the resulting electron density (Figure 2.2A). Subsequently, restrained refinement reduced the free *R*-factor to 24.6% (and the crystallographic *R*-factor to 20.6%) for data between 50 and 2.9 Å resolution (Table 2.1). Residues 10–12 and 514–515 of tVac8, and residues 567–659 and 686–695 of tAtg13, were not modeled due to disordered electron density.

The Vac8ΔH1-tAtg13 complex was crystallized at 4°C by mixing 1 μL of protein solution with the same volume of reservoir solution comprising 15% PEG 3350, 0.1 M N-(2-acetamido)iminodiacetic acid (ADA), pH 6.5, 0.2 M ammonium sulfate. Crystals (space group $P2_12_12_1$, a = 69.475 Å, b = 85.268 Å, c = 272.820 Å) contain two copies of the Vac8ΔH1-tAtg13 complex in the asymmetric unit, and diffract synchrotron X-rays to 3.2 Å resolution. Crystals were transferred to well solution plus 30% ethylene glycol for cryoprotection and flash-frozen in liquid nitrogen. X-ray diffraction data collection and phase calculation were performed as described above. The final model of the Vac8ΔH1-tAtg13 complex was refined to R_{work}/R_{free} values of 21.6/25.5% following iterative rounds of refinement and model building. The model contains residues 47–528 and 561–576 of Vac8ΔH1 for first copy, residues 48–532 and 560–578 of Vac8ΔH1 for second copy, and residues 665–685 of tAtg13 (Figure 2.2B). Diffraction data and refinement statistics are summarized in Table 2.1. All structural images in figures were generated by PyMOL (http://www.pymol.org/).

2.5.3. Analytical ultracentrifugation

The absolute molecular weights of tVac8-tAtg13 (Figure 2.1B) and Vac8ΔH1-tAtg13 (Figure 2.6C) complexes were measured by sedimentation equilibrium analysis using an XL-A analytical ultracentrifuge (Beckman Coulter) as described previously [44]. Protein samples were prepared in buffer C comprising 25 mM Tris-HCl, pH 7.5, 150 mM NaCl, 5 mM β-ME.

2.5.4. Pull-down assay

To assess the interaction between Vac8 and Atg13 (Figure 2.3D), supernatants of *E. coli* cells coexpressing GST-tVac8 and wild-type or mutant His_6-tAtg13 were incubated with 15 μL of Ni-NTA agarose (Qiagen, 30210) for 1 h at 4°C. Beads were washed three times with buffer consisting of 25 mM sodium phosphate, pH 7.4, 400 mM NaCl, 50 mM imidazole, 0.1% Triton X-100 (Sigma-Aldrich, X100). Proteins were eluted with 4 × sodium dodecyl sulfate (SDS) loading buffer, separated by 12% SDS-polyacrylamide gel electrophoresis (PAGE), and stained with Coomassie Brilliant Blue. Protein bands of Vac8 were quantified using ImageJ software. Data are shown as the mean ± SD of three

independent experiments.

2.5.5. Isothermal titration calorimetry

The apparent dissociation constant (K_d) for Vac8 (full-length and Vac8ΔH1) binding to tAtg13 proteins (Figure 2.6B) and full-length Vac8 binding to mutants of tAtg13 (Figure 2.4) was measured by isothermal titration calorimetry (ITC) using a MicroCal iTC200 instrument (GE Healthcare Life Sciences). A 0.7 mM sample of tAtg13 was titrated into 0.05 mM Vac8 protein in buffer C at 25°C. Measurements were obtained over 20 injections of 2 μL with a reference power of 5 μcal/s and a stirring speed of 1,000 rpm. The "one set of sites" model was used to generate titration curves using MicroCal PEAQ-ITC analysis software (Malvern panalytical).

2.5.6. Size-exclusion chromatography analysis

To analyze the relative molecular weight of wild-type and mutant Vac8-Atg13 complexes ($Vac8^{40–515}$-tAtg13 and $Vac8^{40–515,\ A51R\ or\ L55R}$-tAtg13 in Figure 2.8B) and $Vac8^{40–515,\ N62R\ or\ N60R/N62R}$ complexed with tNvj1 or tAtg13 (Figure 2.12 C and D), purified protein complexes were loaded onto a calibrated Superdex 200 10/300 GL column (GE Healthcare Life Sciences, 17517501) in buffer B, and eluted at a flow rate of 0.5 mL/min.

2.5.7. Small-angle X-ray scattering

Small-angle X-ray scattering (SAXS) data were collected at beamline 6D at Pohang Accelerator Laboratory (PAL). Scattering data were collected using 30 s exposures for each protein samples (4 mg/mL) in buffer B, followed by background-subtraction. Further data processing and analysis were performed using the ATSAS package [30]. The radius of gyration (R_g) determined by Guinier analysis was analyzed by PRIMUS [45], and the distance distribution function P(r) and maximum dimension of the particle (D_{max}) were obtained by the indirect Fourier transform method using GNOM [46]. Ab initio modeling of $Vac8^{40–578}$-tNvj1 and $Vac8^{40–578}$-tAtg13 was performed using DAMMIF [47] with 10 independent runs and averaged by DAMAVER [48]. Theoretical scattering curves were generated by CRYSOL [49] using the structure of Vac8ΔH1-tNvj1, in which tVac8 coordinates of the tVac8-tNvj1 were replaced by that of Vac8ΔH1, and Vac8ΔH1-tAtg13 crystal structures. Envelopes generated by DAMAVER were superimposed with structures using the SUPCOMB program [31]. Experimental parameters from SAXS analysis are summarized in Table 2.3.

2.5.8. Cross-linking

For cross-linking analysis, 0.5 mg/mL wild-type or mutant Vac8 ($Vac8^{40–515}$ or $Vac8^{40–515, A51R}$, $Vac8^{40–515, N62R}$, or $Vac8^{40–515, N60R,N62R}$) in complex with tAtg13 or tNvj1 was prepared in buffer comprising 25 mM sodium phosphate, pH 7.5, 150 mM NaCl, 5 mM DTT. Each protein complex was incubated with 0.001% glutaraldehyde (Sigma-Aldrich, G7651) for 30 min at 20°C. The reaction was stopped by the addition of 100 mM Tris-HCl, pH 7.6 and reaction products were analyzed by 8% SDS-PAGE and transferred to a polyvinylidene difluoride (PVDF) membrane using a Trans-Blot SD Semi-Dry Transfer Cell (Bio-Rad). The identity of cross-linked species was analyzed by immunoblotting with anti-Vac8, anti-Atg13, and anti-Nvj1 antibodies.

2.5.9. Yeast strains and vacuole staining with FM 4/64

Yeast strains used in this study are listed in Table 2.2. Vacuoles of growing yeast cells were labeled with FM 4/64 as previously described [24] with minor modifications. Briefly, cells were grown at 30°C to an optical density at 600 nm (OD600) of 0.8 in YPD (10 g/L yeast extract, 20 g/L peptone, 20 g/L dextrose) medium. Cells were then incubated with aeration in YPD medium containing 20 μM FM 4/64 (Molecular Probes, T13320) for 30 min at 30°C, harvested by centrifugation (2,400 × g) at room temperature for 1 min, washed, resuspended in fresh medium, and cultured for a further 3 h at 30°C. After cells were harvested by centrifugation, they were mounted on a pad of 2% low-melting agarose formed in a slide and analyzed using a fluorescence microscope (Nikon Eclipse Ti-U) with a Nikon Plan Apo 100 ×, 1.45/NA oil immersion objective.

2.5.10. CVT and PMN pathway induction

Cells were grown overnight at 30°C with shaking in YPD medium, cultures were adjusted to OD600 = 0.5, FM 4/64 (0.5 μM) was added to visualize vacuoles, and cells were further cultured at 30°C for 2 h. For CVT pathway induction, cells grown in YPD were washed with sterile water three times, resuspended in nitrogen starvation media (SD-N) (1.7g/L yeast nitrogen base, 20g/L dextrose), and further cultured at 30°C for 2 h. For PMN induction, 0.2 μM rapamycin (Sigma-Aldrich, R8781) was added and cells were further incubated at 30°C for 6 h.

2.5.11. Precursor Ape1 processing assay

Yeast cells were grown overnight at 30°C with shaking in YPD medium. Cells were washed with sterile water three times, resuspended in SD-N media, and further cultured at 30°C for 2 h. Cells

were harvested by centrifugation for 10 s at 11,400 × g at room temperature, and the pellet was resuspended in phosphate-buffered saline (PBS; 137 mM NaCl, 2.7 mM KCl, 10 mM $Na_2HPO_4 \cdot 7H_20$, 1.8 mM KH_2PO_4). Cells were vortexed with glass beads for 3 min, mixed with 2 × SDS sample buffer, and boiled for 5 min. After centrifugation, the resulting supernatant was separated by SDS-PAGE and analyzed by immunoblotting with anti-Ape1 antiserum (a generous gift from Dr. Daniel Klionsky, University of Michigan) or anti-actin antibody (a generous gift from Dr. Bill Wickner, Dartmouth College).

2.5.12. Bulk autophagy assay

Yeast cells expressing EGFP-Atg8 were grown overnight at 30°C in YPD medium. Cells were resuspended in SD-N media and further cultured at 30°C for 2 h. Cells were harvested by centrifugation for 10 s at 11,400 × g at room temperature, and the pellet was resuspended in PBS. Cells were vortexed with glass beads for 3 min, mixed with 2 × sodium dodecyl sulfate (SDS) sample buffer, and boiled for 5 min. After centrifugation, the resulting supernatant was separated by SDS-PAGE and analyzed by immunoblotting with anti-GFP antibody (a generous gift from Dr. Bill Wickner, Dartmouth College) or anti-actin antibody (a generous gift from Dr. Bill Wickner, Dartmouth College).

2.5.13. Triton X-114 phase partitioning assay of Vac8.

Lipidation of Vac8 was evaluated by Triton X-114 partitioning assay as previously described [50]. Vacuoles were isolated from wild-type *VAC8* or *VAC8* mutant strains. Recombinant Vac8 protein expressed in *E. coli* was used as a non-lipidated protein control. Isolated vacuoles (200 μg) or recombinant Vac8 protein (10 μg) was mixed with lysis buffer (10 mM Tris-HCl, pH 7.4, 150 mM NaCl, 0.5% Triton X-114 [Sigma-Aldrich, X114], 1 mM PMSF [Sigma-Aldrich, P7626], 10 μM leupeptin [Sigma-Aldrich, 108975]). For separation of proteins, 300 μL of cushion buffer (10 mM Tris-HCl, pH 7.4, 150 mM NaCl, 6% sucrose [Amresco, 0335], 0.06% Triton X-114) was prepared in 1.5-mL microcentrifuge tubes. Lysed samples were overlaid on the sucrose cushion and incubated at 30°C for 3 min. Tubes were then centrifuged at room temperature at 300 × g for 3 min, the upper aqueous phase was collected, mixed with 0.5% Triton X-114, and again overlaid on the same cushion buffer. After samples were incubated and centrifuged again, the aqueous phase was washed with 2% Triton X-114, incubated at 30°C for 3 min, and centrifuged at room temperature at 300 × g for 3 min. Finally, the aqueous phase was collected, and the detergent phase was collected from the bottom of the cushion buffer (oily droplet). Each phase was mixed with SDS sample buffer and analyzed by SDS-PAGE and immunoblotting using anti-Vac8 and anti-Pho8 antibodies.

2.5.14. Phosphopeptide enrichment and LC-MS/MS analysis of Vac8

Protein bands corresponding to Vac8 were excised from the SDS-PAGE gel and digested in-gel with trypsin for LC-MS/MS analysis. Enrichment of phosphopeptides was performed as previously described [51]. Briefly, trypsin-digested proteins were resuspended in equilibration buffer (50% acetonitrile, 0.1% trifluoroacetic acid) before injection onto the Fe-IMAC column (Propac IMAC-10 4 × 50 mm, Thermo Scientific, 063276). Samples were injected (0.1 mL/min over 10 min) onto the Fe-IMAC column, and the column was washed with equilibration buffer (0.3 mL/min over 16 min). Phosphopeptides were eluted with a linear gradient from 0% to 45% Fe-IMAC elution buffer (0.5% NH_4OH; 0.2 mL/min over 60 min). The Fe-IMAC column was re-equilibrated with equilibration buffer (0.5 mL/min over 30 min). Flow-through and eluate fractions were collected according to the UV signal (214 nm), dried, and stored at −80°C. LC-MS/MS experiments were performed on an Ultimate 3000 nanoHPLC system (Thermo Scientific) coupled online to a Q Exactive mass spectrometer (Thermo Scientific). Peptides were injected onto a 20 mm × 75 μm Acclaim PepMap C18 nano-trap column (Thermo Scientific, 164535) at a flow rate of 300 nL/min in 98% solvent A (0.1% formic acid in water). After washing, peptides were separated on a 150 mm × 75 μm Acclaim PepMap C18 reverse phase analytical column (Thermo Scientific, ES800) using a linear gradient from 2% to 40% solvent B (acetonitrile with 0.1% formic acid) over a 65 min gradient with a flow rate of 300 nL/min. Data-dependent scans consisting of one full MS scan (450–2,000 m/z, AGC target 1e6) and 10 data-dependent MS/MS scans were used to generate MS/MS spectra of eluted peptides using the dynamic exclusion option.

2.5.15. Mass spectrometric data analysis

Mass spectrometry-derived data were searched against the canonical *S. cerevisiae* proteome database downloaded from UniProtKB (http://www.uniprot.org/) using Proteome Discoverer software (Thermo Scientific). Mass spectrometry data were searched using the SEQUEST algorithm with carbamidomethylation of cysteine as a fixed modification, and N-terminal acetylation, oxidation of methionine and phosphorylation at serine, threonine, and tyrosine as variable modifications. MS/MS spectra were searched with a precursor mass tolerance of 10 ppm and fragment mass tolerance of 0.02 Da. The search was limited to fully tryptic peptide candidates and a maximum of two missed cleavages were allowed. Data were searched against the target-decoy database and peptide spectral matches (PSM) were validated using percolator based on *q*-values at a 1% false discovery rate (FDR).

2.5.16. Immunoblotting

Samples were separated by SDS-PAGE and analyzed by immunoblotting with indicated antibodies. ECL exposed films were quantitated using ImageJ software. All data are representative of experiments performed at least three times. Actin levels were analyzed and confirmed comparable between samples by comparing band intensities of actin from increasing concentrations of yeast cytosol.

2.5.17. Statistical analysis

Statistical significance was determined from at least three independent experiments using Student's *t*-test. All data represent the mean ± SEM.

2.6. References

[1] E. Jones, G. Webb, and M. Hiller, "Biogenesis and function of the yeast vacuole," *Molecular biology of the yeast Saccharomyces cerevisiae,* vol. 3, 1997.

[2] H. B. van den Hazel, M. C. Kielland-Brandt, and J. R. Winther, "Biosynthesis and function of yeast vacuolar proteases," *Yeast,* vol. 12, no. 1, pp. 1-16, 1996.

[3] M. Thumm and D. H. Wolf, "From proteasome to lysosome: studies on yeast demonstrate the principles of protein degradation in the eukaryote cell," in *Advances in Molecular and Cell Biology*, vol. 27: Elsevier, 1998, pp. 43-70.

[4] M. Forgac, "Structure and properties of the vacuolar (H+)-ATPases," *Journal of Biological Chemistry,* vol. 274, no. 19, pp. 12951-12954, 1999.

[5] L. A. Graham, B. Powell, and T. Stevens, "Composition and assembly of the yeast vacuolar H (+)-ATPase complex," *Journal of Experimental Biology,* vol. 203, no. 1, pp. 61-70, 2000.

[6] M. Baba, K. Takeshige, N. Baba, and Y. Ohsumi, "Ultrastructural analysis of the autophagic process in yeast: detection of autophagosomes and their characterization," *The Journal of cell biology,* vol. 124, no. 6, pp. 903-913, 1994.

[7] K. Takeshige, M. Baba, S. Tsuboi, T. Noda, and Y. Ohsumi, "Autophagy in yeast demonstrated with proteinase-deficient mutants and conditions for its induction," *The Journal of cell biology,* vol. 119, no. 2, pp. 301-311, 1992.

[8] L. S. Weisman, R. Bacallao, and W. Wickner, "Multiple methods of visualizing the yeast vacuole permit evaluation of its morphology and inheritance during the cell cycle," *Journal of Cell Biology,* vol. 105, no. 4, pp. 1539-1547, 1987.

[9] L. S. Weisman, S. D. Emr, and W. T. Wickner, "Mutants of Saccharomyces cerevisiae that block intervacuole vesicular traffic and vacuole division and segregation," *Proceedings of the National Academy of Sciences,* vol. 87, no. 3, pp. 1076-1080, 1990.

[10] L. S. Weisman, "Yeast vacuole inheritance and dynamics," *Annual review of genetics,* vol. 37, no. 1, pp. 435-460, 2003.

[11] J. M. Shaw and W. T. Wickner, "vac2: a yeast mutant which distinguishes vacuole segregation from Golgi-to-vacuole protein targeting," *The EMBO journal,* vol. 10, no. 7, pp. 1741-1748, 1991.

[12] D. Gomes de Mesquita, H. Van den Hazel, J. Bouwman, and C. Woldringh, "Characterization of new vacuolar segregation mutants, isolated by screening for loss of proteinase B self-activation," *European journal of cell biology,* vol. 71, no. 3, pp. 237-247, 1996.

[13] Y. Wang *et al.*, "Multiple classes of yeast mutants are defective in vacuole partitioning yet target vacuole proteins correctly," *Molecular Biology of the Cell,* vol. 7, no. 9, pp. 1375-1389, 1996.

[14] X. Pan and D. Goldfarb, "YEB3/VAC8 encodes a myristylated armadillo protein of the Saccharomyces cerevisiae vacuolar membrane that functions in vacuole fusion and inheritance," *Journal of Cell Science,* vol. 111, no. 15, pp. 2137-2147, 1998.

[15] Y.-X. Wang, N. L. Catlett, and L. S. Weisman, "Vac8p, a vacuolar protein with armadillo repeats, functions in both vacuole inheritance and protein targeting from the cytoplasm to vacuole," *The Journal of cell biology,* vol. 140, no. 5, pp. 1063-1074, 1998.

[16] F. Tang, E. J. Kauffman, J. L. Novak, J. J. Nau, N. L. Catlett, and L. S. Weisman, "Regulated degradation of a class V myosin receptor directs movement of the yeast vacuole," *Nature,* vol. 422, no. 6927, pp. 87-92, 2003.

[17] K. Subramanian, L. E. Dietrich, H. Hou, T. J. LaGrassa, C. T. Meiringer, and C. Ungermann, "Palmitoylation determines the function of Vac8 at the yeast vacuole," *Journal of cell science,* vol. 119, no. 12, pp. 2477-2485, 2006.

[18] P. Roberts, S. Moshitch-Moshkovitz, E. Kvam, E. O'Toole, M. Winey, and D. S. Goldfarb, "Piecemeal microautophagy of nucleus in Saccharomyces cerevisiae," *Molecular biology of the cell,* vol. 14, no. 1, pp. 129-141, 2003.

[19] E. Kvam and D. Goldfarb, "Nucleus-vacuole junctions and piecemeal microautophagy of the nucleus in S. cerevisiae," *Autophagy,* vol. 3, no. 2, pp. 85-92, 2007.

[20] R. Dawaliby and A. Mayer, "Microautophagy of the nucleus coincides with a vacuolar diffusion barrier at nuclear–vacuolar junctions," *Molecular biology of the cell,* vol. 21, no. 23, pp. 4173-4183, 2010.

[21] X. Pan *et al.*, "Nucleus–vacuole junctions in Saccharomyces cerevisiae are formed through the direct interaction of Vac8p with Nvj1p," *Molecular biology of the cell,* vol. 11, no. 7, pp. 2445-2457, 2000.

[22] A. Murley, R. D. Sarsam, A. Toulmay, J. Yamada, W. A. Prinz, and J. Nunnari, "Ltc1 is an ER-localized sterol transporter and a component of ER–mitochondria and ER–vacuole contacts," *Journal of Cell Biology,* vol. 209, no. 4, pp. 539-548, 2015.

[23] S. V. Scott *et al.*, "Apg13p and Vac8p are part of a complex of phosphoproteins that are required for cytoplasm to vacuole targeting," *Journal of Biological Chemistry,* vol. 275, no. 33, pp. 25840-25849, 2000.

[24] H. Jeong *et al.*, "Mechanistic insight into the nucleus–vacuole junction based on the Vac8p–Nvj1p crystal structure," *Proceedings of the National Academy of Sciences,* vol. 114, no. 23, pp. E4539-E4548, 2017.

[25] Y. Fujioka *et al.*, "Structural basis of starvation-induced assembly of the autophagy initiation complex," *Nature structural & molecular biology,* vol. 21, no. 6, p. 513, 2014.

[26] H. Yamamoto *et al.*, "The intrinsically disordered protein Atg13 mediates supramolecular assembly of autophagy initiation complexes," *Developmental cell,* vol. 38, no. 1, pp. 86-99,

2016.

[27] S. W. Suzuki *et al.*, "Atg13 HORMA domain recruits Atg9 vesicles during autophagosome formation," *Proceedings of the National Academy of Sciences,* vol. 112, no. 11, pp. 3350-3355, 2015.

[28] D. Gatica, A. Damasio, C. Pascual, D. J. Klionsky, M. J. Ragusa, and H. Popelka, "The carboxy terminus of yeast Atg13 binds phospholipid membrane via motifs that overlap with the Vac8-interacting domain," *Autophagy,* vol. 16, no. 6, pp. 1007-1020, 2020.

[29] E. Winzeler, B. Lee, J. McCusker, and R. Davis, "Whole genome genetic-typing in yeast using high-density oligonucleotide arrays," *Parasitology,* vol. 118, no. 7, pp. 73-80, 1999.

[30] D. Franke *et al.*, "ATSAS 2.8: a comprehensive data analysis suite for small-angle scattering from macromolecular solutions," *Journal of applied crystallography,* vol. 50, no. 4, pp. 1212-1225, 2017.

[31] M. B. Kozin and D. I. Svergun, "Automated matching of high-and low-resolution structural models," *Journal of applied crystallography,* vol. 34, no. 1, pp. 33-41, 2001.

[32] E. F. Pettersen *et al.*, "UCSF Chimera—a visualization system for exploratory research and analysis," *Journal of computational chemistry,* vol. 25, no. 13, pp. 1605-1612, 2004.

[33] L. J. Holt, B. B. Tuch, J. Villén, A. D. Johnson, S. P. Gygi, and D. O. Morgan, "Global analysis of Cdk1 substrate phosphorylation sites provides insights into evolution," *Science,* vol. 325, no. 5948, pp. 1682-1686, 2009.

[34] N. Dephoure, K. L. Gould, S. P. Gygi, and D. R. Kellogg, "Mapping and analysis of phosphorylation sites: a quick guide for cell biologists," *Molecular biology of the cell,* vol. 24, no. 5, pp. 535-542, 2013.

[35] C. J. Gottardi and B. M. Gumbiner, "Distinct molecular forms of β-catenin are targeted to adhesive or transcriptional complexes," *The Journal of cell biology,* vol. 167, no. 2, pp. 339-349, 2004.

[36] A. H. Huber and W. I. Weis, "The structure of the β-catenin/E-cadherin complex and the molecular basis of diverse ligand recognition by β-catenin," *Cell,* vol. 105, no. 3, pp. 391-402, 2001.

[37] W. Xu and D. Kimelman, "Mechanistic insights from structural studies of β-catenin and its binding partners," *Journal of cell science,* vol. 120, no. 19, pp. 3337-3344, 2007.

[38] J. Park *et al.*, "Purification, crystallization, and X-ray crystallographic analysis of Vac8p complexed with Atg13p from Saccharomyces cerevisiae," 2017.

[39] S.-Y. Park, S.-C. Ha, and Y.-G. Kim, "The protein crystallography beamlines at the pohang light source II," *Biodesign,* vol. 5, no. 1, pp. 30-4, 2017.

[40] Z. Otwinowski and W. Minor, "Processing of X-ray diffraction data collected in oscillation mode," *Methods in enzymology,* vol. 276, pp. 307-326, 1997.

[41] A. J. McCoy, R. W. Grosse-Kunstleve, P. D. Adams, M. D. Winn, L. C. Storoni, and R. J. Read, "Phaser crystallographic software," *Journal of applied crystallography,* vol. 40, no. 4, pp. 658-674, 2007.

[42] P. D. Adams *et al.*, "PHENIX: a comprehensive Python-based system for macromolecular structure solution," *Acta Crystallographica Section D: Biological Crystallography,* vol. 66, no. 2, pp. 213-221, 2010.

[43] P. Emsley, B. Lohkamp, W. G. Scott, and K. Cowtan, "Features and development of Coot," *Acta Crystallographica Section D: Biological Crystallography,* vol. 66, no. 4, pp. 486-501, 2010.

[44] H. Jeong, J. Park, and C. Lee, "Crystal structure of Mdm12 reveals the architecture and dynamic organization of the ERMES complex," *EMBO reports,* vol. 17, no. 12, pp. 1857-1871, 2016.

[45] P. V. Konarev, V. V. Volkov, A. V. Sokolova, M. H. Koch, and D. I. Svergun, "PRIMUS: a Windows PC-based system for small-angle scattering data analysis," *Journal of applied crystallography,* vol. 36, no. 5, pp. 1277-1282, 2003.

[46] D. Svergun, "Determination of the regularization parameter in indirect-transform methods using perceptual criteria," *Journal of applied crystallography,* vol. 25, no. 4, pp. 495-503, 1992.

[47] D. Franke and D. I. Svergun, "DAMMIF, a program for rapid ab-initio shape determination in small-angle scattering," *Journal of applied crystallography,* vol. 42, no. 2, pp. 342-346, 2009.

[48] V. V. Volkov and D. I. Svergun, "Uniqueness of ab initio shape determination in small-angle scattering," *Journal of applied crystallography,* vol. 36, no. 3, pp. 860-864, 2003.

[49] D. Svergun, C. Barberato, and M. H. Koch, "CRYSOL–a program to evaluate X-ray solution scattering of biological macromolecules from atomic coordinates," *Journal of applied crystallography,* vol. 28, no. 6, pp. 768-773, 1995.

[50] C. Bordier, "Phase separation of integral membrane proteins in Triton X-114 solution," *Journal of Biological Chemistry,* vol. 256, no. 4, pp. 1604-1607, 1981.

[51] B. Ruprecht, H. Koch, G. Medard, M. Mundt, B. Kuster, and S. Lemeer, "Comprehensive and reproducible phosphopeptide enrichment using iron immobilized metal ion affinity chromatography (Fe-IMAC) columns," *Molecular & Cellular Proteomics,* vol. 14, no. 1, pp. 205-215, 2015.

Chapter 3. The structure of human EXD2 reveals a chimeric 3′ to 5′ exonuclease domain that discriminates substrates via metal coordination

(Original article : Park J, Lee S-Y, Jeong H, Kang M-G, Haute LV, Minczuk M, Seo JK, Jun Y, Myung K, Rhee H-W, Lee C. *Nucleic Acids Research*. 2019 July 26;*47*(13):7078-93.)

3.1. Abstract

EXD2 (3′-5′ exonuclease domain-containing protein 2) is an essential protein with a conserved DEDDy superfamily 3′-5′ exonuclease domain. Recent research suggests that EXD2 has two potential functions: as a component of the DNA double-strand break repair machinery and as a ribonuclease for the regulation of mitochondrial translation. Herein, electron microscope imaging analysis and proximity labeling revealed that EXD2 is anchored to the mitochondrial outer membrane through a conserved N-terminal transmembrane domain, while the C-terminal region is cytosolic. Crystal structures of the exonuclease domain in complex with Mn^{2+}/Mg^{2+} revealed a domain-swapped dimer in which the central α5−α7 helices are mutually crossed over, resulting in chimeric active sites. Additionally, the C-terminal segments absent in other DnaQ family exonucleases enclose the central chimeric active sites. Combined structural and biochemical analyses demonstrated that the unusual dimeric organization stabilizes the active site, facilitates discrimination between DNA and RNA substrates based on divalent cation coordination and generates a positively charged groove that binds substrates.

3.2. Introduction

EXD2 (3′-5′ exonuclease domain-containing protein 2) was identified as a new component that plays an essential role in mediating the repair of DNA double-strand breaks [1]. It was suggested that EXD2 might be required to facilitate DNA end resection during homologous recombination by functionally interacting with the MRE11-RAD50-NBS1 (MRN) complex. Primary structure analysis revealed a 3′ to 5′ exonuclease domain belonging to the DnaQ (DEDDy) family sharing high sequence similarity with the exonuclease domain of Werner syndrome protein (WRN), an enzyme involved in maintaining genome stability, and recombinant EXD2 exhibits 3′ to 5′ exonuclease activity against DNA in vitro [1].

However, in contrast to previous results, database analysis using The Human Protein Atlas (www.proteinatlas.org) [2], a public resource of immunofluorescence images for the human proteome, raised the possibility that EXD2 might be localized to mitochondria in various mammalian cell lines such as A-431, U-2 OS and U-251 MG. Supporting this possibility, Hensen et al. recently reported that EXD2 is predominantly associated with the mitochondrial outer membrane [3]. Meanwhile, Stracker and colleagues suggested that EXD2 is localized to the inner mitochondrial membrane (IMM) or matrix [4]. According to the report, EXD2 is a mitochondrial ribonuclease that plays important roles in mitochondrial functions such as respiration, ATP production and mitochondrial translation. The sub-location of EXD2 within mitochondria was examined using proteinase K digestion of purified mitochondria in combination with electron microscopy (EM) imaging following staining with immuno-gold [4]. However, such conventional approaches based on protease accessibility of the sub-mitochondrial proteome in purified mitochondria can lead to mis-interpretation if the target protein is unexpectedly resistant to proteases, as demonstrated for NDUFB10 [5]. Furthermore, immuno-gold EM imaging requires cellular permeabilization, which occasionally degrades cellular ultrastructure [6], and treatment with immuno-gold may cause unintended extraction or relocalization of proteins [7].

Interestingly, EXD2 exhibited exonuclease substrate discrimination activity depending on the metal cofactors coordinated [4]. In the presence of $MnCl_2$, EXD2 displays comparable activity toward DNA and RNA substrates, but activity toward DNA substrates is significantly reduced when $MgCl_2$ is used as a cofactor. This is an interesting result because substrate discrimination via divalent cations bound to exonucleases is a novel feature shown only for EXD2. Even in WRN exonuclease, which shares high sequence similarity with EXD2, metal cofactor-driven substrate discrimination has not been observed [8, 9]. Moreover, given that EXD2 acts as a ribonuclease in mitochondria rather than the nucleus, this could be advantageous and allow EXD2 to modulate its activity against DNA or RNA [4]. However, it remains unknown exactly how the exonuclease activity of EXD2 toward DNA

substrates is specifically limited in the presence of the Mg^{2+} cation, considered the likely physiological metal ion within cells. Therefore, molecular-level studies on EXD2 are needed to explore these distinctive features.

In the present study, we demonstrated that EXD2 is an outer mitochondrial membrane (OMM) protein anchored to the membrane through the N-terminal transmembrane (TM) domain, while most of the functional region, including the exonuclease domain, faces the cytosol. Furthermore, we determined crystal structures of the exonuclease domain of EXD2 in complex with Mn^{2+}/Mg^{2+} and (d)GMP, revealing a novel molecular mechanism by which EXD2 can distinguish DNA or RNA substrates depending on metal coordination, unlike other DnaQ family exonucleases reported to date.

3.3. Results

3.3.1. EXD2 is a mitochondrial outer membrane protein facing the cytosol

Hydropathy plot analysis strongly indicated that EXD2 might contain a single TM domain comprising residues 1−37 at the N terminus (Figure 3.1A). Since several previous studies reported that the N-terminal single TM domain could function as a signal motif for targeting to mitochondria [10, 11], we tested whether this domain is crucial for mitochondrial targeting of EXD2. For this experiment, we generated EXD2-Flag (Flag-tagged at the C terminus) constructs and expressed them in cultured cells (Table 3.1). Figure 3.2A shows that EXD2-Flag was obviously targeted to mitochondria, overlapping with TOM20 (Pearson correlation, R = 0.94). By contrast, Flag-EXD2 tagged at the N terminus was not successfully targeted to mitochondria (Figure 3.1B), and the resulting correlation with TOM20 was low (R = 0.43). We also checked that EXD2$^{38–621}$-Flag, which includes the N-terminal TM domain-deleted EXD2 sequence, was also nuclear-localized in mammalian (HeLa) cells (Figure 3.1C). This result indicates that the predicted N-terminal TM domain of EXD2 might play an important role in mitochondrial targeting, as shown for other signal-anchored proteins such as TOM20 or AKAP1 in which the N-terminal single TM domain acts as a signal-anchor peptide at the OMM [10, 11].

To investigate the sub-mitochondrial localization of EXD2 in more detail, constructs encoding EXD2-V5-APEX2 and EXD2$^{1–37}$-V5-APEX2 were expressed in HeLa cells, which were stained with streptavidin (SA)-AF647 after biotinylation. As shown in Figure 3.2B, EXD2-V5-APEX2 was tightly localized to mitochondria and overlapped strongly with TOM20. However, APEX-mediated biotinylated pattern by EXD2-V5-APEX2 was not tightly localized to mitochondria and was instead diffusely distributed in the cytosol. We also observed a similar diffuse pattern for biotinylated EXD2$^{1–37}$-V5-APEX2 (Figure 3.1D). This diffuse biotin labeling pattern in mitochondria was previously observed for several mitochondrial POI (protein of interest)-APEX2 constructs in which the C terminus of POIs is localized to the outside of the IMM [12]. To confirm whether EXD2 is localized to the mitochondrial inter-membrane space (IMS) or at the OMM, we prepared EM samples of EXD2-V5-APEX2 and EXD2$^{1–37}$-V5-APEX2 by following a protocol reported previously for APEX2-EM [13]. As shown in Figure 3.2C, most diaminobenzidine (DAB) staining from EXD2-V5-APEX2 was observed at the OMM. Furthermore, the EM results for EXD2$^{1–37}$-V5-APEX2 yielded a similar OMM pattern (Figure 3.1E). These results strongly indicate that the N-terminal single TM domain of EXD2 is incorporated at the OMM as a signal-anchor domain.

To further confirm the localization of endogenous EXD2 in the OMM, we employed Spot-

BioID proximity labeling, which facilitates profiling of biotin-labeled peptides [14]. This method can identify directly biotinylated protein candidates that can be considered as proximal proteins of POI-pBirA. We performed in situ biotinylation of OMM proteins using TOM20-pBirA, in which pBirA is located at the cytosolic face of the OMM (Figure 3.2D). After biotin labeling, total biotinylated proteins and peptides were enriched and analyzed by mass spectrometry (MS). Five lysine sites (K46, K221, K295, K562 and K611) of endogenous EXD2 were reproducibly biotinylated by TOM20-pBirA, and labeled residues are within the C-terminal region of the predicted TM domain, suggesting that the C-terminal region of EXD2, including the exonuclease domain, functions on the cytosolic face of the OMM (Figures 3.2E and 3.3).

To corroborate the results of proximity labeling, we performed cellular fractionation experiments of HEK293T cells. Endogenous EXD2 was clearly enriched within the mitochondrial fraction, along with mtSSB1 (a well-characterized mitochondrial matrix protein) and TOM22 (a protein localized in OMM) (Figure 3.1F). While mtSSB1 were resistant to proteinase K treatment of the mitochondrial fraction, both EXD2 and TOM22 were degraded in similar conditions, consistent with localization of EXD2 in OMM (Figure 3.1F). Taken together, our data clearly support the notion of EXD2 localizing at the OMM with signal anchored transmembrane domain.

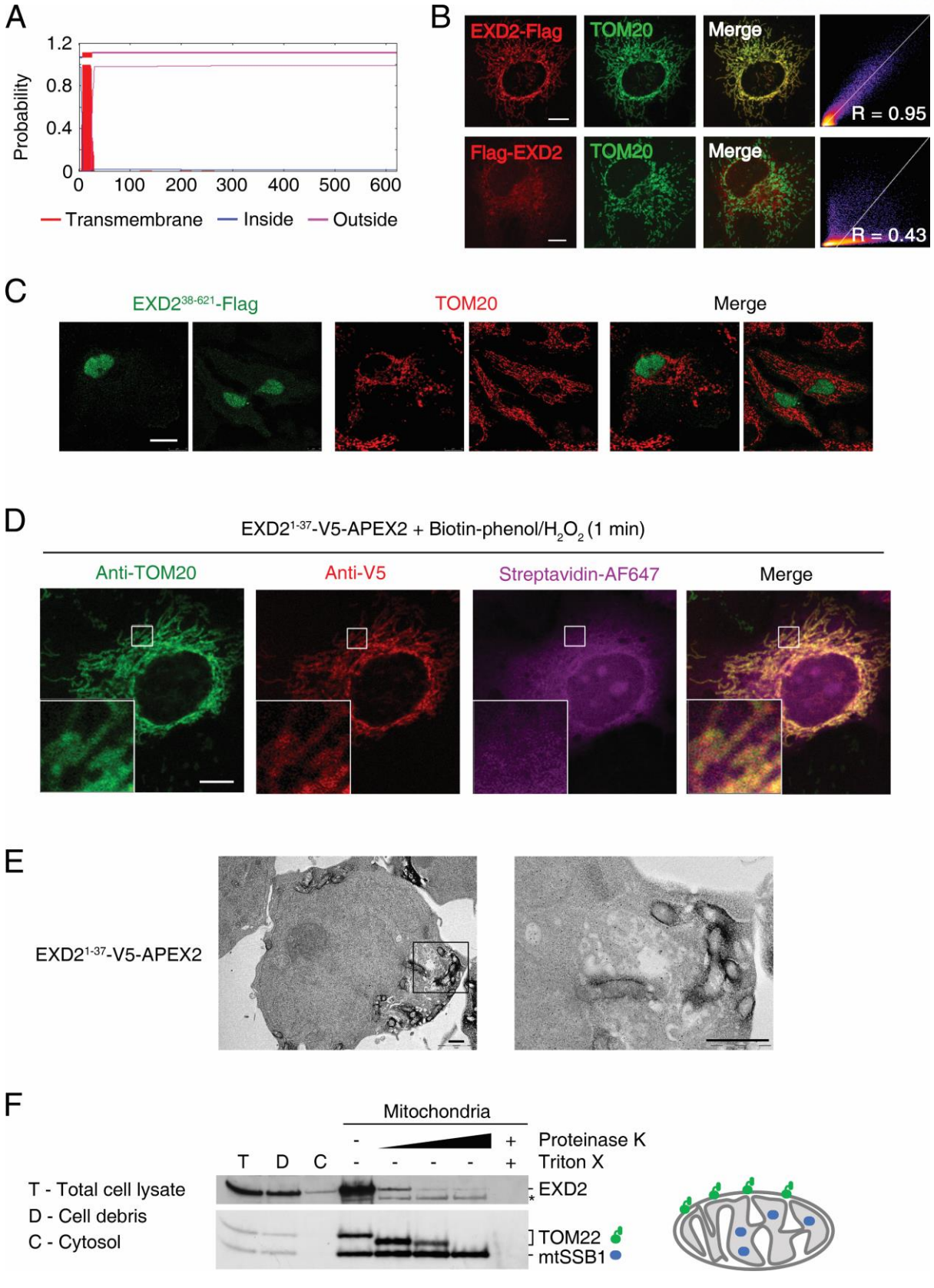

Figure 3.1. EXD2 is an outer mitochondrial membrane (OMM) protein

(A) Hydropathy plot used for EXD2 transmembrane domain prediction.

(B) Confocal imaging of EXD2-Flag and Flag-EXD2. The red channel (anti-Flag) is for analysis of the EXD2-Flag or Flag-EXD2 expression pattern, and the green channel (anti-TOM20) is a mitochondrial marker. Pearson correlation coefficient (R) = 0.95 for EXD2-Flag and 0.43 for Flag-EXD2. Scale bar = 10 μm.

(C) Fluorescence imaging of the truncated N-terminal transmembrane domain (residues 1–37) version of EXD2 ($EXD2^{38–621}$-Flag) in HeLa cells. Immunofluorescence imaging of TOM20 was used as a mitochondrial marker. Scale bar = 20 μm.

(D) Confocal microscopy imaging of $EXD2^{1–37}$-V5-APEX2 in HeLa cells. The green channel (anti-TOM20) is a mitochondrial marker, the red channel (anti-V5) is for analysis of $EXD2^{1–37}$-V5-APEX2 expression, and the magenta channel is for analysis of biotin-phenol labeling. Scale bar = 10 μm.

(E) $EXD2^{1–37}$-V5-APEX2 analysis using the APEX2-EM method. Scale bar = 1 μm.

(F) Proteinase K treatment of mitochondrial fraction of HEK293T cells. Limited proteolysis pattern of EXD2, and marker proteins TOM22 (OMM) and mtSSB1 (mitochondrial matrix) detected by western blotting. Asterisk denotes non-specific band.

Table 3.1. Details of constructs used in this study

Name (expected size)	Features	Promoter/ Vector	Details
EXD2-V5-APEX2 (101 kDa)	*KpnI*-EXD2-*NheI*-V5-APEX2-AP-Stop-*NotI*	CMV/ pcDNA5	EXD2 (NM_001193360) AP: GLNDIFEAQKIEWHE (Acceptor peptide)
$EXD2^{1–37}$-V5-APEX2 (35 kDa)	*KpnI*-$EXD2^{1–37}$-*NheI*-V5-APEX2-AP-Stop-*NotI*	CMV/ pcDNA5	$EXD2^{1–37}$: MSRQNLVALTVTTLLGVAV GGFVLWKGIQRRRRSKTS AP: GLNDIFEAQKIEWHE (Acceptor peptide)
EXD2-Flag (71 kDa)	*AflII*-EXD2-Flag-Stop-*XhoI*	CMV/ pcDNA5	EXD2 (NM_001193360) Flag: DYKDDDDK
Flag-EXD2 (71 kDa)	*AflII*-Flag-EXD2-Stop-*XhoI*	CMV/ pcDNA5	EXD2 (NM_001193360) Flag: DYKDDDDK
TOM20-pBirA-HA (53 kDa)	*KpnI*-TOM20-*BamHI*-linker-pBirA-HA-Stop-*NotI*	CMV/ pcDNA5	TOM20 (NM_014765) Linker: KDNTVPLKLIALLANGEFHSG EQLGETLG pBirA (promiscuous BirA, R118G mutant of wild-type BirA from *E. coli*) HA: YPYDVPDYA
$EXD2^{38–621}$-Flag	*AflII*-$EXD2^{38–621}$-Flag-Stop-*XhoI*	CMV/ pcDNA5	EXD2 (NM_001193360) Flag: DYKDDDDK
$EXD2^{1–295}$-Flag	*AflII*-$EXD2^{1–295}$-Flag-Stop-*XhoI*	CMV/ pcDNA5	EXD2 (NM_001193360) Flag: DYKDDDDK
$EXD2^{1–295, N198P}$-Flag	*AflII*-$EXD2^{1–295, N198P}$-Flag-Stop-*XhoI*	CMV/ pcDNA5	EXD2 (NM_001193360) Flag: DYKDDDDK
EXD2-V5-Avitag	*KpnI*-EXD2-*NheI*-V5-AP-Stop-*NotI*	CMV/ pcDNA5	EXD2 (NM_001193360) AP: GLNDIFEAQKIEWHE (Acceptor peptide)
BirA-NES	*NotI-BirA-HA-NES-Stop-XhoI*	CMV/ pcDNA3	BirA (wild-type from *E. coli*, NP_418404.1) HA: YPYDVPDYA NES: LQLPPLERLTLD

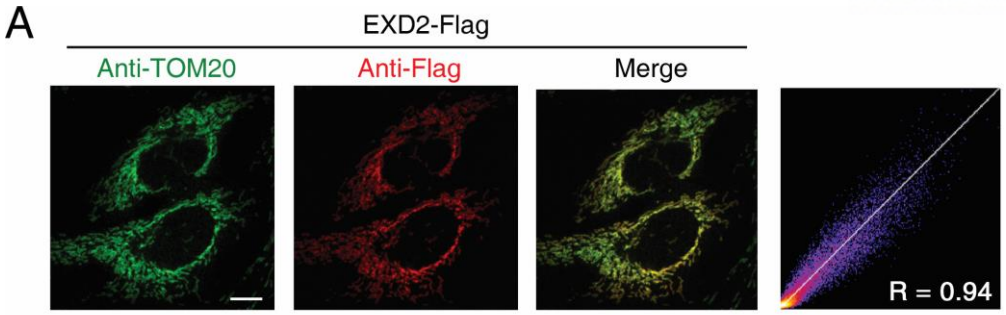

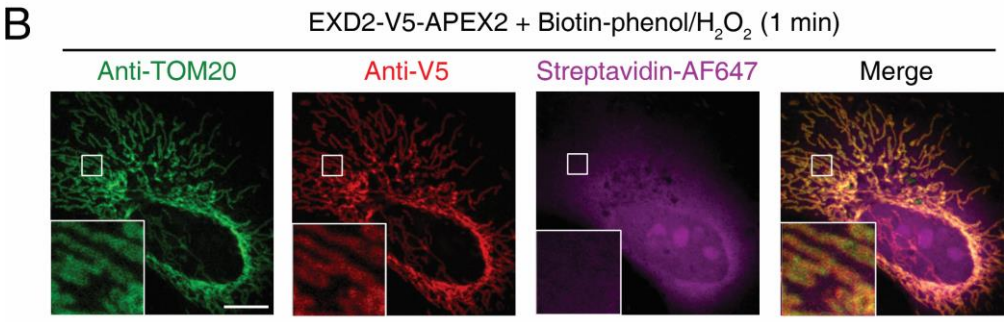

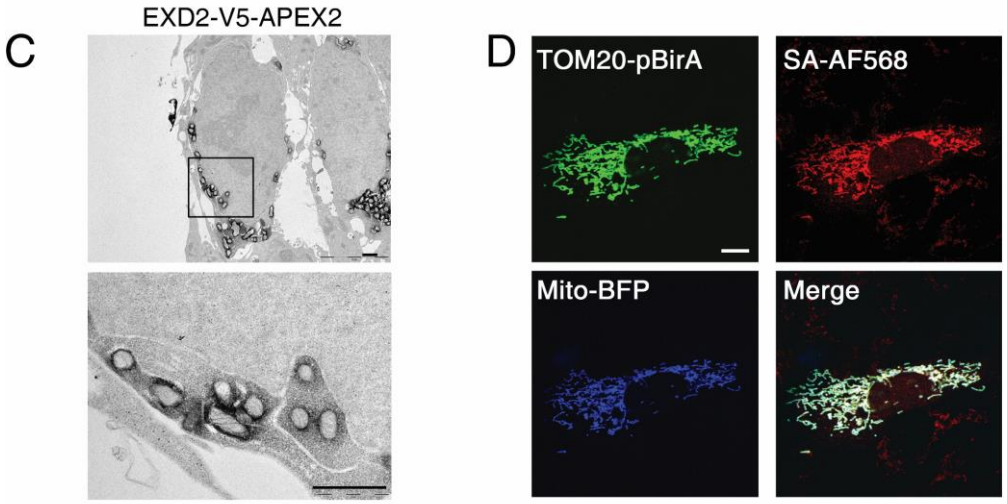

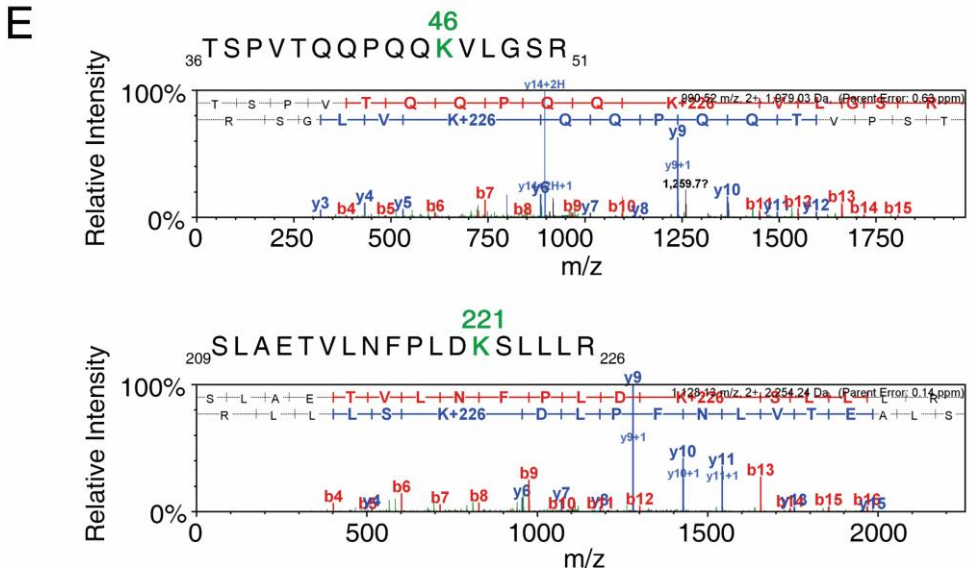

Figure 3.2. EXD2 has an N-terminal single transmembrane (TM) domain and is localized to the outer mitochondrial membrane (OMM)

(A) Confocal microscopy imaging of EXD2-Flag in HeLa cells. The green channel (anti-TOM20) is a mitochondrial marker, and the red channel (anti-Flag) is for analysis of EXD2-Flag expression. Pearson correlation coefficient (R) = 0.94; scale bar = 10 μm.

(B) Confocal microscopy imaging of EXD2-V5-APEX2 in HeLa cells. The green channel (anti-TOM20) is a mitochondrial marker, the red channel (anti-V5) is for analysis of EXD2-V5-APEX2 expression, and the magenta channel is the biotin-phenol labeling pattern; scale bar = 10 μm.

(C) Electron microscopy (EM) imaging of EXD2-V5-APEX2 using the APEX2-EM method; scale bar = 1 μm.

(D) Confocal microscopy imaging of TOM20-pBirA-HA expression in HeLa cells. The green channel (anti-HA) was used to analyze enzyme expression, the red channel (streptavidin, SA-AF568) to analyze the biotinylation pattern, and the blue channel to analyze the mitochondrial marker mito-BFP; scale bar = 10 μm.

(E) Tandem mass spectrometry (MS/MS) spectra of biotin-labeled EXD2 peptides. Biotin-labeled lysine residues are colored green.

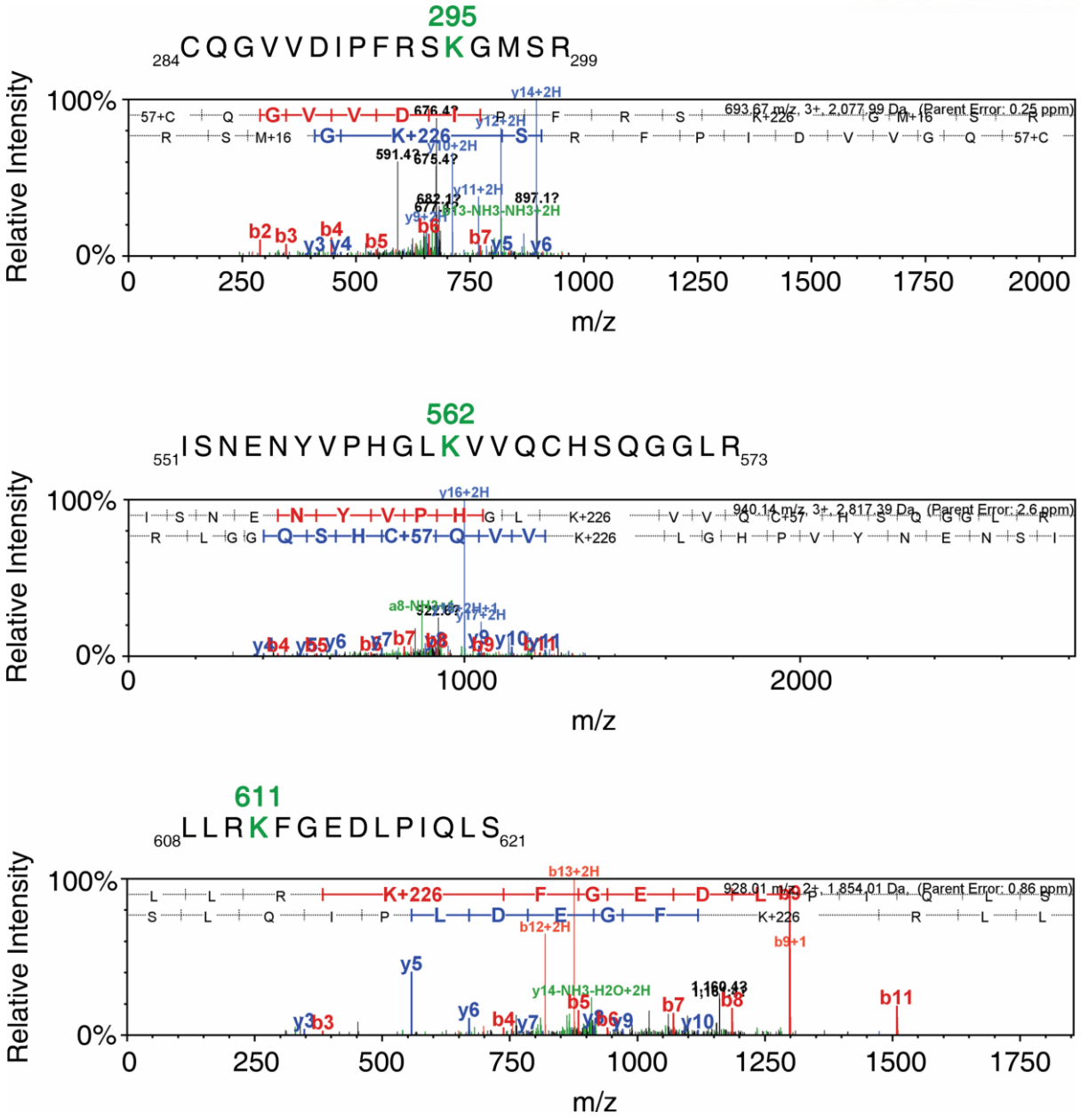

Figure 3.3. Tandem MS/MS spectra

Three MS/MS spectra of biotin-labeled peptides of EXD2 are shown. Biotin-labeled lysine residues are colored green.

3.3.2. Characterization and structure determination of EXD2

Previous biochemical studies showed that EXD2 exhibits a 3′ to 5′ exonuclease activity [1, 4]. To further characterize the exonuclease activity of EXD2 in vitro, we constructed a truncated version of EXD2 (residues 76−564, subsequently designated tEXD2; Figure 3.4A) that is reported to exhibit robust expression in vitro [1] and purified the protein to homogeneity. To test the exonuclease activity of tEXD2, single-stranded 50 nt DNA oligonucleotides labeled with 5-fluorescein amidite (5-FAM) at the 5′ end were incubated with tEXD2 for 30 min, and reaction products were separated by 15% non-denaturing TRIS/Borate/EDTA-polyacrylamide gel electrophoresis (TBE-PAGE) and subjected to fluorescence detection. Figure 3.4B shows that tEXD2 possesses 3′ to 5′ exonuclease activity. Interestingly, tEXD2 displayed metal-specific activity, with strong exonuclease activity only in the presence of Mn^{2+}, and no exonuclease activity with other divalent metal ions such as Mg^{2+}, Zn^{2+} and Ca^{2+}. From these results, we concluded that tEXD2 is a Mn^{2+}-specific 3′ to 5′ exonuclease targeting DNA substrates. Additionally, tEXD2 exhibited enzymatic activity against RNA substrates in the presence of both Mn^{2+} and Mg^{2+} ions, although activity was again stronger with Mn^{2+} ions (Figure 3.5A).

To obtain further structural insight into the metal-specific exonuclease activity of EXD2, we attempted to crystallize the human tEXD2 protein. However, despite extensive screening, we failed to grow crystals suitable for X-ray diffraction experiments. Combined limited proteolysis and sequence conservation analyses of EXD2 from various species identified a compact exonuclease domain of EXD2 comprising residues 76−295 (designated EXD2-exo; Figure 3.4A). Size exclusion chromatography (SEC) analysis revealed that recombinant EXD2-exo was present in both monomeric and dimeric forms in an ~50:50 ratio in solution (Figure 3.4C). Self-oligomerization was also apparent for tEXD2 when analyzed by SEC and analytical ultracentrifugation (AUC; Figure 3.6). Interestingly, EXD2-exo collected from the monomer fractions displayed substantially reduced exonuclease activity in the presence of Mn^{2+} ions. For RNA substrates, monomeric EXD2-exo was inactive regardless of Mn^{2+} or Mg^{2+} metal ions, whereas dimeric EXD2-exo possessed activity comparable with that of tEXD2 against both DNA and RNA substrates (Figures 3.4D and 3.5B).

We only obtained crystals of dimeric EXD2-exo, and these crystals diffracted to 1.6 Å resolution using synchrotron radiation. The crystals belong to space group $P2_12_12_1$ and contain two EXD2-exo molecules in the asymmetric unit. A molecular replacement solution was obtained using human Werner-exo (WRN-exo, PDB code: 2FBT), which shares 28% sequence identity with EXD2-exo, as a search model. Successive rounds of model building and refinement resulted in an R_{work}/R_{free} of 0.192/0.220 with good stereochemistry (Table 3.2).

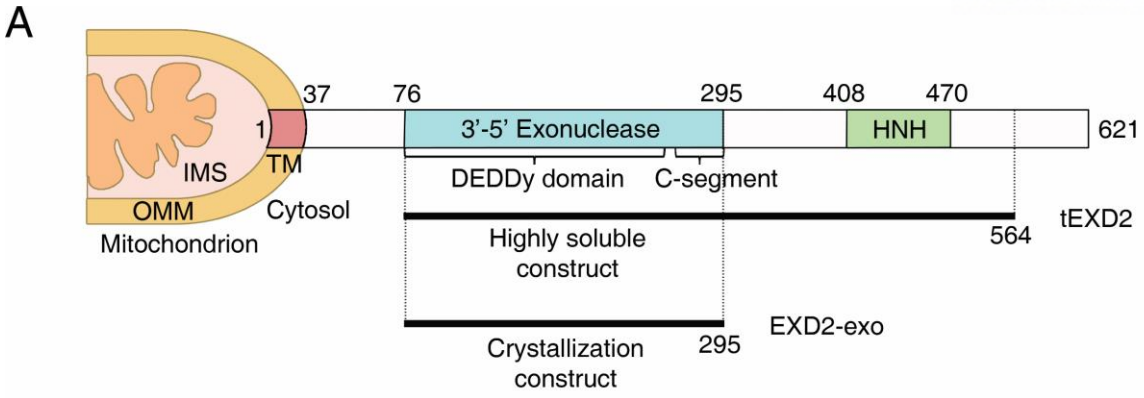

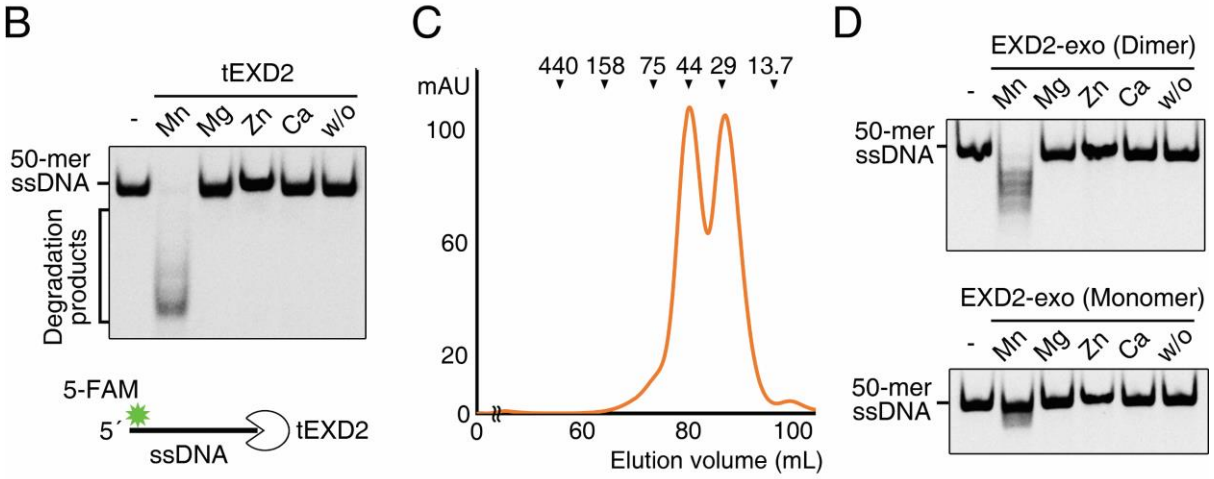

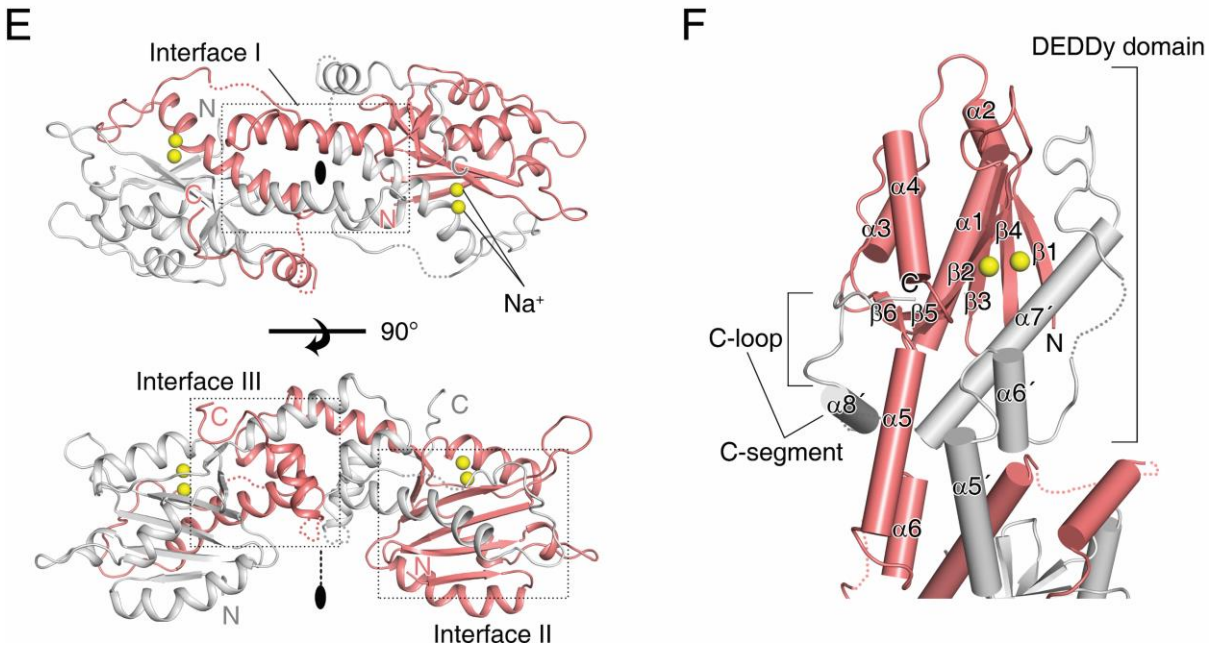

Figure 3.4. Crystal structure of EXD2-exo

(A) Schematic diagram showing the domain structure of human EXD2 and truncated constructs used in this study. Biochemical analyses revealed that EXD2 is anchored to the mitochondrial outer membrane (OMM) by a single TM domain at the N terminus. The cytoplasmic portion of EXD2 contains a 3′-5′ exonuclease domain (residues 76−295) and a predicted HNH-like domain (residues 408−470). Based on the crystal structure, the 3′-5′ exonuclease domain consists of a canonical DEDDy domain followed by an additional C-segment; IMS, mitochondrial inter-membrane space; OMM, mitochondrial outer membrane; TM, transmembrane domain.

(B) Metal cation-dependent 3′-5′ exonuclease activity of tEXD2. A 0.2 μM sample of tEXD2 was incubated with 0.25 μM 5-fluorescein amidite (FAM)-labeled 50-mer single-stranded DNA (ssDNA) for 30 min at 37°C in 20 mM HEPES-KOH pH 7.5, 50 mM KCl, 0.5 mM dithiothreitol (DTT), 0.05% Triton X-100, 0.1 mg/mL BSA, 5% glycerol, 1 mM ATP and 5 mM metal ions ($MnCl_2$, $MgCl_2$, $ZnCl_2$ or $CaCl_2$) or without metal. Non-denaturing TRIS/Borate/EDTA-polyacrylamide gel electrophoresis (TBE-PAGE) showed that tEXD2 cleaves 5-FAM-labeled ssDNA only in the presence of $MnCl_2$.

(C) Size exclusion chromatography (SEC) of EXD2-exo. EXD2-exo proteins were injected onto a Superdex 200 column (GE Healthcare) equilibrated in 25 mM TRIS-HCl, pH 7.5, 150 mM NaCl and 5 mM DTT. EXD2-exo was eluted in both dimeric and monomeric forms at an ~50:50 ratio. Protein standards are shown above the chromatogram curves to compare the relative molecular mass (ferritin, 440 kDa; aldolase, 158 kDa; conalbumin, 75 kDa; ovalbumin, 44 kDa; carbonic anhydrase, 29 kDa; ribonuclease A, 13.7 kDa).

(D) Metal cation-dependent 3′-5′ exonuclease activity of EXD2-exo. A 1.5 μM sample of each protein was mixed with 0.25 μM 5-FAM-labeled 50-mer ssDNA under the same conditions as in (B).

(E) Overall structure of EXD2-exo in the crystallographic asymmetric unit. EXD2-exo forms a dimer through 2-fold rotational symmetry. Protomers are colored red and gray. The crystal structure was determined by molecular replacement (MR) and refined to 1.6 Å resolution (Table 3.2). Three dimeric interfaces are highlighted with black dotted boxes (see also Figure 3.9 for details). Yellow spheres indicate sodium ions bound to the active sites of EXD2-exo.

(F) Ribbon diagram showing the DEDDy exonuclease domain of EXD2-exo. The EXD2-exo protomer consists of six β-strands and eight α-helices. The catalytic site of EXD2-exo is formed by the association of a central domain comprising β1−β6 and α1−α5 of one EXD2-exo molecule, and α6′−α7′ from the other molecule in the EXD2-exo dimer. A chimeric active site is formed by crossing over of the extended α5 helices between the two protomers of the dimer. The C-segments comprising swapped α8 helices and a well-ordered loop (C-loop, residues 285−294) enclose the exonuclease domain and stabilize the overall structure. All disordered regions are indicated by dotted lines.

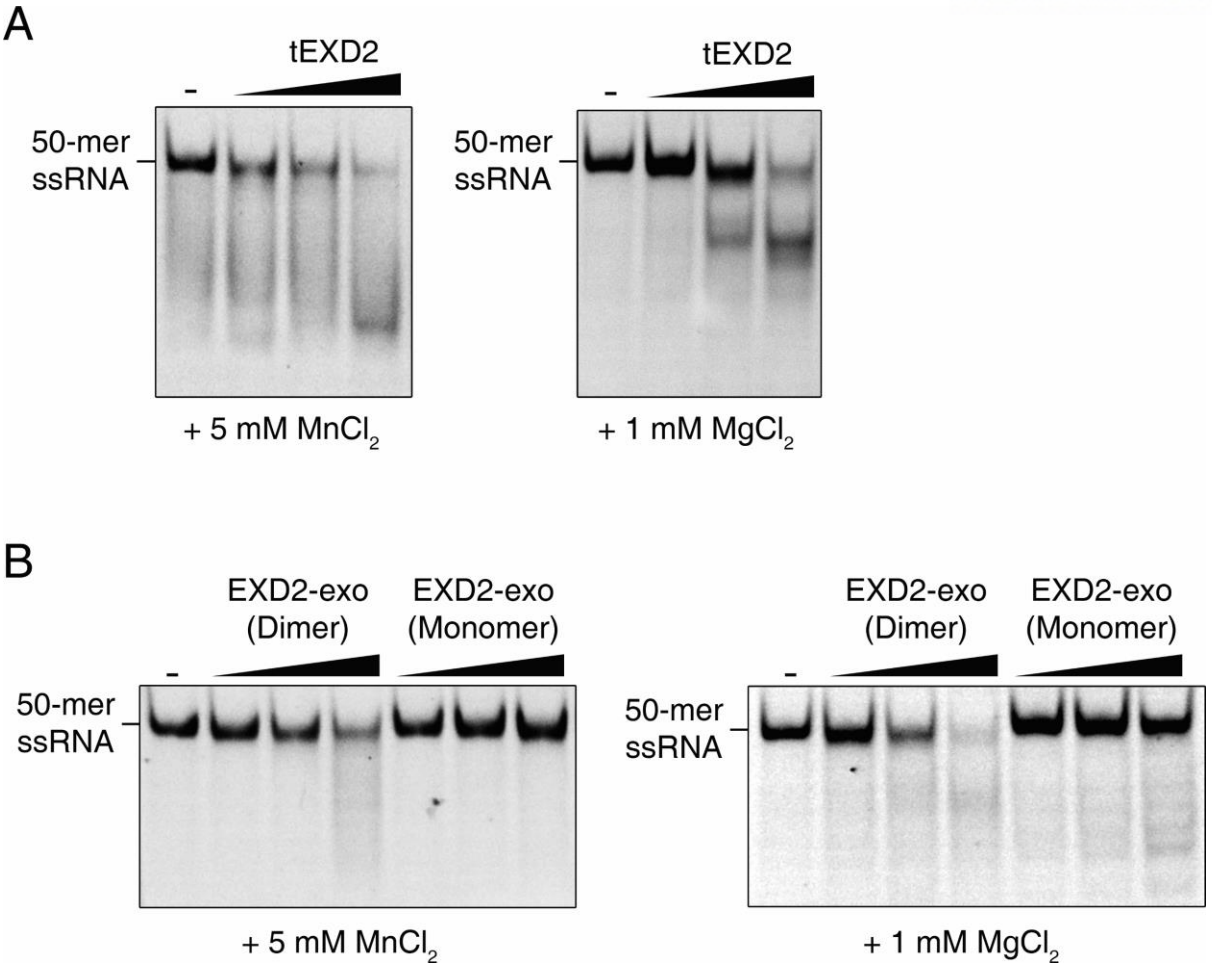

Figure 3.5. EXD2 cleaves ssRNA

Non-denaturing TBE-PAGE showing that EXD2 cleaves 5-FAM-labeled ssRNA in the presence of both $MnCl_2$ and $MgCl_2$.

(A) 0.05–0.2 μM or 0.5–1.5 μM tEXD2 was incubated with 0.25 μM 5-FAM-labeled 50-mer ssRNA with 5 mM $MnCl_2$ or 1 mM $MgCl_2$.

(B) 0.5–2 μM or 20–60 μM EXD2-exo was incubated with 0.25 μM 5-FAM-labeled 50-mer ssRNA with 5 mM $MnCl_2$ or 1 mM $MgCl_2$.

This experiment was performed and analyzed as described in Figure 3.4B except that RNA was used as substrate.

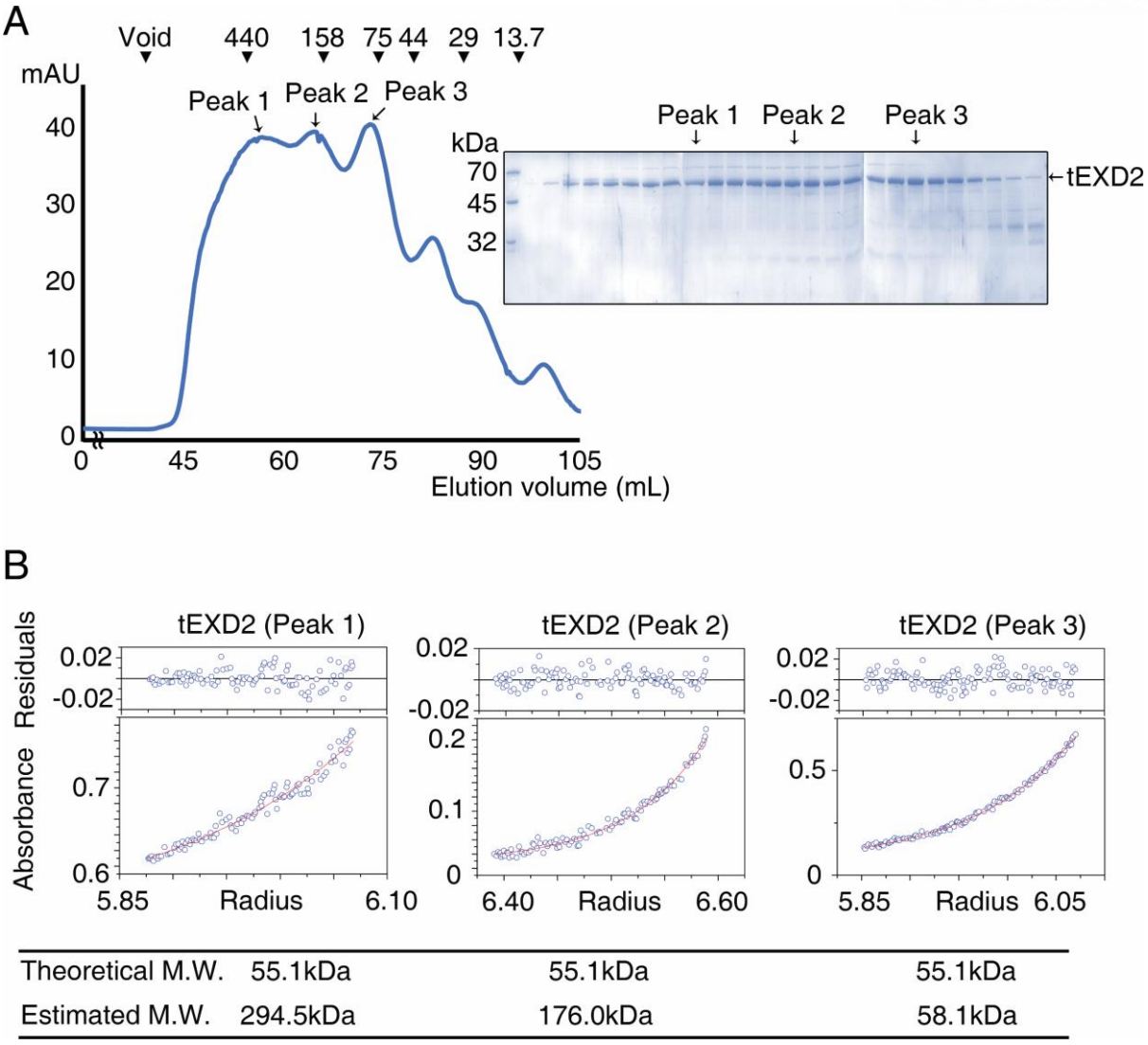

Theoretical M.W.	55.1kDa	55.1kDa	55.1kDa
Estimated M.W.	294.5kDa	176.0kDa	58.1kDa

Figure 3.6. Analysis of tEXD2 oligomerization in solution by SEC and AUC

(A) Elution profile of size exclusion chromatography (SEC) of tEXD2. 15 mg/mL tEXD2 was injected onto a Superdex 200 column (GE Healthcare Life Sciences) equilibrated with buffer consisting of 25 mM TRIS-HCl pH 7.5, 150 mM NaCl, and 5 mM DTT. Fractionated samples of each peak were analyzed by 12% sodium dodecyl sulfate-polyacrylamide gel electrophoresis (SDS-PAGE) and gel was stained with Coomassie blue. Protein standards are shown above the chromatogram curves to compare the relative molecular mass (blue dextran 2000, Void; ferritin, 440 kDa; aldolase, 158 kDa; conalbumin, 75 kDa; ovalbumin, 44 kDa; carbonic anhydrase, 29 kDa; ribonuclease A, 13.7 kDa).

(B) Molecular weights of each peak of tEXD2 in SEC were analyzed by analytical ultracentrifugation (AUC). The bottom panel shows a representative plot of the absorbance profile, and the top panel indicates the residuals between the experimental data and the fitted line. The results are summarized on the bottom table. M.W.; molecular weight.

Table 3.2. X-ray diffraction data collection and refinement statistics

Dataset	Native	Mn^{2+}	Mg^{2+}	Mn^{2+}+Mg^{2+}
PDB ID code	6K17	6K18	6K19	6K1A
X-ray source	Beamline 5C, PAL	Beamline 5C, PAL	Beamline 5C, PAL	Beamline 5C, PAL
Temperature (K)	100	100	100	100
Space group	$P2_12_12_1$	$P2_12_12_1$	$P2_12_12_1$	$P2_12_12_1$
Cell dimensions				
a, b, c (Å)	45.955, 72.607, 135.670	46.217, 73.866, 131.683	46.347, 74.107, 133.477	46.324, 73.664, 131.423
α, β, γ (°)	90, 90, 90	90, 90, 90	90, 90, 90	90, 90, 90
Data processing				
Wavelength (Å)	0.97940	0.97950	0.97950	0.97960
Resolution (Å)	50.0–1.6 (1.63–1.60)	50.0–2.3 (2.34–2.30)	50.0–2.2 (2.24–2.20)	50.0–2.6 (2.64–2.60)
R_{merge} (%)	12.7 (71.5)	10.3 (34.8)	10.0 (35.9)	11.5 (49.2)
I/σ (I)	22.54 (2.16)	12.35 (2.08)	16.35 (1.83)	12.73 (2.06)
Completeness (%)	99.5 (99.5)	98.3 (96.4)	98.1 (94.5)	99.3 (98.0)
Redundancy	5.2 (5.2)	5.2 (4.1)	4.8 (3.1)	3.9 (3.6)
No. of reflections	312,945	105,655	111,177	55,265
No. of unique reflections	60,416	20,317	23,379	14,310
Refinement				
Resolution (Å)	37.3–1.6	43.61–2.3	39.30–2.2	39.22–2.6
No. of reflections	60,315	20,284	23,307	14,262
R_{work}/R_{free} (%)	19.19/21.95	21.05/27.13	19.92/25.15	22.29/25.95
No. of atoms				
Protein	3,069	3,069	3,001	3,037
Ions	4 (Na)	2 (Mn)	2 (Mg)	2 (Mn), 2 (Mg)
Water	593	223	180	88
RMSD				
Bond lengths (Å)	0.010	0.003	0.007	0.004
Bond angles (°)	1.283	0.645	1.070	0.967
B-factors ($Å^2$)				
Protein	20.76	37.85	47.96	54.56
Ions	28.68	34.63	72.47	56.03 (Mn), 72.94 (Mg)
Water	34.42	40.65	50.23	50.39

Dataset	Mn^{2+} soaked with dGMP	Mg^{2+} soaked with dGMP	Mn^{2+} soaked with GMP	Mg^{2+} soaked with GMP
PDB ID code	6K1B	6K1C	6K1D	6K1E
X-ray source	Beamline 5C, PAL	Beamline 5C, PAL	Beamline 11C, PAL	Beamline 11C, PAL
Temperature (K)	100	100	100	100
Space group	$P2_12_12_1$	$P2_12_12_1$	$P2_12_12_1$	$P2_12_12_1$
Cell dimensions				
a, b, c (Å)	46.339, 73.571, 131.951	46.304, 73.989, 133.580	46.528, 73.931, 132.543	46.496, 73.288, 134.086
α, β, γ (°)	90, 90, 90	90, 90, 90	90, 90, 90	90, 90, 90
Data processing				
Wavelength (Å)	0.97960	0.97950	0.97936	0.97936
Resolution (Å)	50.0–2.6 (2.64–2.60)	50.0–2.45 (2.49–2.45)	50.0–3.0 (3.05–3.00)	50.0–2.9 (2.95–2.90)
R_{merge} (%)	13.0 (56.7)	10.1 (53.2)	14.5 (48.0)	10.9 (34.3)
I/σ (I)	17.81 (2.39)	16.19 (2.18)	12.90 (2.02)	13.54 (1.77)
Completeness (%)	99.2 (98.4)	99.9 (99.9)	95.7 (98.5)	96.6 (92.7)
Redundancy	6.2 (5.2)	4.6 (4.8)	5.7 (5.3)	3.9 (2.9)
No. of reflections	88,304	81,786	53,312	40,686
No. of unique reflections	14,231	17,599	9,290	10,440
Refinement				
Resolution (Å)	28.81–2.6	38.15–2.45	49.35–3.0	49.47–2.9
No. of reflections	14,194	17,537	9270	10,406
R_{work}/R_{free} (%)	21.69/27.47	21.38/27.59	21.21/27.71	22.79/26.84
No. of atoms				
Protein	2,990	3,000	2,980	3,043
Ions	4 (Mn)	2 (Mg)	4 (Mn)	4 (Mg)
Water	105	144	18	22
RMSD				
Bond lengths (Å)	0.004	0.004	0.010	0.005
Bond angles (°)	0.804	0.917	1.369	1.051
B-factors ($Å^2$)				
Protein	50.72	55.72	70.05	67.66
Ions	48.61	59.57	63.64	51.29
Water	48.53	53.74	63.34	48.99

*Values in parentheses are for the highest resolution shell. PAL, Pohang Accelerator Laboratory.

3.3.3. Structure of EXD2-exo

Consistent with the biochemical analyses, EXD2-exo forms a dimer with overall dimensions of ~91.0 × 42.7 × 39.3 Å, in which two molecules are arranged with a 2-fold rotational symmetry around the axis perpendicular to the plane (Figure 3.4E). No discernible differences were found in the two molecules, which have a root-mean square deviation (RMSD) of ~0.253 Å for all Cα atoms. Each molecule consists of eight α-helices (α1−α8) and a six-stranded (β1−β6) β-sheet that folds into a canonical DnaQ-like exonuclease domain and contains two active site Na+ ions, neither of which supports nuclease activity (Figures 3.4 E and F, and 3.7). Surprisingly, the α5−α7 helices are exchanged between molecules in the EXD2-exo dimer, resulting in a domain-swapped structure. Most interestingly, both exchanged α7 helices play a pivotal role in completing the exonuclease active sites in the opposing molecule in the EXD2-exo dimer. This unexpected structural perspective revealed why the exonuclease activity was significantly reduced in the EXD2-exo monomer (Figure 3.4D). This unusual conformation is a novel feature that is absent in other DnaQ family exonucleases. Although the structure of the EXD2-exo monomer itself cannot be exclusively superimposed with the exonuclease domains of DnaQ family proteins (RMSD > 3.0 Å), each complete composite monomeric exonuclease domain present in the EXD2-exo dimer strongly resembles the exonuclease domains of WRN, Klenow fragment (KF) and Ribonuclease D (Rnase D), with RMSD values for all Cα atoms of 1.035, 2.273 and 2.212 Å, respectively (Figures 3.8 and 3.10B).

The crystal structure revealed that three direct interfaces are involved in the self-association of EXD2-exo, resulting in a buried surface area of 4024 $Å^2$ (Figures 3.4E and 3.9). The first interface is generated by a 2-fold arrangement of helices α5−α7 in the EXD2-exo dimer. In particular, helices α5 and α5′ from opposing molecules are organized in an antiparallel fashion, resulting in the formation of a coiled coil-like dimer (Figures 3.4E and 3.9, top). In addition, helix α5 also contacts both helix α6′ and the C terminus of helix α7′ in a parallel fashion behind the α5–α5′ interface (Figure 3.9, top left). Notably, the C-terminal ends of helices α7 and α7′ face each other, generating a precise 2-fold center in which the side chains of the two His256 residues are stacked side by side (Figure 3.9, top right). The second interface is formed by an extensive contact between the exchanged loop (residues 227−237) followed by helix α7 (residues 238−260) and the central β-sheet of the active site in the opposing molecule, as described above (Figures 3.4E and 3.9, bottom left). In the third interface, the C-terminal fragment of EXD2-exo (designated as the C-segment) plays a critical role in the interaction, supporting structural integrity (Figures 3.4E and 3.9, bottom right). The active exonuclease domain of WRN-exo ends at residue 230, at the C-terminal end of helix α7 [9], whereas the equivalent helix α7 in EXD2-exo is followed by a flexible loop (residues 261−274) that is disordered, and this in turn is followed by the short helix α8 (residues 275−284) and a well-ordered

loop (C-loop) comprising residues 285−294 (Figures 3.4 E and F, and 3.9, bottom right). Surprisingly, the two additional C-segments mutually enclose each other in the EXD2-exo dimer, and this clearly stabilizes the dimeric organization and assists the formation of stable active sites. In particular, the α8 helix associates with the C terminus of α1′and α6′ and α5′ of the opposing molecule in the dimer (Figures 3.4F and 3.9, bottom right).

Residues 219−222 from the loop connecting helices α6 and α7, and residues 261–274 predicted to form an extended loop, are disordered in the structure. As discussed below, these apparently flexible regions might facilitate the binding of substrates and regulation of activity, respectively.

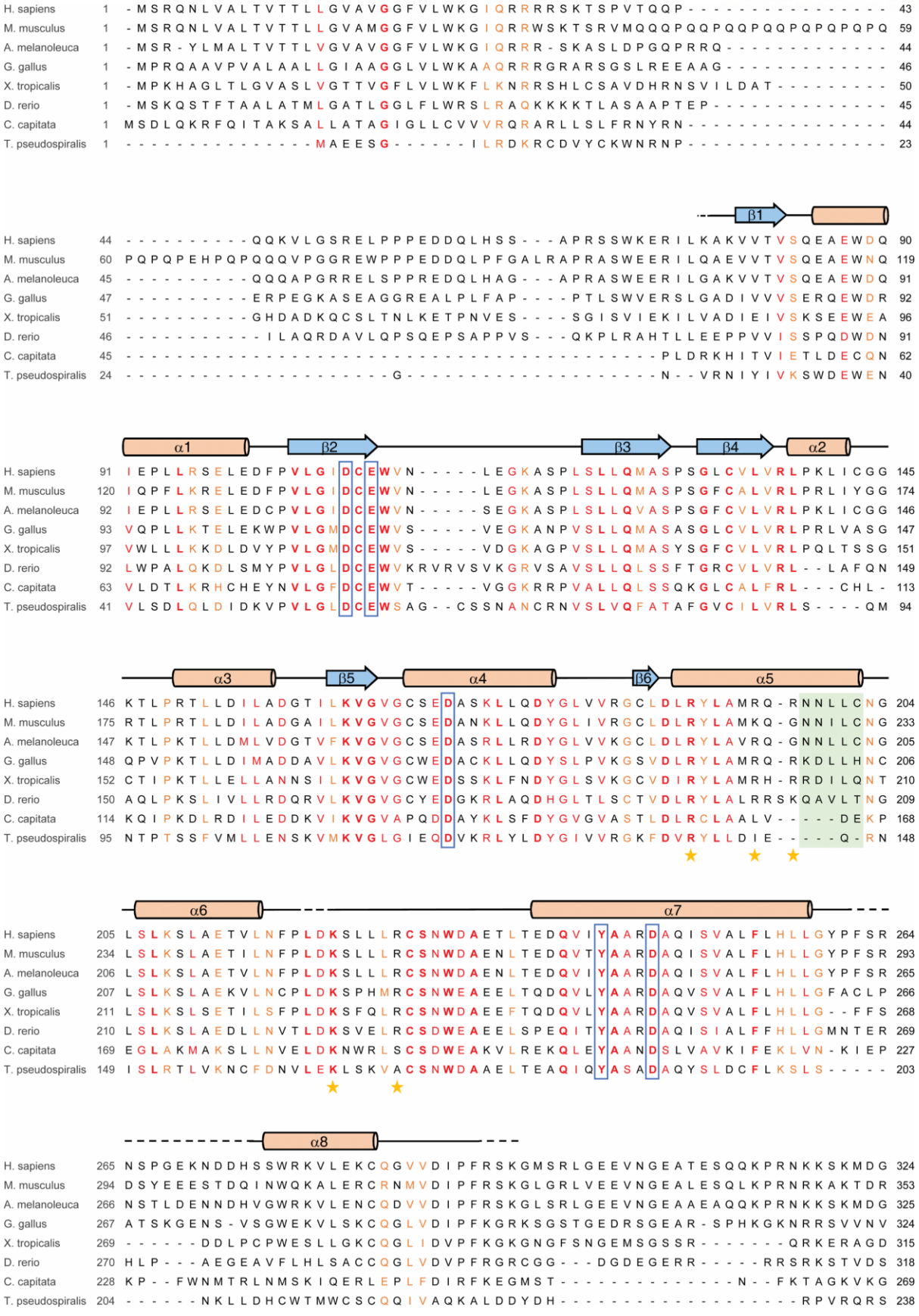

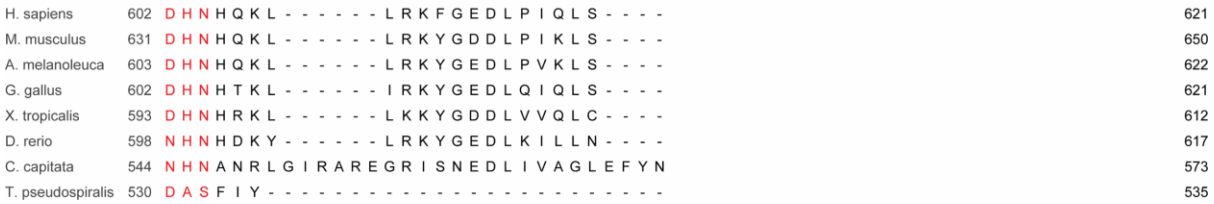

Figure 3.7. Sequence alignment of EXD2 from eight species

Sequence alignment of full-length EXD2 orthologs. Absolutely conserved, highly similar, and similar sequences are highlighted in bold red, red, and orange, respectively. Secondary structure elements of EXD2-exo, based on the crystal structure, are shown above the sequences, with yellow cylinders (α-helices), blue arrows(β-strands), black lines (loops), and black dotted lines (disordered regions). Active site residues involved in metal ion coordination and residues potentially contacting the substrate are indicated by blue boxes and yellow stars, respectively. The extended sequence of helix α5 involved in inducing self-association is indicated by a green box. UniProt entries of EXD2 used for sequence alignment are as follows: *Homo sapiens* (Q9NVH0), *Mus musculus* (Q8VEG4), *Ailuropoda melanoleuca* (D2H5Q3), *Gallus gallus* (E1BXG2), *Xenopus tropicalis* (Q05AQ5), *Danio rerio* (F1QBW6), *Ceratitis capitata* (W8BM66), and *Trichinella pseudospiralis* (A0A0V1G6E7).

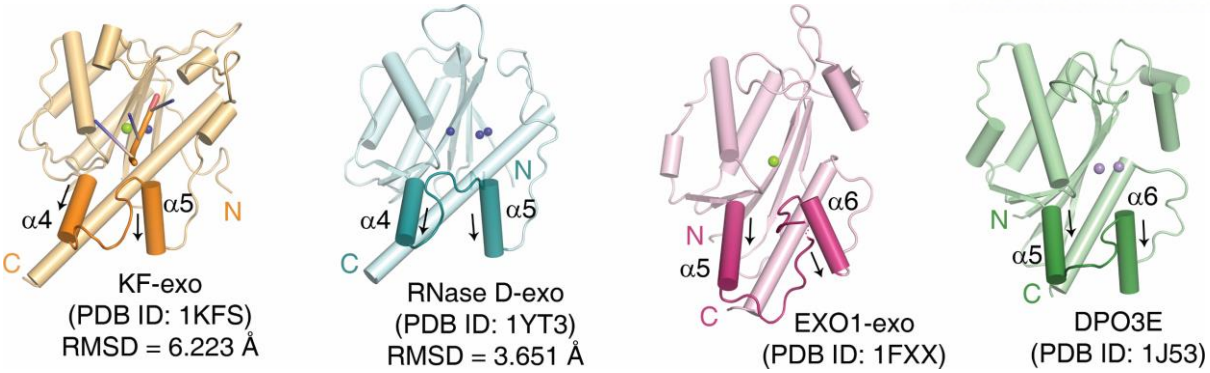

Figure 3.8. Structural comparison of EXD2 with other DnaQ exonucleases

Overall structures of KF-exo, RNase D-exo, EXO1-exo, and DPO3E are shown in the same orientation as in Figure 3.10B to compare the structure of EXD2 with those of other DnaQ exonucleases. In contrast to EXD2, helices α4 (α5 in EXO1 and DPO3E) and α5 (α6 in EXO1 and DPO3E) are organized in a parallel fashion (see arrows). In KF-exo, the trinucleotide bound to the enzyme is shown in cartoon representation. Mg^{2+}, Zn^{2+}, and Mn^{2+} ions are represented by green, deep blue, and purple spheres, respectively.

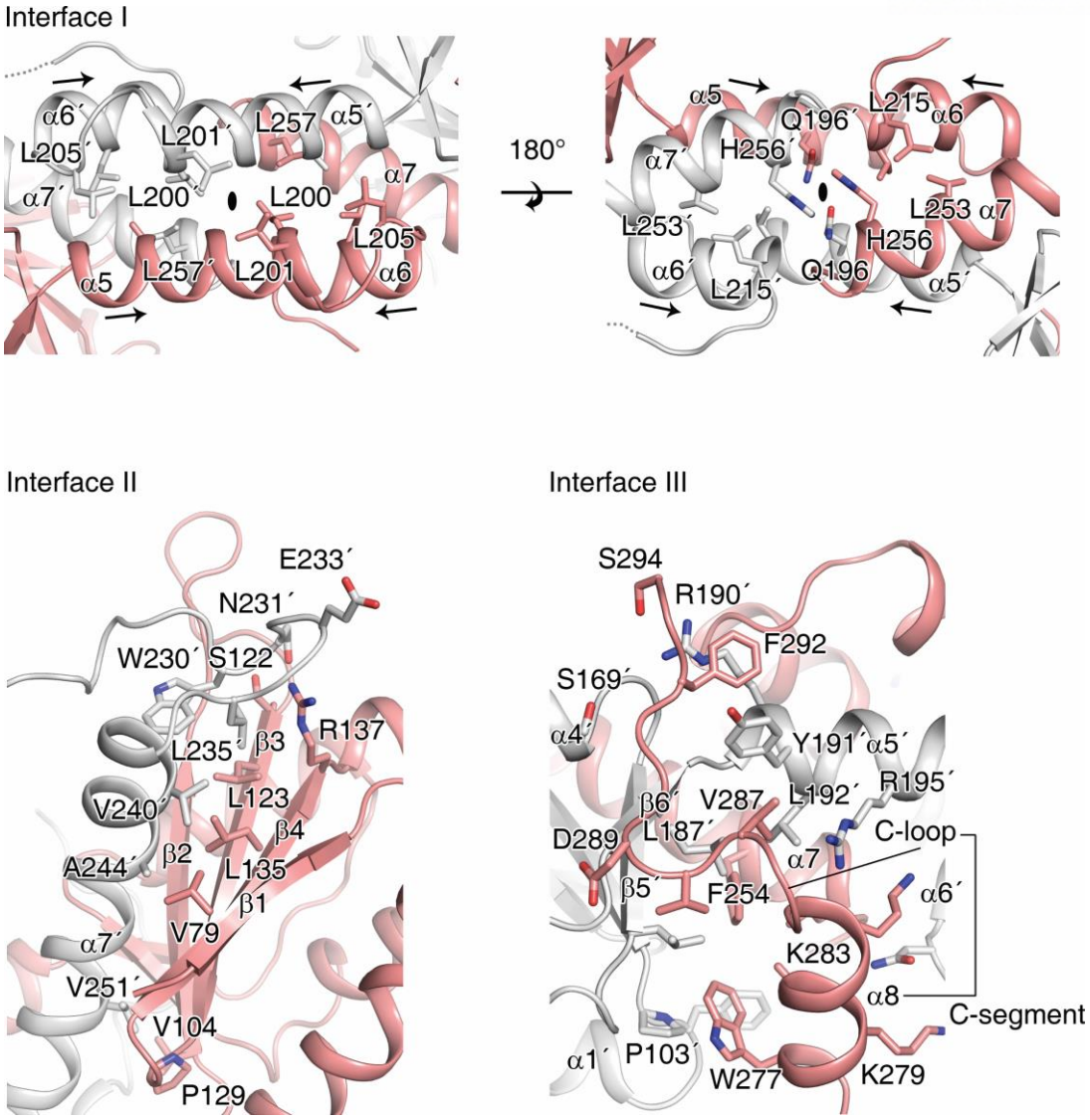

Figure 3.9. Dimeric interface of EXD2-exo

The ribbon diagrams show the dimeric interfaces of EXD2-exo. The arrow indicates the direction of helices. Key residues involved in the interaction are shown in ball-and-stick representation. Oxygen and nitrogen atoms are colored red and blue, respectively.

3.3.4. Extended helix α5 of EXD2-exo confers a domain-swapped structure

Sequence alignment of EXD2-exo with DnaQ family exonucleases including WRN, KF, RNase D, Exonuclease 1 (EXO1) and DNA polymerase III subunit epsilon (DPO3E) revealed that helix α5 of EXD2 is extended by five more residues ($_{198}$NNLLC$_{202}$) than in other compared exonucleases (Figure 3.10A) [9, 15-18]. This extended sequence is conserved in all EXD2 family members above metazoan species, suggesting that self-association through helix α5 might be evolutionally conserved and structurally important for EXD2 function (Figure 3.7). The extended helix α5 clearly affects the overall conformation, and likely induces domain-swapped dimerization in EXD2-exo. Helices α5 and α6 of EXD2-exo are organized in an antiparallel manner, unlike the equivalent helices in other DnaQ family exonucleases, which are arranged in parallel pairs (Figures 3.8 and 3.10 B and C). Helices α6′ and α7′ from the opposing molecule in the EXD2-exo dimer can be perfectly superimposed with helices α5 and α7 of WRN-exo, suggesting that the dimeric configuration of EXD2-exo might not affect exonuclease activity (Figure 3.10C).

To examine the role of the α5 helix in dimer formation, we performed mutagenesis to disrupt the conformation of helix α5. Figure 3.10D shows that both single point (N198P) and deletion (residues Δ198−201) mutants of EXD2-exo eluted from the SEC column only as monomers, suggesting that the extended helix α5 is important for forming a domain-swapped dimer, as would be expected based on the crystal structure. We further tested if the mutants retained the ability to digest DNA, and observed that both mutants impaired exonuclease activity (Figure 3.10E). This result suggests that the formation of a swapped dimer is required for the catalytic activity of EXD2-exo.

Next, we examined whether full-length EXD2 also self-associates in live cells using pull-down assays (Figure 3.10F). For this experiment, we prepared mammalian expression constructs for EXD2$^{1–621}$ (full EXD2 sequence)-V5-Avitag (AP) and EXD2$^{1–621}$-Flag constructs. These constructs were coexpressed in HEK293 cells, and cytosol-targeted bacterial biotin ligase (BirA-NES) was also recombinantly expressed in the same cells for the selective biotinylation of Avitag of EXD2$^{1–621}$-V5-AP for streptavidin (SA)-bead pull-down (Figure 3.10F, left) [19]. After biotinylation following addition of biotin (10 μM) overnight, cells were lysed and biotinylated EXD2$^{1–621}$-V5-AP was collected using SA-coated magnetic beads. Subsequent western blotting of anti-V5 revealed that enrichment of biotinylated EXD2$^{1–621}$-V5-AP was achieved using the SA-beads (Figure 3.10F, right, anti-V5 WB), and EXD2$^{1–621}$-Flag was also enriched using SA-beads bound to EXD2$^{1–621}$-V5-AP (Figure 3.10F, right, sample 1, anti-Flag WB). We also checked that EXD2$^{1–295}$-Flag, which contains the sequence of EXD2 from the N-terminal TM domain to the exonuclease domain, was also coenriched with pulled-down EXD2$^{1–621}$-V5-AP (Figure 3.10F, right, sample 2, anti-Flag WB).

However, in the same conditions, the enrichment level was significantly compromised for the N198P single point EXD2$^{1–295}$ mutant (EXD2$^{1–295, N198P}$-Flag), which was shown to be eluted exclusively as a monomer in SEC experiments (Figure 3.10F, right, sample 3, anti-Flag WB). We confirmed that the coenrichment of Flag-tagged protein did not occur in negative control experiments lacking expression of the bait protein EXD2$^{1–621}$-V5-AP (Figure 3.10F, right, sample 4−6, anti-Flag WB). This result implies that the fully functionalized exonuclease domain of EXD2 forms a homodimer in live mammalian cells.

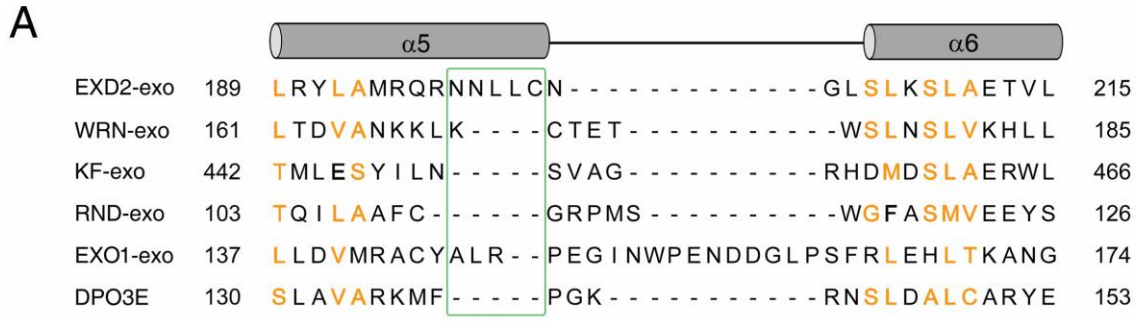

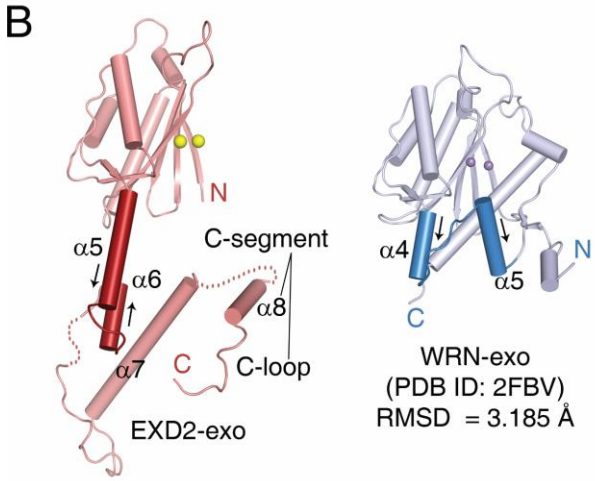

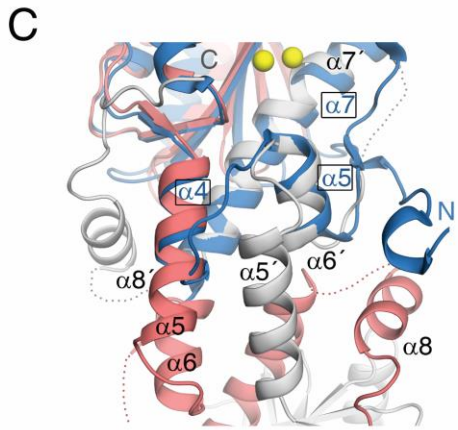

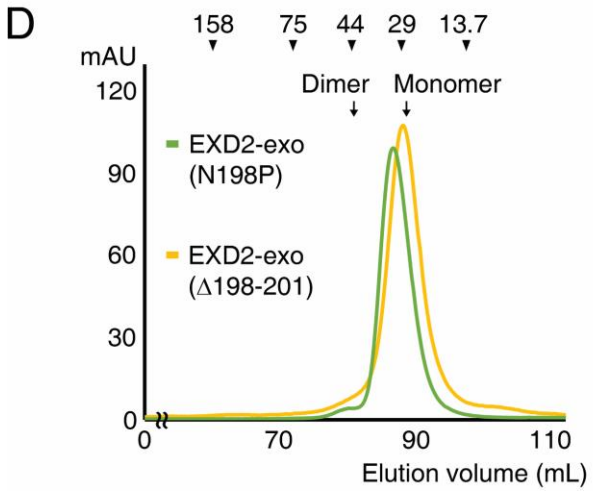

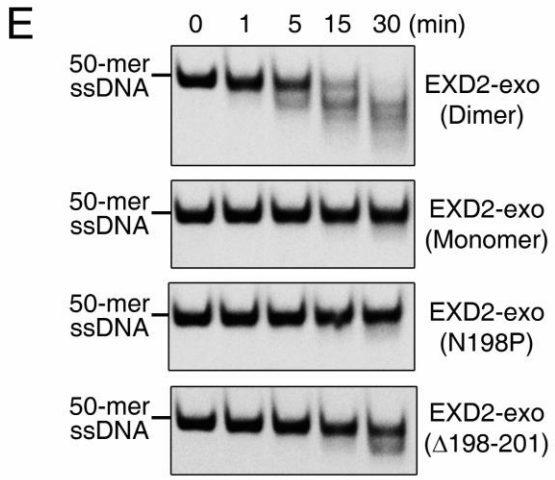

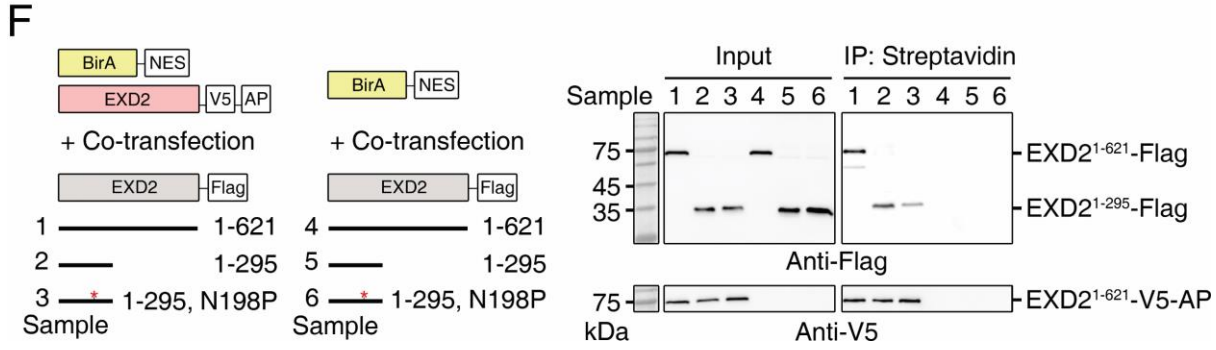

Figure 3.10. The extended α5 helix stabilizes a novel dimeric conformation in EXD2-exo

(A) Structure-based sequence alignment of helices α5 and α6 of human EXD2 and equivalent helices in other DnaQ family exonucleases including Werner syndrome ATP-dependent helicase (WRN, PDB code: 2FBT), DNA polymerase I Klenow fragment (KF, PDB code: 1KFS), ribonuclease D (RND, PDB code: 1YT3), exonuclease 1 (EXO1, PDB code: 1FXX) and DNA polymerase III subunit epsilon (DPO3E, PDB code: 1J53). Sequence alignment reveals that the α5 helix is extended by five additional residues in EXD2 compared with other exonucleases (highlighted in the green box). Conserved residues are colored orange.

(B) Structural comparison of EXD2-exo (red) and WRN-exo (blue) in ribbon representation positioned in the same orientation. Helices α4 and α5 of WRN-exo are arranged in a parallel manner (see arrows), but the equivalent helices (α5 and α6) in EXD2-exo are organized in an antiparallel fashion, resulting in significant conformational changes between helix α6 and the C terminus (swapped in the EXD2-exo dimer; see also Figure 3.8).

(C) Close-up view of the structural superimposition of EXD2-exo and WRN-exo. To highlight the roles of helices α5−α7 of EXD2 in dimerization and formation of the active site, the structure of the composite exonuclease domain of EXD2 (red and gray) formed by domain swapping is aligned with the WRN-exo monomer (blue). Helices of WRN-exo are labeled in black boxes.

(D) SEC chromatogram of EXD2-exo mutants N198P and Δ198−201. The experimental details are the same as in Figure 3.4C.

(E) Time-dependent exonuclease activity of EXD2 mutants N198P and Δ198−201. A 1.5 μM sample of mutant protein was incubated with 0.25 μM 5-FAM-labeled 50-mer ssDNA for 1, 5, 15, or 30 min at 37°C and analyzed by non-denaturing TBE-PAGE.

(F) EXD2 self-association assay in live cells. To analyze whether the full-length and exonuclease domain of EXD2 can physically associate in full-length EXD2 in vivo, full-length human EXD2-V5-Avitag (AP) was cotransfected with Flag-tagged full-length EXD2 ($EXD2^{1-621}$-Flag) or exonuclease domain of EXD2 ($EXD2^{1-295}$-Flag) in HEK293 cells (left, samples 1 and 2). The Avitag of EXD2-V5-AP can be biotinylated by cotransfection with BirA-NES (cytosol) for pull-down assays using SA-beads. Mutant version of the exonuclease domain ($EXD2^{1-295,\ N198P}$-Flag) was used as control (left, sample 3). As negative controls, the bait protein $EXD2^{1-621}$-V5-AP was omitted (left, samples 4, 5 and 6). Input is the crude sample before addition to SA-beads (right).

3.3.5. The EXD2-exo active site

Like other DEDDy superfamily exonucleases, EXD2-exo has two metal ions at the active site (Figure 3.11A, site A is referred to as [M_A] and site B is referred to as [M_B] in the crystal structure of EXD2-exo) [9]. Although the crystallization solution contained 200 mM calcium acetate, sodium rather than calcium was bound to EXD2-exo, suggesting that Ca^{2+} is not a genuine ion supporting activity in EXD2-exo (Figures 3.11A and 3.12A). Indeed, EXD2 was inactive in the presence of calcium (Figure 3.4 B and D). Consistent with other DEDDy exonucleases, two metal ions are coordinated by the catalytic core residues Asp108, Glu110, Asp171, Tyr242 and Asp246 (Figures 3.11A and 3.12A). Among these, Tyr242 and Asp246 are from helix α7′ of the opposing molecule in the EXD2-exo dimer, as described above.

To further examine whether the metal specificity and activity of EXD2 may be related to the structure of the active site, we determined crystal structures of EXD2-exo in complex with Mn^{2+}, Mg^{2+}, (d)GMP plus Mn^{2+} or (d)GMP plus Mg^{2+} (Figures 3.11 B−H and 3.12 B−H). The Mn^{2+} ion was found only in site M_A in the absence of dGMP, which is a mimic for the exonuclease product of DNA (Figure 3.11B). However, two Mn^{2+} ions were distinctly observed at both M_A and M_B sites in the presence of dGMP, although electron density representing dGMP was disordered in the structure (Figure 3.11D). Interestingly, Mg^{2+} ions were only found at site M_B regardless of the presence of dGMP (Figure 3.11 C and E). The M_A site is occupied by two H_2O molecules when EXD2-exo is incubated with Mg^{2+} alone, while no ions (except for a single H_2O molecule) were observed at the M_A site when EXD2-exo was mixed with both Mg^{2+} and dGMP (Figure 3.11 C and E). Moreover, when crystals are soaked in a solution containing both Mn^{2+} and Mg^{2+}, Mn^{2+} and Mg^{2+} ions are separately coordinated at only the M_A and M_B sites, respectively (Figure 3.11F). In summary, Mg^{2+} ions were not definitively located at the M_A site that is key for exonuclease activity, and this unexpected observation might explain why EXD2 is inactive toward DNA substrates in the presence of Mg^{2+} (Figure 3.4 B and D). Interestingly, when crystals of EXD2-exo were soaked in a solution containing Mg^{2+} and GMP, a known ribonucleotide mimic of the RNase product, Mg^{2+} ions were located at both M_A and M_B sites (Figure 3.11G). We assume that the 2′-OH group of GMP might assist in this ion (M_A) capture. This hypothesis is supported by the fact that 2′-deoxyGMP, which lacks the OH group corresponding to the ‘ordered water molecule’, cannot bind to and assist in the capture of a second Mg^{2+}, resulting in only Mg^{2+} in the same site, as observed in unsoaked crystals. This result is consistent with the above data showing that EXD2 can cleave RNA in the presence of Mg^{2+} ion (Figure 3.5). Likewise, Mn^{2+} ions were coordinated at both metal-binding sites in the presence of GMP (Figure 3.11H).

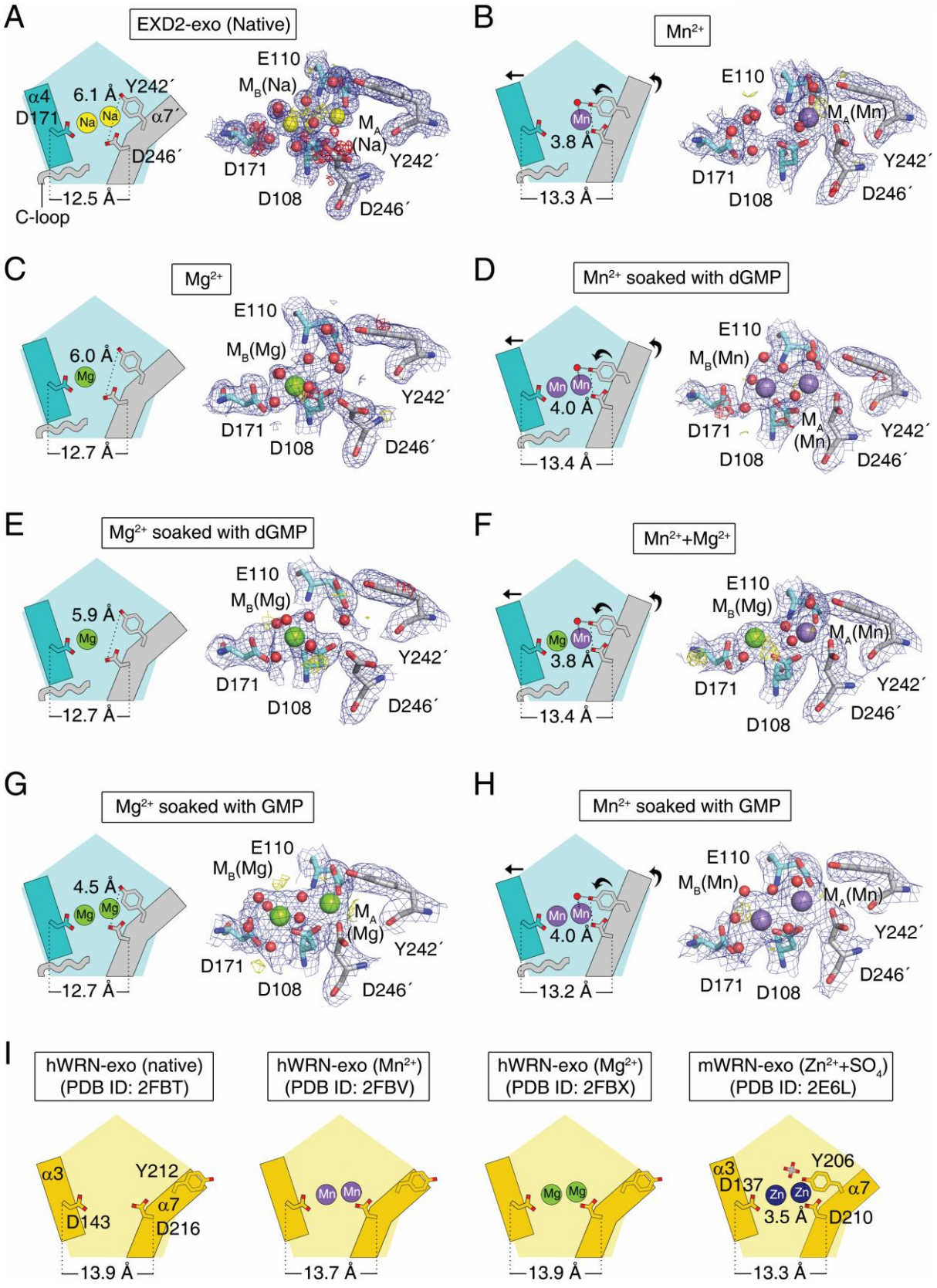

Figure 3.11. Structural basis for the metal and substrate specificities of EXD2-exo

(A−H) Schematic representations (left) based on the crystal structures (right) for native and metal ions and (d)GMP soaked structures showing the substrate discrimination of EXD2-exo resulting from metal coordination: **(A)** native crystal; **(B)** Mn^{2+}; **(C)** Mg^{2+}; **(D)** Mn^{2+} soaked with dGMP; **(E)** Mg^{2+} soaked with dGMP; **(F)** Mn^{2+} and Mg^{2+}; **(G)** Mg^{2+} soaked with GMP; **(H)** Mn^{2+} soaked with GMP. In right panels, 2Fo-Fc maps were contoured at 1.0σ and Fo-Fc difference maps were contoured at 3.0σ (yellow) and -3.0σ (red). In left schematic figures, helices harboring active site residues involved in metal coordination are depicted as cylinders. The C-loop (residues 285−294) from the opposing protomer in the dimer is drawn in worm representation. Black arrows indicate conformation changes occurring when Mn^{2+} ions are bound to the M_A site in the catalytic domain of EXD2-exo (see text for detailed mechanism). Active site residues are shown with ball and stick representation in right panels. All structural elements provided by the opposing molecule in the EXD2-exo dimer are colored gray. Water, sodium, manganese and magnesium ions bound to the active site are shown as red, yellow, purple and green spheres, respectively.

(I) Schematic representation of native and metal-soaked structures of human WRN-exo and Zn^{2+} soaked with sulfate (SO_4) structure of mouse WRN-exo shown in the same orientation as in (A). While Tyr212 in hWRN faces away from the active site, the conserved Tyr206 in mWRN is rotated toward the active site in the presence of sulphate ions (gray), which might act as a mimic of the substrate phosphate moiety. Color scheme of manganese and magnesium ions is the same as (A−H) and zinc ions bound to the active site of mWRN-exo are shown as blue spheres.

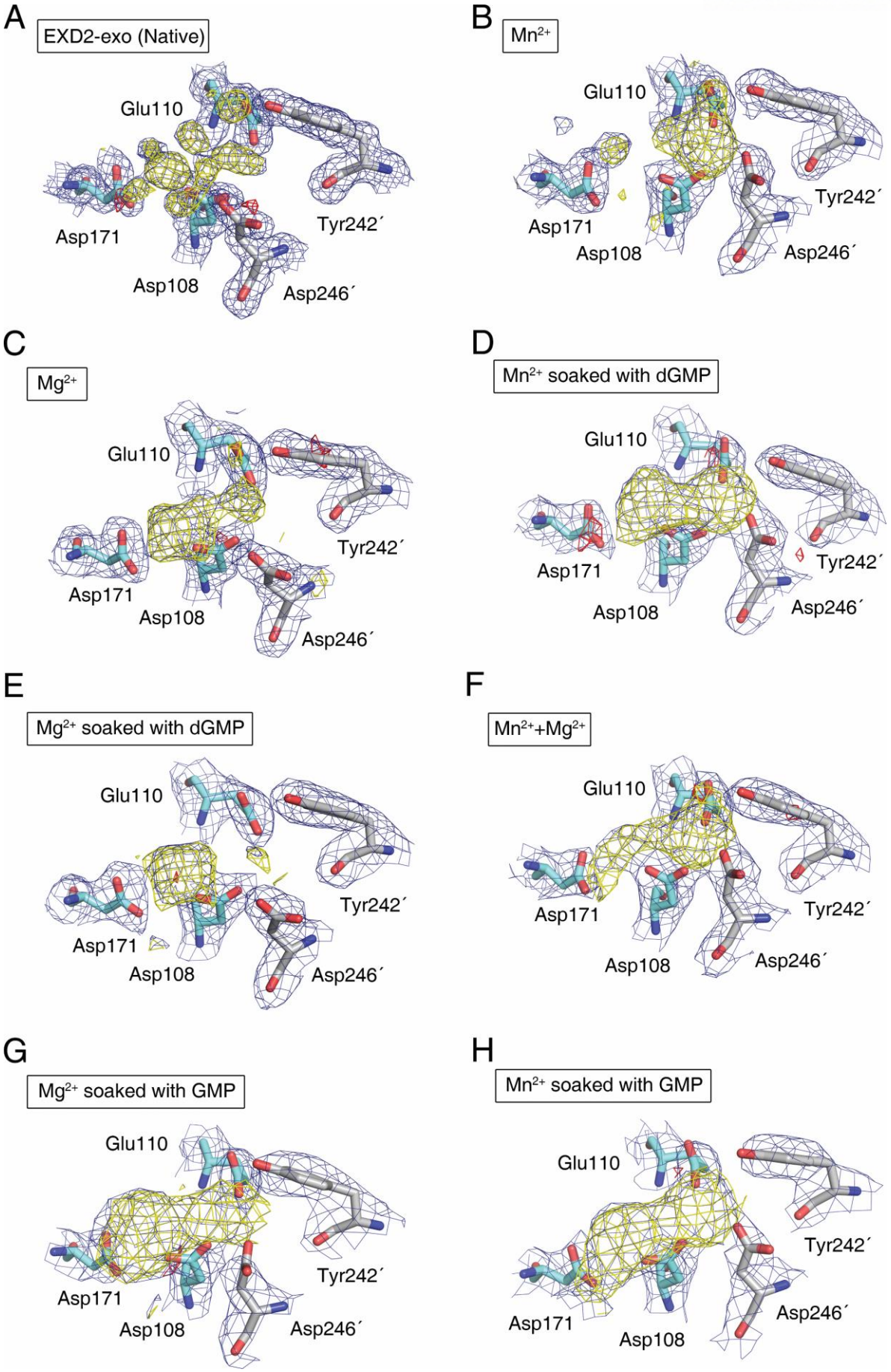

Figure 3.12. Metal coordination density of EXD2-exo active site

To exhibit metal coordination in EXD2-exo, the 2Fo-Fc electron density maps (blue) contoured at 1.0σand Fo-Fc difference electron density maps contoured at 3.0σ (yellow) and -3.0σ (red) at active sites are shown with the EXD2-exo molecular models. The following datasets and maps were obtained after soaking with metal ions and (d)GMP: **(A)** native; **(B)** Mn^{2+}; **(C)** Mg^{2+}; **(D)** Mn^{2+} soaked with dGMP; **(E)** Mg^{2+} soaked with dGMP; **(F)** Mn^{2+} and Mg^{2+}; **(G)** Mg^{2+} soaked with GMP; **(H)** Mn^{2+} soaked with GMP.

3.3.6. Structural basis for the metal and substrate specificity of EXD2-exo

Structural studies on EXD2-exo revealed that the metal coordination influences whether DNA or RNA substrates can be cleaved. We were therefore intrigued by the molecular basis by which EXD2-exo displays metal ion coordination and substrate (DNA or RNA) specificity, unlike WRN-exo, even though the two proteins share high structural similarity. The major difference between EXD2-exo and other DnaQ family exonucleases is that the active site of EXD2-exo is organized as a domain-swapped dimer (Figures 3.8, 3.10B, and 3.11) [9, 15-18]. In particular, helix α7′ is one of the main structural elements provided by the opposing molecule in the EXD2-exo dimer. We speculate that this unusual active site organization might provide structural flexibility via helix α7′. Moreover, the highly conserved loop connecting helices α6′ and α7′ of EXD2-exo was disordered in all structures determined in this study, unlike the equivalent region in WRN-exo that is well ordered (Figure 3.10B) [9]. This presumably suggests that helix α7′ may be more flexible in EXD2-exo than in WRN-exo. In fact, based on the crystal structures, helix α7 adopts two conformations, depending on metal coordination, unlike other DnaQ family exonucleases [9]. As highlighted in Figure 3.11 A, C, and E, helix α7′ forms a slightly bent structure when Mn^{2+} is not bound to the M_A site. In more detail, when metal ions are absent, or when a sodium ion is bound to the M_A site, the distance between side chains Tyr242 and Asp246 in EXD2-exo is ~6 Å, which seems to be too far to facilitate enzymatic action, consistent with the observed lack of exonuclease activity under these conditions (Figure 3.11 A, C, and E). However, the distance narrowed to ~3.8 Å when manganese was bound at the M_A position (Figure 3.11 B, D, F, and H). The manganese ion was coordinated by the side chain of Asp246 and the hydroxyl group of Tyr242 through an ordered water molecule. These intimate interactions eventually affect the conformation of helix α7′, resulting in the straightening of this structural element. The distance of 3.8 Å is likely short enough to support enzyme catalysis by facilitating the cooperation of Tyr242, Asp246 and the ordered water molecule with the DNA substrate. When Mg^{2+} plus GMP is bound to EXD2-exo, although two Mg^{2+} ions are bound to the active site, this Mg^{2+} coordination is unable to induce an equivalent conformational change in helix α7′ (Figure 3.11G). We concluded that the 2′-hydroxyl group of GMP might replace the ordered water molecule, preventing the attraction of Tyr242 (Figure 3.11G).

3.3.7. The role of the C-segment in EXD2 metal selectivity

We therefore wondered why two magnesium ions could not be simultaneously coordinated by EXD2-exo in the presence of DNA as a substrate. Structure analyses indicated that the half coupling of Mg^{2+} to EXD2-exo might be due to insufficient space to accommodate two Mg^{2+} ions. As summarized in Figure 3.11 A−H, the distance between Cα atoms of Asp171 and Asp246 is ∼12.5−12.7 Å when the α7 helix forms a kinked structure. However, this distance is increased to ∼13.4 Å when the helix adopts a straightened (extended) structure caused by the coordination of Mn^{2+} at the M_A site. Nevertheless, a distance of ∼13.4 Å might be insufficient for both Mg^{2+} ions to bind to the active site at the same time. In the previous structure of WRN-exo complexed with Mg^{2+} (PDB code: 2FBX), the distance between equivalent atoms is ∼13.9 Å (Figure 3.11I). Even though EXD2-exo may have sufficient space, EXD2 might not be able to actively increase the distance to an appropriate size. The C-segment provided from the opposing molecule in the EXD2-exo dimer forms extensive contacts not only with helix α4 bearing Asp171, but also with the central β-sheet of the active site, and this may block the movement of helix α4, thereby hindering spatial expansion of the active site (Figures 3.9, 3.11, and 3.13A).

To test our hypothesis that the C-segment might play a pivotal role in regulating metal coordination in EXD2-exo, we generated truncated constructs excluding the C-segment (Figure 3.13B). Surprisingly, $EXD2^{76–284}$ lacking the C-loop that contacts the active site exhibited robust exonuclease activity with DNA as a substrate in the presence of Mg^{2+} as well as Mn^{2+}. By contrast, the $EXD2^{76–260}$ variant lacking the whole C-segment lost all ability to cleave DNA (Figure 3.13C). In fact, the sequence of $EXD2^{76–260}$ (185 residues) precisely corresponds to $WRN^{38–236}$ (199 residues) that possesses full exonuclease activity [9]. Nevertheless, $EXD2^{76–260}$ completely lost exonuclease activity, implying that the C-segment (residues 260–295) is absolutely required for enzymatic activity of EXD2. Furthermore, we tested whether the C-segment supports the structural integrity of EXD2-exo by performing CD spectroscopy in the absence and presence of Mn^{2+}. As shown in Figure 3.13D, EXD2-exo lacking the C-segment displayed a reduction in melting temperature by ∼15°C compared with the wild-type protein, suggesting that the C-segment of EXD2 does indeed contribute to structural integrity and stability, unlike in other DEDDy family exonucleases. Interestingly, the addition of Mn^{2+} to the $EXD2^{76–284}$ variant recovered the melting temperature to that of the wild-type protein (Figure 3.13D, right). This is consistent with the data showing that $EXD2^{76–284}$ retained exonuclease activity in the presence of metal ions (Figure 3.13C). Collectively, these results suggest that the C-segment plays an important role in regulating the exonuclease activity not only by restricting metal ion coordination, but also by stabilizing the overall conformation.

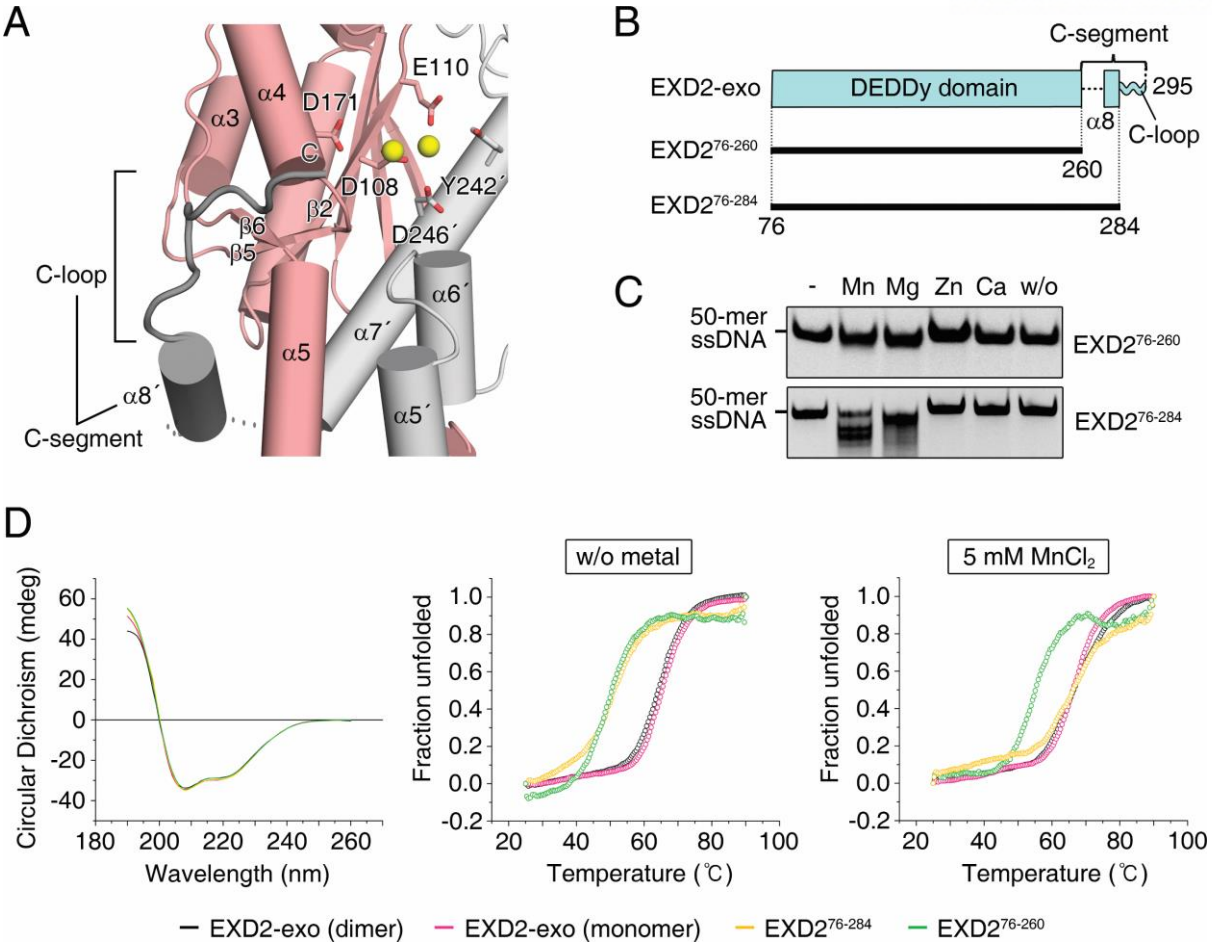

Figure 3.13. The C-segment is required for metal specificity and stability of the exonuclease domain

(A) Close-up view of the C-segment composed of α8 and the C-loop. The metal-binding active site of EXD2-exo is enclosed by the C-segment of the other molecule in the dimer and is restricted spatially.

(B) To test the role of the C-segment in regulating the metal specificity, two truncated constructs ($EXD2^{76–260}$ and $EXD2^{76–284}$) were generated.

(C) Metal cation-dependent exonuclease activities of $EXD2^{76–260}$ and $EXD2^{76–284}$. Protein (2.5 μM) was incubated with 0.25 μM 5-FAM-labeled 50-mer ssDNA for 1 h at 37°C and analyzed by non-denaturing TBE-PAGE.

(D) Far-UV CD spectra of EXD2-exo (dimer and monomer), $EXD2^{76–260}$ and $EXD2^{76–284}$ from 190 to 260 nm (left). Thermal unfolding curves of EXD2-exo (dimer and monomer), $EXD2^{76–260}$ and $EXD2^{76–284}$ were measured by CD spectroscopy without and with 5 mM $MnCl_2$ (middle and right). Melting temperatures without $MnCl_2$ were as follows: EXD2-exo (dimer) = 64.6°C, EXD2-exo (monomer) = 65.2°C, $EXD2^{76–284}$ = 51.6°C, $EXD2^{76–260}$ = 50.3°C. Melting temperatures with 5 mM $MnCl_2$ were as follows: EXD2-exo (dimer) = 65.7°C, EXD2-exo (monomer) = 66.4°C, $EXD2^{76–284}$ = 65.6°C, $EXD2^{76–260}$ = 54.5°C.

3.3.8. The EXD2-exo substrate-binding site

As described above, even in the crystal structures of EXD2 in complex with (d)GMP, no apparent electron density corresponding to (d)GMP was found in the active site. Therefore, we investigated the probable substrate-binding region of EXD2-exo by superimposing the structure of EXD2-exo over that of trinucleotide-bound KF-exo, since the substrate-binding site of WRN-exo was analyzed previously using a similar approach [9]. The overall geometry of residues in the active site of EXD2-exo is more similar to that in WRN-exo than in KF-exo (Figure 3.14A). However, the open conformation of Tyr212 (Tyr242 in EXD2-exo) in human WRN-exo was not observed in all structures of EXD2-exo (Figure 3.11I) [9]. Rather, Tyr242 of EXD2-exo projects into the active site as shown in the structures of KF-exo (Tyr497, PDB code: 1KFS) and mouse WRN-exo (Tyr206, PDB code: 2E6L), and facilitates enzyme catalysis via an ordered water molecule and Mn^{2+} (Figure 3.14A) [8, 15]. In addition, the composite model suggests that the side chain of Arg226 directly stacks against the basic ring of the last nucleotide. The equivalent Arg190 in mWRN-exo forms a H-bond with the oxygen atom of the basic ring. Instead, the side chains of Phe473 in KF-exo and Cys191 in mWRN-exo play a similar role by positioning the last nucleotide. Lys185 in mWRN-exo is believed to be important for substrate binding [8]. However, the equivalent residue in EXD2-exo (Lys221) is not visible in the electron density map and is presumably disordered. Significantly, based on the model, the Arg190 of helix α5 in EXD2-exo directly contacts the ribose ring of the first nucleotide of the trinucleotide and likely stabilizes the overall structure of the ligand (Figure 3.14A). Arg190 is absolutely conserved among members of the EXD2 family, but is absent from mWRN-exo and KF-exo (Figures 3.7 and 3.14A).

We identified the substrate-binding region by alanine-scanning mutagenesis. As shown in Figure 3.14 B and C, R226A single point mutants of EXD2-exo and tEXD2 lost all exonuclease activity, suggesting that Arg226 plays a key role in binding substrate nucleotides. Furthermore, as demonstrated for Lys185 in mWRN-exo [8], mutation of the equivalent Lys221 in EXD2 affected the exonuclease activity. Although this residue is not visible in the structure of EXD2-exo, it is obvious that it is also responsible for substrate recognition. Finally, mutation of Arg190 in both EXD2-exo and tEXD2 resulted in variants unable to cleave DNA substrates (Figure 3.14 B and C).

Analysis of surface electrostatic potential revealed that EXD2-exo has a positively charged patch located just beneath the active sites (Figure 3.14D). This patch is mainly composed of Arg190, Arg195 and Arg197 from helix α5, and these residues are highly conserved among species (Figure 3.7). We therefore infer that substrates to be cleaved might enter the catalytic site through this positively charged groove. The importance of Arg190 in substrate binding was verified by

biochemical data (Figure 3.14 B and C). Additionally, we confirmed that mutation of Arg195 or Arg197 impaired enzymatic activity (Figure 3.14E). As mentioned above, the structure of helix α5 is extended, and this structural change seems to be essential for the formation of the EXD2-exo dimer (Figure 3.10 A and B). In fact, if helix α5 is kinked, as is the case in WRN-exo and KF-exo, EXD2-exo forms a monomer, which could prevent EXD2-exo from forming a positively charged surface of sufficient length to guide substrate entry. In fact, mutation of equivalent residues in WRN and KF did not affect exonuclease activity (Figure 3.15).

In contrast to WRN-exo and KF-exo, it is noteworthy that EXD2-exo has two active sites per dimer, related by 2-fold symmetry (Figure 3.14D). The distance between the two active sites is ~46 Å. Unfortunately, at present it is difficult to explain why EXD2 has two catalytic sites that are closely associated, but future biochemical studies should address the role of this unusual catalytic domain arrangement. Nevertheless, it is clear that formation of the EXD2 dimer might be important for recruiting substrates to the active site by providing a positively charged patch of sufficient length.

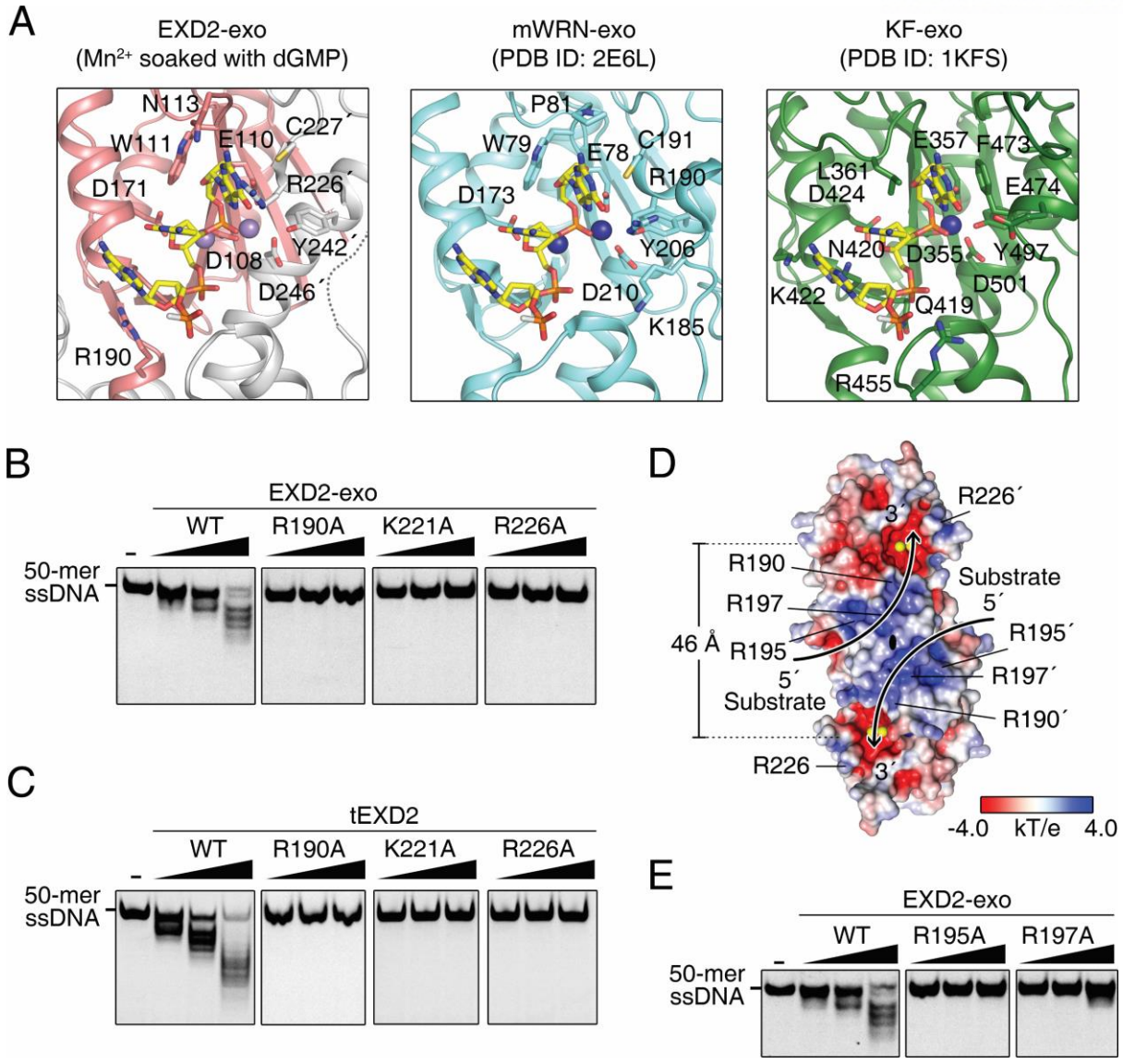

Figure 3.14. Dimerization of EXD2-exo is important for substrate binding

(A) Close-up views showing trinucleotide-bound EXD2-exo (left), mWRN-exo (middle) and KF-exo (right) in the same orientation to compare substrate-binding regions. Structural models were generated by superimposing structures of EXD2-exo (soaked with Mn^{2+} and dGMP, from this study) and mWRN-exo (PDB code: 2E6L) with the structure of trinucleotide-bound KF-exo (PDB code: 1KFS). In EXD2-exo, the two protomers are colored red and gray. The trinucleotide (yellow) and the side chains contacting the substrate are shown in ball-and-stick representation. Nitrogen and oxygen atoms are colored blue and red, respectively.

(B) Exonuclease activity of EXD2-exo mutants (R190A, K221A, and R226A). Mutant proteins (from the left, 0.5, 1, and 2 μM) were mixed with 5-FAM-labeled ssDNA as described in Figure 3.4B.

(C) Exonuclease activity of tEXD2 mutants (R190A, K221A, and R226A). The tEXD2 mutant proteins (from the left, 0.05, 0.1, and 0.2 μM) were analyzed as described in Figure 3.4B.

(D) Electrostatic potential of the EXD2-exo molecular surface. The dimeric interface formed by the α5–α5′ crossover beneath the active sites generates a highly positively charged groove. Based on the trinucleotide-bound EXD2-exo model (A) combined with nuclease activity analyses (B and C), putative substrate-binding pathways are indicated by arrows. The electrostatic potential was calculated using the Adaptive Poisson-Boltzmann Solver (APBS) [20] and visualized (-4 kT/e, red, to +4 kT/e, blue) with PyMol (https://pymol.org/2/, version 1.7.4.4).

(E) Exonuclease activity of EXD2-exo mutants (R195A and R197A). Experimental procedures were the same as in (B).

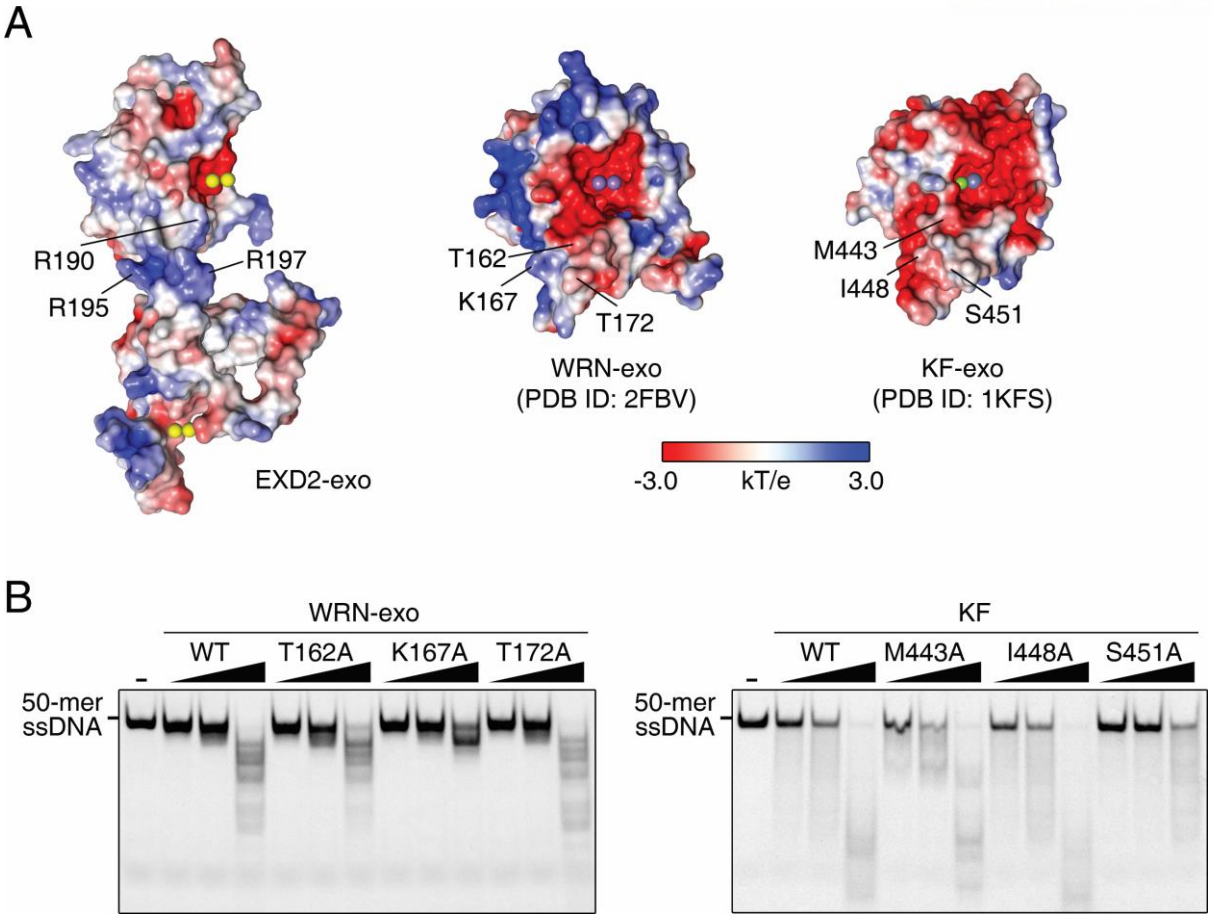

Figure 3.15. EXD2 has a more extensive positive patch than WRN and KF for DNA binding

(A) Electrostatic surface potential of EXD2-exo protomer (left), WRN-exo (middle), and KF-exo (right). Positively charged residues (R190, R195, and R197) of EXD2-exo in α5 and corresponding residues in WRN-exo and KF-exo are labeled. Electrostatic surface potential was calculated using the Adaptive Poisson-Boltzmann Solver (APBS) [20] and visualized (-3 kT/e in red to +3 kT/e in blue) with PyMol (https://pymol.org/2/, version 1.7.4.4).

(B) Exonuclease activity of WRN-exo mutants (T162A, K167A, and T172A, left) and KF mutants (M443A, I448A, and S451A, right). WRN-exo (0.5–2 μM) and KF (0.1–0.4 μM) were incubated with 0.25 μM 5-FAM-labeled 50-mer ssDNA and analyzed as described in Figure 3.4B.

3.4. Discussion

In this study, we first determined the crystal structure of the human EXD2 exonuclease domain, revealing a novel structure in which the catalytic site is generated by chimeric arrangement of molecules in a domain-swapped dimer (Figure 3.4). Dimeric exonucleases have been proposed in several previous studies [21-24]. However, this is the first report of an exonuclease domain that is only active when the enzyme is oligomerized. We also revealed the formation of a dimeric structure that might generate a positively charged groove of sufficient length to guide substrate entry in EXD2 (Figure 3.14). Moreover, this unusual active site organization and the presence of a unique C-segment could endow EXD2 with the novel ability to discriminate between DNA and RNA substrates via metal cation coordination (Figures 3.11 and 3.13). In fact, EXD2 only digests RNA and not DNA in the presence of Mg^{2+}, even though EXD2 hydrolyzes both DNA and RNA when Mn^{2+} ions are bound (Figures 3.4 and 3.5). This is consistent with a previous study in which EXD2 was suggested to act as an RNase in the presence of Mg^{2+} in mitochondria [4]. In addition to substrate discrimination, the dimeric organization might confer the ability to regulate catalytic activity because the exonuclease activity of EXD2 appears to be turned on only following self-association. Given that EXD2 is a membrane protein that is tightly anchored to the mitochondrial membrane, it might be geometrically difficult for molecules to associate with each other, suggesting that EXD2 might not always be active. It has not yet been tested whether the two EXD2 molecules are associated within the intra-mitochondrial membrane (homotypic interaction) or through inter-membrane interactions (heterotypic interaction) between two neighboring mitochondria (Figure 3.16). In the latter case, EXD2 might be involved in mitochondrial tethering or mitochondrial dynamics such as fusion events [3, 25-27]. In any case, the geometrical restriction indicated herein implies that the activity of EXD2 could be modulated by unknown cellular factors.

EXD2 is an important player in the DNA double-strand break repair system [1]. However, its biological role in the nucleus has been contradicted by its mitochondrial localization revealed in this and other studies [3, 4]. Thus, identification of its sub-mitochondrial localization is crucial to understanding its role in mitochondria. Mitochondrial matrix localization was recently demonstrated by fractionation, and it was concluded that it processes messenger RNA within mitochondria [4]. Very recently, however, Hensen et al. provided further evidence of the OMM localization of EXD2 using proteinase K digestion with isolated mitochondria [3]. In the present work, we confirmed OMM localization using a proximity labeling approach and APEX2-EM imaging (Figure 3.2). Furthermore, we revealed that EXD2 contains an N-terminal single TM domain that anchors it to the OMM and a C-terminal domain that is mainly localized to the cytosolic face of the OMM (Figures 3.1 and 3.2). These results suggest that the exonuclease domain of EXD2 may have a novel function at the OMM

that has not yet been proposed.

Due to the absence of known DNA populations near the OMM, we propose that EXD2 might be involved in the processing of RNA in the vicinity of the OMM. In particular, we speculate that EXD2 might be involved in the biogenesis of Piwi-interacting RNA (piRNA) since the OMM is recognized as a hub for processing piRNA, which is crucial for germ cell development [26, 28]. Our hypothesis is supported by the published data showing that germ stem cell attrition is significantly accelerated in EXD2-deficient ovaries of drosophila [4]. Moreover, EXD2 is also highly expressed in reproductive organs in human [29]. In the Gtex portal [30], EXD2 expression is reportedly higher in testes and brain than in other tissues. Because many piRNA biogenesis proteins, such as PIWIL1, TDRKH and MitoPLD, are overexpressed in testes for the generation of the large amounts of piRNA needed to protect the genetic stability of germ cell lines [31], a similar testis-specific expression pattern of EXD2 in humans could indicate its possible involvement in piRNA biogenesis. In the process of piRNA biogenesis, we further speculate that EXD2 could function as a Trimmer, which digests the 3′ ends of pre-piRNA molecules, although PNLDC1 [32] and EXD3 (also known as Nibbler in drosophila) [33] have been proposed to be Trimmers in different models. As regards its possible role in piRNA biogenesis, it is intriguing to suggest that the homotypic dimer of EXD2 may engage in functional interactions with the homodimeric complex of MitoPLD at the OMM, which also contains a signal anchoring the TM helix at the N terminus [34]. The heterotypic interaction mode of EXD2 might function at the inter-mitochondrial cement, which is observed in spermatogenesis in mammals [35]. Future work will be required to address the role that dimerization of the EXD2 exonuclease domain may play in regulating physiological function.

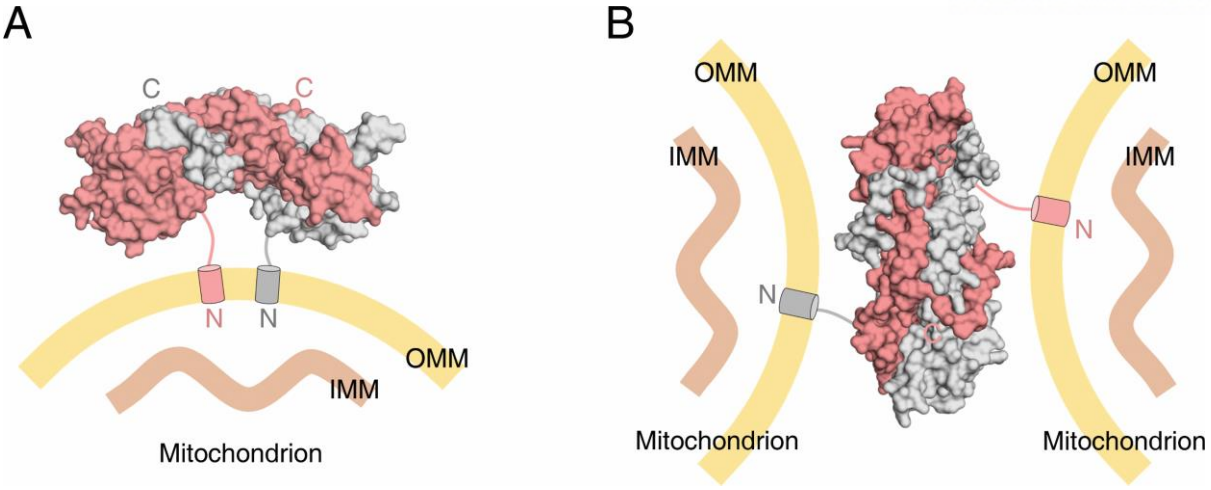

Figure 3.16. Working model of EXD2 at the outer mitochondrial membrane

Surface representation showing a putative working model of EXD2 anchored to the mitochondrial outer membrane. Given that EXD2 must form a dimer for exonuclease activity, two EXD2 molecules could be associated with each other via intra-mitochondrial membrane contacts (**A**, homotypic) or EXD2 molecules from two different mitochondria could be associated via inter-mitochondrial membrane contacts (**B**, heterotypic). In both cases, self-association might be regulated by metal ions or other unknown cellular factors. IMM, mitochondrial inner membrane.

3.5. Materials and Methods

3.5.1. Mammalian cell culture and transfection

HEK293 cells from the Korean Cell Line Bank (Seoul, Korea) were cultured in Dulbecco's modified Eagle's medium (DMEM; Gibco) supplemented with 10% fetal bovine serum (FBS), 50 units/mL penicillin and 50 μg/mL streptomycin at 37°C under 5% CO2. HeLa cells from the Korean Cell Line Bank were cultured in the same conditions. Cells were transfected at 60−80% confluence using Lipofectamine 2000 (Life Technologies) according to the manufacturer's instructions.

3.5.2. Fluorescence microscopy imaging

At 18−24 h after transfection in HeLa cells, the medium of the EXD2-V5-APEX2-transfected sample was changed to fresh growth medium containing 500 μM biotin-phenol. This culture was incubated for 30 min and labeled according to a previously published protocol (10). Next, H2O2 was added to a final concentration of 1 mM, and the plate was gently agitated for 1 min at room temperature. The reaction was quenched by washing twice with Quencher solution consisting of Dulbecco's phosphate-buffered saline (DPBS) containing 5 mM Trolox, 10 mM sodium azide and 10 mM sodium ascorbate. The biotin labeling step was omitted for Non-APEX2 samples. Biotin-labeled and non-labeled cells were fixed with 4% paraformaldehyde. Cells were then washed with DPBS and permeabilized with cold methanol at −20°C for 5 min. Cells were washed again with DPBS and blocked for 1 h with blocking solution consisting of 2% bovine serum albumin (BSA) in TRIS-buffered saline with Tween 20 (TBST) at room temperature.

To detect APEX2-fusion expression, cells were incubated with both mouse anti-V5 antibody (Invitrogen, cat. no. R960-25, 1:5000 dilution) and rabbit anti-TOM20 (Santa Cruz, cat. no. sc-11415, 1:200 dilution) as a mitochondrial marker for 1 h at room temperature. To detect Flag-tagged EXD2 expression, cells were incubated with both mouse anti-Flag antibody (Sigma Aldrich, cat. no. F1804, 1:3000 dilution) and rabbit anti-TOM20 for 1 h at room temperature. After washing with TBST, cells were simultaneously incubated with secondary Alexa Fluor 568 goat anti-mouse IgG (Invitrogen, cat. no. A-11004, 1:1000 dilution) and Alexa Fluor 488 goat anti-rabbit IgG (Invitrogen, cat. no. A-11008, 1:1000 dilution) for 30 min at room temperature. SA-Alexa Fluor 647 IgG (Invitrogen, cat. no. S32357, 1:1000 dilution) was incubated with biotin-labeled samples in dialyzed blocking solution. Cells were then washed with TBST and maintained in DPBS on ice for imaging using an FV1000SPD instrument (Olympus) at the UNIST Optical Biomed Imaging Center (UOBC) in the Ulsan National Institute of Science and Technology (UNIST), Korea.

3.5.3. Transmission electron microscopy (TEM) imaging

Cells transiently expressing EXD2-V5-APEX2 or EXD2$^{1-37}$-V5-APEX2 were grown in plastic six-well plates (Falcon, 353078) to 90% confluence. Cells were fixed and stained with diaminodenzidine (DAB) according to a previously published method [5]. Briefly, cells were fixed using 2% glutaraldehyde and 2% paraformaldehyde in 0.1 M sodium cacodylate buffer pH 7.4 over 30−60 min. Unreacted glutaraldehyde was quenched by 20 mM glycine and cells were washed again in cold buffer. Freshly diluted 1 mg/mL (2.8 mM) DAB and 10 mM H_2O_2 in phosphate-buffered saline (PBS) were added. After 20 min, cells were again washed with PBS. Post-fixation was performed using 2% (w/v) osmium tetroxide (Electron Microscopy Sciences) for 40 min on ice and cells were rinsed with chilled distilled water. Cells were brought to room temperature, washed with distilled water, carefully scraped, resuspended and centrifuged at 1500 × g for 1 min. The pellet was dehydrated in a graded ethanol series (50−100%) for 15 min for each step. The sample was then mixed 1:1 with EMBED-812 resin (Electron Microscopy Sciences) and anhydrous ethanol for 1 h. The mixture was incubated overnight in 2:1 (v/v) resin and then exchanged with 100% resin for 2 h before transferring to fresh resin, followed by polymerization at 60°C for 24 h. Embedded cell pellets were cut with a diamond knife into 50 nm sections and imaged on a FEI-Tecnai G2 Spirit Bio Twin TEM instrument (operated at 120 kV) at the Korea Basic Science Institute in Chuncheon, Korea.

3.5.4. TOM20-pBirA stable cell line selection, culturing and labeling

Flp-In T-REx 293 cells (Life Technologies) were cultured under the same conditions as HEK293 cells. Stable cell generation, culturing and labeling were performed according to previously published methods [5]. Briefly, stable cell lines were generated by cotransfection with the pcDNA 5/FRT/TO expression construct and the pOG44 plasmid (1:9). After 24 h of transfection, cells were treated with an appropriate concentration of hygromycin B (100−200 μg/mL). Media containing hygromycin B were changed every 3−4 days. After 2−3 weeks, 3−4 colonies were picked and cultured continuously. To induce protein expression and biotin labeling of stable cells, cells at 60−80% confluence were treated with 100 ng/mL doxycycline (Sigma Aldrich) and 50 μM biotin. After incubation for 18−24 h, cells were lysed for subsequent analyses.

3.5.5. TOM20-pBirA mass spectrometry (MS) sample preparation

MS sample preparation was carried out according to a previously published method [14]. Briefly, after biotin labeling overnight, cells were washed several times with DPBS and lysed with 1.5 mL of RIPA lysis buffer, 1 × protease inhibitor cocktail (Sigma Aldrich, cat. no. P8849) and 1 mM

phenylmethylsulphonyl fluoride (PMSF) for 10 min at 4°C. Lysates were clarified by centrifugation and samples from two T75 flasks were combined (~3 mL).

For removal of free biotin, 3 mL of cell lysate was filtered with an Amicon filter (Merck Millipore, UFC801096) three times using PBS containing 1 mM PMSF and 1 × protease inhibitor cocktail. The final ~1 mL concentrated cell lysate was transferred to a 1.5 mL Lobind tube and 300 µL of washed SA-beads (Pierce) were added. After rotating for 1 h, beads were washed twice with PBS, and after removing PBS, samples were denatured in 100 µL denaturing solution (6 M urea, 2 M thiourea, 10 mM HEPES). The solution was reduced using 20 µL of 100 mM dithiothreitol (DTT) in 50 mM ammonium bicarbonate (ABC) at 56°C. Alkylation was performed by adding 35 µL of 300 mM iodoacetamide in 50 mM ABC in the dark. The sample was diluted with 50 mM ABC to 1 mL. Trypsin digestion was performed by adding 8 µL of 1 mg/mL trypsin. The solution was incubated at 37°C with shaking at 900 rpm overnight. Beads were washed with PBS four times and eluted by boiling at 95°C for 10 min after adding 250 µL of 95% formamide and 10 mM EDTA (pH 8.2), and 750 µL of 3% acetonitrile/0.1% formic acid was added to a final volume of 1 mL. The solution was desalted using a Varian Bond ELUT column (Agilent, 12109301).

3.5.6. MS detection of labeled peptides and data processing

An LTQ-Orbitrap mass spectrometer (Thermo, Bremen, Germany) equipped with a nanoelectrospray ion source was employed for MS detection. All MS analyses and data processing were performed as described previously [14].

3.5.7. Cell fractionation, proteinase K digestion assay, and western blotting

HEK293T cells were cultured in DMEM supplemented with 10% FBS. Detached cells were washed twice with PBS and resuspended in homogenization buffer containing 0.6 M mannitol, 10 mM TRIS, 0.1 mM EDTA (pH 7.4), and protease inhibitors (Roche). Cells were homogenized with a glass Dounce homogenizer. Next, differential centrifugation was used to obtain the different cell fractions (1,000 × g for 10 min to remove cell debris and nuclei, next for 10 min at 10,000 × g to pellet the mitochondria). The pellet containing the mitochondrial fraction was resuspended in 50 mM TRIS-HCl pH 7.4 with 150 mM NaCl and divided in four fractions of which three were used for treatment with proteinase K using different enzyme concentrations: 0.2 µg / 5 mg for 10 min, 2 µg / 5 mg for 20 min and 20 µg per 5 mg mitochondrial proteins for 30 min. For western blot analysis, 10–30 µg of extracted proteins were loaded on SDS-PAGE 4–12% BIS-TRIS gels (Life Technologies) and transferred onto a membrane using iBlot 2 Dry Blotting System (Thermo Fisher Scientific). The

following antibodies were used: mouse anti-TOM22 (Abcam, ab10436, 1:2000 dilution), mouse anti-mtSSB1 (a kind gift of Prof. D. Kang, 1:4000 dilution), and anti-EXD2 (Sigma Aldrich, HPA005848, 1:1000 dilution).

3.5.8. Cloning, protein expression and purification

DNA fragments encoding a highly soluble construct of human EXD2 (residues 76−564, tEXD2) and the 3′-5′ exonuclease domain (residues 76−295, EXD2-exo) were amplified by PCR using Homo sapiens cDNA as template and cloned into the pcDNA5, pET28b-SMT3 and pETDUET-1 vectors. The resulting pcDNA5 constructs were used in mammalian transfection for imaging and pull-down experiments. The pETDUET-1 vector was previously modified to include a tobacco etch virus (TEV) protease cleavage site before the first amino acid of the EXD2 protein. Expression plasmids were transformed into *Escherichia coli* BL21 (DE3) competent cells, protein expression was induced with 0.3 mM isopropyl-β-D-1-thiogalactopyranoside (IPTG) when cells reached an absorbance at 600 nm (OD600 nm) of 0.6 and culturing was continued at 18°C for 18 h. Cells were harvested by centrifugation at 3,200 × g for 18 min and resuspended in buffer containing 25 mM sodium phosphate pH 7.8, 400 mM sodium chloride and 10 mM imidazole. After cell lysis by sonication, tEXD2 and EXD2-exo proteins were purified by Ni^{2+}-immobilized metal affinity chromatography (IMAC). The His_6-SMT3 tag of tEXD2 and the His_6 tag of EXD2-exo were cleaved by Ulp1 protease and TEV protease at a ratio of 1:500 and 1:30 (w/w), respectively, during dialysis against 25 mM TRIS-HCl, pH 7.5, 150 mM NaCl and 4 mM β-mercaptoethanol at 4°C overnight. Cleaved tags and non-cleaved fusion proteins were removed by a second round of Ni^{2+}-IMAC. For further purification, proteins were applied to a Superdex 200 column (GE Healthcare) equilibrated with 25 mM TRIS-HCl, pH 7.5, 150 mM NaCl and 5 mM DTT. Proteins were concentrated to 10 mg/mL and flash-frozen at −80°C for later use. All point mutants and deletion mutants were generated by PCR-based mutagenesis, and mutations were confirmed with DNA sequencing. All mutants were purified as described above.

3.5.9. Crystallization and structure determination

Crystals grew when EXD2-exo was mixed with an equal volume of reservoir liquor containing 18% polyethylene glycol (PEG) 8000, 100 mM 2-(N-morpholino)ethanesulfonic acid, pH 6.0, 0.2 M calcium acetate and 5 mM DTT by the hanging-drop vapor diffusion method at 4°C. Crystals were cryoprotected by transferring into a reservoir solution augmented with 30% ethylene glycol and flash-frozen in liquid nitrogen. X-ray diffraction data were collected at beamline 5C of the Pohang Accelerator Laboratory at 100 K. The best crystals diffracted to 1.6 Å resolution and complete

datasets were processed using HKL2000 [36]. Phases were calculated by molecular replacement using Phaser in the PHENIX suite [37] with the coordinates of WRN-exo (PDB code: 2FBT) as a search model. Phaser found two EXD2 molecules in the asymmetric unit of the $P2_12_12_1$ space group. Model building and refinement were performed using Coot [38] and PHENIX refine [39], respectively. The R_{free} of the refined model was 21.95%. The following residues of EXD2-exo were disordered in the electron density map and therefore not modeled: residue 76, residues 219−222, residues 261−274 and residue 295 in the first copy; residue 76, residues 219−223, residues 261−274 and residues 293−295 in the second copy.

To solve the metal-coordinated structures, crystals of EXD2-exo were transferred to reservoir solution supplemented with 20−50 mM $MnCl_2$ or $MgCl_2$ and 5 mM dGMP or GMP for at least 1 day, and flash-frozen in liquid nitrogen. Structures were solved by difference Fourier methods. To reduce the effect of model bias, we refined the protein chains without water molecules and ions using simulated annealing before calculating difference maps for detection of positive peaks corresponding to ions and solvent molecules. Model building and refinement were performed as described above. Detailed crystallographic data and data processing and refinement statistics are summarized in Table 3.2.

3.5.10. In vitro exonuclease activity assay

In vitro nuclease activity assays were conducted as reported previously [1]. In our experiments, DNA or RNA substrates were labeled using 5-fluorescein amidite (5-FAM) at the 5′ end instead of [γ-^{32}P] 5′ labeling. DNA or RNA substrates at a concentration of 0.25 μM were incubated with 0.05−0.2 μM or 0.5−1.5 μM tEXD2, or 0.5−2 μM or 20−60 μM EXD2-exo, for 30 min at 37°C in reaction buffer consisting of 20 mM HEPES-KOH, pH 7.5, 50 mM KCl, 0.5 mM DTT, 0.05% (v/v) Triton X-100, 0.1 mg/mL BSA, 5% (v/v) glycerol, 1 mM ATP and 5 mM metal ions ($MnCl_2$, $MgCl_2$, $ZnCl_2$ or $CaCl_2$) or without metals. After reaction, products were separated by non-denaturing 15% TRIS/Borate/EDTA-polyacrylamide gel electrophoresis (TBE-PAGE) and fluorescence was detected using an ImageQuant LAS 4000 instrument (GE Healthcare).

3.5.11. Size exclusion chromatography analysis

Analysis of the relative molecular mass (Figures 3.4C, 3.6A, and 3.10D) was carried out by SEC. Proteins were concentrated to 15−20 mg/mL and injected onto a Superdex 200 16/60 column (GE Healthcare) equilibrated with buffer containing 25 mM TRIS-HCl, pH 7.5, 150 mM NaCl and 5 mM DTT.

3.5.12. Analytical ultracentrifugation (AUC)

The absolute molecular weights of tEXD2 proteins were measured by the sedimentation equilibrium method using an XL-A analytical ultracentrifuge (Beckman Coulter) as described previously [40]. Each tEXD2 protein sample was prepared in buffer containing 25 mM TRIS-HCl pH 7.5, 150 mM NaCl, and 5 mM β-mercaptoethanol.

3.5.13. Pull-down assay

For pull-down assays, cells were prepared in a six-well plate. Full-length human EXD2-V5-Avitag (1,000 ng), EXD2-Flag (1,000 ng) and BirA-NES (500 ng) were cotransfected in HEK293 cells. After overnight biotinylation following addition of 10 μM biotin, cells were lysed with 200 μL of Cell Extraction Buffer (Life Technologies, cat. no. FNN0011) containing 1 × protease inhibitor cocktail (Sigma Aldrich, cat. no. P8849) and 1 mM PMSF for 30 min at 4°C. Lysates were transferred into Eppendorf tubes, vortexed for 2 min and clarified by centrifugation at 15,000 × g for 10 min at 4°C.

A 20 μL of SA magnetic beads (Invitrogen, cat. no. 88816) were incubated with 170 μL of cell lysate for 1 h. The flow-through (FT) fraction was retained and beads were washed three times with Cell Extraction Buffer. Biotinylated EXD2-V5-Avitag was eluted with 2 × Laemmli buffer (BioRad, cat. no. 161-0737) supplemented with 20 mM DTT and 2 mM biotin by heating to 95°C for 10 min. Crude and elution samples were separated by 10% sodium dodecyl sulphate (SDS)-PAGE and transferred to a nitrocellulose membrane that was subsequently stained with 0.1% Ponceau S in 5% acetic acid/water for 10 min. After blocking with 2% (w/v) BSA and 0.1% Tween 20 in TBST at 4°C overnight or at room temperature for 1 h, blots were immersed in anti-V5 (Invitrogen, cat. no. R960-25, 1:5000 dilution) or anti-Flag (Sigma Aldrich, cat. no. F1804, 1:3000 dilution) in blot blocking buffer at room temperature for 60 min, then rinsed with blot blocking buffer four times for 5 min each time. Blots were then immersed in secondary antibody (anti-mouse-HRP, BioRad, cat. no. 1721011) in blot blocking buffer for between 30 min and 1 h at room temperature. Membranes were then washed again for 4 × 5 min in TBST before imaging with Clarity reagent (BioRad) on a G:BOX Chemi XRQ instrument (Syngene).

3.5.14. Circular dichroism (CD) spectroscopy

Secondary structures of EXD2-exo, $EXD2^{76–284}$ and $EXD2^{76–260}$ were monitored by CD spectroscopy on a Jasco J-815 instrument (Jasco, UK) from 190 to 260 nm. Conformational changes

were also monitored by CD spectroscopy with temperature scanning from 25 to 90°C over a 13 min period with detection at 222 nm. Protein samples for wavelength scans (0.2 mg/mL) and temperature scans (1 mg/mL) were prepared in 25 mM sodium phosphate pH 7.5 with 150 mM sodium fluoride and 5 mM β-mercaptoethanol.

3.6. References

[1] R. Broderick *et al.*, "EXD2 promotes homologous recombination by facilitating DNA end resection," *Nature cell biology,* vol. 18, no. 3, pp. 271-280, 2016.

[2] P. J. Thul *et al.*, "A subcellular map of the human proteome," *Science,* vol. 356, no. 6340, 2017.

[3] F. Hensen, A. Moretton, S. van Esveld, G. Farge, and J. N. Spelbrink, "The mitochondrial outer-membrane location of the EXD2 exonuclease contradicts its direct role in nuclear DNA repair," *Scientific reports,* vol. 8, no. 1, pp. 1-9, 2018.

[4] J. Silva *et al.*, "EXD2 governs germ stem cell homeostasis and lifespan by promoting mitoribosome integrity and translation," *Nature cell biology,* vol. 20, no. 2, pp. 162-174, 2018.

[5] S.-Y. Lee *et al.*, "Architecture mapping of the inner mitochondrial membrane proteome by chemical tools in live cells," *Journal of the American Chemical Society,* vol. 139, no. 10, pp. 3651-3662, 2017.

[6] G. E. Sosinsky, B. N. G. Giepmans, T. J. Deerinck, G. M. Gaietta, and M. H. Ellisman, "Markers for Correlated Light and Electron Microscopy," *Methods in Cell Biology,* vol. 79, pp. 575-591, 2007/01/01/ 2007.

[7] U. Schnell, F. Dijk, K. A. Sjollema, and B. N. Giepmans, "Immunolabeling artifacts and the need for live-cell imaging," *Nature methods,* vol. 9, no. 2, p. 152, 2012.

[8] J. M. Choi, S. Y. Kang, W. J. Bae, K. S. Jin, M. Ree, and Y. Cho, "Probing the roles of active site residues in the 3′-5′ exonuclease of the Werner syndrome protein," *Journal of Biological Chemistry,* vol. 282, no. 13, pp. 9941-9951, 2007.

[9] J. J. P. Perry *et al.*, "WRN exonuclease structure and molecular mechanism imply an editing role in DNA end processing," *Nature structural & molecular biology,* vol. 13, no. 5, pp. 414-422, 2006.

[10] G. C. Shore, H. M. McBride, D. G. Millar, N. A. Steenaart, and M. Nguyen, "Import and insertion of proteins into the mitochondrial outer membrane," *EJB Reviews,* pp. 1-10, 1995.

[11] D. Rapaport, "Finding the right organelle: Targeting signals in mitochondrial outer-membrane proteins," *EMBO reports,* vol. 4, no. 10, pp. 948-952, 2003.

[12] S.-Y. Lee, M.-G. Kang, J.-S. Park, G. Lee, A. Y. Ting, and H.-W. Rhee, "APEX fingerprinting reveals the subcellular localization of proteins of interest," *Cell reports,* vol. 15, no. 8, pp. 1837-1847, 2016.

[13] S. S. Lam *et al.*, "Directed evolution of APEX2 for electron microscopy and proximity labeling," *Nature methods,* vol. 12, no. 1, pp. 51-54, 2015.

[14] S.-Y. Lee *et al.*, "Proximity-directed labeling reveals a new rapamycin-induced heterodimer of FKBP25 and FRB in live cells," *ACS central science,* vol. 2, no. 8, pp. 506-516, 2016.

[15] C. A. Brautigam and T. A. Steitz, "Structural principles for the inhibition of the 3′-5′ exonuclease activity of Escherichia coli DNA polymerase I by phosphorothioates," *Journal of molecular biology,* vol. 277, no. 2, pp. 363-377, 1998.

[16] Y. Zuo, Y. Wang, and A. Malhotra, "Crystal structure of Escherichia coli RNase D, an exoribonuclease involved in structured RNA processing," *Structure,* vol. 13, no. 7, pp. 973-984, 2005.

[17] W. A. Breyer and B. W. Matthews, "Structure of Escherichia coli exonuclease I suggests how processivity is achieved," *Nature structural biology,* vol. 7, no. 12, pp. 1125-1128, 2000.

[18] S. Hamdan, P. D. Carr, S. E. Brown, D. L. Ollis, and N. E. Dixon, "Structural basis for proofreading during replication of the Escherichia coli chromosome," *Structure,* vol. 10, no. 4, pp. 535-546, 2002.

[19] M. G. Cull and P. J. Schatz, "Biotinylation of Proteins in Vivo and in Vitro Using Small Peptide Tags," *Methods in enzymology,* pp. 430-439, 2000.

[20] N. A. Baker, D. Sept, S. Joseph, M. J. Holst, and J. A. McCammon, "Electrostatics of nanosystems: application to microtubules and the ribosome," *Proceedings of the National Academy of Sciences,* vol. 98, no. 18, pp. 10037-10041, 2001.

[21] M. Brucet *et al.*, "Structure of the dimeric exonuclease TREX1 in complex with DNA displays a proline-rich binding site for WW Domains," *Journal of Biological Chemistry,* vol. 282, no. 19, pp. 14547-14557, 2007.

[22] Y. Zuo *et al.*, "Crystal structure of RNase T, an exoribonuclease involved in tRNA maturation and end turnover," *Structure,* vol. 15, no. 4, pp. 417-428, 2007.

[23] Y.-Y. Hsiao, A. Nakagawa, Z. Shi, S. Mitani, D. Xue, and H. S. Yuan, "Crystal structure of CRN-4: implications for domain function in apoptotic DNA degradation," *Molecular and cellular biology,* vol. 29, no. 2, pp. 448-457, 2009.

[24] M. Wu, M. Reuter, H. Lilie, Y. Liu, E. Wahle, and H. Song, "Structural insight into poly (A) binding and catalytic mechanism of human PARN," *The EMBO journal,* vol. 24, no. 23, pp. 4082-4093, 2005.

[25] D. C. Chan, "Fusion and fission: interlinked processes critical for mitochondrial health," *Annual review of genetics,* vol. 46, 2012.

[26] S.-Y. Choi, P. Huang, G. M. Jenkins, D. C. Chan, J. Schiller, and M. A. Frohman, "A common lipid links Mfn-mediated mitochondrial fusion and SNARE-regulated exocytosis," *Nature cell biology,* vol. 8, no. 11, pp. 1255-1262, 2006.

[27] P. Mishra and D. C. Chan, "Mitochondrial dynamics and inheritance during cell division, development and disease," *Nature reviews Molecular cell biology,* vol. 15, no. 10, pp. 634-646, 2014.

[28] E.-M. Weick and E. A. Miska, "piRNAs: from biogenesis to function," *Development,* vol. 141,

no. 18, pp. 3458-3471, 2014.

[29] M. Uhlén *et al.*, "Tissue-based map of the human proteome," *Science,* vol. 347, no. 6220, 2015.

[30] A. I. Su *et al.*, "A gene atlas of the mouse and human protein-encoding transcriptomes," *Proceedings of the National Academy of Sciences,* vol. 101, no. 16, pp. 6062-6067, 2004.

[31] D. Anastasakis *et al.*, "Mammalian PNLDC1 is a novel poly (A) specific exonuclease with discrete expression during early development," *Nucleic acids research,* vol. 44, no. 18, pp. 8908-8920, 2016.

[32] N. Izumi *et al.*, "Identification and functional analysis of the pre-piRNA 3′ trimmer in silkworms," *Cell,* vol. 164, no. 5, pp. 962-973, 2016.

[33] R. Hayashi, J. Schnabl, D. Handler, F. Mohn, S. L. Ameres, and J. Brennecke, "Genetic and mechanistic diversity of piRNA 3′-end formation," *Nature,* vol. 539, no. 7630, pp. 588-592, 2016.

[34] J. J. Ipsaro, A. D. Haase, S. R. Knott, L. Joshua-Tor, and G. J. Hannon, "The structural biochemistry of Zucchini implicates it as a nuclease in piRNA biogenesis," *Nature,* vol. 491, no. 7423, pp. 279-283, 2012.

[35] S. Chuma, M. Hosokawa, T. Tanaka, and N. Nakatsuji, "Ultrastructural characterization of spermatogenesis and its evolutionary conservation in the germline: germinal granules in mammals," *Molecular and cellular endocrinology,* vol. 306, no. 1-2, pp. 17-23, 2009.

[36] Z. Otwinowski and W. i. Minor, "Processing of X-ray diffraction data collected in oscillation mode," *Methods in Enzymology,* vol. 276, pp. 307-326, 1997.

[37] A. J. McCoy, R. W. Grosse-Kunstleve, P. D. Adams, M. D. Winn, L. C. Storoni, and R. J. Read, "Phaser crystallographic software," *Journal of applied crystallography,* vol. 40, no. 4, pp. 658-674, 2007.

[38] P. Emsley, B. Lohkamp, W. G. Scott, and K. Cowtan, "Features and development of Coot," *Acta Crystallographica Section D: Biological Crystallography,* vol. 66, no. 4, pp. 486-501, 2010.

[39] P. D. Adams *et al.*, "PHENIX: a comprehensive Python-based system for macromolecular structure solution," *Acta Crystallographica Section D: Biological Crystallography,* vol. 66, no. 2, pp. 213-221, 2010.

[40] H. Jeong, J. Park, and C. Lee, "Crystal structure of Mdm12 reveals the architecture and dynamic organization of the ERMES complex," *EMBO reports,* vol. 17, no. 12, pp. 1857-1871, 2016.

Acknowledgements

2014년 처음 실험이라는 것을 제대로 배우며 생명과학에 대한 흥미를 가졌고, 학부연구생 2년과 대학원 5년의 긴 기간 동안 최선을 다해 실험에 몰두하고 연구에 집중하였습니다. 졸업을 앞둔 지금, 처음 단백질 결정을 얻었던 날, 처음 단백질 구조를 풀었던 날, 논문이 출판되던 날 등 소중하고 값진 모든 순간이 주마등처럼 지나가면서 감회가 새롭습니다. 그 동안 많은 분들의 도움을 받았기에, 학위 논문을 마무리하며 짧게 감사의 인사를 전합니다.

먼저 지도교수님이신 이창욱 교수님. 부족했던 저에게 아낌없는 조언과 격려로 좋은 연구자의 길이 무엇인지 알려주시고, 이끌어 주셔서 진심으로 존경하고 또 감사드립니다. 대학원 생활이 힘들고 지칠 때 교수님께서 해 주신 말씀들이 많은 힘이 되었습니다. 연구에 대한 열정, 참된 과학자의 연구자세 등 교수님의 가르침을 항상 마음에 새기며 좋은 과학자가 되기 위해 노력하겠습니다. 그리고 논문 심사 위원으로 많은 조언과 응원을 보내주신 강병헌 교수님, 임정훈 교수님, 기정민 교수님, 채영찬 교수님께도 다시 한번 감사의 말씀을 드립니다.

오랜 시간동안 동고동락해오며 식구처럼 지낸 학봉 선배, 동영이, 현우, 서황이 그리고 혜진이 모두 감사합니다. 함께 지내며 많은 의지가 되었고, 좋은 인연을 만들게 되어 값진 대학원 생활이 되었습니다. 교수님의 지도를 잘 따라서, 좋은 결과 잘 얻어서 원하는 바 이룰 수 있기를 항상 응원하겠습니다.

그리고 좋은 선배이자 든든한 지원군으로 물심양면으로 도와주고, 응원과 격려해주며 항상 힘이 되어준, 존경하는 선배에서 이제는 평생 함께 할 배우자가 된 정한빈 박사님, 고맙고, 사랑합니다.

무엇보다도 세상에서 제일 소중한 우리 가족이 저에게 준 무한한 믿음, 응원과 격려 덕분에 힘든 과정 속에서도 잘 견뎌내고, 잘 마무리할 수 있었습니다. 제가 선택한 길을 언

제나 지지해주신 아빠와 엄마, 진심으로 존경하고 감사드립니다. 또, 옆에 있는 것 만으로도 행복을 주고, 위로가 되어준 사랑하는 두 동생, 지윤이와 재민이도 고맙고 사랑해. 너희가 가려는 길도 많이 힘들고 지치겠지만, 내가 언제나 응원하고 있을게. 그리고 늘 예뻐해주시고 응원해주시는 시부모님과 아가씨께도 감사드립니다. 남편과 함께 초심을 잃지 않고 서로 잘 이끌어가는 좋은 모습 보여드리겠습니다.

일일이 언급하지는 못했지만, 대학원 기간동안 도움을 주셨던 많은 분들께도 감사의 말씀을 드립니다. 모든 분들의 도움과 응원을 항상 기억하며, 좋은 연구자의 길을 걸어갈 수 있도록 항상 정진하고, 또 좋은 모습으로 보답 드리겠습니다.

다시 한번 모든 분들께 감사의 마음을 전합니다.